

The Initial Conditions of High Mass Star-Formation

Thushara Pillai

Dissertation

zur

Erlangung des Doktorgrades (Dr. rer. nat.) der

Mathematisch-Naturwissenschaftlichen Fakultät

der

Rheinischen Friedrich-Wilhelms-Universität Bonn

vorgelegt von

Thushara Pillai

aus

Thiruvananthapuram, Indien
Bonn, December 2005

Angefertigt mit Genehmigung
der Mathematisch-Naturwissenschaftlichen Fakultät
der Rheinischen Friedrich-Wilhelms-Universität Bonn

Referenten: Prof. Dr. Karl M Menten^{1,2}
Prof. Dr. Frank Bertoldi²

¹ Max-Planck-Institut für Radioastronomie

² Universität Bonn

Diese Dissertation ist auf dem Hochschulschriftenserver der ULB Bonn
http://hss.ulb.uni-bonn.de/diss_online elektronisch publiziert 2006

Abstract

The field of star formation has seen a division in the last decades into two categories: *low-mass star formation* and *high-mass star formation (HMSF)*. The theoretical models for low mass star formations are at a far better footing in providing an explanation consistent with observations. However, theories fail to explain the formation of a high mass star (i.e. masses $M > 7 M_{\odot}$). Studies on the “real” initial stages alone will be able to solve the puzzle of the formation of a massive star. Only recently have clouds with the potential of forming high-mass stars and/or clusters, but still yet largely devoid of stellar objects, been identified: *Infrared Dark Clouds (IRDCs)*. My thesis focuses on the properties of these dark clouds that make them potential sites of the formation of high mass stars.

I studied the physical and chemical properties of this relatively new class objects. IRDCs were identified as dark patches against the bright mid-infrared emission in the galactic plane. My thesis work started with using NH_3 as the temperature probe on a sample of 9 dark clouds. Our observations allow the most reliable determination of gas temperatures in IRDCs to date. The gas emission is remarkably coextensive with the extinction seen at infrared wavelengths and with the submillimeter dust emission. Our results show that IRDCs are on average cold ($T < 20$ K) and have variations among the different cores. IRDC cores are gravitationally bound, are massive ($M > 100 M_{\odot}$), highly turbulent ($1 - 3 \text{ km s}^{-1}$) and exhibit significant velocity structure (variations around $1 - 2 \text{ km s}^{-1}$ over the cloud). We find a trend in temperature from colder IRDCs with high ammonia column density to high mass protostellar objects and hot core/Ultracompact HII regions, believed to trace different stages of early high-mass star formation.

In the next phase of the project, fractionated Ammonia (NH_3) observations were used to estimate the deuteration in a larger sample of massive cores. We find that 65% of the observed sources have strong NH_2D emission and a high degree of deuteration ($\geq 1\%$). We show that high deuteration is a definitive signature of pre/protocluster (thus cold) cores. The enhancement in deuteration coincides with strong CO depletion onto dust grains. In addition, we present interferometer observations of NH_3 and NH_2D using the VLA, BIMA and PdBI for two sources. The spatial distribution of NH_2D is clearly different from NH_3 as well as thermal dust continuum. The appearance of a protostar, as evidenced by outflow activity, destroys the deuterium-bearing molecules. Deuteration thus appears to signposts the cold, earliest stages of evolution in high mass molecular clouds. The cores identified within the clouds are massive and virial equilibrium calculations show that these cores are self-gravitating. The non-thermal motions in these cold clouds are clearly supersonic. Furthermore, turbulence appears to be the byproduct of an outflow activity, it steadily decays down with distance from the embedded protostar. These findings suggest that these high mass cold cores are the raw materials out of which high mass stars and star clusters form in the vicinity of Ultracompact HII regions.

Subsequently, we analysed the mid-infrared extinction properties of Infrared dark clouds (IRDCs). IRDCs are enveloped in lower density material and the masses we derive confirm the previous findings that IR dark clouds have high mass. We use a simple method of analysing the fractal nature of the cloud indirectly by studying the extinction count distribution. Subsequently, from the extinction PDFs, we

infer that self-similarity in IRDCs break down at scales of 0.2 – 0.5 pc. This scale regime is very much consistent with the turbulent Jeans length and therefore, IRDCs might be exhibiting a transition from turbulent fractals to thermal coherent cores at the sub-parsec scales.

Since 6.7 GHz CH₃OH maser and 22.2 GHz H₂O maser signpost active star formation, we performed a high resolution imaging survey of both maser types in a sample of infrared dark cloud cores. The survey has been carried out with the Very Large Array and the Australian Telescope Compact Array, as follow up of observations made at lower resolution with the Effelsberg 100 m telescope. The maser detection is a clear evidence of active star formation already ongoing in Infrared dark clouds.

Further, we did a comprehensive case study of an object heavily embedded in an IRDC. We find moderate to high-mass star formation in this dark cloud where we discovered class II methanol and water maser emissions at 6.7 GHz and 22.2 GHz, respectively. We also observed the object in ammonia inversion transitions. Strong emission from the (3,3) line indicates a hot (60 K) compact component associated with the maser emission. To further constrain the physical parameters of the source, we derived the spectral energy distribution (SED) of the dust continuum by analysing data from the 2MASS survey, HIRAS, MSX, the Spitzer Space Telescope, and interferometric 3mm observations. The SED was modelled in a radiative transfer program. The near IR data can be explained by scattering from tenuous material above a hypothetical disk.

Finally, we studied the properties of the dense cores in IRDCs at high angular resolution in NH₃ and N₂H⁺. The cloud morphology in NH₃ bears remarkable similarity to that observed in extinction seen with Spitzer and N₂H⁺ emission observed with the Berkeley-Illinois-Maryland-Association interferometer (BIMA). At high angular resolution, the filaments appear to fragment into dense cores. The clumps have significant velocity gradients. The mass estimates from our BIMA 3 mm continuum observations as well as from virial equilibrium calculations reveal that the cores are massive and stable entities. The observed line widths are much higher than the thermal line width. The warm material traced by NH₃ (3,3) is confined to only the densest core while the secondary cores are pre-dominantly cold. On the basis of this data, we can confirm that there is a clear bifurcation in the initial conditions of a high and low mass pre-stellar core.

To summarise, we can now infer that IRDCs comprise of a continuum from cores with all the expected characteristics for precluster cores which are gravitationally bound, cold, depleted and deuterated and turbulent to cores harboring clusters at very early stage which are slightly warmer and drive outflows. Thus, this work has provided evidence that within IRDCs, the long sought progenitors of high mass stars can be found.

Bonn, 2006 February 20
Thushara Pillai

Contents

1	Introduction	1
1.1	Dichotomy in Star Formation: Low & High Mass Stars	1
1.2	Infrared Dark Clouds	2
1.3	Galactic Distribution and Distances	3
1.4	Physical Parameters of IRDCs	4
1.4.1	Density, Column density and Temperature	4
1.4.2	Chemistry of IRDCs	6
1.5	Ongoing Star-Formation in IRDCs	6
1.6	The Aim and Structure of this Thesis	6
2	Ammonia in High Mass Infrared Dark Clouds	8
2.1	Introduction	8
2.2	Observations	9
2.3	Data Reduction and Analysis	10
2.4	Results	10
2.4.1	Cloud Morphology	10
2.4.2	Source Sizes	13
2.4.3	Line Profiles	13
2.4.4	Linewidth	13
2.4.5	Kinetic Temperature	16
2.4.6	Velocity Structure	18
2.4.7	Column Density, NH ₃ Abundance and Masses	18
2.5	Discussion	23
2.5.1	Gas Temperature and Distribution	23
2.5.2	Physical Properties, Chemistry & Lifetime	23
2.5.3	IRDCs and Other Star-forming Regions	24
2.5.4	IRDCs Formed by Interaction with SNRs ?	24
2.5.5	IRDCs in the Framework of an Evolutionary Sequence	25
2.6	Conclusions	27
3	Deuteration and Depletion in High Mass Clumps	33
3.1	Introduction	33
3.2	Observations	35
3.2.1	Single Dish Observations & Results	35
3.2.2	Interferometric Observations & Results	40
3.3	Analysis and Discussion	50
3.3.1	CO Depletion	50
3.3.2	NH ₃ Deuteration	53

3.3.3	Variations in HCN Isotopic Abundance	55
3.3.4	Probing Deuteriation at High Angular Resolution	57
3.3.5	Mass	59
3.3.6	Velocity Structure and Outflows : Kinematics	59
3.3.7	Comparison with MIR Morphology	61
3.4	Conclusion	61
4	Structure of High-Mass IR-Dark Clouds	66
4.1	Introduction	66
4.2	Archival Data from the Spitzer GLIMPSE Survey	67
4.3	Source Selection	67
4.4	Extinction: Map and PDF	68
4.5	Results and Discussion	69
4.5.1	Extinction Maps	69
4.5.2	Thermal Dust Continuum Emission and Absorption	74
4.5.3	Do We See Non-self Similar Structures?	76
4.6	Conclusion	77
5	Tracing Active Star Formation in IR-Dark Clouds	80
5.1	Introduction	80
5.2	Observations	81
5.2.1	Single-dish H ₂ O and CH ₃ OH Maser Observations	81
5.2.2	H ₂ O Maser Observations with the VLA	82
5.2.3	CH ₃ OH Maser Observations with the ATCA	82
5.3	Results	82
5.4	Discussion	86
6	High mass star formation in the IR-Dark Cloud G11.11–0.12	88
6.1	Introduction	88
6.2	Observations	89
6.2.1	CH ₃ OH Maser	89
6.2.2	Ammonia Observation	89
6.2.3	VLA H ₂ O Maser Observation	89
6.2.4	BIMA Observation	89
6.3	Results	90
6.3.1	CH ₃ OH Maser	90
6.3.2	3mm Continuum Emission	91
6.3.3	H ₂ O Maser	92
6.3.4	Ammonia towards G11.11P1	92
6.3.5	Archival Data	94
6.4	Discussion	95
6.4.1	CH ₃ OH Maser Disk Scenario	95
6.4.2	Mass & Luminosity Estimates	95
6.4.3	SED	96
6.5	Conclusion	98

7	Properties of Dense Cores in IR-Dark Clouds at High Angular Resolution	100
7.1	Introduction	100
7.2	Observations	101
7.2.1	VLA Observations	101
7.2.2	Short spacing : Effelsberg 100m observations	101
7.2.3	BIMA Observations	101
7.3	Data Reduction	102
7.4	Results, Interpretation and Discussion	102
7.4.1	From Parsec to Sub-parsec Scale	102
7.4.2	Core Properties	106
7.4.3	Gas Kinematics	109
7.4.4	NH ₃ (3,3) and Maser Emission	110
7.4.5	Dense Cores in IRDCs and Orion	110
7.5	Conclusions	113
8	Summary	118
8.1	Introduction	118
8.2	Ammonia in Infrared Dark Clouds	118
8.3	Deuteration and Depletion in High Mass Cold Cores	119
8.4	Structure of High-Mass Cold IR-Dark Clouds	119
8.5	Tracing Active Star Formation in Infrared Dark Clouds	120
8.6	High mass star formation in an Infrared Dark Cloud.	120
8.7	High Angular Resolution Observation Toward Infrared Dark Clouds	120
8.8	Outlook	121
8.8.1	Evolutionary sequence for Massive YSOs	121
8.8.2	Very Compact Radio Emission from the Massive Protostar with VLA	121
A	Radiative Transfer Calculations	123
A.1	Radiative Transfer Equations used for Column Density Determination	123
A.2	Radiative Transfer Model	123
B	List of Publications	125
	Acknowledgements	126
	Curriculum Vitae	127

Chapter 1

Introduction

This chapter is based on an invited review for the IAU Symposium 227.

1.1 Dichotomy in Star Formation: Low & High Mass Stars

The field of star formation has seen a division in the last decades into two categories: *low-mass star formation* and *high-mass star formation*. Observations reveal that while low-mass stars appear to form via both the isolated and the clustered mode of star formation, massive stars (i.e. masses $M > 7 M_{\odot}$) form only in massive clusters together with a large number of low-mass stars (Ward-Thompson 2002; Pudritz 2002).

The overwhelming advances in technology, with both space and ground based telescopes, have resulted in a far better understanding of star formation and evolution in general and low mass star formation in particular. However, there are several hurdles difficult to cross, when it comes to understanding the formation of a high mass star: they are more distant, are scarce in number, heavily extincted, have short evolution time scales, and dynamic and complex environments.

The theoretical models for low mass star formation are at a far better footing in justifying the available observations. We now know that the life of a low mass star begins with the collapse of a dense core in a cloud to form a protostar. The remnant cloud material further falls onto the protostar in a process called *accretion*, and the protostar grow in mass and size. In turn, the protostar exerts radiation warming up the incoming matter. Subsequently, deuterium burning starts followed by convection. All this while, matter keeps accreting onto the contracting protostar that eventually gains enough internal energy to ignite hydrogen. This model fairly well explains the formation of low and intermediate stars. However, the same model cannot explain the formation of a high mass star. For a high mass protostar, effects of strong winds and radiation pressure would halt any accretion of material once a mass $\geq 8 M_{\odot}$ has accumulated (Wolfire & Cassinelli 1987). Therefore, theoretically, high mass stars should not exist.

Two main theories have since been put forward to explain the formation of a massive star: *i*) high mass stars and clusters can form very similar to low mass stars via fragmentation of molecular clouds and subsequent accretion, however with a much higher rate of accretion (Padoan & Nordlund 2002) *ii*) HMSF is the result of a coalescence of lower mass protostars (Bonnell et al. 1998).

The advent of near infrared (NIR) array detectors in the last decade made NIR surveys of embedded clusters possible. These studies resulted in a path-breaking finding: the young stellar objects have a morphological sequence based on their spectral energy distribution (Lada 1987). They came to be known as Class I, II and III sources, corresponding to the youngest to the most evolved stage. Subsequent advances in bolometer technology added one more stage to the sequence, a still earlier protostar driving powerful outflows; Class 0 object, which is only detectable by the dust envelope it is enveloped in (André

et al. 1993). Again, the limitations of far-distant sources, large amounts of extinction, scarcity of samples etc has not so far allowed for such a classification scheme being established for high mass stars.

The large concentration of massive stars in regions of young clusters has been taken as an evidence for the coalescence theory (Zinnecker & Bate 2002). However, recent large scale surveys based on IRAS selected objects (Molinari et al. 2002, Beuther et al. 2002b) reveal deeply embedded objects with high bolometric luminosity which drive strong molecular outflows similar to their low mass counterparts. The discovery of these high mass protostellar objects (now known as HMPOs) have naturally favoured the accretion theory. However, even these supposed early stages are critically affected by the presence of multiple exciting sources and complex morphology.

What we are interested in is the stage just prior to the formation of a massive protostar. Studies on the “real” initial stages alone will be able to solve the puzzle of the formation of a massive star. Only recently have clouds with the potential of forming high-mass stars and/or clusters, but still yet largely devoid of stellar objects, been identified: *Infrared Dark Clouds*. My thesis focuses on the properties of these dark clouds that make them potential sites of high mass stars.

1.2 Infrared Dark Clouds

First recognized in mid-infrared images from the Infrared Space Observatory (ISO) and Midcourse Space Experiment (MSX) satellites, Infrared Dark Clouds (IRDCs) appear in silhouette against the Galactic mid-infrared (MIR) background, frequently in filamentary shapes. Perault et al. (1996) report that ISOGAL¹ images show “unexpectedly, a number of regions which are optically thick at $15\mu\text{m}$ which are likely due to absorption” and “a convincing correlation with a depletion in $2\mu\text{m}$ source counts”. They estimate $A_V > 25$ and put forward “that these would be good candidates for precursors of star formation sites.” Even before IRDCs became generally known as a distinct class of objects, Lis & Menten (1998) found absorption in the $45\mu\text{m}$ ISO LWS detector band against the MIR background and emission in the $173\mu\text{m}$ band toward M0.25+0.11, the low Galactic longitude end of the Galactic center “dust ridge”, a string of submillimeter (submm) condensations found by Lis & Carlstrom (1994) which terminates with the prominent Sgr B2 star-forming region at its high longitude end. M0.25+0.11 was studied, even earlier, in detail by Lis et al. (1994), who found very little, if any (a weak H_2O maser) signs of star formation in it. Lis & Menten (1998) performed grey body spectral fits to the far-infrared data combined with their previous $350 - 800\mu\text{m}$ submillimeter measurements and obtained a low temperature, $\sim 18\text{ K}$, for the bulk of the dust in M0.25+0.11’s core. In addition, they found that the grain emissivity is a very steep function of frequency ($\nu^{2.8}$). Lis & Menten derived a gigantic mass of $1 \times 10^6 M_\odot$ for this object, comparable to the core of the “mini starburst region” Sgr B2.

The first extensive dataset on IRDCs was compiled with the SPIRIT III infrared telescope aboard the Midcourse Space Experiment (MSX; see Price 1995), which surveyed the whole Galactic plane in a $b = \pm 5\text{ deg}$ wide strip (Price et al. 2001) in four MIR spectral bands between 6 and $25\mu\text{m}$ at a spatial resolution of $\sim 18''$. In an initial census of a $\sim 180\text{ deg}$ long strip of the Galactic plane (between $269\text{ deg} < l < 91\text{ deg}$, $b = \pm 0.5\text{ deg}$), Egan et al. (1998) find ~ 2000 “compact objects seen in absorption against bright mid-infrared emission from the Galactic plane. Examination of MSX and IRAS images of these objects reveal that they are dark from 7 to $100\mu\text{m}$.”

The IRDCs are best identified in the $8\mu\text{m}$ MSX “A” band, because, first, the 7.7 and $8.6\mu\text{m}$ PAH features associated with star-forming regions contribute to a brighter background emission and, second, the MSX A band is more sensitive than the satellite’s other bands. M0.25+0.11 and the other condensations of the Galactic center dust ridge also appear conspicuously in absorption on an $8\mu\text{m}$ MSX image presented by Egan et al. (1998). Hennebelle et al. (2001) in a systematic analysis of the ISOGAL images extracted a total of ~ 450 IRDCs, for which they derive $15\mu\text{m}$ opacities of 1 to 4.

¹ISOGAL is a 7 and $15\mu\text{m}$ survey with ISOCAM (the ISO 3 – $20\mu\text{m}$ camera) of $\sim 12\text{ deg}$ in the Galactic Plane interior to $|l| = 45\text{ deg}$.

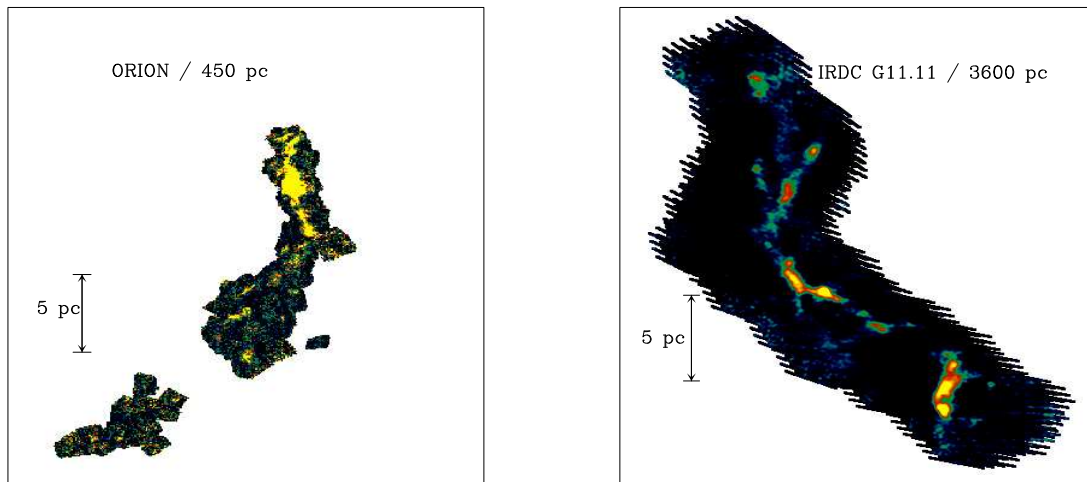


Figure 1.1: *Left panel:* 1.2 mm dust continuum map of the Orion Molecular Cloud 1 (courtesy T. Stanke). *Right panel:* 850 μm map of G11.11-0.12 (Johnstone et al. 2003).

Very recently Simon et al. (2005) used the 8.3 μm mid-infrared images acquired with the Midcourse Space Experiment satellite to identify and catalog Infrared Dark Clouds (IRDCs) in the first and fourth quadrants of the Galactic plane. Simon et al. (2005) identify 10,931 candidate infrared dark clouds and 12,774 cores. The catalog contains the position, angular size, orientation, area, peak contrast, peak contrast signal-to-noise, and integrated contrast of the candidate IRDCs and their cores.

How do IRDCs compare to the Orion Molecular Cloud I (OMC-1), probably the best-studied high-mass molecular cloud/star-forming region complex? In Fig.1.1, we show the 1.2 mm dust continuum emission from OMC-1 mapped with MAMBO² and the 850 μm SCUBA³ dust continuum map of IRDC G11.11-0.12 (Johnstone et al. 2003). At a distance of 3.6 kpc G11.11-0.12 has a remarkable resemblance with the integral-shaped Orion filament, both, in structure and in dimensions. The bright MIR emission along the Galactic plane favours the identification of a massive cold cloud as infrared dark, which the OMC-1 region is not due to the absence of a MIR background caused by its location outside of the Galactic plane. One glaring difference though exists between the two maps: the prominent maximum in OMC-1, marking the very active BN/KL high-mass stars-forming region.

1.3 Galactic Distribution and Distances

Using a standard Galactic rotation curve, Carey et al. (1998) determined kinematic distances for some of the IRDCs in their sample. They obtain distances between 2.2 and 4.8 kpc, proving without a doubt that the clouds are not local. Their distances agree with those of HII regions in their vicinity.

Recently, Simon et al. (2004) prepared a catalogue of ~ 380 IRDCs identified from the MSX survey, based on the morphological correlation of MIR extinction and ^{13}CO emission, as observed in the BU-FCRAO Galactic ring survey (GRS) of the inner Milky Way. They find that the majority of the dark clouds are concentrated in the Galactic ring at a galactocentric radius of 5 kpc. The kinematic distances derived range from 2 – 9 kpc. From the latest IRDC catalog, Simon et al. (2005) find that the distribution

²The MAx-Planck Millimeter BOlometer array is operated at the IRAM 30m telescope on Pico Veleta, Spain.

³The Submillimeter Common User Bolometer Array is operated at the 15 m James-Cleck-Maxwell Telescope on Mauna Kea, Hawaii.

of IRDCs closely follow the Galactic diffuse mid-infrared background and peaks toward prominent star forming regions, spiral arm tangents, and the so-called 5 kpc Galactic molecular ring.

The large extinctions at optical wavelengths had delayed the discovery of these distant clouds. This is clearly seen in Fig.1.2, where we compare the extinction map of the galactic plane with the MIR emission.

The cloud sizes as reported by Carey et al. (1998) are from 0.4 – 15 pc while Teyssier et al. (2002) report structures of filaments down to sizes ≤ 1 pc.

1.4 Physical Parameters of IRDCs

1.4.1 Density, Column density and Temperature

Based on observations of the formaldehyde molecule (H_2CO), Carey et al. (1998) argue that the IRDCs have dense ($n > 10^5 \text{ cm}^{-3}$), cold ($T < 20 \text{ K}$) cores, apparently without surrounding envelopes. However in a later work on a different IRDC sample, Teyssier et al. (2002) report that large field maps obtained with the 4-m Nanten telescope in the $^{13}\text{CO } J=1-0$ line, which probes relatively low densities, (Zagury et al., unpublished data) indicate that at least these IRDCs may indeed have lower density envelopes. We have confirmed this for the Carey et al. sample with hitherto unpublished $^{13}\text{CO } J=1-0$ maps retrieved from the GRS.

Carey et al. (1998) conclude that the IRDCs they have studied have extinctions in excess of 2 mag at $8 \mu\text{m}$. Using the infrared (visual through $30 \mu\text{m}$) extinction law (Lutz et al. 1996) derived for the Galactic center, this indicates visual extinctions of > 30 mag. How representative Lutz et al.’s law is for other lines of sight is unknown. Certainly it does lack the pronounced minimum for standard graphite-silicate mixes in the $4 - 8 \mu\text{m}$ range predicted by Draine & Lee (1984), which seems well-established by observations toward various lines-of-sight (see references therein).

Actually, IRDC opacities at two wavelengths (e.g. 7 and $15 \mu\text{m}$) can be used as a check on the extinction curve and its possible variation with different lines of sight; see Teyssier et al. (2002). These authors find a (marginally) lower 7 to $15 \mu\text{m}$ opacity ratio for clouds located away from the Galactic center compared to clouds that appear in the Galactic center direction. For the latter value they derive ~ 1 , which is consistent with Lutz et al.’s law.

Using the relation given by Bohlin et al. (1978), assuming that all the hydrogen is in molecular form and a “standard” ratio of total to selective extinction of 3.1, hydrogen column densities in excess of $3 \times 10^{22} \text{ cm}^{-2}$ is derived.

Carey et al. (2000) imaged a sample of 8 IRDCs in 450 and $850 \mu\text{m}$ dust emission using SCUBA. Since it is impossible to determine, both, T_{D} and β with just two data points, Carey et al. calculated dust color temperatures for three different values of β , 1.5, 1.75, and 2 and note that higher β -values (meaning lower temperatures) yield a better fit to the low temperatures Carey et al. (1998) obtained from H_2CO observations. The (high) column densities implied by choosing $\beta = 2$ are around $5 \times 10^{22} \text{ cm}^{-2}$ for 4 sources of their sample and around $13 \times 10^{22} \text{ cm}^{-2}$ for three. Three of the cores corresponding to the brightest submm peaks have masses around $100 M_{\odot}$, two other have 400 and $1200 M_{\odot}$, respectively. Two clouds in the Cygnus region have masses around $40 M_{\odot}$, but we note that distance estimates for that region are very uncertain and probably a short distance (1 kpc used by Carey et al. 1998) was chosen for the latter calculations. For $\beta = 1.75$, all these values are to be reduced by a factor of 2.

As reported above (see §1.2), for M0.25 Lis & Menten derive a very high value of β of 2.8. They take that to indicate the presence of dust grains covered with thick ice mantles.

The values for the high densities and low temperatures deduced by Egan et al. (1998) are confirmed by Carey et al. (1998), who made, for 10 IRDCs, millimeter-wavelength observations of H_2CO , which is a well-established density probe (Mangum & Wootten 1993). Since they observed several transitions, they were able, using a Large Velocity Gradient method, to determine temperatures and abundances. Unfortunately, these authors do not discuss their results source by source, but only give general statements.

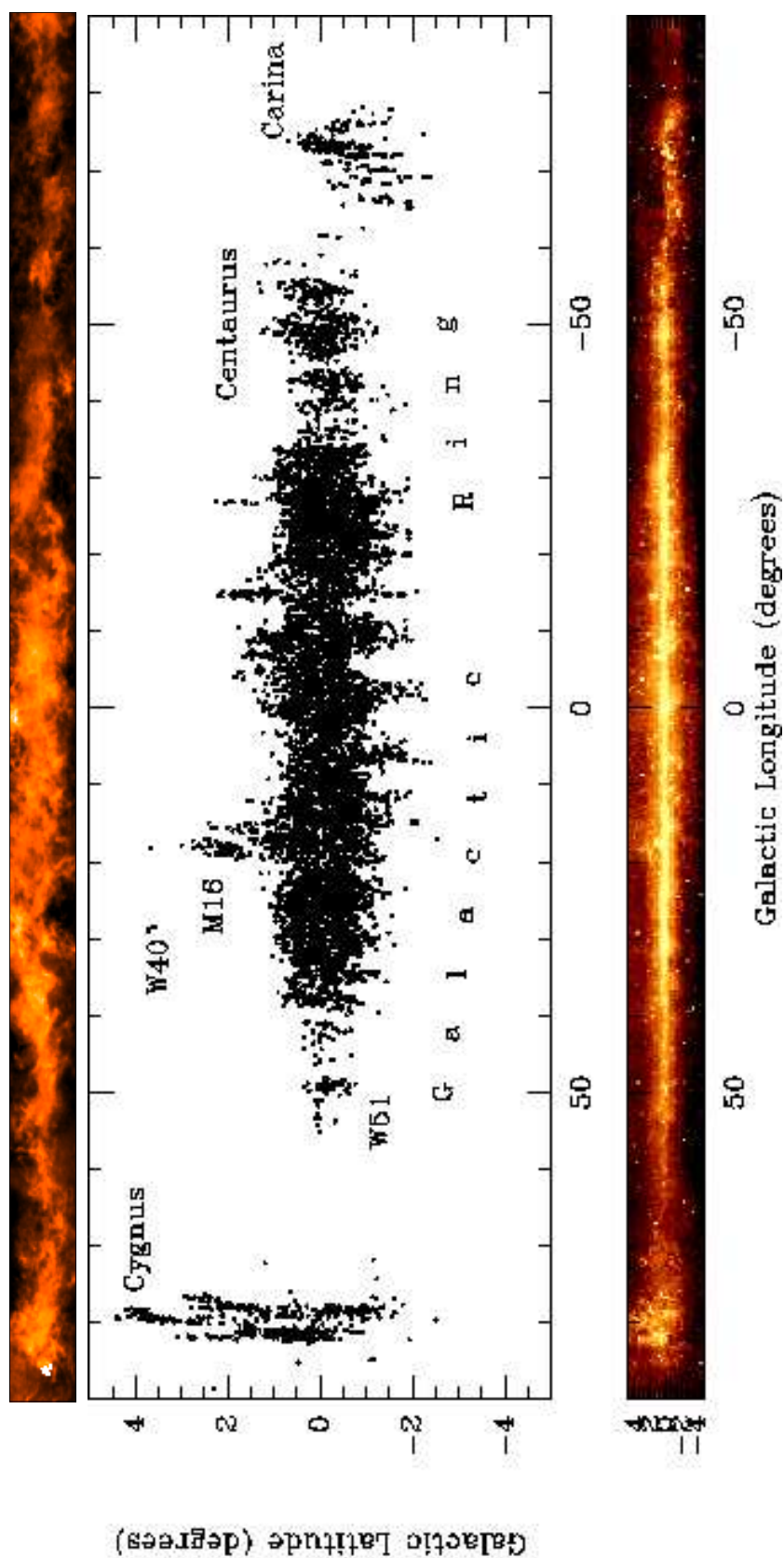


Figure 1.2: *Bottom panel:* MSX image of $8.3\mu\text{m}$ emission along the first and the fourth quadrant of the galactic plane. *Middle panel:* The distribution of IRDCs along the same region. The prominent star formation regions are labelled. (Simon et al. 2005) *Top panel:* An extinction map of the same region derived by using the optical database Digitized Sky Survey I (DSS) (Dobashi et al. 2005).

Leurini et al. (2004) has shown that methanol (CH_3OH) is a highly useful interstellar density and temperature probe. Consequently, she conducted observations of IRDCs in a selected series of lines of that molecule, which she showed to be overabundant in these sources and, thus, easy to detect. Leurini also corroborates the high densities ($\sim 10^5 - 10^6 \text{ cm}^{-3}$) indicated by the H_2CO data. However, she only observed positions of submillimeter emission peaks, some of which (if not all) harbour embedded sources. Her analysis does, thus, not necessarily apply to general, cool IRDC material, but to gas that is influenced by embedded protostars.

1.4.2 Chemistry of IRDCs

Observations of molecules in IRDCs so far have concentrated on just a few species: CO (several isotopomers), H_2CO and CH_3OH . In addition, Teyssier et al. (2002) observed several HC_3N lines and two k -series of CH_3CCH . The latter, a symmetric top, can be used as a temperature probe and its observations yield values for the kinetic temperature, T_{kin} , between 8 and 25 K; the higher values found toward embedded objects. Large Velocity Gradient (LVG) model calculations of HC_3N , ^{13}CO , and C^{18}O yield densities larger than 10^5 cm^{-3} in the densest parts. Teyssier et al. ascribe the relatively low observed intensities (a factor of a few lower than in TMC-1) to a very low kinetic temperature (difficult to understand, as TMC-1 is cold, too, $\approx 10 \text{ K}$), a small filling factor or depletion on grains.

Systematic searches for other molecules will yield a more complete picture of the chemistry of IRDCs, which, while certainly interesting in itself, will also shed light on general formation mechanisms of complex molecules. Moreover, they might help identify new temperature and density tracers and allow studies of (molecule-)selective depletion.

1.5 Ongoing Star-Formation in IRDCs

While large volumes of IRDCs appear to be devoid of signposts of ongoing star formation, such as ultracompact HII regions and/or CH_3OH , OH or H_2O masers, isolated centers of high or intermediate star formation are found in many clouds.

Teyssier et al. (2002) found that OH and class II CH_3OH masers are associated with positions of (not overly pronounced) peak emission from the column density tracer C^{18}O in the IRDCs DF+9.86-0.04 and DF+30.23-0.20. These are close to dust emission peaks.

Ormel et al. (2005) modelled the $450\mu\text{m}$ and $850\mu\text{m}$ continuum and HCO^+ line observations of three distinct cores of an infrared dark cloud (IRDC) in the W51 GMC. They find that sources of $\approx 300 L_{\odot}$ are embedded within the cores and all three cores have similar masses of about $70 - 150 M_{\odot}$. Rathborne et al. (2005) conducted a multiwavelength study of the infrared dark cloud MSXDC G034.43+00.24. Their observations reveal three compact cores within this infrared dark cloud with masses of $170 - 800 M_{\odot}$ and sizes $< 0.5 \text{ pc}$. Their millimeter-to-mid-IR continuum spectral energy distributions reveal very high luminosities, ($9000 - 32,000 L_{\odot}$).

Combining mid-infrared data from the SPITZER Space Telescope with cold gas and dust emission observations from the Plateau de Bure Interferometer, Beuther et al. (2005) characterize the Infrared Dark Cloud IRDC18223-3 at high spatial resolution. They find a $184 M_{\odot}$ gas core with a projected size of 28000 AU that has no associated protostellar mid-infrared counterpart. Based on the detection of $4.5 \mu\text{m}$ emission at the edge of the core and broad CO and CS spectral line-wing emission, they claim to find evidence of an early stage of massive star formation.

1.6 The Aim and Structure of this Thesis

The earliest phases of high-mass star formation are expected to take place in massive (a few hundred to thousand M_{\odot}), cold ($10 - 20 \text{ K}$) and quiescent clouds, emitting primarily at (sub)mm wavelengths and

containing no obvious IR sources or star formation tracers. One approach to identify the earliest, cold phases of massive star formation is to search for objects which appear in absorption at MIR wavelengths. Thus IRDCs are the most potential candidates for studying these initial conditions. Extensive studies of their energetics, kinematics and chemistry are essential to ascertain their role in forming stars, massive or otherwise. These would be the ideal test grounds for testing the existing theories of forming massive stars.

In Chapter 2 we begin with an analysis of single dish NH_3 (1,1) and (2,2) observations toward a sample of 9 IRDCs. We study the temperature structures and velocity fields and gain information on the chemical evolution in IRDCs. A deuteration and depletion study toward a large sample of high mass cold clumps are discussed in Chapter 3. In this chapter, we discuss the deuteration results at high angular resolution for two sources and discover the chemical signature of a massive pre-protostellar core. In Chapter 4, we probe the fractal nature of four IRDCs and estimate their characteristic size scale. Active star formation that might have begun in the most evolved cores is traced by methanol and water maser emission. Chapter 5 discusses the survey results. A case study toward an IRDC at multi-wavelengths is reported in Chapter 6. Finally, we present interferometer observations that reveal for the first time, the core properties and the dynamics of the environment in Chapter 7.

The results of this work are summarized in Chapter 8 and an outlook for the project is developed.

Chapter 2

Ammonia in High Mass Infrared Dark Clouds

This chapter is based on a paper accepted by Astronomy & Astrophysics.

We mapped the $(J, K) = (1, 1)$ and $(2, 2)$ inversion transitions of ammonia in 9 infrared dark clouds (IRDCs), amongst them some of the best-studied sources of this type. Toward all of the sources in our sample previously submillimeter dust continuum emission and millimeter rotational lines of H_2CO had been studied. Our observations allow the most reliable determination of gas temperatures in IRDCs to date. We analyse temperature structures and velocity fields and gain information on chemical evolution. The gas emission is remarkably coextensive with the extinction seen at infrared wavelengths and with the submillimeter dust emission. Our results show that IRDCs are on average cold ($T < 20$ K) and have variations among the different cores. IRDC cores are in virial equilibrium, are massive ($M > 100 M_\odot$), highly turbulent ($1 - 3 \text{ km s}^{-1}$) and exhibit significant velocity structure (variations around $1 - 2 \text{ km s}^{-1}$ over the cloud). We find a trend in temperature from colder IRDCs with high ammonia column density to high mass protostellar objects and hot core/Ultracompact HII regions, believed to trace different stages of early high-mass star formation. The line widths of IRDCs are smaller than those observed in high mass protostellar objects and Ultracompact HII regions. On the basis of this sample, and by comparison of the ammonia gas properties (line widths, mass, and temperature) within a cloud and between different clouds, we infer that while active star formation is not yet pervasive in most IRDCs, local condensations might collapse in the future or have already begun forming stars including high-mass ones.

2.1 Introduction

Observations of molecules in IRDCs so far have concentrated on just a few species. Up to now there has been no systematic study on the temperature distribution, velocity fields, chemical and physical state toward this new cloud population. Knowing these properties is crucial for understanding the presence, absence and the very potential of star formation. The present paper aims at addressing these questions. We have started with a survey of a sample of 9 IRDCs in $(1, 1)$ and $(2, 2)$ cm rotational transitions of ammonia (NH_3). This sample, as described earlier in this section, which has been studied before by Carey et al. (1998), Carey et al. (2000), and have been selected on the basis of their large extent and high contrast against the MIR background.

Ammonia has proven to be an important tool in measuring the physical conditions in molecular clouds (Ho & Townes 1983). Since only the lowest NH_3 energy levels are expected to be populated for cool dark clouds ($T < 20$ K), their physical conditions can be probed using the $(1, 1)$ and $(2, 2)$ inversion transitions

in the metastable (J, K) rotational levels of ammonia. Radiative transitions between different K -ladders are forbidden, therefore the lowest levels are populated only via collisions. The optical depth can be determined from the ratio of the hyperfine satellites. Thus, the population of the different levels can be estimated and hence the temperature of the gas determined. In addition, recent chemical models reveal that NH_3 (and also N_2H^+), does not deplete from the gas phase for the densities observed in IRDCs ($< 10^6 \text{ cm}^{-3}$) (Bergin & Langer 1997). Thus NH_3 is an excellent tracer of the dense gas where many other molecules would have heavily depleted.

In §2.2, we give details on our observation with the Effelsberg 100m telescope. In §2.3, we discuss the data reduction and present the correlation between gas emission and MIR absorption. In §2.4, we derive the rotational temperature, gas kinetic temperature and NH_3 column density. Furthermore, we analyse the velocity structure, estimate dust mass, virial mass and NH_3 abundance. In §2.5, we compare the core gas properties (temperature, NH_3 line widths and column density) with that of other populations of objects that are thought to trace the early stages of high mass star formation. We do a similar comparison with local dark clouds well-studied in NH_3 . Finally, we speculate on a possible formation mechanism of IRDCs involving supernova remnants.

2.2 Observations

We mapped the IRDCs listed in Table. 2.1 with the Effelsberg 100m telescope of the Max-Planck-Institut für Radioastronomie in October 1999. The frontend was the facility 1.3 cm maser receiver tuned to a frequency of 23.7 GHz centered between the NH_3 (1,1) and (2,2) transitions. The spectrometer was a 8192 channel auto-correlator used with 2 subunits of 20 MHz bandwidth each. The resulting spectral resolution was $\approx 0.2 \text{ km s}^{-1}$ after smoothing the data to increase the signal-to-noise ratio. The beamwidth at the frequencies of the NH_3 lines is $40''$ (FWHM). The observations were conducted in frequency switching mode with a frequency throw of 7.5 MHz. The maps toward all sources covered the extinction seen in the MSX images and were made with half power beamwidth (HPBW) spacing ($40''$). Alternate scans were inter-spaced at half the full beamwidth resulting in $\approx 20 \times \sqrt{2}$ spacing. Pointing was checked at roughly hourly intervals by means of continuum drift scans on nearby pointing sources. We found the pointing to be accurate to within $12''$.

Absolute calibration is not an issue in determining the rotational temperature, because it is solely governed by the ratio of the $\text{NH}_3(1,1)$ hyperfine lines and the (1,1) and (2,2) brightness temperatures. However, in order to estimate the excitation temperature and the column density the data needs to be calibrated. The calibration procedure is documented on our webpage¹. The important steps are mentioned below. The 100m data (normally in CLASS format) is in arbitrary noise tube units (T_N) and has to be converted to main beam brightness temperature units. We observe a standard flux calibrator with known flux S_λ at wavelength λ and thus estimate the conversion factor from T_N scale to Jy.

The main beam brightness temperature T_{MB} of the calibrator for a given beamwidth θ and wavelength λ is then given by

$$(T_{\text{MB}}/\text{K}) = \frac{(S_\lambda/\text{Jy}) \times (\lambda/\text{cm})^2}{(\theta/\text{arcmin})^2 \times 2.65}. \quad (2.1)$$

The primary flux calibration is based upon continuum scans of NGC7027 assuming a flux density of $\approx 5.6 \text{ Jy}$ (Ott et al. 1994). The Ultracompact HII (UCHII) regions G10.62-0.38 and G34.26+0.15 and the quasar J1743-038 were used as secondary calibrators which span the entire elevation range and an elevation-dependant calibration factor was derived. The maximum rms uncertainty in calibration for elevations lower than 19° is 15%.

¹www.mpifr-bonn.mpg.de/staff/tpillai/eff_calib/index.html.

2.3 Data Reduction and Analysis

The spectra were reduced using the CLASS package (Forveille, Guilloteau, & Lucas 1989). For a given source, the spectra were averaged and a polynomial baseline of order 3 – 5 subtracted.

The maps were generated by convolving the original data using a Gaussian function with a HPBW of 40". Table 2.1 reports the coordinates of the central position for each map.

MSX 8 μ m images of these clouds with superimposed contours of the NH₃ (1,1) integrated intensity are shown in Fig. 2.1. The velocity range used for integration is within ± 25 km s⁻¹ of the 'Local Standard of Rest Velocity', V_{LSR} , hence including the satellite lines. The NH₃ maps of G79.27+0.38 and G33.71-0.01 have clumpy structures. Some of the clumps may be artificial and caused by the low signal-to-noise ratio.

The reduced (1,1) and (2,2) spectra for the NH₃ peak positions of the observed sources are shown in Fig. 2.2. NH₃(1,1) observations were reduced using "METHOD NH3(1,1)" in CLASS to fit the hyperfine structure and derive optical depths and linewidths. The standard procedure to analyse the NH₃ (1,1) and (2,2) lines have been described in detail by Bachiller et al. (1987).

The hyperfine structure of the (2,2) line is too weak to be observed; therefore, the optical depth could be obtained only for NH₃(1,1). The NH₃(1,1) and (2,2) main beam brightness temperatures are obtained by fitting the main line with a single Gaussian. The (1,1) and (2,2) linewidth is obtained by the hyperfine fitting which accounts for the line broadening due to optical depth effects excluding self-absorption. The parameters obtained from the fits to the (1,1) hyperfine lines are listed in Table 2.2.

The basic physical parameters, namely the excitation temperature, rotational temperature, the kinetic temperature and ammonia column density, have been derived using the standard formulation for NH₃ spectra (Ho & Townes 1983). Table 2.3 summarises the estimates of these parameters toward the cores. We give the formal errors (1σ), derived from Gaussian error propagation.

2.4 Results

Our sample consists of both 'Infrared dark clouds', with extents of ~ 1 –10 pc, and 'Infrared dark cloud complexes', which are comprised of multiple individual clouds. IRDC G11.11-0.12 would thus be a complex (> 4 pc) while G24.63+0.15 would be a dark cloud. The IRDCs G79.34+0.33 and G79.27+0.38 are essentially two parts of the same extended filament in the Cygnus-X region connected by a bright patch of dust emission as seen in SCUBA and MSX images (Redman et al. 2003).

2.4.1 Cloud Morphology

There is generally a close match between the ammonia emission and the mid-infrared extinction as shown in Fig. 2.1. In G24.72–0.75 and G79.34+0.33, the NH₃ emission peak is however correlated with bright and compact MIR emission. Redman et al. (2003) find that the MIR emission in G79.34+0.33 corresponds to a luminous 'Young Stellar Object' (YSO) with a strong IR excess which might be interacting with the foreground IRDC. No such interaction has been reported for the IRDC G24.72–0.75 and the nature of the MIR object is unknown.

In general, the cloud geometry is extended and filamentary and in no case close to spherical. The mean aspect ratio determined by fitting 2D ellipse to the entire NH₃ emitting region is 2.2 and the total extent of the clouds ranges from 0.4 – 8.3 pc. G11.11-0.12 is a filamentary cloud as revealed by the 8 μ m extinction and the 850 μ m dust emission as shown in Fig. 2.3. The peaks of the submm emission are strikingly coincident with the ammonia cores. The NH₃ map reveals at least two peaks toward the north-east segment and another set of peaks towards the southwest extension of the filament suggesting that there are several unresolved sub-structures or cores within the extended filament.

The strongest submm emission peak P2 in G28.34 is in the close vicinity of the IRAS source 18402-0403. But the peak of the ammonia emission for the northern extension seems to be offset from that of

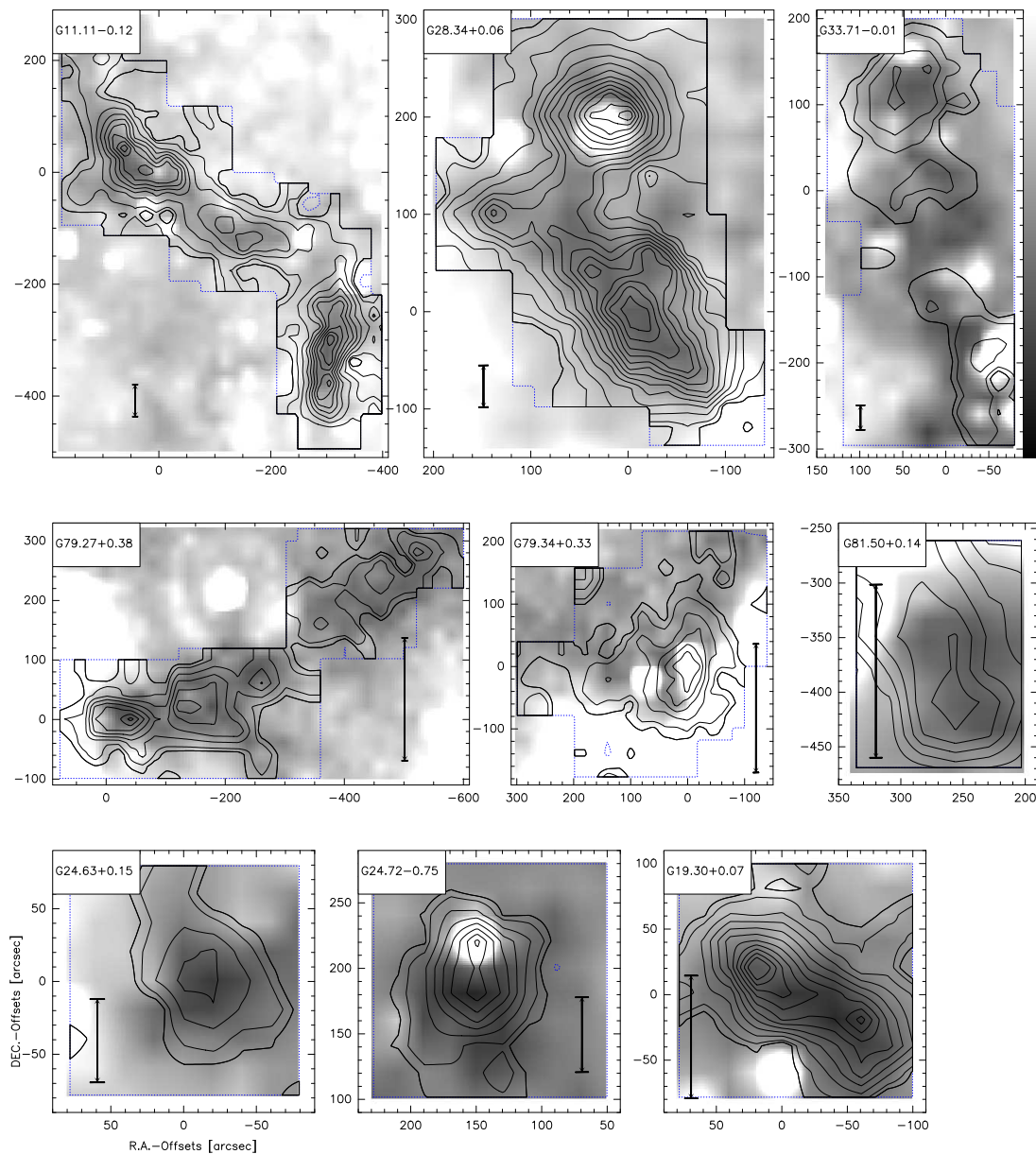


Figure 2.1: MSX image of the clouds at $8.3\mu\text{m}$ (greyscale) with NH_3 (1,1) integrated intensity as contours. The NH_3 (1,1) maps have a resolution of $40''$ and the same spacing. The greyscale corresponds to intensity range shown by the wedge in the upper right corner (from dark to light). The contour levels are -2σ , 1σ , 2σ , 4σ , 6σ ... The rms noise levels are given in Table 2.2. The approximate map boundary is also indicated. Tick marks are coordinate offsets (in arcseconds) relative to the positions given in Table 2.1. The bar indicates a length of 1 pc at the distance of each IRDC.

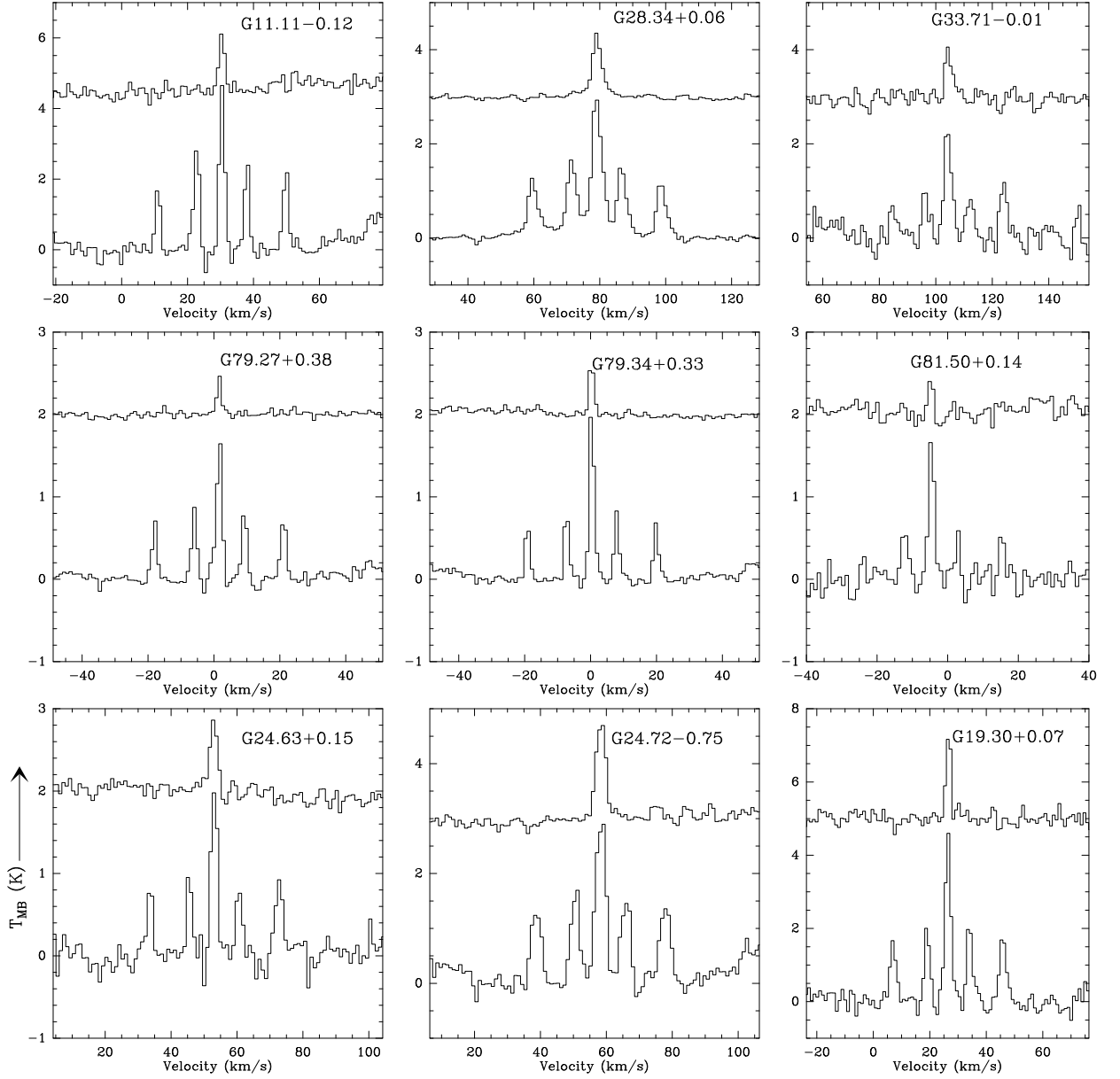


Figure 2.2: $\text{NH}_3(1,1)$ (lower histogram in each panel) and $(2,2)$ (upper histogram, offset from 0 K for clarity) spectra toward the brightest position of the 9 observed sources. The brightest positions are referred to as NH_3 P1 in Table 2.3.

the IRAS source (see Fig. 2.4). This could be due to the interaction of the IRAS source with the cloud.

2.4.2 Source Sizes

Due to the large distances to the clouds, the compact structures within the cloud are marginally resolved with the $40''$ beam of our NH_3 observations. Hence, estimating the size of the core from NH_3 might only deliver upper limits of the order of the beam size. We use channel maps to solve the problem of identifying clumps. The information in the third dimension enables us to disentangle clumps that are sufficiently well separated in velocity. For those sources with SCUBA $850\mu\text{m}$ data, we cross-identify the clumps within half the NH_3 beam ($\sim 20''$) at the higher SCUBA resolution ($\sim 14''$) and estimate the source size by a 2D Gaussian fit to the clumps in the SCUBA data. In cases where we do not have dust emission maps, we use the 2D Gaussian fit routine in GRAPHIC. It searches for the brightest pixel in each velocity channel of the channel map across the NH_3 (1,1) main component and fits a 2D Gaussian to determine source size. The output is then cross-checked over the different channels and the fit obtained for the brightest emission is used. We find 1 – 5 clumps for each cloud. The source sizes after correcting for the beam size (after subtracting the Gaussian beam size in quadrature) are listed in Table 2.3. The dense cores within these IRDCs are thus not resolved with the $40''$ 100m beam. We find several secondary peaks offset by $> 1\sigma$ in most sources; offsets from the central position are given in Table 2.3. Table 2.3 should be referred to for the nomenclature of the clumps identified in the NH_3 maps and/or the SCUBA $850\mu\text{m}$ images hereafter.

2.4.3 Line Profiles

In general, NH_3 lines are brighter than the mm rotational H_2CO transitions observed by Carey et al. (1998). As given in Table 2.2, the (2,2) peak line intensity is on average 40% of that of the (1,1) line. Gaussian line profiles with extended wings have been reported for H_2CO lines in most of the clouds (Carey et al. 1998) but we do not observe any pronounced wings in NH_3 . Leurini et al. (2006 submitted) find line profiles similar to those observed in H_2CO in the mm transitions of CH_3OH .

2.4.4 Linewidth

The width of a spectral line is an important parameter because it is a measure of the total kinetic energy of the cloud. The $\text{NH}_3(1,1)$ linewidths for all sources lie between $0.8 - 3\text{ km s}^{-1}$. The H_2CO linewidths are significantly larger (factor 2) than the NH_3 linewidths in all cases except G81.50+0.14, where the NH_3 linewidths are twice as large.

The NH_3 linewidths for our sample are higher than those of NH_3 cores reported in Jijina et al. (1999), which are mostly low mass cores. The large linewidths might be explained as due to clumping. Clumps with smaller linewidth but with a higher clump-to-clump velocity dispersion may add up to the observed linewidths. The sources closest to us (G79 IRDCs) have the smallest linewidth and belong to the Cygnus-X region. In order to test whether the larger linewidth we observe at larger distance is a distance effect, we average the G79 IRDC linewidth over an area $\delta A \propto (d_{\text{far}}/d_{\text{Cyg}})^2$ where d_{far} is the distance to a source farther than Cyg and with a much higher linewidth. On comparing the resultant scaled values, we find that the linewidths are still significantly larger for the sources at larger distances after accounting for the larger region in each beam for the more distant cores.

To illustrate this point, let us take the example of the two extreme values of linewidths from our sample. Dark core G79.27+0.38 NH_3 P2 (at 1 kpc) has a linewidth at the brightest position of 0.83 km s^{-1} while G28.34+0.06 NH_3 P2 (at 4.8 kpc) has a linewidth of 2.65 km s^{-1} . Neither of the two cores have a MIR counterpart which might indicate any deeply embedded protostar influencing its immediate environments. Averaging all the emission in G79.27+0.38 over an area of $\sim 200 \times 200''$, we obtain a linewidth of

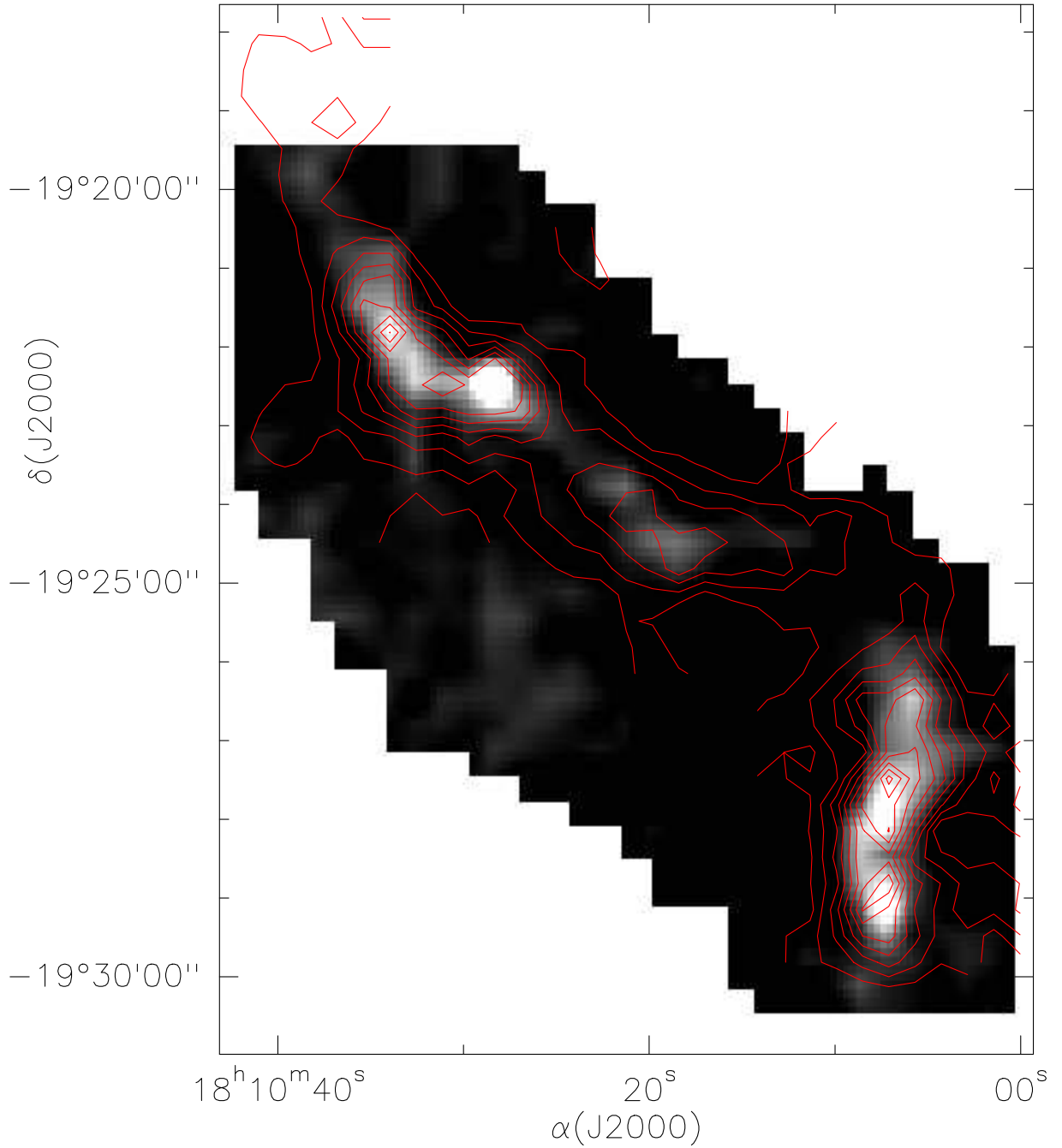


Figure 2.3: SCUBA $850\mu\text{m}$ image (Carey et al. 2000) of the cloud G11.11-0.12 with $\text{NH}_3(1,1)$ integrated intensity as contours. The contour levels are multiples of 2σ . SCUBA image has a resolution of $14''$.

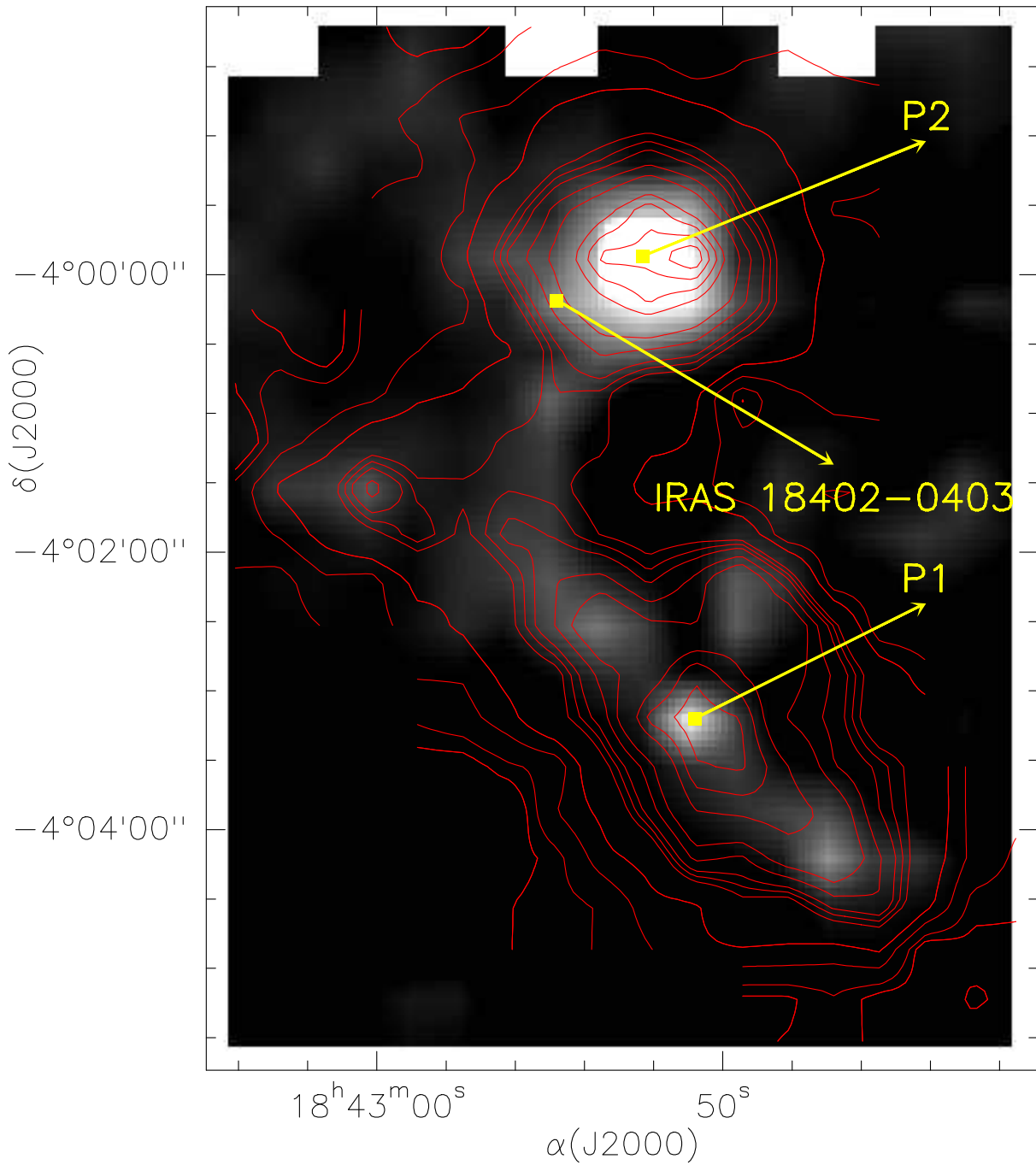


Figure 2.4: SCUBA 850 μ m image of G28.34 with NH₃ (1,1) integrated intensity as contours. The contour levels are (2 σ , 4 σ , 6 σ ...).

1.5 km s⁻¹, still smaller than 2.65 km s⁻¹. Therefore, the large linewidths derived appears to be mainly due to the velocity dispersions within the beam.

One of the assumptions made to derive the temperature is that the beam filling factor is the same for both inversion lines; that is, the two lines are emitted by the same volume of gas. The (2,2) linewidths are slightly larger than the (1,1) linewidths (cf. Table 2.2) toward only some cores, suggesting that the same gas is not exactly traced by both lines in those sources.

The linewidths exhibited by these sources are much larger than the thermal linewidth, Δv_{th} , which for $T_{\text{kin}} \sim 20\text{K}$ should be ~ 0.22 km s⁻¹ as per the relation

$$\Delta v_{\text{th}} \sim \sqrt{\frac{8 \ln(2) k T_{\text{kin}}}{m_{\text{NH}_3}}}, \quad (2.2)$$

where k is Boltzmann's constant and m_{NH_3} is the mass of the ammonia molecule. Average linewidths ~ 2 km s⁻¹ could be explained in terms of velocity gradients due to rotation of the cloud, or turbulent cloud movements. The linewidths seems to be especially high towards the cloud G28.34+0.06, where there are several unresolved NH₃ clumps, identified in the SCUBA images. In the G79 IRDC the linewidth decreases from G79.34+0.33 NH₃ P1 (1.22 ± 0.03 km s⁻¹) to G79.27+0.38 NH₃ P3 (0.82 ± 0.03 km s⁻¹). As shown in Fig. 2.5, we find that the linewidth anti-correlates with optical depth for G28.34 while there is a possible positive correlation G79.27.

G79.27+0.38 NH₃ P1 seems to be more quiescent than its surroundings. In the G79 cloud complex, there is considerable difference in linewidth (~ 0.5 km s⁻¹) between the different clumps along the cloud from east to west. Thus, these clouds might be harbouring objects at different stages of evolution (Redman et al. 2003).

2.4.5 Kinetic Temperature

Since the optical depth is known, we derive the excitation temperature of the NH₃ (1,1) inversion transition (Table 2.3) via the relation

$$T_{\text{EX}} = \frac{T_{\text{MB}}}{1 - e^{-\tau}} + 2.7 \text{ K}, \quad (2.3)$$

where T_{MB} and τ represents the temperature and the optical depth of the of the (1,1) line. By fitting the main and the hyperfine components of the (1,1) line and the main component of the (2,2) line, we obtain the rotational temperature. An analytical expression (Tafalla et al. 2004) has been used to estimate the kinetic temperature from the rotational temperature. The kinetic temperature is given by the expression

$$T_{\text{kin}} = \frac{T_{\text{rot}}}{1 - \frac{T_{\text{rot}}}{42} \ln[1 + 1.1 \exp(-16/T_{\text{rot}})]}, \quad (2.4)$$

The typical temperatures for the cores range from 11 – 17 K as displayed in Table 2.3. In some cases, we find that the fit to the NH₃(1,1) line slightly underestimates the peak intensity.

We find that the kinetic temperature is significantly higher than the excitation temperature, as given in Table 2.3. The beam filling factor η is a measure of the fraction of the beam filled by the observed source. Assuming that the cores are in local thermodynamic equilibrium (LTE), we may estimate this fraction as $\eta = T_{\text{EX}}/T_{\text{kin}}$ where T_{kin} is the kinetic temperature of the gas. We derive filling factors of $\sim 0.3 - 0.5$ for all the clumps. These low filling factors suggest either sub-thermal excitation (non LTE conditions) or clumping within the beam. From our estimation of the sizes (Table 2.3), we find most of the cores are unresolved with the 40'' beam. Thus clumping is more likely to explain the small filling factors.

We find hints of temperature gradients (inside-out) within the cores in three sources and a reverse gradient in one source. However the large error bars associated with the rotational temperature does

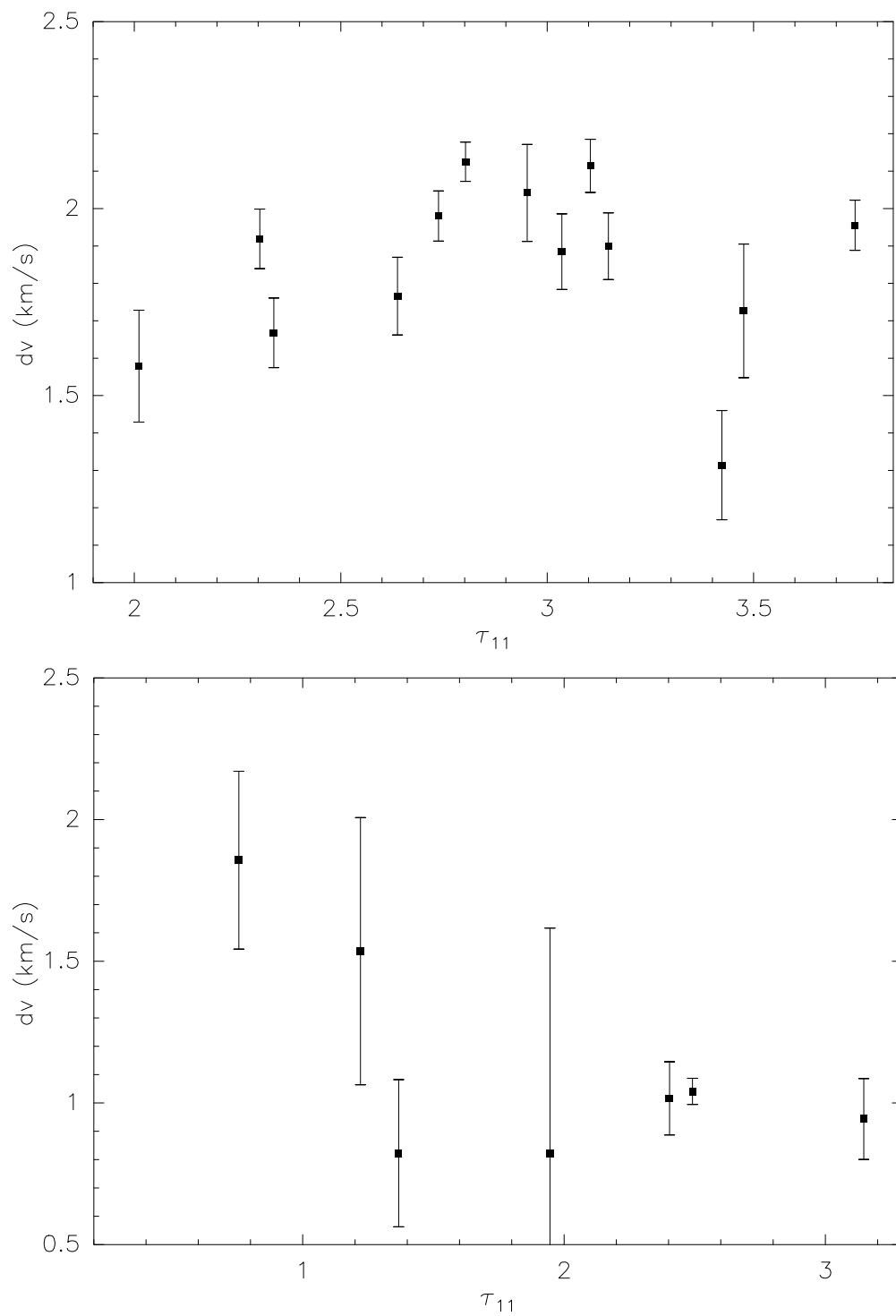


Figure 2.5: Correlation plot between the $\text{NH}_3(1,1)$ optical depth and the $\text{NH}_3(1,1)$ linewidth. *Bottom panel:* G79.27+0.38 NH_3 P1, *Top panel:* G28.34+0.06 NH_3 P2.

not allow us to make a convincing case. The temperature structure will be analysed in detail in a future paper with observations at high angular resolution (Pillai et al. 2006 in prep).

There is also a variation in temperature within the different cores of the same cloud. In G11.11-0.12, with a projected extent of a few pc, the average (over the core size) temperatures of the southern cores are 2 – 3 K (10.9 ± 1 K) lower than the northern cores (13.4 ± 1 K).

In G28.34+0.06, the gas temperature derived towards NH₃ P3, 12.7 ± 1 K and NH₃ P5, 13.6 ± 1 K is significantly lower than in the rest of the cloud. CH₃OH observations on the P1 position (Leurini et al. 2006 submitted) reveal a cold and a hot component, the latter with a small filling factor. We obtain kinetic temperatures of ~ 16 K towards the peaks of NH₃ P1 and NH₃ P2. Higher angular resolution observations are needed to confirm a hot component of small extent also in ammonia.

In G19.30+0.07, the temperature at the position of peak NH₃ emission P1 is 17.9 ± 1.6 K, much warmer than the rest of the cloud (13.1 ± 1.0 K).

In the G79 complex, we find that the temperature in G79.34+0.33 NH₃ P1 is higher (14.3 ± 0.8 K) than the other 2 cores G79.27+0.38 NH₃ P1 (12.2 ± 0.8 K) & G79.27+0.38 NH₃ P2 (11.1 ± 1.2 K) in the western part of the filament.

2.4.6 Velocity Structure

The average velocity-position diagram along an axis with position angle of $+40^\circ$ (to align the position axis roughly with the direction of the filament on the sky) for the cloud G11.11-0.12 is shown in Fig. 2.6. At every position along the position axis, the NH₃ (1,1) spectra were averaged along a line perpendicular to the position axis. There is a clear trend for the velocities to decrease from the south to the P1 position and increase to the north of the NE filament. This is also seen in the channel maps shown in Fig. 2.7 where the different clumps in the north and south appear at distinctly separate velocities. Given that the NH₃ (1,1) linewidth at all positions is ≤ 2.5 km s⁻¹, this velocity shift (> 5 km s⁻¹) between the peaks is certainly significant. The unresolved clump G11.11–0.12 NH₃ P4 is more associated with the G11.11–0.12 NH₃ P2 clump while P3 fades away at those velocities.

Recently, this filament had been studied in absorption against the diffuse 8 μ m Galactic background and in emission from cold dust at 850 μ m (Johnstone et al. 2003). They model the 850 μ m emission by fitting a non-magnetic isothermal cylinder profile to the radial structure of the entire filament (south and north segment). The velocity structure observed in NH₃ (1,1), however, shows several distinct clumps. This suggests that the density structure of the filament cannot be rigorously described by a simple continuous cylinder.

The channel maps for G28.34+0.06 are shown in Fig. 2.8. The two extensions of the cloud around P1 and P2 differ in velocity by about 1.5 km s⁻¹. This is the difference in velocity for the two peaks at which they are brightest. From the channel maps it appears that there is a bridge between the two parts of the cloud connecting P1 and P2. At the velocity of 80.16 km s⁻¹, the three unresolved clumps, which are identified in dust continuum emission but not clearly identified in the NH₃ (1,1) integrated intensity emission, are revealed.

G33.71–0.01 shows another interesting case of distinct velocity variations across a cloud. The average velocity position map along the declination axis is displayed in Fig. 2.9. The velocity increases from the south at ~ 103 km s⁻¹ towards the north to ~ 106 km s⁻¹ while showing a very wide weak component at ~ 105 km s⁻¹ at the (0,0) position. Its detection at (0,0) is only at the 2σ level but is also observed in NH₃ (2,2). A possible interaction with the nearby SNR G33.6+0.1 is discussed in §5.2.

2.4.7 Column Density, NH₃ Abundance and Masses

We have estimated the column densities and total masses for the bright, compact sources for which the SCUBA 850 μ m maps are available, after smoothing the data to the resolution of 100m beam (40'').

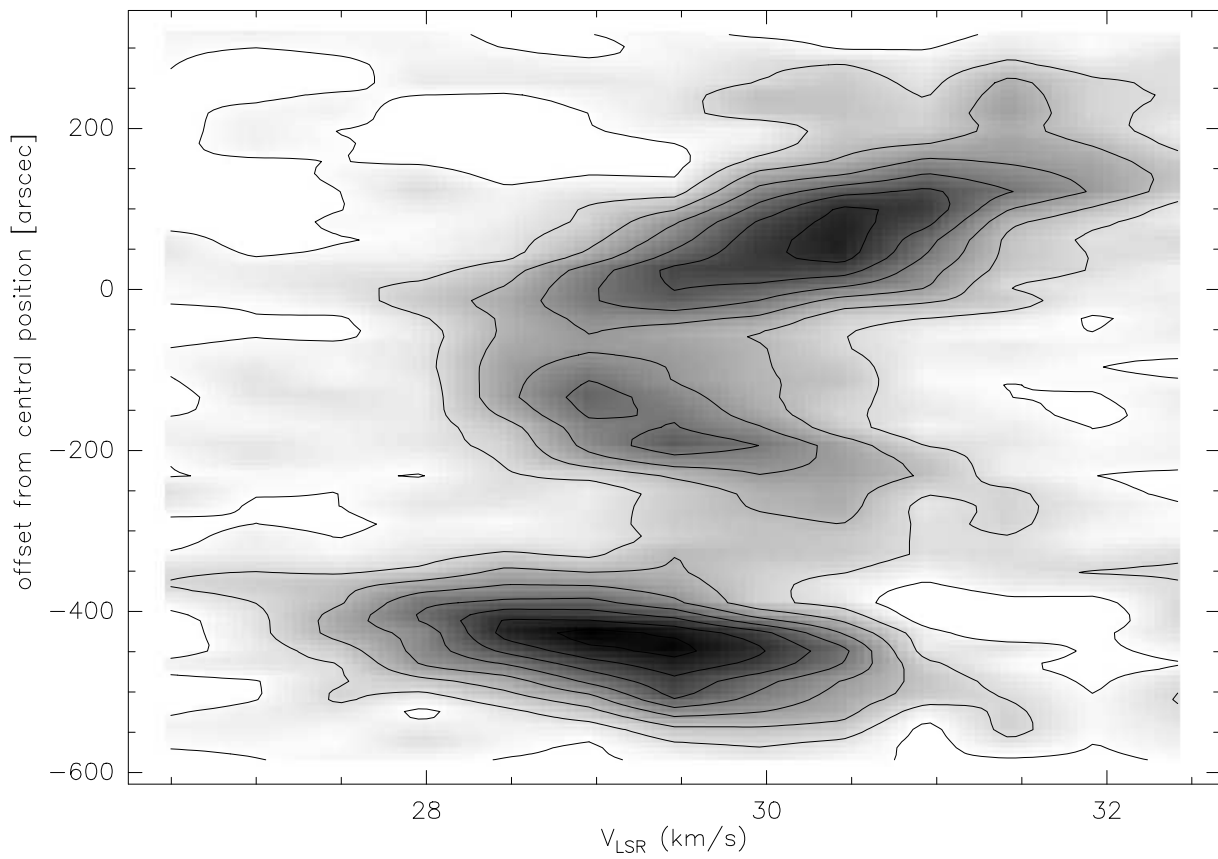


Figure 2.6: The average velocity-position map of NH₃ (1,1) for the cloud G11.11-0.12 at a position angle of $\sim 40^\circ$. Note that the Y axis is the offset from the reference position, given in Table 2.1. offsets run from south-west (negative offsets) to north-east (positive offsets).

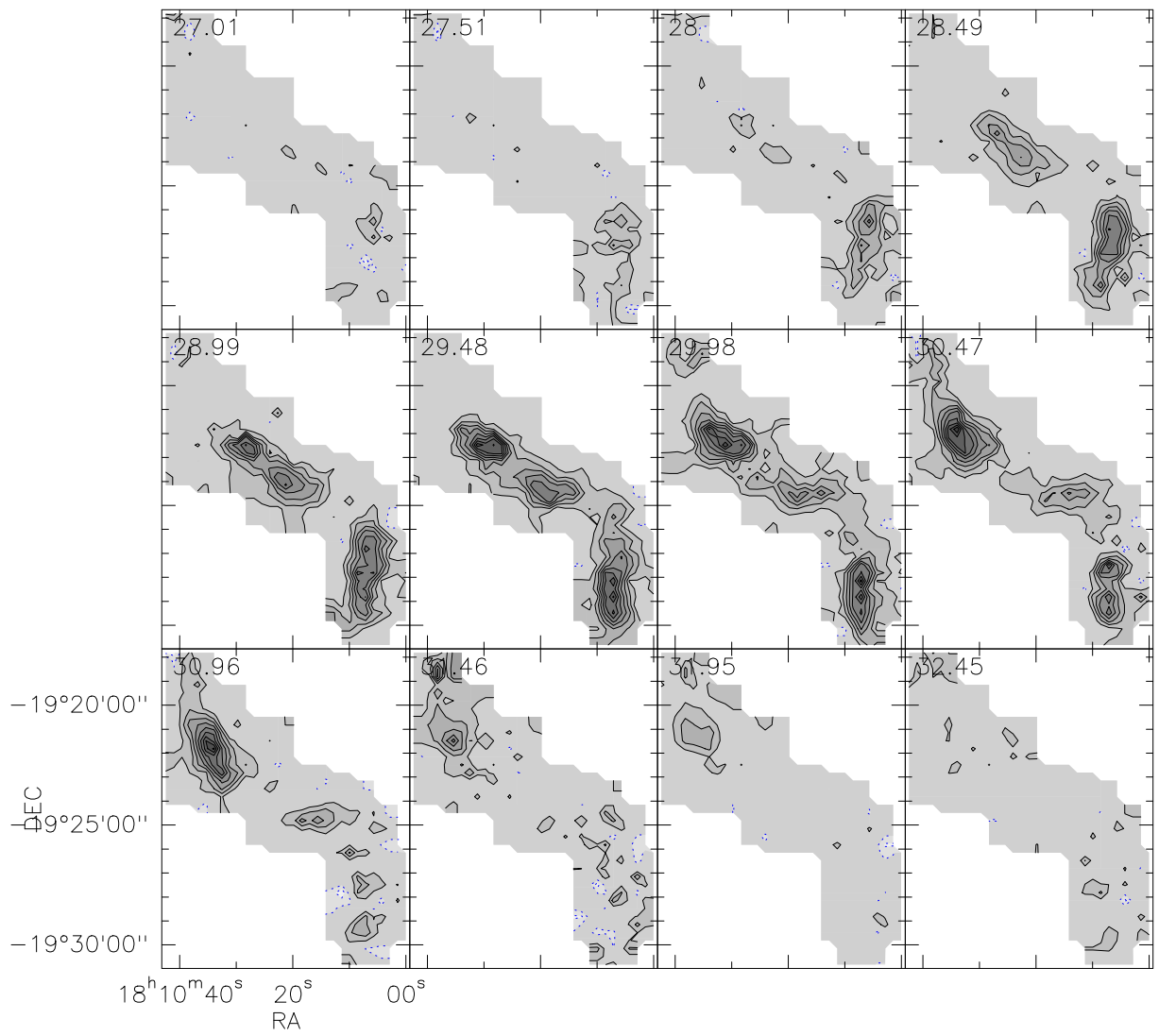


Figure 2.7: Channel maps for G11.11–0.12 over the main component for the $\text{NH}_3(1,1)$ transition.

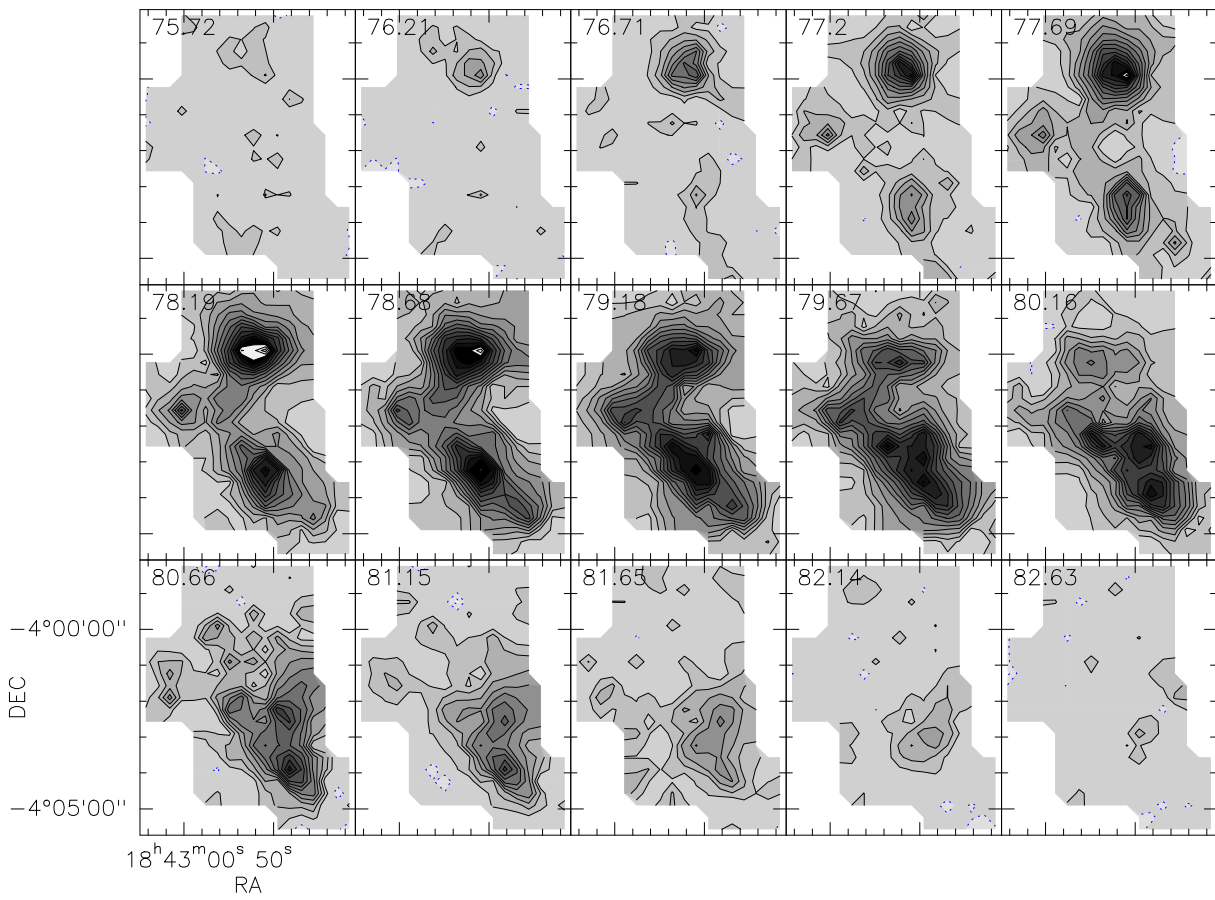


Figure 2.8: channel map for G28.34+0.06 over the main component for the $\text{NH}_3(1,1)$ transition.

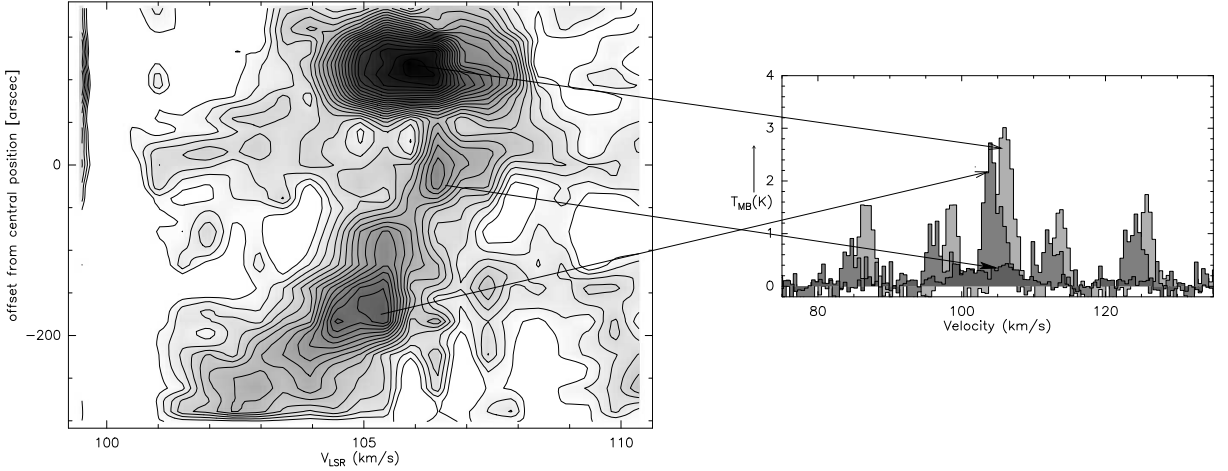


Figure 2.9: *Left panel:* The average velocity-position map of NH_3 (1,1) along the declination axis for the cloud G33.71–0.01. *Right panel:* The spectra obtained at the corresponding position in the map (indicated by the arrows). Note the large linewidth component toward the centre part of the cloud and the change in LSR velocity from south to north.

Assuming a dust opacity of κ_m of $1.85 \text{ cm}^2/\text{g}$ at $850 \mu\text{m}$ for grains with thick ice mantles and gas density $n(\text{H}) = 10^6 \text{ cm}^{-3}$ (Ossenkopf & Henning 1994), the effective H_2 column density is (Launhardt 1996)

$$N(\text{H}_2) = \frac{6.2 \times 10^{16} S_\nu^{\text{beam}} \lambda^3 e^{\frac{1.44 \times 10^4}{T_d \lambda}} Z_\odot}{\kappa_m(\lambda) \theta^2} \frac{Z}{Z_\odot} \quad (2.5)$$

where S_ν^{beam} is the flux density in Jy/beam, λ the wavelength in μm , Z/Z_\odot is the metallicity relative to the solar metallicity (we assume $Z/Z_\odot = 1$) and θ is the FWHM of the 100 m beam in arcseconds. Here we assume that the dust temperature T_d is approximately equal to the gas temperature. We derive an effective H_2 column density of the order of $6 - 20 \times 10^{22} \text{ cm}^{-2}$ toward the peaks of the dust emission. Together with the NH_3 column density, this is used to determine the ammonia abundance ($\chi_{\text{NH}_3} = N(\text{NH}_3)/N(\text{H}_2)$). We determine the peak effective H column density from the SCUBA map and the NH_3 column density for the same position for each clump and get an upper limit for the fractional NH_3 abundance as listed in Table 2.3. The average abundance is $\sim 4 \times 10^{-8}$, however has a low value towards G79.27+0.38 NH_3 P2 (7×10^{-9} , as listed in Table 2.3).

The mass of the each cloud can be determined from the dust continuum and from NH_3 emission. The gas mass is derived from the dust using the relation (Launhardt & Henning 1997)

$$M(\text{H}_2)[M_\odot] = 1.8 \times 10^{-14} \frac{S_\nu \lambda^3 d^2 e^{\frac{1.44 \times 10^4}{T_d \lambda}} Z_\odot}{\kappa_m(\lambda)} \frac{Z}{Z_\odot} [M_\odot] \quad (2.6)$$

where S_ν is the integrated flux density in Jy and the other parameters are the same as in eq. (2.5).

Our estimates for the mass and H_2 column density are in general agreement with the previous work of Carey et al. (2000) for the submillimeter cores.

The total gas mass can be derived from the NH_3 column density maps assuming a uniform fractional abundance of the molecule, for those sources without dust continuum data. The gas mass derived from SCUBA observations can be directly compared with the virial mass estimate. The virial parameter

(Bertoldi & McKee 1992) for a clump is defined as

$$\alpha = \frac{5\sigma^2 R}{GM} \quad (2.7)$$

where σ is the three dimensional root mean square (r.m.s) velocity dispersion and R is the radius of the clump, and M is the gas mass. Note that $\sigma = \sqrt{3/8\ln 2} \times \text{FWHM}$. The virial mass is defined as $M_{\text{vir}} = 5\sigma^2 R/G$. For the clumps to be stable against collapse, $\alpha \sim 1$. We find an average value of 2.1 for the virial parameter toward the individual cores. As the uncertainty in the dust opacity alone is a factor of 2, $\alpha \sim 1$, and most of these cores appear to be virialised. Therefore, the core structure is consistent with them being supported by turbulent pressure without any evidence of external bounding pressures. G28.34+0.06 NH₃ P4 is an extreme case, where $\alpha = 6.53$.

2.5 Discussion

2.5.1 Gas Temperature and Distribution

In G11.11–0.12, the position NH₃ P2 is a faint MSX source with no counterpart in the visible or NIR; it is very likely that this is a heavily embedded protostar (Pillai et al. 2006b). The southern clumps are colder by $\sim 2 - 3$ K than the northern clumps. Thus, these southern filaments may be at an earlier stage of evolution than the cores belonging to the northern filament, where star formation activity might heat up the gas. The core to core variation in temperature within an IRDC is observed toward several other sources (see §2.4.5). Therefore, these dense cores in IRDCs are ideal sites for investigating the initial conditions in forming a massive star.

The gas temperatures we derive generally agree with the dust temperatures of Carey et al. (2000) based on submm observations and an assumed dust emissivity index $\beta = 1.75$. T_{gas} might be lower limits for those sources that show up as bright and compact objects in the submm dust emission, indicating the presence of a heavily embedded object, but reasonable for the cold gas envelope.

2.5.2 Physical Properties, Chemistry & Lifetime

The excellent correlation between the NH₃ line and submm continuum emission is consistent with the predictions of chemical models that NH₃ is relatively more abundant in high density region than other molecules (Bergin 2003). The column densities translate to extremely high extinction values of 55 – 450 mag. The discrepancies in NH₃ and H₂CO linewidths reported by Carey et al. (1998) (see §2.4.4) indicate the differences in the gas volume traced by the two molecules. The line wings seen in H₂CO and CH₃OH (Leurini et al. 2006 submitted) gas toward some sources are most likely high-velocity outflows. The critical density of the H₂CO lines studied (10^6 cm^{-3}) is much higher than that of the NH₃ inversion lines (10^4 cm^{-3}). Hence, while physical parameters derived from NH₃ are representative of the general, cool IRDC material, H₂CO probes the dense gas, which might be influenced by embedded protostars. The derived NH₃ abundance of $0.7 - 10.1 \times 10^{-8}$ together with the centrally condensed NH₃ emission is consistent with the chemical model predicted for pre-protostellar cores (Bergin & Langer 1997). These values imply that NH₃ is overabundant by factors of 5 – 10 relative to "normal" (= lower density) and less turbulent dark clouds. In contrast, H₂CO is under-abundant by a factor of ~ 50 (Carey et al. 1998). Hence the IRDCs appear to exhibit a complex chemistry.

We derive the flow crossing time, for the cloud to disperse due to its own internal motions. Perturbations within the cloud would disintegrate the cloud unless the propagation wavelength is much smaller than the distance across the cloud which it traverses. The estimated dynamical timescales of $\sim 0.5 - 2$ Myrs, provide an upper limit to the life time of these clouds.

The virial masses for the different clumps span a wide range from 50 to 7880 M_{\odot} . As typical for intermediate to high mass star-forming regions, most of the masses are skewed to values $> 500 M_{\odot}$. The virial parameter ~ 1 for most of the clumps which are stable against collapse.

2.5.3 IRDCs and Other Star-forming Regions

In a comparison of our NH_3 results with the potential low mass counterpart B68 (Lai et al. 2003), we find that the linewidths and the virial masses are much higher towards our cores. The sizes and the column density and most importantly the masses we derive are also significantly higher, thus making IRDCs potential candidates as sites of high-mass star formation. The (1,1) and (2,2) linewidths for IRDCs are slightly lower but the NH_3 column densities are comparable to the massive dense cloud identified in NH_3 in NGC6334 I(N) by Kuiper et al. (1995). In terms of masses and sizes and temperatures, our sources are similar to those of Garay et al. (2004). Star formation probably has already started in some of them.

In Table 2.4, we present the mean properties of the dense cores of our sample with those of the cores in Taurus, Perseus and the Orion A complex as given in Ladd et al. (1994). It is evident that IRDC cores are on average highly turbulent, larger with much higher masses than the other cores while having similar temperature as the other cores. The IRDC masses derived here are for an NH_3 abundance of 10^{-7} as used by Ladd et al. (1994). But this is almost an order of magnitude higher than what we derive and hence the mean mass quoted in Table 2.4 will be an order of magnitude higher, several 1000 M_{\odot} instead of several 100. Compared to local dark clouds, IRDCs pile up significantly large amounts of mass and have supersonic internal motions. But how much of this mass goes into forming stars of low, intermediate or high mass is yet to be answered.

Tan (2005) find that a group of local IRDCs have masses of a few $10^3 - 10^4 M_{\odot}$ and mean surface density of $\Sigma \sim 0.1 \text{ g cm}^{-2}$. They find that this is 3 times the mean surface density of a Giant Molecular Cloud (GMC) and very similar to the values found in more evolved systems like the Orion Nebula Cluster (ONC). Subsequently, they suggest that IRDCs forming from GMCs are the initial conditions for star clusters.

Tan (2005) define Σ as $\Sigma = M/(\pi R^2)$, and if we compute the mean surface density for our sample and the local dark clouds (the mean Mass and the size as given in Table 2.4), we arrive at values between 0.08 – 0.4. If the mean surface density were to be a measure of star formation efficiency, then IRDCs have a higher value compared to Taurus but not very much higher than Perseus which is understood to be an intermediate star forming region.

Studies of relatively local cluster forming regions like the ρ Ophiuchus cloud, the Serpens molecular cloud and Orion B molecular cloud (Motte et al. 1998, Testi & Sargent 1998, Johnstone et al. 2001) find that the mass spectrum of their cores are very similar to that of the stellar IMF. If this is indeed true, then the fraction of the core mass going into forming stars would be independent of mass and the stellar IMF would mainly be determined by the cloud fragmentation process (Blitz & Williams 1999). If we assume a star formation efficiency of 30% in an IRDC core of mean mass $\sim 500 M_{\odot}$ and adopt the standard IMF (with power law indices 2.3 ± 0.3 , 1.3 ± 0.5 and 0.3 ± 0.7 for masses > 0.5 , $0.08 - 0.5$ and $< 0.05 M_{\odot}$ respectively), then ~ 116 stars could form in the core. Out of this, ~ 2 stars could be of high-mass stars ($\geq 8 M_{\odot}$) while 64 would be low-mass/intermediate stars ($0.5 \leq M/M_{\odot} \leq 8$) while the rest would be very low mass and sub-stellar objects. Indeed there is growing evidence of star formation in these cores (Rathborne et al. 2005, Pillai et al. 2006b, Ormel et al. 2005).

2.5.4 IRDCs Formed by Interaction with SNRs ?

From the velocity structure, G11.11–0.12 NH_3 P2 appears blue shifted while the clump NH_3 P1 towards the north and NH_3 P4 towards the south appears redshifted relative to the LSR velocity. This is thus not a case of smooth velocity gradient along the filament. It might be possible to explain the observed velocity structure, if we assume that the entire filament seen in projection is part of a unbound system where P1

and P4 lie at the same distance along the line-of-sight (l.o.s) at diametrically opposite ends while P2 is further in the front. A massive wind-driven process which might have taken place in the close vicinity of the cloud could explain such a structure. Recent wide field MIR images of this region released from Spitzer show that this cloud has a filamentary concave structure spread over several parsecs with a significant density enhancement in the center (Menten, Pillai, & Wyrowski 2005). The morphology bears remarkable similarity to the structures predicted by 3-D numerical calculations simulating the impact of a planar shock front on an isolated globule (Boss 1995). The best known case of an ongoing SN-cloud interaction is in IC 443, where a 10^4 yr old SNR in the GEM OB1 association with a shock speed of 40 km s^{-1} impacts the cloud resulting in highly excited molecular gas with very broad linewidths. However, a weaker shock (likely from a more evolved SNR) would result in temporary distortion and compression of the molecular cloud, followed by rebound to an equilibrium. An evolved SNR at an age of 10^5 yr with a shock speed of 100 km s^{-1} , is one of the three likely weak shock waves that Boss (1995) propose to influence a cloud without destroying it. Such a shock wave would have already traversed 25 pc. Brogan et al. (2004) recently discovered the supernova remnant G11.03–0.05 which is within $7'$ of the cloud. They claim that the SNR is not young.

The SNR has a shell-like appearance with a diameter of $\sim 8'$ and very weak emission at centimeter wavelengths. Brogan et al. (2004) find that a pulsar PSRJ1809–1917 is located about $8.5'$ from the SNR and is probably associated with the SNR. Considering the respective uncertainties of their distance estimates, the pulsar (4 ± 1 kpc) and G11.11–0.12 (3.6 ± 0.5 kpc) appear at or near the same distance.

In G33.71–0.01, we find another where the cloud seems to have undergone a shock at the centre (see Fig. 2.9). Note that there is a large linewidth towards the central core of this filament. The (0,0) velocity is also different from the cores toward the south and north segment of the filament. The SNR G33.6+0.1 is within $5'$ of this core and previous observations by Green (1989) shows an unusually broad OH absorption feature near 105 km s^{-1} towards this SNR. The HCO^+ and $^{12}\text{CO } J = 1 - 0$ observations by Green & Dewdney (1992) reveal material shocked by the interaction of the SNR with the adjacent molecular cloud. The 2σ detection of a large linewidth feature $\Delta v \geq 8 \text{ km s}^{-1}$ centered at 105 km s^{-1} in NH_3 (1,1) and (2,2) might also be a sign of interaction of the cloud with the SNR.

All IRDCs except those in the Cygnus-X region have a SNR in their vicinity, although an association, which would require observations with shock tracers, cannot be verified yet. To estimate the chance occurrence of an IRDC and SNR on the sky, we sample ~ 17.6 square degrees in which (Green 2002) and Brogan et al. (2004) have identified a total of 22 remnants. The likelihood of a chance positional occurrence within $7'$ of an IRDC is small (≤ 0.05) given a SNR surface density of 1.25 remnants per square degree. It is very likely that the SNRs are physically associated with the IRDCs G11.11 and G33.71–0.01.

2.5.5 IRDCs in the Framework of an Evolutionary Sequence

To obtain general statistics on IRDCs we compare in Fig. 2.10 the core gas properties of our sample of 9 sources with the cores presented in the Jijina et al. (1999) NH_3 database. The database consists of 264 dense cores, with and without associations with young stellar objects. For the large linewidths of IRDCs ($\Delta v > 0.8 \text{ km s}^{-1}$), there is a distinct trend for the IRDCs to be colder relative to the cores from the database. The NH_3 column density is also higher for the IRDCs, surpassed only by a few high column densities from low mass cores observed with the high angular resolution of the VLA, which evidently sees more of the core interiors that are possibly associated with YSOs.

In Fig. 2.11 we present a similar comparison with a sample of UCHII regions from the Wood & Churchwell (1989) catalogue and the sources from the Beuther et al. (2002a) study of high-mass protostellar objects (HMPOs). While recent studies reveal that HMPOs are in a pre-UCHII region phase (Molinari et al. 2002, Beuther et al. 2002a), the nature of the stage preceding HMPOs has not been studied in detail. IRDCs are ideal candidates for this pre-HMPO stage. In Fig. 2.11 we present properties of source samples believed to cover the earliest phases of massive star formation based on NH_3 observations. There is no clear trend in linewidths, however IRDCs have a significantly lower average linewidth ($\Delta \bar{v} = 1.51 \text{ km s}^{-1}$)

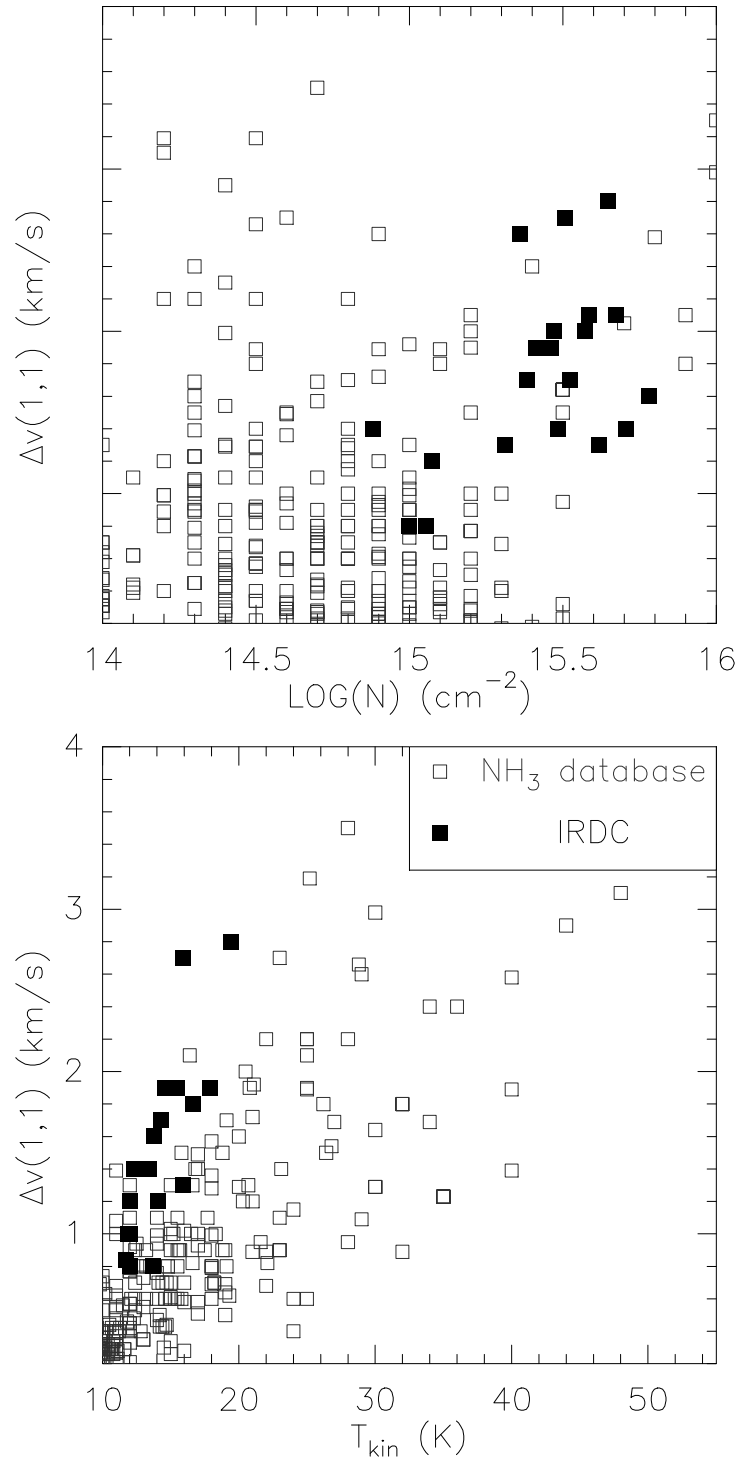


Figure 2.10: *Bottom panel:* The correlation plot of kinetic temperature with the linewidths. The black filled squares indicate the IRDCs and the grey unfilled squares the cores from the NH_3 database. IRDCs have larger velocity dispersions while the rotational temperatures are comparable. *Top panel:* The correlation plot of NH_3 column density with the linewidths shows that the average column density of IRDCs are higher.

than HMPOs ($\Delta\bar{v} = 2.05 \text{ km s}^{-1}$) and UCHII regions ($\Delta\bar{v} = 2.52 \text{ km s}^{-1}$). There is a distinct temperature trend from the low temperatures of the IRDCs ($\bar{T} = 13.9 \text{ K}$) to increasing temperatures for the IRAS selected high-mass objects ($\bar{T} = 18.34 \text{ K}$) and high temperatures for the objects associated with UCHII regions ($\bar{T} = 22.6 \text{ K}$). Temperature and linewidths must be understood as averages over the core and parts of the envelope since the beam is $40''$.

There is no clear trend in column density. However, on average the column densities of IRDCs are high compared to the other two samples. We interpret the clear trend in temperature and the tentative differences in NH_3 linewidths and column densities ($N[\text{NH}_3]$) as possible manifestation of an evolutionary sequence. Starless cores on the verge of star formation are expected to be cold ($T \leq 20 \text{ K}$), to have high column densities and smaller linewidths. The temperature and the linewidth in a core will increase after the formation of an embedded protostar (via radiative heating and injection of turbulence through outflows and winds), while the envelope will be dispersed via outflows and winds and thus column densities will decrease with time.

One would expect the highest ammonia column densities for the hot sources due to evaporation of ammonia from the grains although in some cases IRDCs have higher column densities. However, this effect might be very localised to the hot cores (0.1 pc and smaller) and not be true for the larger scale emission. Additionally some molecular material might already be dispersed in the hot sources by the interaction of the young OB clusters with their environment.

2.6 Conclusions

In this paper, we discussed ammonia observations of a selected set of IRDCs and the derived physical properties. Our results are as summarised below.

The ammonia emission correlates very well with MIR absorption and ammonia peaks distinctly coincide with dust continuum peaks. Several cores are detected within the clouds with deconvolved sizes smaller than the $40''$ FWHM beam size. We can constrain the average gas temperature to between 10 and 20 K.

We observe high linewidths ($1 \leq \Delta v/\text{km s}^{-1} \leq 3.5$), hence turbulence plays an important role in the stability of an IRDC. There are significant velocity gradients observed between the cores. The effect of external shock/outflow tracers, on the gas kinematics is suggestive in some cases, but needs to be investigated further.

The column densities translate to extremely high A_V values (55 – 450 mag), therefore any active star formation would be heavily embedded. The total cloud gas mass derived from the NH_3 data ranges from $10^3 - 10^4 M_\odot$. The virial parameter is ~ 1 for most of the clumps, and the cores appear to be stable against gravitational collapse. As a result IRDCs are potential sites for star formation. If we were to adopt the stellar IMF and a star formation efficiency of 30%, then every IRDC core could fragment to form > 100 stars, with at least two high mass stars ($> 8 M_\odot$).

The fractional abundance of NH_3 (relative to H_2) is $0.7 - 10.0 \times 10^{-8}$. This, together with the excellent correlation in morphology of the dust and gas, is consistent with the time dependent chemical model for NH_3 of Bergin & Langer (1997) and implies that NH_3 remains undepleted. The derived abundance is a factor 5 – 10 larger than that observed in local dark clouds while H_2CO is underabundant by a factor of ~ 50 . Hence, the chemistry governing these IRDCs might be complex and could be different from other parts of the dense ISM.

The time scales we derive for the clouds to disperse due to their own internal motions of a few Myrs provides an upper limit to the life time of these clouds. We suggest that SNRs might be the triggering mechanism responsible for the formation of an IRDC.

The comparison of the physical properties from ammonia of our IRDCs sample with other source samples – HMPO's and UCHII's – strongly suggests that most of these IRDCs are the most likely candidates for pre-protostellar cores of massive star formation.

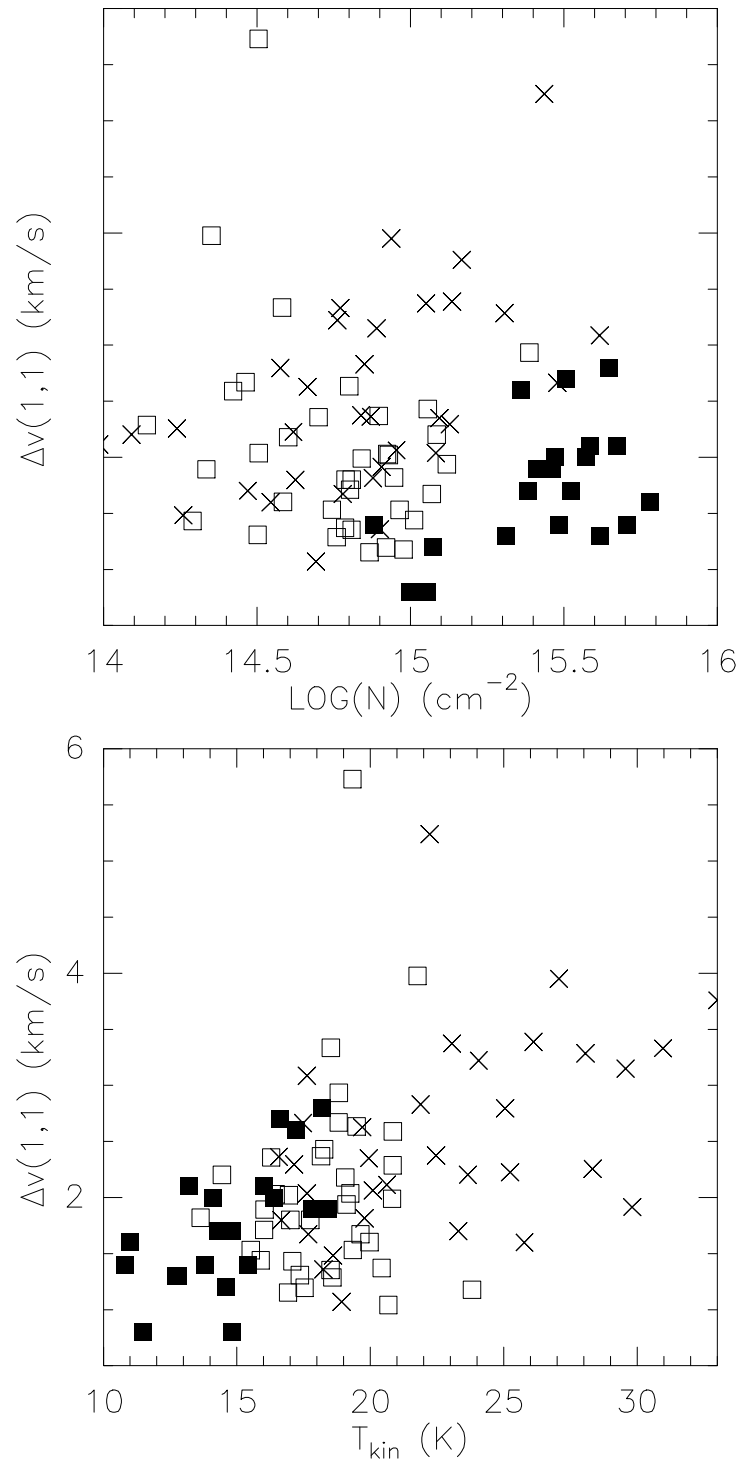


Figure 2.11: *Bottom panel:* The correlation plot of kinetic temperature with the linewidth. The black filled squares indicate the IRDCs, the crosses the sources from the Wood and Churchwell catalogue and the unfilled squares Beuther et al. (2002a) sources. IRDCs are colder and on average have lower linewidths. *Top panel:* The correlation plot of NH_3 column density with the linewidths.

Table 2.1: List of IRDCs Observed in $\text{NH}_3(1,1)$ and $(2,2)$

Name	R.A.(J2000)	Dec.(J2000)	V_{LSR} [km s^{-1}]	D [kpc]
G11.11-0.12 P1	18:10:29.27	-19:22:40.3	29.2	3.6
G19.30+0.07	18:25:56.78	-12:04:25.0	26.3	2.2
G24.72-0.75	18:36:21.07	-07:41:37.7	56.4	1
G24.63+0.15	18:35:40.44	-07:18:42.3	54.2	3.6
G28.34+0.06 P1	18:42:50.9	-04:03:14	78.4	4.8
G28.34+0.06 P2	18:42:52.4	-03:59:54	78.4	4.8
G33.71-0.01	18:52:53.81	+00:41:06.4	104.2	7.2
G79.27+0.38	20:31:59.61	+40:18:26.4	1.2	1
G79.34+0.33	20:32:21.803	+40:20:08.00	0.1	1
G81.50+0.14	20:40:08.29	+41:56:26.4	8.7	1.3

Notes: Columns are name, right ascension, declination, LSR velocity, distance. Positions and Distances are taken from Carey et al. (1998). The coordinates correspond to the reference positions of the maps.

Table 2.2: NH₃ (1,1) and (2,2) Map Results: Peak Position.

Source	Transition	V_{LSR} [km s ⁻¹]	T_{MB} [K]	FWHM [km s ⁻¹]	τ_{main}	1σ [K km s ⁻¹]
G11.11−0.12 NH ₃ P1	1−1	30.44 (±0.02)	5.47 (±0.96)	1.27 (±0.06)	3.52 (±0.39)	0.42
	2−2	30.42 (±0.09)	1.97 (±0.32)	1.56 (±0.30)		
G19.30+0.07 NH ₃ P1	1−1	26.45 (±0.03)	5.17 (±0.8)	1.88 (±0.08)	1.88 (±0.26)	0.53
	2−2	26.64 (±0.06)	2.86 (±0.27)	1.57 (±0.17)		
G24.72−0.75 NH ₃ P1	1−1	58.37 (±0.07)	2.76 (±0.45)	2.57 (±0.12)	2.81 (±0.47)	0.25
	2−2	58.47 (±0.12)	1.99 (±0.23)	2.97 (±0.24)		
G24.63+0.15	1−1	53.11 (±0.04)	2.40 (±0.34)	1.7 (±0.09)	2.36 (±0.43)	0.16
	2−2	52.89 (±0.09)	0.98 (±0.12)	2.42 (±0.24)		
G28.34+0.06 NH ₃ P1	1−1	79.14 (±0.02)	2.88 (±0.42)	2.67 (±0.04)	2.00 (0.11)	0.16
	2−2	79.15 (±0.04)	1.37 (±0.05)	3.29 (±0.11)		
G33.71−0.01 NH ₃ P1	1−1	104.31 (±0.09)	2.52 (±0.43)	2.64 (±0.2)	1.5 (±0.52)	0.12
	2−2	104.4 (±0.17)	1.14 (±0.22)	2.40 (±0.35)		
G79.27+0.38 NH ₃ P1	1−1	1.65 (±0.02)	2.28 (±0.38)	1.04 (±0.05)	2.49 (±0.27)	0.31
	2−2	1.63 (±0.05)	0.61 (±0.08)	0.98 (±0.14)		
G79.34+0.33 NH ₃ P1	1−1	0.31 (±0.01)	2.53 (±0.30)	1.23 (±0.03)	1.45 (±0.13)	0.19
	2−2	0.25 (±0.04)	0.79 (±0.07)	1.29 (±0.13)		
G81.50+0.14	1−1	−4.53 (±0.05)	2.21 (±0.35)	1.35 (±0.15)	0.37 (±0.46)	0.27
	2−2	−4.69 (±0.12)	0.67 (±0.21)	1.00 (±0.34)		

Notes: Columns are name, NH₃ (J,K) transition, LSR velocity, (1,1) main beam brightness temperature, full linewidth at half maximum, main group optical depth and the 1 sigma noise level in the NH₃ (1,1) integrated intensity map (2.1). The error estimates are given in brackets.

Table 2.3: Physical Properties of Observed IRDCs.

Source	Offsets [arcsecs]	T_{EX} [K]	T_{ROT} [K]	T_{KIN} [K]	$N(\text{NH}_3)$ [10^{14} cm^{-2}]	$N(\text{H} + \text{H}_2)$ [10^{22} cm^{-2}]	χ_{NH_3} [10^{-8}]	Mass M_{\odot}	Size [arcsecs]	M_{vir} [M_{\odot}]	α	M_{NH_3} [$10^4 M_{\odot}$]
G11.11-0.12 NH ₃ P1	(80,40)	7.6 (± 0.7)	12.3 (± 1.2)	12.7	41.5 (± 6.4)	8.4	4.9	485	27	468	1.0	18.1
G11.11-0.12 NH ₃ P2	(0,0)	6.6 (± 0.4)	13.4 (± 1.0)	13.8	30.5 (± 3.3)	10.2	2.9	172	13	268	1.6	
G11.11-0.12 NH ₃ P3	(-300,-325)	7.1 (± 0.3)	14.1 (± 9.7)	14.5	60.4 (± 11.4)	8.7	6.9	647	32	860	1.3	
G11.11-0.12 NH ₃ P4	(-300,-400)	5.7 (± 0.5)	10.5 (± 1.0)	10.8	50.9 (± 10.6)	16.1	3.2	788	25	555	0.7	
G19.30+0.07 NH ₃ P1 ⁿ	(20,20)	8.2 (± 0.9)	17.6 (± 2.0)	18.4	25.9 (± 3.2)				38	893		0.9
G19.30+0.07 NH ₃ P2 ⁿ	(-60,-20)	5.9 (± 0.7)	13.8 (± 1.8)	14.3	33.3 (± 6.9)				45	823		
G24.72-0.17 NH ₃ P1 ⁿ	(150,220)	6.6 (± 0.6)	17.4 (± 2.2)	18.2	44.3 (± 5.7)				34	2450		1.4
G24.63+0.15 ⁿ	(0,0)	5.0 (± 0.5)	14.3 (± 1.4)	14.8	24.1 (± 4.4)				43	1358		0.7
G28.34+0.06 NH ₃ P1	(0,0)	5.7 (± 0.2)	16.0 (± 1.2)	16.6	32.1 (± 2.2)	5.8	5.5	904	22	2280	2.5	25.4
G28.34+0.06 NH ₃ P2	(20,200)	5.5 (± 0.2)	15.4 (± 1.4)	16.0	38.6 (± 3.2)	32.7	1.2	2310	45	2928	1.3	
G28.34+0.06 NH ₃ P3	(-60,-60)	4.8 (± 0.2)	12.8 (± 1.2)	13.2	47.2 (± 6.1)	5.9	8	374	21	1398	3.7	
G28.34+0.06 NH ₃ P4	(-30,50)	4.8 (± 0.2)	15.9 (± 2.2)	16.4	37.4 (± 4.9)	3.7	10.1	147	16	960	6.5	
G28.34+0.06 NH ₃ P5	(50,40)	5.6 (± 0.3)	13.6 (± 1.3)	14.1	29.6 (± 3.8)	6.3	4.7	528	24	1378	2.6	
G33.71-0.01 NH ₃ P1 ⁿ	(-40,-200)	5.6 (± 1.1)	16.6 (± 2.3)	17.2	23.0 (± 6.6)				52	7880		15.6
G33.71-0.01 NH ₃ P2 ⁿ	(60,100)	5.3 (± 0.3)	17.1 (± 2.0)	17.8	29.0 (± 3.3)				60	4928		
G79.27+0.38 NH ₃ P1	(-20,0)	4.8 (± 0.2)	12.4 (± 0.9)	12.8	20.5 (± 2.5)	14.2	1.4	84	32	155	1.8	0.4
G79.27+0.38 NH ₃ P2	(-140,40)	6.0 (± 0.7)	11.2 (± 1.4)	11.5	11.3 (± 2.7)	12.1	0.9	55	25	53	1.0	
G79.27+0.38 NH ₃ P3	(-250,70)	3.3 (± 2.2)	11.7 (± 1.6)	12.0	10.0 (± 25.0)	6.5	1.5	19	20	40	2.1	
G79.34+0.33 NH ₃ P1	(0,0)	5.8 (± 0.3)	14.1 (± 0.8)	14.6	11.9 (± 1.0)	17.5	0.7	143	39	178	1.2	0.2
G81.50+0.14 ⁿ	(260,-375)	5.6 (± 1)	14.9 (± 1.3)	15.4	7.6 (± 2.0)				78	570		0.1

Notes: Columns are name, offset position from reference, excitation temperature, NH₃ rotational temperature, kinetic temperature, NH₃ column density, H₂ column density, NH₃ abundance, gas mass estimated from SCUBA data, size of the cores, virial masses from NH₃ the alpha parameter defined as in total cloud mass from NH₃. The formal errors are given in brackets. ⁿ are those sources for which the sizes have been derived from NH₃ data. The H₂ column densities are estimated from 850 μm SCUBA map (Carey et al. 2000)).

Table 2.4: Mean Values of NH₃ Core Samples.

Sample	FWHM (km s ⁻¹)	T_{kin} (K)	size(pc)	M_{NH_3} (M_{\odot})	Σ
Taurus	0.33	10	0.06	1.1	0.08
Perseus	0.55	13	0.12	9	0.16
Orion	1.12	17	0.15	21	0.24
IRDC cores	1.7	15	0.57	492	0.40

Notes: Columns are the source sample, the mean FWHM of the NH₃ (1,1) line, kinetic temperature, size of the core, mass as determined from NH₃ assuming a fractional abundance of NH₃ relative to H₂ and the mean surface density. The mean values for dense cores in Taurus, Perseus and Orion have been taken from Ladd et al. (1994).

Chapter 3

Deuteration and Depletion in Massive Cold Cores: Probing the initial conditions of High Mass Star formation

This chapter is based on a paper to be submitted to Astronomy & Astrophysics.

We report on a study of ammonia deuteration and CO depletion toward a new sample of massive pre/protocluster cores. We searched for massive pre/protocluster cores by taking a complete wide-field (10×10 arcmin) census of cloud cores in ≈ 30 massive star-forming regions, harbouring UCHII regions and showing evidence of secondary cores. Using the IRAM 30m telescope, we find that 65% of the observed sources have strong NH_2D emission and a high degree of deuteration ($\text{NH}_2\text{D}/\text{NH}_3 \geq 1\%$). We show that high deuteration is a definitive signature of pre/protocluster (thus cold) cores and that there is a trend of significant decrease in deuteration with temperature. The enhancement in deuteration coincides with strong CO depletion onto dust grains. Based on simultaneously observed HCN and H^{13}CN lines, the galactocentric gradient of the $^{12}\text{C}/^{13}\text{C}$ ratio is revisited with no evidence for a trend between 1 and 6 pc from the Sun. In addition, we present interferometer observations of NH_3 and NH_2D using the VLA, BIMA and PdBI¹ for two sources from the SCAMPS project. The spatial distribution of NH_2D is clearly different from that of NH_3 as well as thermal dust continuum. The appearance of a protostar, as evidenced by outflow activity, destroys the deuterium-bearing molecules. Deuteration thus appears to be a signpost for the cold, earliest stages of evolution in high mass molecular clouds. The cores identified within the clouds are massive and virial equilibrium calculations show that they are self-gravitating. The non-thermal motions in these cold clouds are clearly supersonic. Furthermore, turbulence appears to be the byproduct of an outflow activity, it steadily decays down with distance from the embedded protostar. These findings prove that these high mass cold cores are the raw materials out of which high mass stars and star clusters form in the vicinity of Ultracompact HII regions.

3.1 Introduction

The prevalent theory on high mass star formation is that massive stars are born in dense clumps within giant molecular clouds (GMCs). Within these clumps, Ultracompact HII regions (UCHII) are indicators of newly formed massive stars. Observations (Cesaroni et al. 1994, Cesaroni et al. 1998) have shown that

these are often associated with warm ($T > 100$ K), compact (< 0.1 pc) and very dense ($n_{\text{H}_2} > 10^7$ cm $^{-3}$) cores known as hot molecular cores (HMCs). An evolutionary sequence has been sketched out based on recent observations (Codella et al. 2004, Beuther & Shepherd 2005) with the HMC stage preceding the formation of UCHII regions. But the very initial stage has not yet been studied. Since many UCHII regions are located in clusters, one expects to find even earlier phases of massive star formation and the raw material out of which massive stars/star clusters form in the vicinity of UCHIIIs.

This has prompted us to embark upon a program to search for massive pre/protocluster cores by taking a complete wide-field (10×10 arcmin) census of cloud cores in ≈ 30 massive star-forming regions, harbouring UCHII regions (Wood & Churchwell 1989) and with evidence of secondary cores. Our program is known as SCAMPS (the SCUBA Massive Pre/Protocluster core Survey; Thompson et al. 2005).

We discovered a multitude of secondary, cold condensations and warmer cores that might contain heavily embedded massive protostars. Many of the sources are seen as dark patches in MSX infrared images of the region, very similar to infrared dark clouds (IRDCs; Menten, Pillai, & Wyrowski 2005) and must have dust temperatures below 30 K (as evidenced by MIR/FIR upper limits) and have masses of a few 100 to a 1000 M_{\odot} . These cores thus could reveal a colder pre-protostellar phase.

In order to study the physical and chemical conditions of these cores, we did a multi-wavelength survey toward them in various molecular tracers. Here, we report on our study using ammonia to probe the temperature and deuteration in the cores and CO to estimate depletion of neutral molecules from the gas phase. NH_3 has proven to be an important tool in measuring the physical conditions in molecular clouds (Ho & Townes 1983). Since only the lowest NH_3 energy levels are expected to be populated for cool dark clouds ($T < 20$ K), their physical conditions can be probed using the (1,1) and (2,2) inversion transitions in ($J = K$) rotational levels of ammonia. Radiative transitions between different K -ladders are forbidden, therefore the lowest levels are populated only via collisions. The optical depth can be determined from the ratio of the hyperfine satellites. Thus, the population of the different levels can be estimated and hence the temperature of the gas determined. In addition, recent chemical models reveal that NH_3 (and also N_2H^+), does not deplete from the gas phase for the densities observed in dark clouds ($< 10^6$ cm $^{-3}$) (Bergin & Langer 1997). Thus NH_3 is an excellent tracer of the dense gas where many other molecules would have heavily depleted. High densities in the earliest phase is expected to enhance depletion of molecules (mainly CO) onto grains (Bacmann et al. 2003). The freeze out of abundant gas phase molecules along with the low temperatures (≤ 20 K) prevalent in these cores leads to a high degree of deuteration (Roueff et al. 2005, Hatchell 2003, Shah & Wootten 2001, Saito et al. 2000). Thus estimation of deuteration and depletion in cores can be used as a chemical and physical chronometer.

In §3.2.1 and §3.2.2, we describe our single dish and interferometer observations respectively, along with the different telescopes used. We also discuss the data reduction and present the derived physical parameters for different molecules. We show that high-mass cold cores exhibit very high deuteration and depletion. The fractionation of NH_3 is compared with depletion of CO from the gas phase. The possible origin of deuterated species and variation of deuteration with gas temperature is also discussed. We compare the degree of deuteration estimated from high resolution observations with the Plateau de Bure Interferometer (PdBI) and the Very Large Array (VLA) with dust continuum (PdBI) for two sources. We find that NH_2D deuteration is localised and offset from dust condensations. Subsequently, we show that enhanced deuteration is a signature of the earliest stages of high-mass cold cores. Furthermore, we analyse the velocity structure, estimate dust mass and the virial mass. We end the discussion with our interpretation of the HCN isotopic abundance with galactic distance.

3.2 Observations

3.2.1 Single Dish Observations & Results

IRAM 30m Observation

The NH_2D and C^{18}O observations were made at the IRAM 30m telescope on Pico Veleta in August 2003 toward 28 pre/protocluster cores given in Table 3.2.1. We performed 9 point maps with $10''$ spacing around the peak to be able to compare independent of the beam, the different lines at different frequencies. All line parameters listed are averaged over the map. Individual positions were observed with an integration time of 2 minutes per point in position switch mode. The receivers A100, B100, A230 and B230 tuned to 86.13, 109.975, 219.56 and 231.32 GHz respectively were used at the front end. The parameters of the molecular transitions covered with this setup is given in Table 3.2.1. In Table 3.2, we give the source list.

The VESPA autocorrelator was used at the backend, with a spectral resolution of 40 KHz and 320 KHz at 100 and 230 GHz respectively. We had average summer weather conditions with maximum system temperature (T_{sys}) of 248 K at 110 GHz. Towards selected sources we also have C^{17}O ($2\rightarrow 1$) and NHD_2 ($1_{10}-1_{01}$) observations. The half power beam width (HPBW) of the 30m telescope is $22''$ at 110 GHz and $11''$ at 230 GHz. The main beam efficiency at these frequencies is 0.75 and 0.52, respectively.

Table 3.1: Parameters of observed rotational transitions.

Species	Transition	E_1 (K)	ν (MHz)
NH_3	(1,1)	22.70	23694.496
NH_3	(2,2)	63.89	23722.633
NH_2D	$1_{11}-1_{01}$	16.55	85926.3
NH_2D	$1_{11}-1_{01}$	15.98	110153.6
NHD_2	$1_{10}-1_{01}$	13.33	110812.9
NHD_2	$1_{10}-1_{01}$	13.091	110896.7
C^{18}O	1-0	0.0	109782.1734
C^{18}O	2-1	5.27	219560.3568
C^{17}O	2-1	5.39	224714.3850
H^{13}CN	J=1-0, F=2-1	0.0	86340.184
HC^{15}N	1-0	0.0	86054.961

Effelsberg 100m Observation

We observed the NH_3 (1,1) and (2,2) transitions with the Effelsberg 100 m telescope in April 2004 in all sources. With the AK 8192 backend, we were able to observe the (1,1), (2,2), (3,3) and (4,4) transitions in both polarisations simultaneously using the K-band receiver. With 8 subunits of 10 MHz bandwidth, the resulting spectral resolution was $\approx 0.2 \text{ km s}^{-1}$ after smoothing the data to improve the signal-to-noise ratio. The beam at the NH_3 frequencies was $40''$. The observations were performed in the frequency switching mode. Pointing was checked at hourly intervals by continuum scans on G10.62. We estimate the pointing to be accurate to within $6''$. The pointing scans were used for the absolute calibration.

NH_3 Single Dish Observations

The ratio of the NH_3 (1,1) and (2,2) transitions along with the optical depth, can be used to estimate the rotational temperature. For temperatures $< 20 \text{ K}$ typical of cold dark clouds, the rotational temperature is

Table 3.2: Positions and Velocities of the Observed Sources. IRDC Positions are Taken From Carey et al. (1998).

Source	R.A.(2000)	Dec.(2000)	v_{LSR} [km/s]
SCAMPS			
G8.13+0.25	18:02:55.697	-21:47:46.72	19.4
G8.68-0.37	18:06:23.248	-21:37:14.16	35.2/38.1
G8.71-0.37	18:06:26.516	-21:35:46.67	38.1
G10.21-0.31	18:09:20.634	-20:15:04.54	12.8
G10.21-0.32	18:09:24.523	-20:15:41.47	12.8
G10.15-0.34	18:09:21.387	-20:19:32.80	12.8
G10.61-0.33	18:10:15.629	-19:54:46.68	74.0
G13.18+0.06	18:14:00.920	-17:28:41.29	51.6
G15.01-0.67	18:20:21.229	-16:12:42.22	26.2
G15.03-0.65	18:20:18.805	-16:11:22.69	26.2
G15.01-0.69	18:20:24.227	-16:13:22.87	26.2
G18.17-0.30	18:25:07.534	-13:14:32.74	54.9
G18.21-0.34	18:25:21.558	-13:13:39.55	54.9
G23.41-0.23	18:34:45.745	-08:34:21.22	104.2
G23.42-0.23	18:34:48.167	-08:33:56.10	104.2
G23.44-0.18	18:34:39.253	-08:31:36.23	104.2
G27.29+0.15	18:40:34.703	-04:57:18.13	26.0
G27.31+0.18	18:40:32.454	-04:55:03.80	26.0
G81.74+0.59	20:39:00.373	+42:24:36.65	-3.1
G12.19-0.12	18:12:41.671	-18:25:19.80	27.6
G29.97-0.05	18:46:12.253	-02:39:05.90	100.4
G35.19-1.73	19:01:45.45	+01:13:21.5	42.4
IRDCs			
G11.11-0.12 P1	18:10:34.043	-19:21:49.0	29.2
G11.11-0.12 P3	18:10:07.250	-19:27:29.0	29.2
G11.11-0.12 P4	18:10:07.250	-19:28:49.0	29.2
G19.30+0.07 P1	18:25:58.14	-12:04:45.0	26.3
G19.30+0.07 P2	18:25:52.69	-12:04:45.0	26.3
G28.34+0.06 P1	18:42:50.9	-04:03:14	78.4
G28.34+0.06 P2	18:42:52.4	-03:59:54	78.4
G33.71-0.01	18:52:53.81	+00:41:06.4	104.2
G79.34+0.33	20:32:26.20	+40:19:40.9	0.1
Reference Position for PdBI Interferometer Observations			
G29.96e	18:46:12.787	-02:39:11.84	100.4
G35.20w	19:01:42.113	01:13:33.49	42.4

a close estimate of the gas kinetic temperature (Walmsley & Ungerechts 1983). Like NH_3 , its isotopologue NH_2D also has hyperfines which allows the estimation of optical depth and hence the column density assuming that NH_2D and NH_3 are coextensive and hence have the same gas temperature. Thus the fractionation ratio can be estimated. The main assumptions involved in determining the ratio are that NH_3 and NH_2D spatially coexist and are at the same temperature.

Out of the 32 sources, NH_2D with hyperfines are detected in 21 sources with a high S/N ratio ($> 3\sigma$) while we have a 100% NH_3 detection. The fits to the hyperfines for NH_3 and NH_2D were done using CLASS method NH_3 (1,1) and HFS respectively (Forveille et al. 1989). The line parameters from the resultant fits are given in Table 3.3. For those sources with a high uncertainty in the NH_2D optical depth, the main line is fitted with a single Gaussian and the integrated intensity is quoted. The spectra are shown in Fig. 3.1.

The basic physical parameters, namely the rotational temperature, the kinetic temperature and ammonia column density, have been derived using the standard formulation for NH_3 spectra (Bachiller et al. 1987). The expression used to estimate the column densities from the radiative transfer equations for all other molecules including NH_2D are given in Appendix A. The deduced physical parameters are given in Table 3.2.1. The uncertainties given in brackets are formal errors obtained by a Gaussian error propagation. The rotational temperatures are in a range from 11 to 24 K, with ammonia column densities from 1.3 to $5 \times 10^{15} \text{ cm}^{-3}$. We get $[\text{NH}_2\text{D}/\text{NH}_3]$ ratios from 0.002 – 0.66. In 10 out of the 21 sources with NH_2D detection, we get abundance ratio ≤ 0.02 while the rest of the sources have a high degree of deuteration ($\geq 13\%$). These 10 sources with low ratios show optically thin NH_2D emission and two of them (G8.13+0.25 and G8.68-0.37) have 2 (or more) velocity components.

In Fig. 3.2, the correlation between the velocities and line widths corresponding to the NH_2D and NH_3 emission is shown. Velocities and line widths are clearly different in some sources, with the NH_2D line widths being smaller. This could be either due to NH_2D and NH_3 tracing different regions or due to the slightly different beams at the two frequencies in which case, clumping might contribute to a larger line width. In §3.2.2, we clarify this issue with our interferometer observations.

CO Observations

The C^{18}O ($1 \rightarrow 0$) and ($2 \rightarrow 1$) observations were done simultaneously with NH_2D at 85.9 GHz. Fig. 3.3 shows the spectra toward all sources for which both transitions were detected (in 30 out of 32 sources). In Table 3.2.1 we list the observed line parameters based on Gaussian fits and in Table 3.2.1, the column density and rotational temperature estimates (see Appendix A) and the C^{18}O abundances. The H_2 column densities for deriving the fractional abundance of C^{18}O is from the 850 μm dust continuum emission using SCUBA after smoothing it to the 20'' resolution of the C^{18}O data.

The C^{18}O line might be optically thick and column densities would only be a lower limit. In order to check this, we observed the rarer isotopomer C^{17}O toward two of our sources, G35.20 and G81.74+0.59 as shown in Fig. 3.4. The line parameters are given in Table 3.2.1

H^{13}CN and HC^{15}N Observations

We also observed the isotopic species of HCN, H^{13}CN and HC^{15}N in our 1 mm setup. H^{13}CN was detected in almost all sources except G19.30P1/P2 and G10.15-0.34. In Fig. 3.5, we show the spectra toward all sources where both H^{13}CN and HC^{15}N are detected with sufficient S/N ($\geq 3\sigma$). H^{13}CN line has hyperfines, which allows to estimate the optical depth. However, we find that H^{13}CN is optically thin in almost all cases. The line parameters are given in Table 3.8 along with their column densities. The column density is computed using the gas temperature derived from NH_3 as the excitation temperature (see Appendix A).

Table 3.3: NH₂D and NH₃ Line Parameters with Uncertainties (in brackets) From the Hyperfine/Gaussian Fits.

Source	NH ₃ (1,1)			NH ₃ (2,2)		NH ₂ D 85.93 GHz	
	T_{MB} (K)	Δv km s ⁻¹	τ_{mg}	T_{MB} (K)	$T_{\text{MB}} \times \Delta v$ K km s ⁻¹	Δv km s ⁻¹	τ_{tot}
G8.13+0.25	1.9 (0.4)	1.48 (0.1)	1.48 (0.3)	1 (0.2)	0.32 (0.03)	1.27	–
G8.13+0.25	2.4 (0.4)	1.33 (0.08)	1.9 (0.27)	1.3 (0.2)	0.36 (0.04)	1.8	–
G8.68-0.37	5.3 (0.5)	1.12 (0.04)	4.95 (0.35)	2.3 (0.3)	–	1.24 (0.08)	2.23 (0.68)
G8.71-0.37	3.5 (0.4)	1.33 (0.04)	4.2 (0.29)	1.7 (0.2)	–	1.06 (0.04)	3.66 (0.59)
G10.21-0.31	2.9 (0.4)	1.9 (0.05)	3.92 (0.31)	1.8 (0.1)	–	1.17 (0.12)	3.41 (1.35)
G10.21-0.32	4.6 (0.4)	1.87 –	4.63 (0.15)	2.7 (0.1)	–	1.35 (0.12)	2.34 (0.99)
G10.61-0.33	2 (0.2)	1.9 (0.08)	1.76 (0.26)	1.1 (0.1)	0.27 (0.03)	1.48	–
G11.11-0.12P1	5.1 (1)	1.27 (0.05)	3.52 (0.38)	1.9 (0.3)	–	1.03 (0.11)	3.59 (1.49)
G11.11-0.12P4	4.3 (0.9)	1.53 (0.11)	3.15 (0.64)	0.9 (0.4)	0.35 (0.04)	1.34	–
G13.18+0.06	5.4 (0.5)	2.35 (0.03)	3.31 (0.11)	3.7 (0.1)	–	2.2 (0.14)	1.98 (0.47)
G15.01-0.69	3.3 (0.2)	2.63 (0.08)	0.5 (0.13)	2.3 (0.1)	0.2 (0.03)	1.16	–
G18.17-0.30	2.9 (0.3)	1.59 (0.04)	3.26 (0.23)	1.7 (0.1)	–	1.49 (0.11)	4.4 (1.05)
G18.21-0.34	3.8 (0.4)	1.53 (0.05)	2.81 (0.22)	2 (0.2)	–	1.33 (0.09)	1.99 (0.8)
G23.41-0.23	3 (0.3)	2.01 (0.06)	1.18 (0.15)	1.6 (0.2)	–	1.65 (0.23)	2.1 (1.33)
G23.44-0.18	3.6 (0.2)	3.58 (0.09)	1.66 (0.14)	2.8 (0.1)	0.74 (0.03)	1.87	–
G27.29+0.15	1.7 (0.2)	2.49 (0.07)	1.58 (0.17)	0.9 (0.1)	0.31 (0.04)	1.53	–
G28.34+0.06P2	2.8 (0.5)	1.98 (0.07)	2.74 (0.28)	1.5 (0.2)	1.07 (0.04)	2.2	–
G29.97-0.05	0.8 (0.2)	1.99 (0.05)	2.44 (0.17)	0.3 (0.3)	–	1.42 (0.06)	3.02 (0.6)
G33.71-0.01	2 (0.4)	2.35 (0.16)	2.92 (0.63)	1.5 (0.2)	0.35 (0.04)	1.55	–
G34.81-0.28	4.7 (0.5)	1.41 (0.04)	1.63 (0.17)	2.2 (0.1)	0.68 (0.04)	1.68	–
G35.19-1.73	4.7 (0.4)	1.58 (0.03)	1.8 (0.11)	2.4 (0.1)	–	1.36 (0.04)	2.74 (0.36)
G79.34+0.33	2.4 (0.3)	1.23 (0.03)	1.51 (0.12)	0.7 (0.1)	–	1.03 (0.91)	1.1 (0.1)

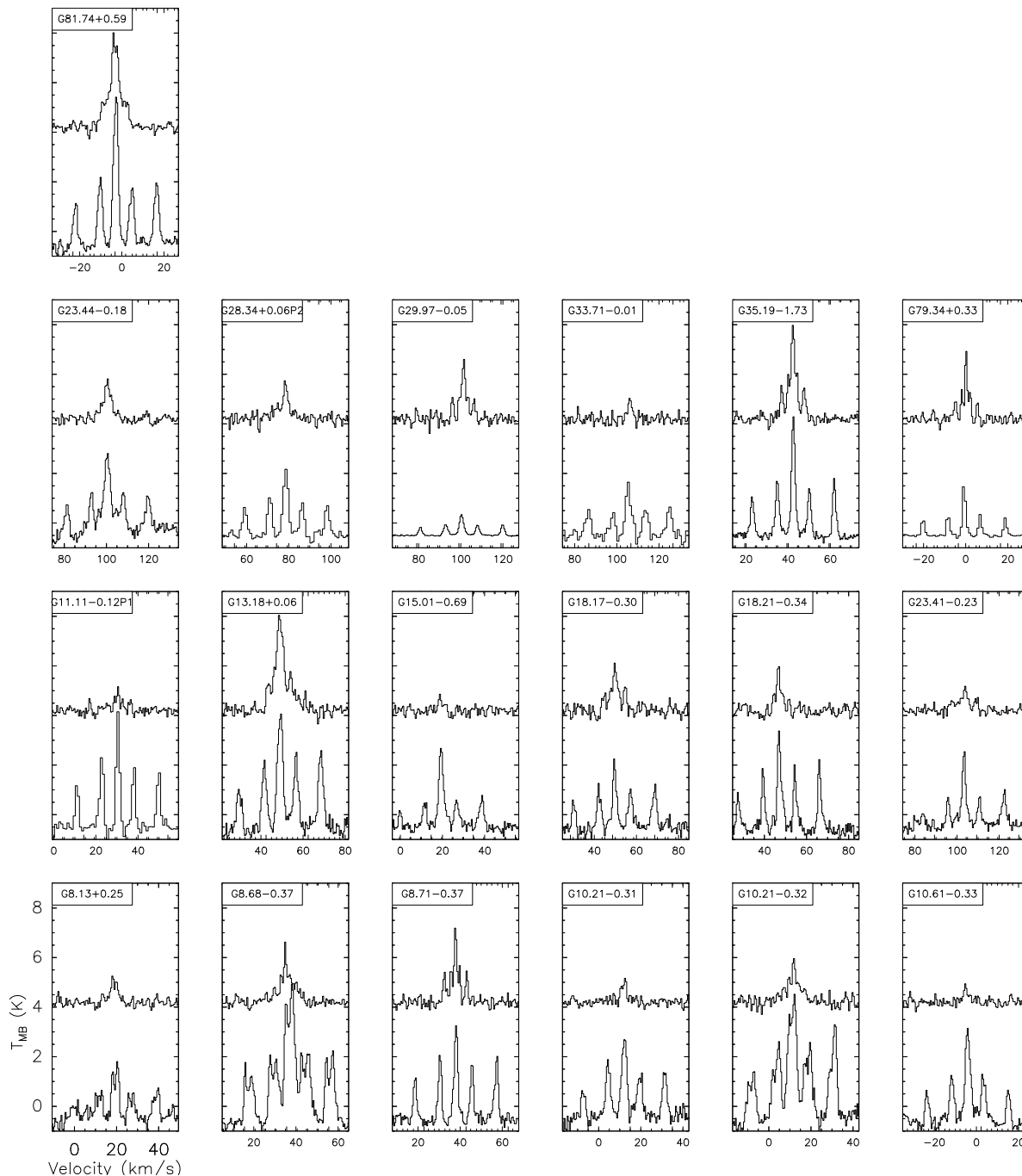


Figure 3.1: *Lower spectrum:* Effelsberg 100m observation of the NH_3 (1,1) emission. *Upper spectrum:* 30m observation of the NH_2D at 85.9 GHz. The NH_2D is scaled by a factor 3.5 to amplify the emission relative to NH_3 in the absolute units. The velocity range is $\pm 30 \text{ km s}^{-1}$ of the systemic velocity given in Table 3.2.

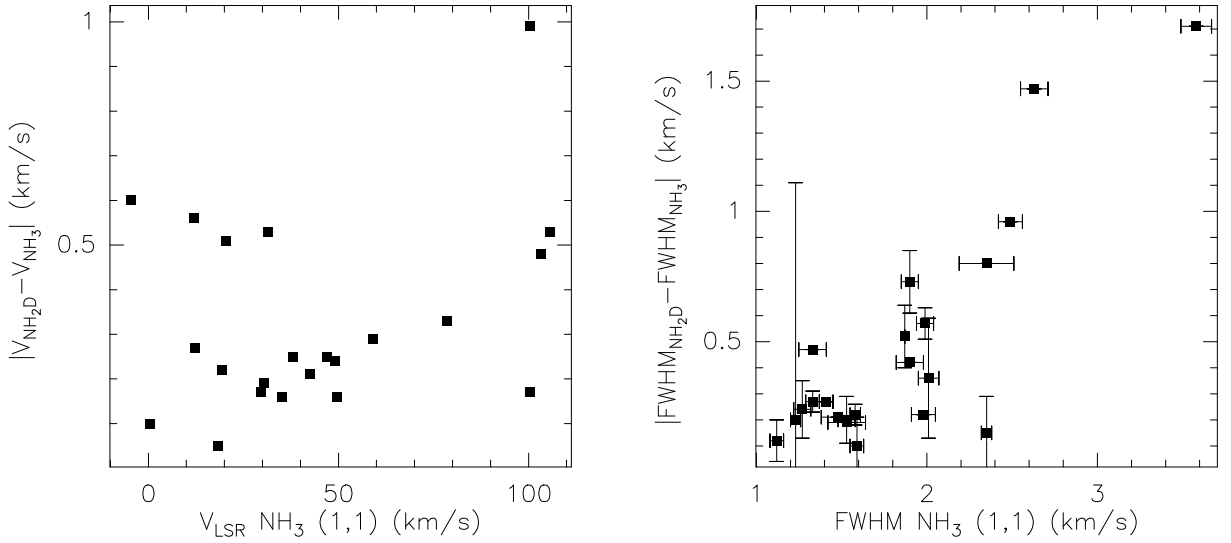


Figure 3.2: *Left panel:* The correlation plot between the LSR velocities of NH_3 and NH_2D . *Right panel:* The correlation plot between their line widths. Points with no y axis error bars are those for which line width has been fixed based on the hfs fit to the optically thin emission, to derive the NH_2D integrated intensity.

3.2.2 Interferometric Observations & Results

PdBI Observation

G29.96 East and G35.20 West have been observed with the Plateau de Bure Interferometer in its C and D configurations on Mar 27/28th and Apr 20/21st 2004. The 3mm receivers were tuned to the NH_2D line at 86.086 GHz in single sideband mode. Simultaneously, this allowed to observe as a bonus H^{13}CN and HC^{15}N (1-0). The 1.3mm receivers were tuned to the C^{18}O (2-1) line at 219.560 GHz in DSB mode. The 3 and 1mm lines were observed with resolutions of 80 and 320 KHz, respectively, and at both wavelengths two 320 MHz wide correlator windows were used to probe the continuum emission.

Hexagonal mosaics with a spacing of 10 arcsec were used to increase the field of view. This kept the sensitivity at the mosaic center very high for the 3mm observations and lead to fully sampled mosaics at 1.3mm. The phase center for the observations were 18:46:12.786, -02:39:11.84 (G29E) and 19:01:42.112, 01:13:33.49 (G35W).

Using natural weighting, the synthesized beam sizes at 3 and 1mm were $5.5 \times 4.1''$ and $2.2 \times 1.6''$ with a position angle of 43° .

VLA Observation

The 23 GHz NH_3 observations are reported for two sources G35.20 and G29.96. We retrieved the data for NH_3 (1,1) and (2,2) transitions at 1.3 cm from the VLA archive² toward G35.20, while for G29.96, we report our observations with the VLA.

The 23 GHz NH_3 observations were done with the Very Large Array (VLA) on 24 August 2004 in its D configuration and in 2 polarisations with a spectral resolution of 0.33 km s^{-1} , a synthesized HPBW of $\sim 8.0 \times 7.4''$ with a position angle (pa) of 12° and a primary beam of $\sim 120''$. The standard interferometer mode was used with a total integration time of 20 minutes on source split into sessions. Phase calibration

²The National Radio Astronomy Observatory is a facility of the National Science Foundation operated under cooperative agreement by Associated Universities, Inc.

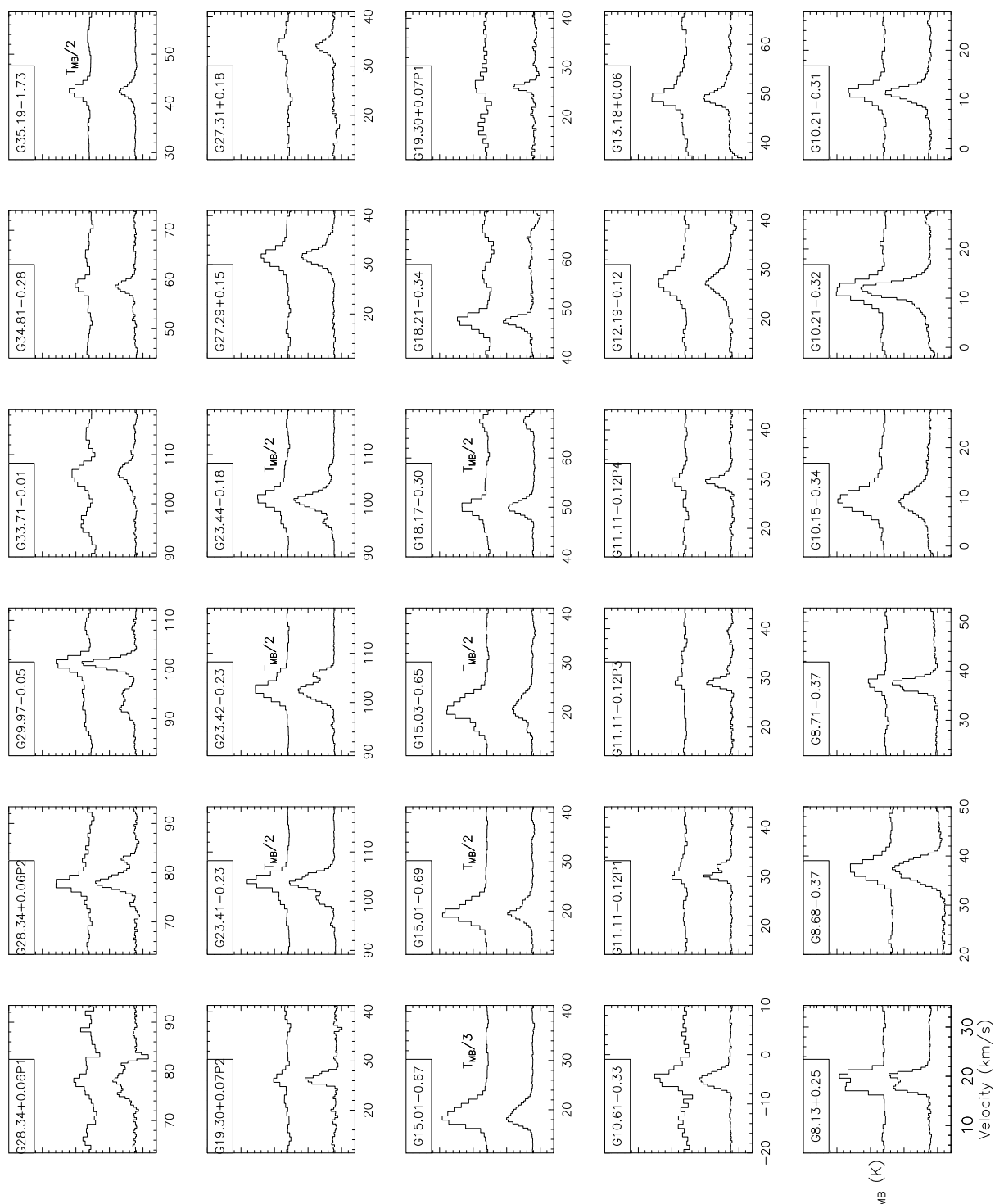


Figure 3.3: lower spectrum: 30m C^{18}O ($1 \rightarrow 0$). upper spectrum: 30m C^{18}O ($2 \rightarrow 1$). The velocity range is $\pm 15 \text{ km s}^{-1}$ of the systemic velocity.

Table 3.4: NH₃ Rotational Temperatures, NH₂D and NH₃ Column densities, and Fractionation. The Respective Uncertainties are Given (in brackets).

source	T_{rot} (K)	N_{NH_3} $10^{15}(10^{14}) \text{ cm}^{-2}$	$N_{\text{NH}_2\text{D}}$ 10^{13} cm^{-2}	$[\text{NH}_2\text{D}/\text{NH}_3]$
G8.13+0.25	17.7 (2.9)	1.8 (3.4)	1.1 (0.1)	0.0061 (0.0013)
G8.13+0.25	17.3 (2.1)	1.6 (2.3)	1.2 (0.1)	0.0075 (0.0012)
G8.68-0.37	12 (0.8)	1.3 (1.4)	39.2 (12.4)	0.3015 (0.1008)
G8.71-0.37	13.2 (0.9)	1.5 (1.5)	59.3 (10.4)	0.3953 (0.0798)
G10.21-0.31	15.3 (1.5)	2.1 (2.7)	70.4 (29.7)	0.3352 (0.1479)
G10.21-0.32	14.1 (0.8)	2.1 (1.6)	51.3 (22.3)	0.2443 (0.1078)
G10.61-0.33	18.1 (1.5)	2.3 (2.2)	0.9 (0.1)	0.0039 (0.0006)
G11.11-0.12P1	12.3 (1.2)	1.4 (2.2)	53.3 (23.2)	0.3807 (0.1762)
G11.11-0.12P4	10.6 (1.6)	1.8 (5.4)	1.5 (0.3)	0.0083 (0.0030)
G13.18+0.06	17.1 (1.3)	2.8 (2.4)	87.0 (22.8)	0.3107 (0.0857)
G15.01-0.69	24.3 (1.6)	4.0 (2.9)	0.7 (0.1)	0.0018 (0.0003)
G18.17-0.30	15.7 (1.4)	1.8 (1.9)	118.9 (31.9)	0.6606 (0.1904)
G18.21-0.34	15.5 (1.1)	1.7 (1.7)	47.3 (19.6)	0.2782 (0.1186)
G23.41-0.23	18.7 (1.5)	2.5 (2.2)	77.2 (50.7)	0.3088 (0.2046)
G23.44-0.18	23.4 (1.7)	5.3 (4.0)	2.6 (0.1)	0.0049 (0.0004)
G27.29+0.15	17.5 (1.5)	2.9 (3.0)	1.1 (0.1)	0.0038 (0.0005)
G28.34+0.06P2	15.6 (1.9)	2.2 (3.5)	3.7 (0.2)	0.0168 (0.0028)
G29.97-0.05	14.4 (1.6)	2.2 (3.4)	71.1 (16.4)	0.3232 (0.0897)
G33.71-0.01	19.9 (5.2)	3.0 (8.4)	1.2 (0.1)	0.0040 (0.0012)
G34.81-0.28	16.4 (1.1)	1.6 (1.3)	2.3 (0.1)	0.0144 (0.0013)
G35.19-1.73	17 (1)	1.8 (1.3)	74.0 (11.2)	0.4111 (0.0689)
G79.34+0.33	14 (0.9)	1.8 (1.2)	18.3 (16.3)	0.1307 (0.1170)

was done using J1733-130 and the flux calibrator was 3C286. The synthesized HPBW for G35.20 is $\sim 8.8 \times 6.9''$ and $\text{pa} = 42^\circ$.

BIMA Observation

G35.20 and G29.96 were observed with BIMA in its D configuration in Jul/Aug. 2003 in three tracks. The receivers were tuned to the NH₂D frequency. Simultaneously H¹³CN and HC¹⁵N (1-0) was observed and HCO+ (1-0) in the upper sideband. The frequency resolution is 0.1 MHz. The synthesized beam sizes are 30x17'', 22x18'' and 21x19''. Towards G29.96 a 5 point mosaic was observed to cover both the hot core and the SCAMPS source in the east.

The beam and its position angle, as well as the rms for each interferometer data whose discussion follows in further sections is given in Table 3.2.2.

Dust Continuum Observed with PdBI

The dust continuum at 3 mm towards G35.20 is shown in Fig.3.6 compared with a SCUBA image of the region (Thompson et al. in prep.). The strong continuum emission in the east is due to the bright HII region W48, hence most of the emission there is likely due to free-free emission. The field of view (i.e. the width of the primary beam) of the PdBI observations is indicated. Although the Ultracompact HII region G35.20 is 1 arcmin away and clearly out of the PdBI primary beam, it is so strong that it has

Table 3.5: C¹⁸O (1 → 0) and (2 → 1) Line Parameters with Uncertainties (in brackets).

Source	C ¹⁸ O (1 → 0)		C ¹⁸ O (2 → 1)	
	$T_{\text{MB}} \times \Delta v$ K km s ⁻¹	Δv km s ⁻¹	$T_{\text{MB}} \times \Delta v$ K km s ⁻¹	Δv km s ⁻¹
G8.13+0.25	7.62 (0.19)	1.99 (0.05)	15.58 (0.43)	2.28 (0.07)
G8.13+0.25	7.89 (0.19)	1.91 (0.05)	12.76 (0.43)	1.72 (0.06)
G8.68-0.37	25.58 (0.19)	5.01 (0.04)	31.18 (0.58)	4.48 (0.1)
G8.71-0.37	12.58 (0.13)	2.78 (0.03)	6.18 (0.46)	2.24 (0.18)
G10.15-0.34	15.97 (0.26)	5.43 (0.11)	37.95 (0.51)	5.23 (0.08)
G10.21-0.31	14.04 (0.13)	3.21 (0.04)	18.65 (0.36)	3.2 (0.07)
G10.21-0.32	9.17 (0.69)	7.7 (0.29)	–	–
G10.21-0.32	19.63 (0.66)	3.19 (0.06)	33.38 (0.63)	4.21 (0.09)
G10.61-0.33	10.43 (0.17)	3.22 (0.06)	11.82 (1.76)	2.6 (0.5)
G11.11-0.12P1	3.18 (0.07)	1.19 (0.21)	3.93 (0.33)	1.72 (0.15)
G11.11-0.12P3	4.75 (0.12)	1.87 (0.05)	3.19 (0.41)	1.93 (0.34)
G11.11-0.12P4	5.01 (0.07)	1.97 (0.21)	3.5 (0.5)	1.72 (0.2)
G12.19-0.12	12.26 (0.18)	5.15 (0.09)	20.77 (0.47)	4.84 (0.13)
G13.18+0.06	7.9 (0.88)	2.82 (0.26)	18.59 (0.83)	3.5 (0.21)
G15.01-0.67	22.54 (1.08)	4.1 (0.09)	92.67 (0.94)	4.48 (0.05)
G15.01-0.69	12.86 (0.19)	2.74 (0.05)	44.39 (0.62)	3.1 (0.05)
G15.03-0.65	8.12 (0.19)	2.89 (0.08)	49 (0.88)	3.72 (0.08)
G15.03-0.65	10.49 (0.09)	4.03 (0.09)	11.35 (0.58)	2.45 (0.11)
G18.17-0.30	15.07 (0.13)	2.92 (0.03)	24.16 (1.05)	2.88 (0.15)
G18.21-0.34	6.82 (0.17)	2.36 (0.07)	13.57 (1.01)	2.77 (0.24)
G19.30+0.07P1	3.81 (0.15)	1.59 (0.08)	5.38 (1.31)	2.68 (0.83)
G19.30+0.07P2	6.63 (0.13)	2.09 (0.05)	4.5 (0.65)	2.11 (0.37)
G23.41-0.23	18.91 (2.57)	2.12 (0.2)	37.21 (0.69)	2.82 (0.06)
G23.42-0.23	25.28 (0.28)	3.53 (0.21)	24.91 (0.19)	2.27 (0.01)
G23.42-0.23	6.2 (0.28)	1.58 (0.21)	9.17 (0.35)	2.72 (0.12)
G23.44-0.18	27.4 (0.17)	3.51 (0.03)	37.03 (0.8)	3.71 (0.09)
G27.29+0.15	11.3 (0.14)	3.53 (0.05)	16.14 (0.48)	3.73 (0.13)
G27.31+0.18	4.73 (0.15)	2.65 (0.09)	5.57 (0.43)	3.18 (0.3)
G28.34+0.06P1	7.43 (0.52)	3.28 (0.27)	10.55 (1.15)	3.66 (0.41)
G28.34+0.06P2	12.42 (0.14)	2.86 (0.04)	17.62 (0.46)	2.96 (0.1)
G29.97-0.05	12.09 (0.18)	2.27 (0.04)	17.12 (0.73)	3.18 (0.17)
G33.71-0.01	7.06 (0.2)	4.33 (0.16)	10.43 (1.09)	3.49 (0.35)
G34.81-0.28	4.9 (0.16)	2.51 (0.09)	6.1 (0.49)	2.52 (0.22)
G35.19-1.73	8.17 (0.09)	2.66 (0.04)	16.79 (0.49)	2.59 (0.09)
G79.34+0.33	3.75 (0.27)	1.3 (0.04)	9.95 (0.14)	2.25 (0.04)
G81.74+0.59	15.25 (0.12)	2.5 (0.02)	31.1 (0.26)	2.74 (0.03)

Table 3.6: $C^{18}O$ Column Density and Abundance from $(1 \rightarrow 0)$ and $(2 \rightarrow 1)$ Transitions. The Formal Errors are Quoted (in brackets).

Source	T_{ROT} K	$C^{18}O (1 \rightarrow 0)$			$C^{18}O (2 \rightarrow 1)$		
		$N(H_2)$ 10^{23} cm^{-2}	$N_{C^{18}O}$ cm^{-2}	$\chi_{C^{18}O}$ 10^{-8}	$N_{C^{18}O}$ cm^{-2}	$\chi_{C^{18}O}$ 10^{-8}	
G8.13+0.25	17.7 (2.9)	2.63	9.19E15 (9.79E14)	3.49	8.17E15 (5.50E14)	3.10	
G8.13+0.25	17.3 (2.1)	–	9.38E15 (7.44E14)	–	6.68E15 (3.70E14)	–	
G8.68-0.37	17.2 (1)	7.87	3.03E16 (1.12E15)	3.85	1.63E16 (4.50E14)	2.07	
G8.71-0.37	13.2 (0.9)	3.51	1.29E16 (4.52E14)	3.66	3.31E15 (2.50E14)	9.43	
G10.15-0.34	21.4 (2.7)	3.83	2.19E16 (1.96E15)	5.70	2.05E16 (1.29E15)	5.36	
G10.21-0.31	15.3 (1.5)	2.25	1.55E16 (8.78E14)	6.90	9.76E15 (3.20E14)	4.34	
G10.21-0.32	14.3 (1.5)	7.39	9.76E15 (9.17E14)	1.32	–	–	
G10.21-0.32	14.1 (0.8)	–	2.07E16 (9.35E14)	–	1.76E16 (3.90E14)	–	
G10.61-0.33	18.1 (1.5)	2.72	1.28E16 (7.09E14)	4.69	6.21E15 (9.50E14)	2.28	
G11.11-0.12P1	12.3 (1.2)	1.08	3.14E15 (1.55E14)	2.91	2.14E15 (1.80E14)	1.98	
G11.11-0.12P3	13.3 (3.9)	0.79	4.87E15 (7.22E14)	6.14	1.70E15 (2.30E14)	2.14	
G11.11-0.12P4	10.6 (1.6)	1.41	4.66E15 (2.56E14)	3.31	2.04E15 (2.90E14)	1.45	
G12.19-0.12	14.9 (0.8)	2.44	1.33E16 (4.45E14)	5.48	1.09E16 (2.90E14)	4.47	
G13.18+0.06	17.1 (1.3)	6.32	9.33E15 (1.13E15)	1.48	9.73E15 (5.10E14)	1.54	
G15.01-0.67	24.4 (1.6)	16.61	3.39E16 (2.31E15)	2.04	5.21E16 (1.95E15)	3.14	
G15.01-0.69	24.3 (1.6)	11.64	1.93E16 (9.78E14)	1.66	2.49E16 (9.60E14)	2.14	
G15.03-0.65	24.7 (6.8)	12.26	1.23E16 (2.53E15)	1.01	2.77E16 (4.26E15)	2.26	
G15.03-0.65	22.6 (5.3)	–	1.49E16 (2.51E15)	–	6.23E15 (8.10E14)	–	
G18.17-0.30	15.7 (1.4)	3.26	1.69E16 (8.88E14)	5.18	1.26E16 (6.40E14)	3.87	
G18.21-0.34	15.5 (1.1)	2.51	7.59E15 (3.63E14)	3.02	7.10E15 (5.50E14)	2.83	
G19.30+0.07P1	16.9 (1.7)	–	4.47E15 (3.27E14)	–	2.81E15 (6.90E14)	–	
G19.30+0.07P2	13.8 (1.9)	–	6.93E15 (5.12E14)	–	2.38E15 (3.50E14)	–	
G23.41-0.23	18.7 (1.5)	9.29	2.36E16 (3.44E15)	2.55	1.96E16 (7.40E14)	2.11	
G23.42-0.23	18.9 (1.7)	3.81	3.18E16 (1.91E15)	8.36	1.32E16 (5.00E14)	3.46	
G23.42-0.23	15.7 (2.3)	4.57	6.95E15 (6.70E14)	1.52	4.79E15 (2.80E14)	1.05	
G23.44-0.18	23.4 (1.7)	7.74	4.00E16 (2.12E15)	5.17	2.06E16 (9.10E14)	2.65	
G27.29+0.15	17.5 (1.5)	1.73	1.35E16 (7.47E14)	7.82	8.46E15 (3.70E14)	4.89	
G27.31+0.18	17.4 (2.4)	1.74	5.65E15 (5.19E14)	3.24	2.92E15 (2.70E14)	1.68	
G28.34+0.06P1	15.9 (1.4)	1.51	8.40E15 (7.30E14)	5.55	5.51E15 (6.20E14)	3.64	
G28.34+0.06P2	15.6 (1.9)	7.84	1.39E16 (9.90E14)	1.77	9.21E15 (4.00E14)	1.17	
G29.97-0.05	14.4 (1.6)	2.62	1.29E16 (7.99E14)	4.93	9.01E15 (4.50E14)	3.44	
G33.71-0.01	19.9 (5.2)	–	9.20E15 (1.64E15)	–	5.56E15 (8.70E14)	–	
G34.81-0.28	16.4 (1.1)	–	5.64E15 (2.92E14)	–	3.19E15 (2.70E14)	–	
G35.19-1.73	17 (1)	–	9.61E15 (3.64E14)	–	8.78E15 (3.10E14)	–	
G79.34+0.33	14 (0.9)	2.14	3.95E15 (3.14E14)	1.84	5.26E15 (1.00E14)	2.46	
G81.74+0.59	18.3 (1.1)	4.67	1.88E16 (7.43E14)	4.03	1.64E16 (4.10E14)	3.51	

Table 3.7: $C^{17}O (2 \rightarrow 1)$ Line Parameters with Uncertainties (in brackets).

Source	$C^{17}O (2 \rightarrow 1)$	
	$T_{\text{MB}} \times \Delta v$ K km s^{-1}	Δv km s^{-1}
G35.19-1.73	7.0630 (0.097)	3.279 (0.055)
G81.74+0.59	5.4679 (0.099)	3.295 (0.071)

Table 3.8: H¹³CN and HC¹⁵N Line Parameters and Column Density.

Source	H ¹³ CN J=1-0, F=2-1				HC ¹⁵ N J=1-0		
	$T_{\text{MB}} \times \Delta v$ K km s ⁻¹	Δv km s ⁻¹	T_{ROT} K	$\log(N_{\text{H}^{13}\text{CN}})$ cm ⁻²	$T_{\text{MB}} \times \Delta v$ K km s ⁻¹	Δv km s ⁻¹	$\log(N_{\text{HC}^{15}\text{N}})$ cm ⁻²
G10.21-0.31	0.93 (0.06)	3.54	15.3 (1.5)	2.25E12 (0.20E12)	0.19 (0.04)	1.21 (0.38)	0.46E12 (0.30E12)
G10.21-0.32	0.73 (0.06)	2.4	14.3 (1.5)	1.70E12 (0.17E12)	0.56 (0.24)	5.57 (2.21)	1.31E12 (0.94E12)
G13.18+0.06	3.01 (0.10)	3.68	17.1 (1.3)	7.80E12 (0.46E12)	0.73 (0.06)	3.31 (0.35)	1.91E12 (1.25E12)
G15.01-0.67	7.27 (0.23)	3.36	24.4 (1.6)	24.21E12 (1.42E12)	2.55 (0.24)	2.80 (0.25)	8.56E12 (6.50E12)
G15.01-0.69	4.78 (0.15)	2.74	24.3 (1.6)	15.87E12 (0.93E12)	1.57 (0.09)	2.44 (0.17)	5.25E12 (3.97E12)
G15.03-0.65	4.2 (0.13)	3.59	24.7 (6.8)	14.11E12 (2.97E12)	0.29 (0.12)	1.36 (0.35)	0.98E12 (0.85E12)
G15.03-0.65	1.81 (0.09)	1.67	22.6 (5.3)	5.69E12 (1.02E12)	1.35 (0.19)	4.96 (0.57)	4.28E12 (3.20E12)
G23.41-0.23	1.25 (0.05)	2.01	18.7 (1.5)	3.44E12 (0.23E12)	0.46 (0.06)	2.64 (0.46)	1.27E12 (0.88E12)
G23.42-0.23	1.35 (0.06)	3.42	18.9 (1.7)	3.74E12 (0.28E12)	0.39 (0.05)	2.59 (0.36)	1.09E12 (0.76E12)
G28.34+0.06P2	1.08 (0.07)	3.1	15.6 (1.9)	2.64E12 (0.26E12)	0.73 (0.07)	3.67 (0.47)	1.80E12 (1.12E12)
G35.19-1.73	1.94 (0.07)	2.35	17.0 (1.0)	5.01E12 (0.26E12)	0.55 (0.06)	2.00 (0.30)	1.43E12 (0.94E12)
G79.34+0.33	0.81 (0.03)	1.45	14.0 (0.9)	1.86E12 (0.10E12)	0.23 (0.03)	1.18 (0.19)	0.53E12 (0.31E12)
G81.74+0.59	3.18 (0.10)	2.8	18.3 (1.1)	8.62E12 (0.44E12)	1.11 (0.05)	2.75 (0.15)	3.03E12 (2.04E12)

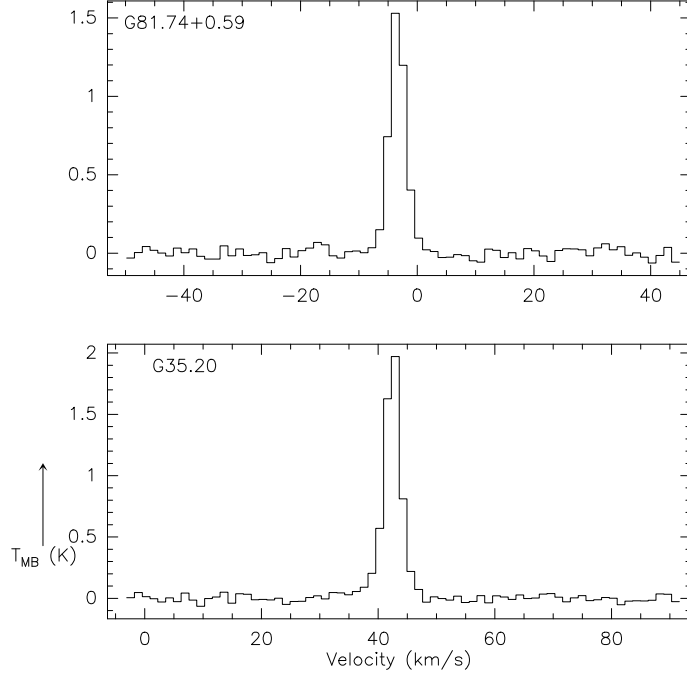


Figure 3.4: 30m $C^{17}O$ ($2 \rightarrow 1$) spectra toward G35.20 and G81.74+0.59.

Table 3.9: The Effective Beam Parameters for the Interferometer Observations.

Instrument	Wavelength(Type) mm	$\theta_{\text{maj}} \times \theta_{\text{min}}$ arcsec	pa degrees	rms mJy/beam
G29.96e				
PdBI	1	2.177×1.631	44.47	2.1
PdBI	3	5.509×4.131	43.39	0.47
BIMA	3.36(HCO ⁺)	21.74×17.64	14.33	70
BIMA	3.49 (NH ₂ D)	21.15×18.97	17.71	60
PdBI	3.49 (NH ₂ D)	5.518×4.137	43.38	40
VLA	13 (NH ₃)	8.001×7.431	12.14	0.86
G35.20w				
PdBI	1	1.753×1.639	52.98	2.41
PdBI	3	4.453×4.213	45.26	0.45
BIMA	3.36(HCO ⁺)	19.15×18.28	-20.88	10
VLA	13 (NH ₃)	8.759×6.957	42.33	0.40
PdBI	3.49(NH ₂ D)	4.459×4.220	45.31	30

Notes: Columns are the Interferometer array used, the wavelength with the molecule in brackets for line observations, the major and minor axis of the effective beam, its position angle and the the rms noise in the final image. We discuss G35.20w, followed by G29.96e in each subsection below.

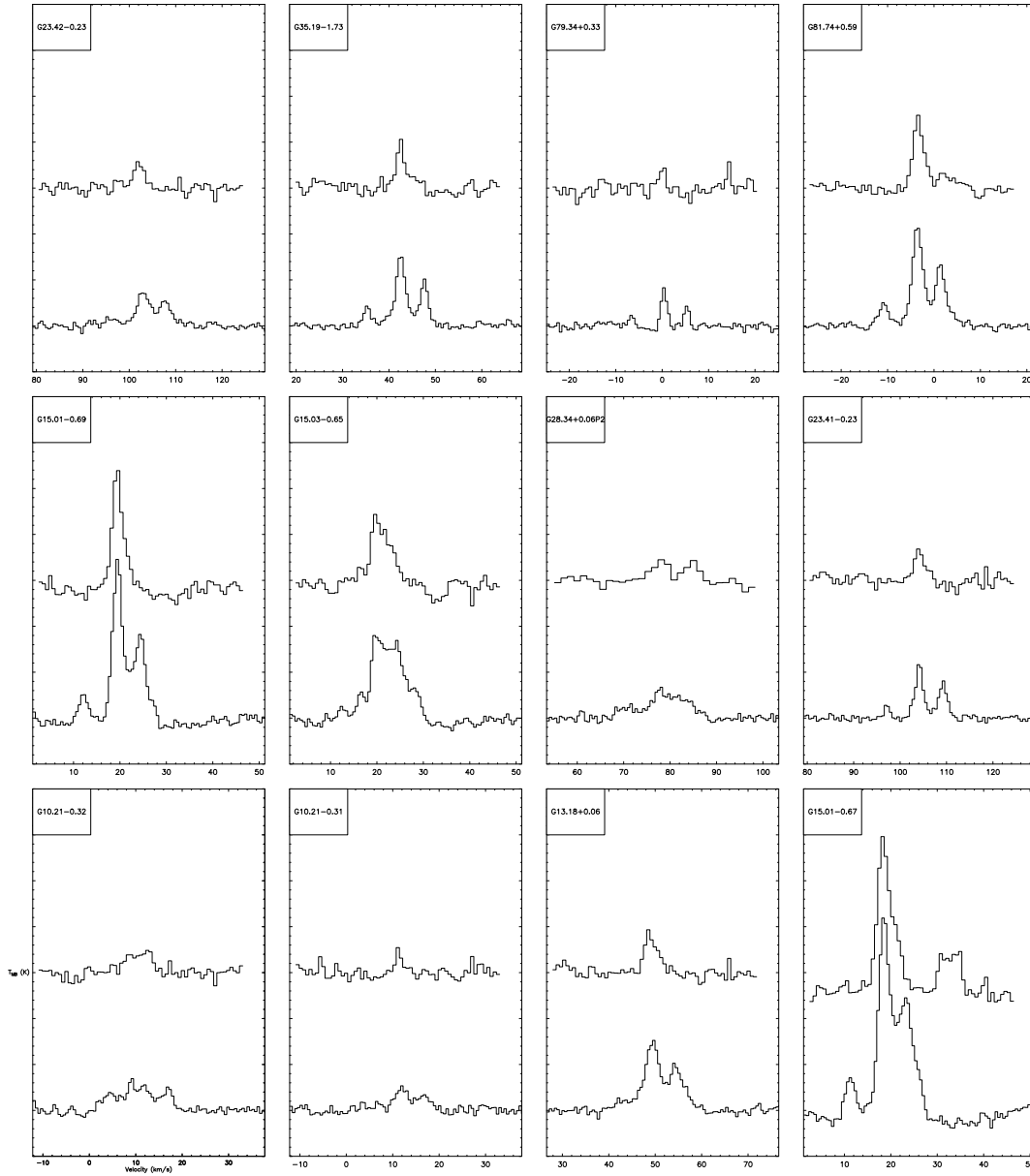


Figure 3.5: Lower spectrum: 30m observation of H^{13}CN . Upper spectrum: 30m observation of HC^{15}N . The HC^{15}N is scaled by a factor 2 to amplify the emission relative to H^{13}CN in the absolute units. The velocity range is $\pm 25 \text{ km s}^{-1}$ of the systemic velocity.

to be taken into account for the deconvolution of the 3mm image and is therefore shown in the figure. Note, that the 3mm morphology towards the HII cannot be trusted in detail, since it is so far out of the primary beam. The dust continuum emission in the west peaks toward a warm core, as evident from methyl cyanide observations (Goedhart et al. in prep), and extends along a ridge with several secondary clumps. In general, the 3mm and 850 μ m emission show the same morphology in the ridge, but the 3mm observations reach already a factor 3 higher in angular resolution. At the high resolution of the 1 mm data, we find very compact emission while the large scale structure is significantly filtered out by the Interferometer. We therefore use the 3 mm data in the following for estimates of dust masses.

The mass of the clump is determined from the 3 mm dust continuum following the relation

$$M(\text{H}_2) \propto \frac{S_\nu d^2}{\kappa_m(\nu) B_\nu(T)}. \quad (3.1)$$

Here, $B_\nu(T)$ is the Planck function corresponding to the wavelength, λ , and temperature, T . Substituting the values, the equation can be expressed as (Launhardt & Henning 1997)

$$M(\text{H}_2)[M_\odot] = 1.8 \times 10^{-14} \frac{S_\nu \lambda^3 d^2 e^{\frac{1.44 \times 10^4}{T_d \lambda}}}{\kappa_m(\lambda)} \frac{Z_\odot}{Z} [M_\odot] \quad (3.2)$$

where S_ν is the integrated flux density in Jy, λ the wavelength in μ m, Z/Z_\odot is the metallicity relative to the solar metallicity (we assume 1) and d is the distance to the source. We used a dust mass absorption coefficient, κ_m , of 0.21 cm^{-2}/g at 3 mm for dust grains with thick ice mantles and gas density $n(\text{H}) = 10^6 \text{ cm}^{-3}$ (Ossenkopf & Henning 1994). Here we assume that the dust temperature, T_d , is approximately equal to the gas temperature. We derive masses from 100 – 270 M_\odot toward the 6 brightest clumps.

For G29.96, the 3 mm dust continuum breaks up the SCUBA clump into a N-S filament (Fig.3.7). This filament as seen at 1 mm is then resolved into several cores, with a strong peak whose morphology hint towards further substructure. Since the 3mm emission remains largely unresolved, we determine only the total mass of this filament, which is 3000 M_\odot .

NH₂D Obtained with PdBI

G35.20, as a relatively nearby (3.2 kpc) SCAMPS source, allows us the highest spatial resolution view of our source sample so far. As shown in Fig.3.6, NH₂D is clearly resolved in the PdBI image, with several cores embedded in a streamer-like morphology. The channel maps were used to estimate the position and the size of the different clumps. At a S/N ratio $\geq 5\sigma$ (≈ 1 K), we identified 14 clumps over the mapped region. We use a clump finding algorithm that starts with a single Gaussian component fit to the brightest source position in each velocity channel. The image is then cleaned by subtracting the identified clump and searches for the next clump and so on. The output is then further sorted out based on the FWHM of the observed beam which is $\approx 4.5''$ for the PdBI and the algorithm identifies only those clumps with an overlap of $< 50\%$ of the beam. The results appear reasonable and similar to those obtained by running GAUSSCLUMPS (Stutzki & Guesten 1990).

Toward G29E, NH₂D is spread along the filament with the brightest NH₂D clump coinciding well with the continuum emission (Fig.3.6). But there are also several weak secondary peaks offset from the continuum emission. As for G35W, we identified clumps with our algorithm, although at a distance of 7.4 kpc the clumps might remain still unresolved. The line parameters of NH₂D are given in Table 3.10.

VLA NH₃ Data

The ammonia (1,1) emission in G35.20 closely follows the 3 mm dust continuum but does not correlate well with the NH₂D emission (Fig.3.6), the peaks of both molecules are clearly anti-correlated, although

Table 3.10: NH₂D and NH₃ Line Parameters with Uncertainties (in brackets) From the Hyperfine/Gaussian Fits.

Offsets	NH ₃ (1,1)		τ_{mg}	NH ₃ (2,2)		NH ₂ D 85.93 GHz	
	T_{MB} (K)	Δv km s ⁻¹		T_{MB} (K)	$T_{\text{MB}} \times \Delta v$ K km s ⁻¹	Δv km s ⁻¹	τ_{tot}
G35.20							
(-21 , 1)	2.47 (0.64)	1.1 (0.11)	2.94 (1.01)	0.64 (0.44)		0.51 (0.03)	5.34 (0.89)
(-16 , -13)	3.11 (0.92)	1.03 (0.12)	4.89 (1.09)	2.55 (0.7)		0.57 (0.03)	6.09 (0.92)
(-14 , -10)	4.49 (1.22)	1.03 (0.54)	4.04 (1.01)	3.09 (0.73)		0.66 (0.02)	5.54 (0.56)
(-13 , -5)	5.12 (1.03)	1.11 (0.07)	2.18 (0.47)	3.42 (0.72)		0.77 (0.02)	4.55 (0.38)
(-8 , 5)	5.71 (1.18)	1.4 (0.1)	2.31 (0.51)	3.32 (0.63)		1.12 (0.02)	3.81 (0.35)
(-5 , 7)	5.18 (1.11)	1.38 (0.07)	2.83 (0.42)	2.59 (0.53)		0.78 (0.06)	3.96 (0.68)
(-5 , 7)	5.18 (1.11)	1.38 (0.07)	2.83 (0.42)	2.59 (0.53)		0.8 (0.02)	2.88 (0.3)
(-3 , 4)	6.06 (0.98)	1.6 (0.04)	2.47 (0.2)	4.36 (0.66)		0.88 (0.05)	3.61 (0.3)
(-3 , 4)	6.06 (0.98)	1.6 (0.04)	2.47 (0.2)	4.36 (0.66)		0.78 (0.04)	3.57 (0.44)
(7 , 4)	7.76 (1.84)	1.51 (0.05)	3.24 (0.32)	5.37 (0.85)		1.14 (0.03)	1.94 (0.36)
(8 , 0)	7.97 (1.98)	1.58 (0.04)	3.7 (0.29)	5.33 (0.86)		0.95 (0.03)	3.74 (0.51)
(3.2 , 0.58)	8.05 (2.06)	1.74 (0.06)	3.29 (0.31)	5.61 (0.93)		1.22 (0.12)	4.23 (0.98)
(19.1 , 0.25)	10.81 (2.29)	1.89 (0.07)	1.87 (0.25)	6.75 (0.37)		1.18 (0.2)	3.09 (2.26)
G29.96							
(-6 ,-4)	0.59 (0.13)	1.32 (0.09)	2.54 (0.46)	0.23 (0.06)	–	0.69 (0.05)	1.34 (0.76)
(-1 ,-26)	0.31 (0.1)	1.3 (0.2)	4.59 (1.24)	0.14 (0.06)	–	1.01 (0.06)	6.35 (1.05)
(0 , 8)	0.78 (0.19)	2.06 (0.09)	2.9 (0.38)	0.54 (0.1)	–	1.25 (0.03)	4.34 (0.37)
(3 ,-13)	0.59 (0.16)	1.93 (0.16)	2.77 (0.68)	0.31 (0.06)	–	0.9 (0.04)	5.39 (0.71)
(4 , 3)	0.49 (0.13)	2.06 (0.18)	2.97 (0.74)	0.34 (0.07)	–	1.35 (0.04)	1.99 (0.34)
(10 ,-18)	0.36 (0.11)	1.09 (0.13)	2.57 (1.22)	0.08 (0.05)	–	0.69 (0.03)	2.64 (0.57)
(12 ,-14)	0.37 (0.09)	1.03 (0.15)	1.77 (0.78)	0.09 (0.06)	1.74 (0.09)	0.88 (0.07)	–

towards the NH_2D peaks, 3mm continuum as well the main ammonia isotope is still present on a low level.

The line parameters of the NH_3 and NH_2D spectra extracted toward the center of the clumps identified in NH_2D is given in Table 3.10. The rotational temperature, column densities and fractionation ratio were derived in the same way as for the single dish data (§3.2.1) using Eq.A.1 and are given in Table 3.2.2. As for the single dish data, the level of deuteration varies between clumps from low values (<5%) to over 80%. These values for the NH_3 brightest peaks which do not coincide with NH_2D emission is also listed in the two tables.

Table 3.11: NH_3 Rotational Temperatures, NH_2D and NH_3 Column densities, and Fractionation toward G29.96 and G35.20. The Respective Uncertainties are Given (in brackets).

Offsets (arcsec)	T_{rot} (K)	N_{NH_3} $10^{15}(10^{14}) \text{ cm}^{-2}$	$N_{\text{NH}_2\text{D}}$ $10^{14}(10^{13}) \text{ cm}^{-2}$	$[\text{NH}_2\text{D}/\text{NH}_3]$
G35.20				
(-21 , 1)	11.47 (2.86)	1.63 (7.5)	3.74 (8.89)	0.22 (0.11)
(-16 , -13)	17.77 (8.12)	1.8 (5.5)	7.26 (41.90)	0.40 (0.26)
(-14 , -10)	16.31 (4.49)	1.96 (11.5)	6.91 (22.78)	0.35 (0.23)
(-13 , -5)	19.27 (4.33)	1.26 (2.3)	8.10 (24.30)	0.64 (0.22)
(-8 , 5)	17.29 (3.15)	1.91 (3.8)	8.63 (20.39)	0.45 (0.13)
(-5 , 7)	15.05 (2.35)	2.20 (3.8)	5.35 (13.33)	0.24 (0.07)
(-5 , 7)	15.05 (2.35)	2.20 (3.8)	3.99 (7.79)	0.18 (0.04)
(-3 , 4)	19.79 (3.78)	2.43 (2.1)	7.60 (20.30)	0.31 (0.08)
(-3 , 4)	19.79 (3.78)	2.43 (2.1)	6.66 (18.72)	0.27 (0.08)
(7 , 4)	17.65 (3.93)	3.20 (4.3)	4.58 (15.04)	0.14 (0.05)
(8 , 0)	16.48 (3.48)	3.94 (5.6)	6.80 (18.98)	0.17 (0.05)
(3.2 , 0.58)	17.66 (4.23)	3.88 (5.4)	1.07 (4.39)	0.02 (0.01)
(19.1 , 0.25)	19.06 (2.92)	3.34 (3.5)	8.32 (23.99)	0.24 (0.07)
G29.96				
(-6 ,-4)	13.88 (2.12)	0.88 (2.1)	1.47 (8.71)	0.17 (0.10)
(-1 ,-26)	12.7 (2.97)	1.56 (6.3)	9.48 (24.53)	0.61 (0.29)
(0 , 8)	18.36 (4.45)	1.37 (2.2)	11.80 (37.01)	0.86 (0.30)
(3 ,-13)	15.53 (2.96)	1.28 (3.6)	8.69 (21.60)	0.68 (0.25)
(4 , 3)	18.42 (5.24)	1.29 (3.6)	5.87 (23.12)	0.46 (0.21)
(10 ,-18)	11.45 (2.53)	0.85 (4.8)	2.49 (6.52)	0.29 (0.18)
(12 ,-14)	12.51 (3.05)	0.50 (2.6)	0.64 (0.89)	0.12 (0.06)

3.3 Analysis and Discussion

3.3.1 CO Depletion

Since on the observed sample we have dust continuum and CO observations available, the depletion can be studied for the first time on a massive clump sample.

Recent observational studies on the condensation of CO in prestellar cores reveal that in the initial cold and dense evolutionary stage, CO is heavily depleted onto the dust grains (Caselli et al. 1999, Kramer et al. 1999, Bacmann et al. 2002). We follow the definition for the depletion factor (η) as given by Kramer

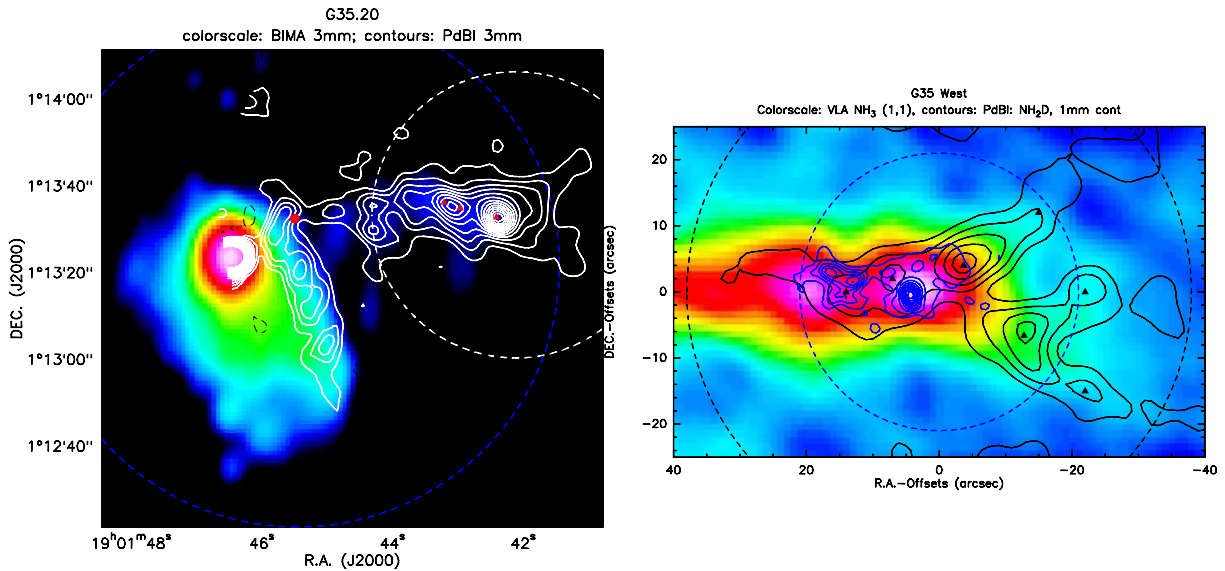


Figure 3.6: *Left panel:* SCUBA 850 micron continuum (colorscale) and PdBI 3 mm dust continuum (contours). *Right panel:* VLA NH₃ (1,1) (colorscale) and PdBI NH₂D at 85.9 GHz (black contours), and PdBI 1 mm dust continuum (blue contours). The field of view (FOV) at 1 and 3 mm is indicated by the dashed circles.

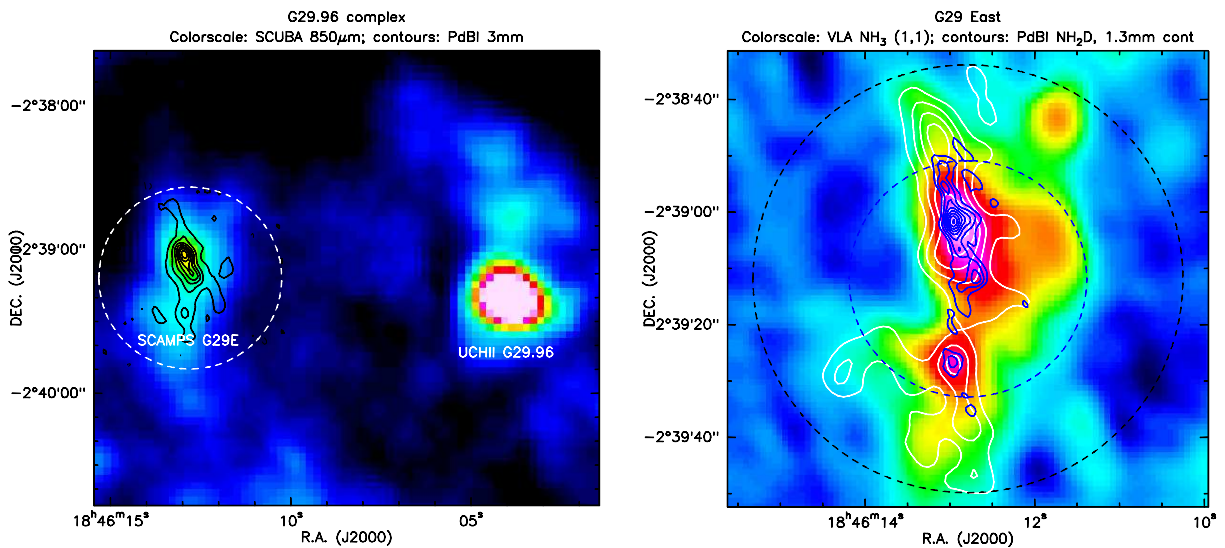


Figure 3.7: *Left panel:* BIMA 3 mm dust continuum (colorscale) and PdBI 3 mm dust continuum (contours). *Right panel:* VLA NH₃ (1,1) (colorscale) and PdBI NH₂D at 85.9 GHz (black contours), and PdBI 1 mm dust continuum (blue contours). The field of view (FOV) at different frequencies is indicated by the dashed circles.

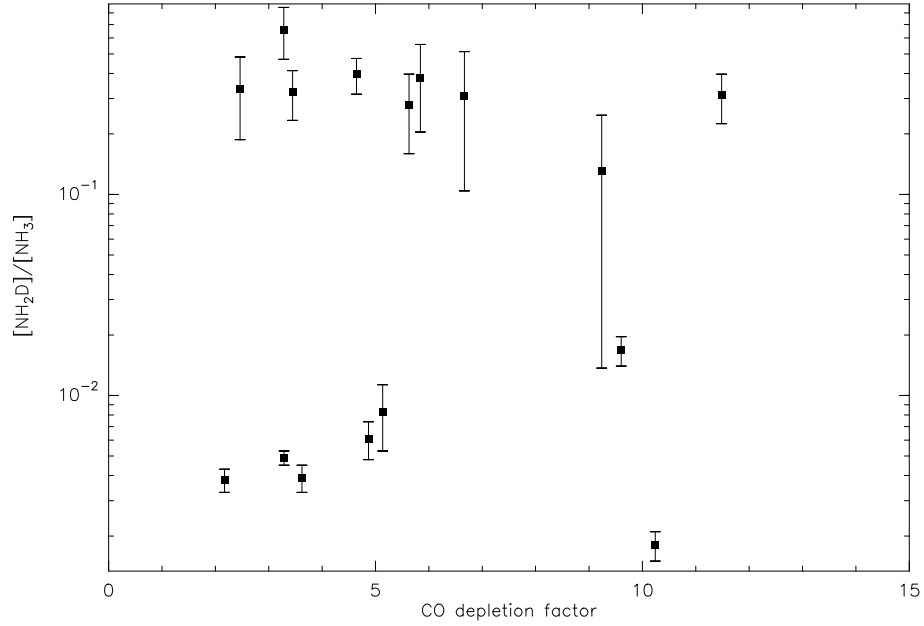


Figure 3.8: Comparison of NH_3 fractionation and CO depletion factor for the dense cores in our sample. The error bar on CO depletion factor is quite large mainly due to the uncertain dust opacities adopted (see §3.3.1).

et al. (1999).

$$\frac{[\text{C}^{18}\text{O}]}{[\text{H}_2]}_{\text{observed}} = \eta \frac{[\text{C}^{18}\text{O}]}{[\text{H}_2]}_{\text{canonical}}. \quad (3.3)$$

The H_2 column density is given by,

$$N(\text{H}_2) \propto \frac{S_\nu}{\kappa_m(\nu)\theta^2 B_\nu(\text{T})}. \quad (3.4)$$

Here, the effective H_2 column density (Launhardt 1996) is calculated from,

$$N(\text{H}_2)[\text{cm}^{-2}] = \frac{6.2 \times 10^{16} S_\nu \lambda^3 e^{\frac{1.44 \times 10^4}{T_d \lambda}}}{\kappa_m(\lambda)\theta^2} \frac{Z_\odot}{Z} [\text{cm}^{-2}] \quad (3.5)$$

where S_ν is the flux density in Jy/beam due to dust, θ is the FWHM of the beam at wavelength, λ , and the other parameters are the same as in eq.(3.2). The degree of depletion we derive are a factor 2 or higher (≤ 15) than the canonical value (Frerking et al. 1982).

Is C^{18}O Optically Thin?

As mentioned in §3.2.1, the CO column density as determined from C^{18}O transitions might be underestimated, in case C^{18}O is optically thick. However, the rarer isotopomer C^{17}O is expected to be optically thin. The canonical value of relative abundance of C^{18}O with respect to C^{17}O $A(18, 17)$, is 3.65 (Wilson & Rood 1994). As discussed in Kramer et al. (1999), the measured ratios of the integrated intensities of the C^{18}O and C^{17}O lines can then be used to predict the C^{18}O optical depth. If $R^{18,17}$ denotes the ratio of the integrated intensities of the C^{18}O and C^{17}O lines, then

$$R^{18,17} = \frac{1 - \exp(-\tau_{18}^{18,17})}{1 - \exp(-\tau_{18}^{18,17}/A(18, 17))}. \quad (3.6)$$

The assumptions involved in deriving Eq.3.6, are that the both isotopomers have the same excitation temperatures and beam filling factors.

For G35.20, we find that $\tau_{18}^{18,17} = 1.35$, which implies that the correction factor for column density given by $\tau/(1 - \exp(-\tau)) = 1.8$, clearly smaller than the observed depletion. However, for G81.74+0.59, the ratio itself $R^{18,17} \sim 6$, suggesting that Eq.(3.6) is not valid anymore. This implies that C¹⁸O and C¹⁷O might have slightly different excitation conditions or extent of emission. Another fact, that excludes an artificial “depletion” due to high optical depths in C¹⁸O is the agreement in excitation temperature between CO and ammonia. A high C¹⁸O optical depth would lead to much smaller values for the rotational temperatures. Additionally, the observed relatively small peak temperatures for C¹⁸O exclude high optical depth in this line.

3.3.2 NH₃ Deuteration

How do we account for the high deuteration we observe in these prestellar cores? There are three main pathways to bring about deuteration (Rodgers & Charnley 2001, Millar 2002, Millar 2003, Roueff et al. 2005) ; a) gas-phase reactions, b) production of deuterium bearing molecules on grain surfaces, c) accretion of neutrals onto the dust grains that would otherwise destroy H₂D⁺. Processes b and c obviously invoke direct and indirect role of dust grains, respectively. Upto now all these processes have been used to explain fractionation in different sources.

In pre/protostellar cores, ion-molecule exchange reactions prevalent at low temperatures along with the depletion of CO from gas phase are preferred over grain chemistry (Shah & Wootten 2001, Caselli et al. 2003). This is because, molecules (deuterated and non-deuterated) remain frozen onto the grains until temperatures of ~ 90 K are reached when the ice mantles sublime and molecules return to the gas phase. Such high temperatures are seldom reached for pre/protostellar cores and hence cannot account for the observed deuteration.

The freeze-out of molecules from the gas onto the dust grains, particularly that of heavy molecules like CO in the cold initial phase has been predicted by chemical models (Brown & Millar 1989b, Roberts & Millar 2000a,b, Rodgers & Charnley 2001). The elements H and D are mainly in the form of H₂ and HD in molecular clouds. The primary reaction that dominates at low temperatures (< 20 K) out of the three main reactions that initiate fractionation is



This primary fractionation then can be transferred to other species producing secondary fractionation and finally molecules like NH₂D. Neutral molecules like CO can effectively destroy H₂D⁺, thereby lowering the deuterium enhancement. Therefore, the depletion of CO, the second most abundant molecule, from the gas phase can lead to an enhancement in the [H₂D⁺]/[H₃⁺] ratio and thereby the molecular D/H ratios.

Roberts & Millar (2000b) show that at 10 K, accretion of neutrals, especially CO, leads to the formation of doubly deuterated molecules such as NHD₂ and D₂CO. Based on these arguments, we expect to see a correlation between deuteration and CO depletion. In Fig.3.8, we compare the NH₃ fractionation and the degree of CO depletion (depletion factor). As seen from the correlation plot, there is a large scatter in the values and we do not see any obvious trend of high depletion following high deuteration. Nevertheless, the main result is that we find that very high deuterium fractionation and CO depletion go together.

Depletion could well occur on scales much smaller than the beam for sources at the distances typical for these sources (several kpc). In that case, due to the “beam dilution” the CO depletion we measure is an underestimate of the true depletion. The NH₂D emission, on the other hand, is probably dominated by the dense cores. This could explain why the CO depletion does not appear to track the deuteration in Fig.3.8. The error bars on the CO depletion factors are quite large, mainly due to the uncertainty in

the H_2 column density estimate from the $850\mu\text{m}$ dust continuum. The largest uncertainty is in the dust opacity at $850\mu\text{m}$ that has a spread over a factor 4 (Ossenkopf & Henning 1994, Krügel & Siebenmorgen 1994, Draine & Lee 1984). But we note, that with the choice of the Ossenkopf & Henning opacities, the derived column densities are already lower than for e.g. Savage & Mathis (1979) dust properties. Additionally the contribution of the line intensity to the measured flux may be significant, especially in active star forming regions.

The two study other than ours that directly compares CO depletion and deuterium fraction is by Bacmann et al. (2003) and Crapsi et al. (2005). Bacmann et al. use the D_2CO to H_2CO ratios in determining the deuteration. Their sample is much smaller (5 sources) compared to ours and hence the scatter in data points, also smaller. They claim to find a correlation between D_2CO to H_2CO ratios and depletion and argue that the presence of a significant amount of O (which is also an important H_3^+ destroyer) in the gas phase still undepleted might be responsible for the large scatter observed. Crapsi et al. observed N_2H^+ and N_2D^+ toward 31 low-mass starless cores and find a good correlation between deuterium fractionation and CO depletion.

If $f(\text{X})$ is the fractional abundance of species X relative to H_2 and $R(\text{XD})$ is the abundance ratio of XD relative to XH, then under the assumption of steady-state and equating formation and destruction in Eq.(3.7), one finds (Millar 2003)

$$R(\text{H}_2\text{D}^+) = S_{\text{H}_2\text{D}^+}(T)f(\text{HD}). \quad (3.8)$$

where $S_{\text{H}_2\text{D}^+}(T)$ is a function of the different rate coefficients. (forward, backward and dissociative recombination rates) given by

$$S_{\text{H}_2\text{D}^+}(T) = \frac{k_{1f}}{k_{1r} + \alpha_1 f(e) + \Sigma k_{\text{M}} f(\text{M})} f(\text{HD}). \quad (3.9)$$

Here, k_{1f} , k_{1r} are the forward and reverse rate coefficients such that $k_{1r} = k_{1f} \exp(-\Delta E_1/T)$ and $\alpha_1 \propto 1/\sqrt{T}$ is the dissociative recombination rate, $f(e)$ is the electron fraction and Σk_{M} is the rate coefficient of H_2D^+ with species M. ΔE_1 is the exothermal energy (~ 220 K), also given in Eq.(3.7).

At low temperatures ($T < 20$ K) observed in cold cores, the primary fractionation reactions are dominated by the forward reaction in Eq.(3.7). At higher temperatures, the reverse reaction becomes important in removing H_2D^+ very rapidly from the gas phase. Consequently, the decrease in primary fractionation produces a corresponding decrease in secondary fractionation reactions responsible for deuterium enhancements in molecules. Therefore, one expects to find an anti-correlation between temperature and deuterium fractionation. In Fig.3.9, we plot the NH_3 fractionation vs temperature for our sources and for pre/protostellar cores from the literature. The latest gas-phase predictions for $[\text{NH}_3]/[\text{NH}_2\text{D}]$ as a function of temperature (Roueff et al. 2005) are also plotted. This model assumes a density of $n(\text{H}_2) = 10^5 \text{ cm}^{-3}$, Carbon and Oxygen depletion factors of 5 and 15, respectively, while the Nitrogen abundance is kept constant. Our data points nicely fills in the missing observed data points between 10 – 20 K. However, the agreement with the model is moderate. This might imply that in Fig.3.9, we are seeing the effect of the turn on of a heating protostar on the D/H ratios. However, note that most of the low D/H ratios and the high temperatures are from the sources where we could not measure the optical depth in NH_2D . Therefore, these D/H ratios are really lower limits. However, we could be seeing rapid removal of the NH_2D once the core temperature gets too high. The exact temperature which we measure for a core of course depends on the combination of hot/cold gas in the beam, which can explain the scatter of 15 – 18 K; in some cases we are still seeing a lot of deuteration and in others it has already disappeared.

On average, the fractionation observed in sources in our sample are very high. However, note that some sources at temperatures above 15 K show an order of magnitude lower deuteration than the model predictions, while some others show extremely high deuterations, much higher than those found in low mass pre/protostellar cores.

There could be three main reasons for the very low fractionation estimated for a few sources. First, one of the main assumptions in deriving the $[\text{NH}_3]/[\text{NH}_2\text{D}]$ ratio is that the filling factors for both molecular transitions are the same. Any deviation from this assumption might result in a discrepant ratio. Second, these sources might be relatively more evolved. Should this be the case, the kinetic temperatures derived from the NH_3 (1,1) and (2,2) lines might only be a lower limit. Third, the sources could be chemically young, hence the timescale to reach the high deuteration in these sources is larger than their age. Tafalla & Santiago (2004) recently discussed such a chemically young low mass core.

The possible systematical errors influencing the calculation are that NH_2D might be tracing different regions than the NH_3 (see §3.3.4, though note that similar deuteration is seen at higher angular resolution with the interferometer), and that the temperature derived from NH_3 may not be the temperature of the NH_2D .

Upper Limits from NHD_2

A simple model for formation of multiply deuterated molecules on grain surfaces is considered by Brown & Millar (1989a) and predicts the abundances of deuterated species, with the goal to be able to differentiate between the relative importance of gas and grain chemistry. According to their predictions, the abundances of deuterated species (Rodgers & Charney 2001) scale as $[\text{NHD}_2]/[\text{NH}_3] = \frac{1}{3}([\text{NH}_2\text{D}]/[\text{NH}_3])^2$ for grain surface formation. Very deep observations of the NHD_2 $1_{10}-1_{01}$ line for two sources (G35.20 and G81.84), did not result in any detection at an rms noise level of 14 – 15 mK. Based on the 1σ upper limits, we then derive the $[\text{NHD}_2]/[\text{NH}_3]$ ratio and find that,

$$\begin{aligned} ([\text{ND}_2\text{H}]/[\text{NH}_3])_{\text{observed}} &= (0.004)_{\text{G35.20}}; (0.003)_{\text{G81.74}} \\ (\frac{1}{3}([\text{NH}_2\text{D}]/[\text{NH}_3])^2)_{\text{predicted}} &= (0.08)_{\text{G35.20}}; (0.03)_{\text{G81.74}}. \end{aligned}$$

The model prediction is based purely on probability arguments assuming that the fractionation is proportional to gas-phase atomic D/H ratio and that there are three different pathways for inserting the D atom into the chain of reactions that form multiply deuterated NH_3 . Even if one accounts for the simplicity of the model, the prediction is an order of magnitude higher than the derived upper limits in both cases. Moreover, there is the added difficulty of removing grain mantle material at temperatures of 15 – 20 K observed in these cores. Hence, there are clear indications that we may disregard active grain chemistry in explaining the high deuteration we observe. While a gas-phase model along with condensation of neutral species onto grain mantles adequately explains moderate deuteration observed towards some sources, the very high fractionation we derive remains unexplained.

3.3.3 Variations in HCN Isotopic Abundance

Let us define the abundance ratio, R_{iso} , as

$$R_{\text{iso}} = \frac{^{12}\text{C } ^{15}\text{N}}{^{13}\text{C } ^{14}\text{N}}. \quad (3.10)$$

R_{iso} is found to vary with the distance from the Galactic center (Wilson & Rood 1994, Wielen & Wilson 1997). The observed correlations are explained by Galactic chemical evolution. Other observational studies (Ikeda et al. 2002, Langer & Penzias 1993, Dahmen et al. 1995) find significant source-to-source variation of the isotopic ratios among a group of clouds located at nearly the same distance from the galactic centre.

The isotopic species of HCN, H^{13}CN and HC^{15}N with their $J = 1 - 0$ transition have been often observed toward various local molecular clouds (Dahmen et al. 1995, Hirota et al. 1998, Ikeda et al. 2002) to estimate the ratio R_{iso} . These transitions can be observed with the same receiver and hence the ratio derived will be independent of calibration errors. Moreover the optical depth can be measured from the three hyperfine components of the H^{13}CN line.

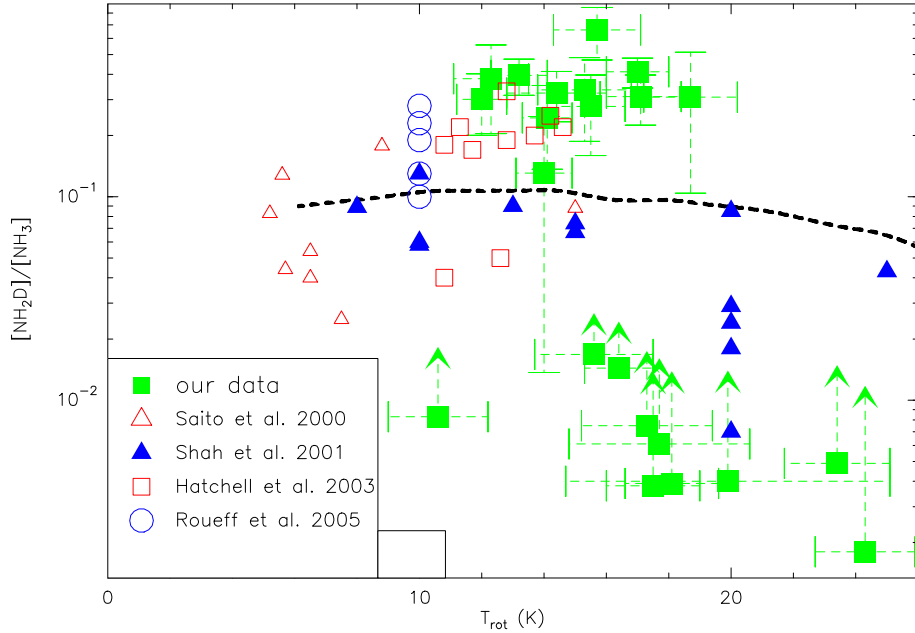


Figure 3.9: Plot of NH_3 fractionation versus gas temperature as derived from NH_3 . The dashed line is the latest gas phase model predictions (Roueff et al. 2005). The filled and unfilled squares mark the SCAMPS sources and Hatchell (2003) respectively, filled and unfilled triangle, the values found toward low mass pre/protostellar cores by Shah & Wootten (2001) and Saito et al. (2000) respectively and the circle marks Roueff et al. (2005) sources. Note that our sample has the highest deuteration for the observed gas temperatures.

In Fig.3.10, we plot the abundance ratio of H^{13}CN and HC^{15}N as a function of distance from the galactic centre. The ratio of the abundances does not seem to correlate with the distance. As mentioned in §3.2.1, H^{13}CN is optically thin in almost all cases and hence the observed ratios must indicate the double abundance ratio R_{iso} , since the column density estimates are free from bias due to photon trapping effects. However, the formal error bars are too large to be able to make any strong argument against a correlation of R_{iso} with galactocentric distance.

If we adopt the canonical values for the $^{12}\text{C}/^{13}\text{C}$ of 60 and $^{14}\text{N}/^{15}\text{N}$ of 270 (Lucas & Liszt 1998) toward the interstellar medium (ISM), then the implied H^{13}CN to HC^{15}N ratio abundance ratio would be $270/360 \sim 4.5$. From our data, we find that there is a very large scatter from this value ($>$ factor 10).

Our results are in agreement with the finding of Ikeda et al. (2002) that there is a non-uniform elemental isotope abundance ratio in molecular clouds. The deviation from the canonical value could be due to a complex chemistry or environment in these clouds. The SCAMPS are in the close vicinity of massive star forming regions and hence the energetic UV radiation could cause isotope-selective photo-destruction (Schilke et al. 1992). Chemical fractionation is also likely to play an important role in the observed high values. If at all chemical fractionation were to play a role, it must be attributed to an anomalous fractionation in the isotopes of either N or C. The effect of nitrogen fractionation in interstellar clouds could lead to at most a 30% fractionation of ^{15}N in HCN at low temperatures of 10 K. However, the chemical fractionation of ^{13}C into ^{13}CO could lead to a very high ^{12}C to ^{13}C ratio (Ikeda et al. 2002). Since our values are skewed to a higher ratio relative to the canonical value (mean ~ 7.6), this implies either low ^{15}N fractionation or ^{13}C fractionation in HCN. The latter case is more likely considering the high depletion factors we derive. Thus our finding is consistent with carbon bearing molecules readily accreting onto the grains at the low temperatures, observed in prestellar cores.

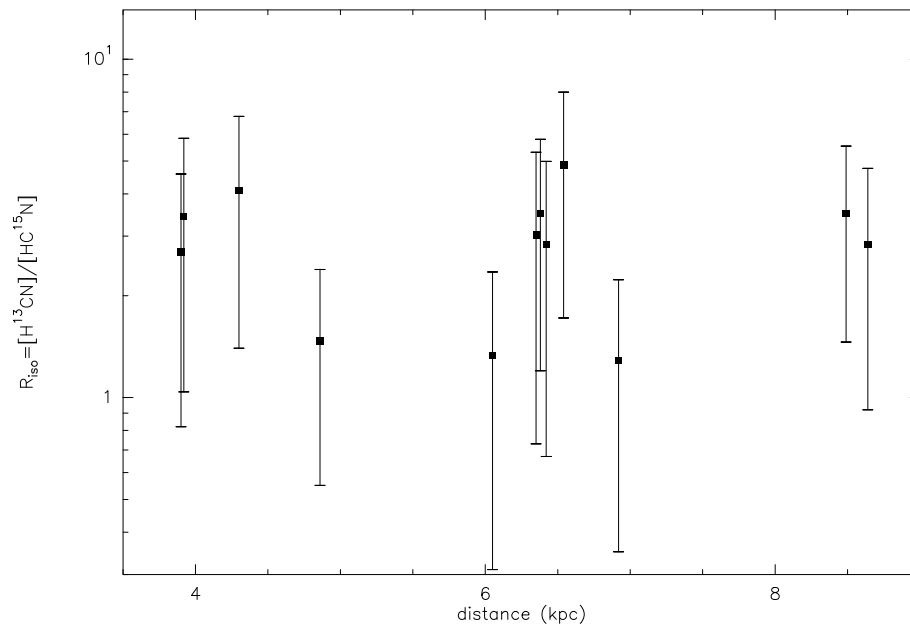


Figure 3.10: H^{13}CN and HC^{15}N abundance ratio as a function of the distance from the galactic centre for 12 sources in our sample of massive pre/protostellar cores detected with sufficiently high S/N. The ratio of the abundances does not seem to correlate with the distance.

3.3.4 Probing Deuteriation at High Angular Resolution

NH_3 , NH_2D and Dust Continuum Morphologies

The BIMA NH_2D observations with field of view (FOV) of several arcminutes were conducted towards two sources of the sample, the GMCs associated with the two well known massive star forming regions G29.96 and G35.20 (see Fig.3.7 and Fig.3.6). Deuterated ammonia is only found towards the SCAMPS; we term them G29.96e and G35.20w.

The gas and the dust continuum in G35.20w stretches across the field of view, streaming away from the ionised UCHII region. The dust and the gas distribution ends up as a clear tri-furcation in NH_2D (Fig.3.11). The spatial distribution of NH_2D is more complex than the the NH_3 (1,1) or the dust continuum strribution, but is clearly resolved in the PdBI image. The NH_3 (1,1) peaks strongly at the brightest dust continuum position (Fig.3.11) and appears to have a similar morphology as the 3 mm dust continuum emission. There is no correlation between the deuteriated ammonia and NH_3 (as well as dust continuum) suggesting that chemistry and kinematics of NH_2D clumps are significantly different. The range in NH_3 fractionation across the filament is comparable with the range of ratios derived from the single-dish data, with $\text{NH}_2\text{D}/\text{NH}_3$ ratios of less than 5% to 80%. The 1 mm emission (Fig.3.11) reveals very compact structures distinctly offset from NH_2D . The brightest mm continuum source (P1) has the lowest deuteration. This is not entirely unexpected since P1 is associated with an outflow as indicated by the presence of high velocity gas in HCO^+ (Fig.3.11). Therefore, the warm gas from the outflow or surrounding the embedded protostar destroys NH_2D . This is a clear indication that this source is more evolved.

In G29.96e, the dust filament seen with SCUBA is now resolved into a N-S filament with the PdBI at 3 mm (see Fig.3.12). At 1 mm (with highest resolution), the filament fragments into more than twice as many clumps as seen at 3 mm. BIMA NH_2D observations (see Fig.3.12) that cover the G29.96 complex reveal that only the G29.96e filament shows strong deuteration. The high resolution PdBI observations

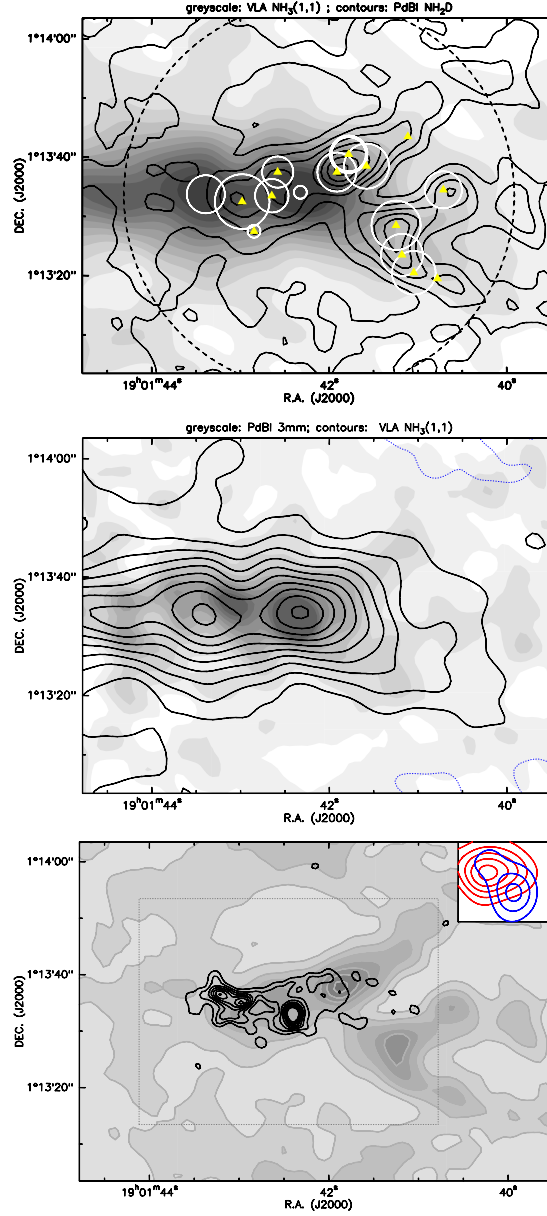


Figure 3.11: *top to bottom:* a) VLA NH₃ (1,1) integrated intensity plotted in grey-scales with NH₂D overlay in black contours for G35.20. The PdBI primary beam is shown as dashed black circle. The contour levels are -3σ , 1σ , 2σ , 3σ .. in steps of 1σ . The positions of the NH₂D clumps given in Table 3.10 are marked with filled triangles. Circles represent the degree of deuteration given in Table 3.2.2 for the different clumps. Note that the brightest NH₃ and NH₂D peak coincide. b) PdBI 3 mm continuum plotted in grey-scales with VLA NH₃ (1,1) overlay in black contours. The contour levels are -1σ , 3σ .. in steps of 3σ . c) PdBI 1 mm continuum plotted in grey-scales with NH₂D overlay in black contours. The contour levels are -3σ , 1σ , 2σ , 3σ .. in steps of 1σ . Inset: Blue(red) contours represent the blue(red) shifted emission between velocities (LSR) of $30.5 - 35.5 \text{ km s}^{-1}$ ($48.5 - 53.5 \text{ km s}^{-1}$) for the region within the grey square. The contours are $+2\sigma$... in steps of 2σ .

show that the bright dust continuum clumps in G29.96e have associated deuterated gas. Moreover, there are several deuterated clumps offset from dust continuum peaks. The brightest continuum source (P1) is driving an outflow. The high velocity gas is seen in the BIMA HCO⁺ observations (see Fig.3.12). However contrary to the results obtained for G35.20w, we observe very high deuteration toward P1 and that the gas and dust are coextensive. Nonetheless, the resolution at 7.4 kpc is not high enough to discard the possibility of several clumps offset from the dust continuum emission within 1 interferometer synthesised beam.

3.3.5 Mass

The gas mass has been derived from the 1 mm and 3 mm dust continuum emission for the different clumps identified at both wavelengths. Note that while any large scale information is lost in the 1 mm data, it provides us with the highest resolution to be able to zoom into the region.

In G35.20w, clumps of masses $\sim 20 - 200 M_{\odot}$ are identified in the 3 mm dust continuum within 0.1 pc while the 3 mm clumps in G29.96e have masses of $200 - 600 M_{\odot}$ within 0.3 pc (at 7.4 kpc). Therefore, the clumps in G29.96e might have further sub-structure unresolved by the PdBI beam. This is also confirmed by our 1 mm observations where twice as many clumps have been identified as at 3 mm. These have masses comparable to the 3 mm clumps in G35.20w.

The gas mass derived from PdBI observations (for both filaments) can be directly compared to the virial mass estimate based on NH₂D. The virial parameter (Bertoldi & McKee 1992) for a clump is defined as

$$\alpha = \frac{5\sigma^2 R}{GM} \quad (3.11)$$

where σ is the three dimensional root mean square (r.m.s) velocity dispersion and R is the radius of the clump, and M is the gas mass. Note that $\sigma = \sqrt{3/8 \ln 2} \cdot \text{FWHM}$. The virial mass is defined as $M_{\text{vir}} = 5\sigma^2 R/G$. For the clumps to be stable against collapse, α has to be 1. We arrive at an average value of 1 toward the individual clumps, thus these cores appear to be virialised. The core structure is consistent with the clumps being supported by turbulent pressure without any evidence of external bounding pressures.

In a few cases, we find two (or more) velocity components for a clump. Since the line widths are comparable, the virial mass estimated will be a factor of 2 higher.

3.3.6 Velocity Structure and Outflows : Kinematics

In G35.20w, NH₂D emission appears to largely trace quiescent material because the NH₂D lines are narrower ($< 1 \text{ km s}^{-1}$) than the NH₃ lines ($> 1 \text{ km s}^{-1}$) throughout the filament (see Table 3.2.2). The broadest lines in NH₂D occur near the position of the dust continuum source (P1) in G35.20. P1 is associated with an outflow as indicated by the presence of high velocity gas in HCO⁺ (Fig.3.11). Although the spatial resolution of the HCO⁺ map is much inferior to the resolution obtained with the PdBI, the outflow appears to be oriented along the northeast-southwest line. There is no evidence for such an outflow component in the NH₃ (1,1), (2,2) lines and neither in the NH₂D lines. Since our NH₃ (1,1) and (2,2) maps have been smoothed to a coarser resolution, the presence of weak NH₃ emission (if any) at high velocities in the outflow would be smoothed out. However, this does not apply to the NH₂D maps that have high spectral resolution. Our NH₂D maps obtained with PdBI has the high spatial and velocity resolution necessary for investigating the variation in velocity and linewidth as a function of radius. Here, the centre is the brightest source P1 that is driving an outflow. In Fig.3.13, we show the correlation between linewidth – LSR velocity and linewidth – radius for the clumps identified in the NH₂D and mm dust continuum maps. For NH₂D there is a clear indication that the linewidth decreases away from position P1. Similar correlation plots for the mm clumps appear to be scattered. There is a

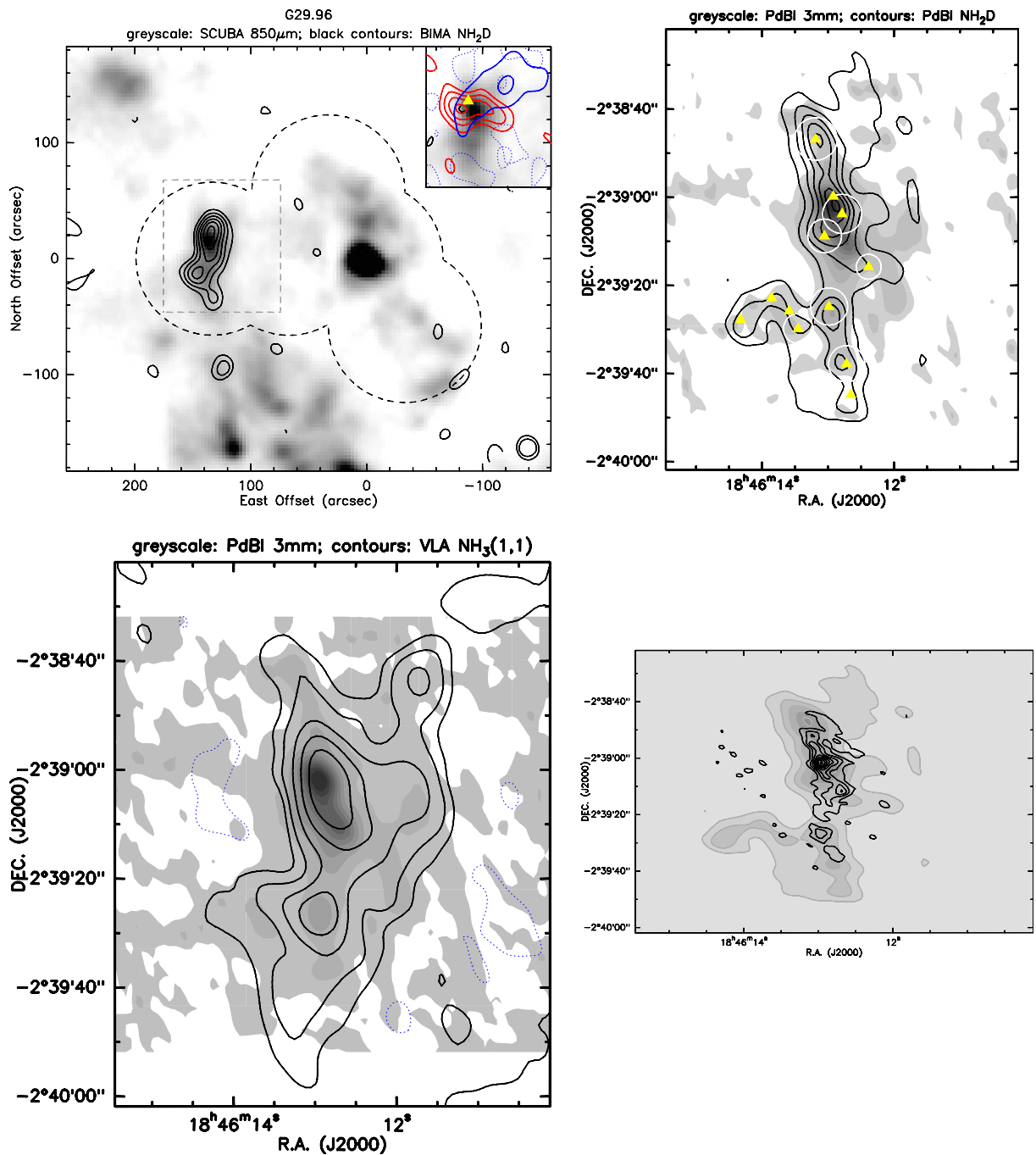


Figure 3.12: *Top left to bottom left clockwise:* a) SCUBA 850 μ m image of G29.96e plotted in grey-scales with BIMA NH₂D overlay in black contours. The contour levels are -3σ , 1σ , 2σ , 3σ .. in steps of 1σ . Inset: Blue(red) contours represent the blue(red) shifted emission between velocities (LSR) of $93.5 - 96.5 \text{ km s}^{-1}$ ($109 - 112 \text{ km s}^{-1}$). The contours are -3σ , 3σ in steps of 3σ . The triangle mark the position of methanol masers (Walsh et al. 1998) b) PdBI 3 mm continuum plotted in grey-scales with NH₂D overlay in black contours. The contour levels are -3σ , 1σ , 2σ , 3σ .. in steps of 1σ . The positions of the NH₂D clumps given in Table 3.10 are marked with filled triangles. Circles represent the degree of deuteration given in Table 3.2.2 for the differet clumps. Note that NH₂D emission is very clumpy and distinctly offset from the dust continuum. Moreover, NH₃ deuteration is lowest toward the brightest dust continuum peak c) PdBI 1 mm continuum plotted in grey-scales with NH₂D overlay in black contours. The contour levels are -3σ , 1σ , 2σ , 3σ .. in steps of 1σ d) PdBI 3 mm continuum plotted in grey-scales with VLA NH₃ (1,1) overlay in black contours. The contour levels are -3σ , 1σ , 3σ .. in steps of 3σ .

steady decline in linewidth with the LSR velocity for both mm and NH_2D clumps. Therefore, it appears that NH_2D is not yet associated with any star formation activity and the gas is pre-dominantly quiescent.

We find that the deuterated NH_3 traces quiescent gas also in G29.96e. However, the large distance to the cloud is a severe limitation in analysing the velocity structure. The HCO^+ outflow shown in Fig.3.12 is oriented approximately along the northwest-southeast direction. A Class II methanol (CH_3OH) maser (CIIMM) is found in the intimate vicinity of the molecular material close to the continuum source (Walsh et al. 1998).

Recent theoretical models on star-formation, particularly emphasising the role of turbulence (McKee & Tan 2003) are relevant here. In such a model, a high mass star forms from a massive coherent gas core that is in approximate pressure equilibrium with its surroundings. The total pressure is dominated by contributions from turbulent motions and magnetic fields. In our source, turbulence appears to be the byproduct of disturbed gas, here the outflow associated with P1. The clumps are approximate virialised structures (see §3.3.5) and the line width is highest toward P1 while steadily decreasing away from it. Therefore, our observations are consistent with this simple turbulent core model of high mass star formation.

In summary, there is strong indication that heat and outflow from P1, on chemical grounds tend to destroy NH_2D near the embedded protostar: a) The deuteration is lowest toward P1 in G35.20w b) deuterated species peaks distinctly offset from P1 (in G35.20w and G29.96e). P1 is the most evolved object in the filament. NH_2D clumps appears to be not coextensive with the NH_3 or dust. The fractionation ratios derived for the clumps are high ($> 10\%$). The origin of this high ratios can be explained by gas-phase reactions, grain chemistry or compression by an outflow shock. Since we observe that the small line widths occurred throughout the filament, we may rule out the third possibility. If the production of the deuterated species were from the dust grains, then one would expect coexistence of dust and gas, which we do not observe. Therefore, we suggest that gas-phase interactions plays significant role in the high deuteration observed in cold dark clouds.

3.3.7 Comparison with MIR Morphology

An important test for the evolutionary state of the cores detected in NH_2D is whether they are associated with MIR emission surveys or not. In Figs. 3.14 and 3.15 we show overlays of the NH_2D emission observed with the PdBI and the MIR 8 micron images from Glimpse and MSX. Towards G29E, the correlation between MIR absorption and NH_2D is very high, supporting the interpretation of the NH_2D cores as the cold raw material for the formation of massive stars. Even the arclike extension in the southeast, which had no counterpart in the 3 mm continuum or ammonia emission, is clearly traced in MIR absorption. The contrast in the MIR absorption is not as high as in NH_2D which shows that we trace in NH_2D a much larger range in column density than in the MIR absorption. The central massive YSO, which we detected by its associated outflow, is also not detected as a MIR point source, making this MIR-quiet object one of the youngest massive YSOs known. Unfortunately, no GLIMPSE data are available for G35W, which is at a galactic latitude below the range covered by GLIMPSE. A comparison with the low resolution MSX image in Fig. 3.15 demonstrates that there is also no MIR associated with NH_2D in G35W and shows that the NH_2D streamers originate right at the edge of the strong MIR of the W48 HII region.

3.4 Conclusion

In this paper we report the study of physical and chemical properties of a new sample of high-mass cold cores in deuterated ammonia. Our observations suggest large deuterium enhancement (upto 66%), largest reported so far. With our interferometer observations, we show that the spatial distribution of deuterated ammonia does not coincide with its non-deuterated species as well as thermal dust continuum. This confirms the previous findings in low mass protostellar cores, that protostellar activity destroys

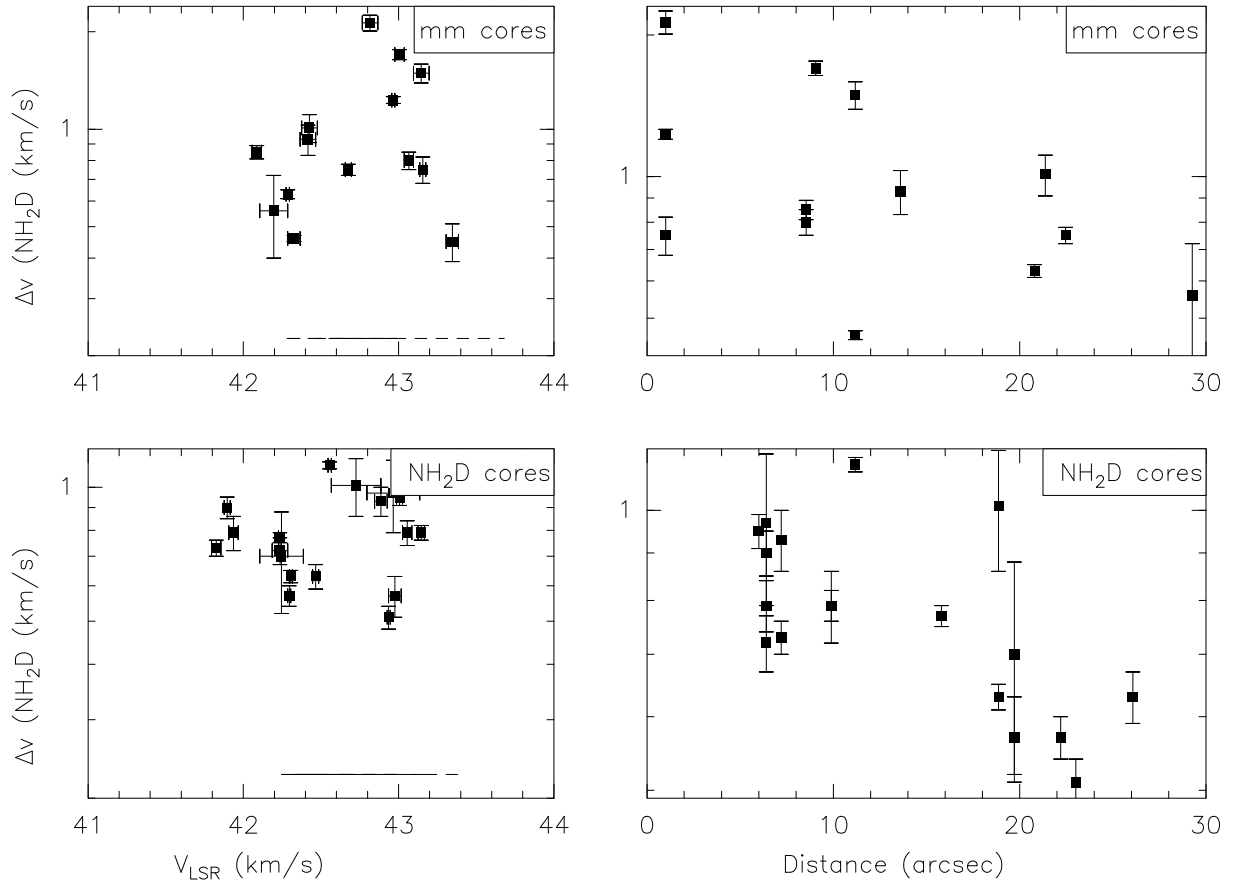


Figure 3.13: *Top left to bottom left clockwise:* a) NH₂D linewidth vs the LSR velocity for the mm clumps in G35.20 b) NH₂D linewidth vs the distance from the brightest mm continuum source for the mm clumps in G35.20 c) NH₂D linewidth vs the distance from the brightest mm continuum source for the NH₂D clumps in G35.20 d) NH₂D linewidth vs the LSR velocity for the NH₂D clumps in G35.20. There is a clear indication that the linewidth decreases away from position P1 for the NH₂D cores. Similar correlation plots for the mm clumps appear to be scattered. Note also the steady decline in linewidth with the LSR velocity for both mm and NH₂D clumps.

Table 3.12: Cores Identified from the 1 mm and 3 mm Continuum Emission

Offsets (arcsecs)	radius (arcsec)	M_{dust} M_{\odot}	M_{vir} M_{\odot}	alpha
G29.96 1 mm				
(2 ,10)	4	158	100	0.6
(-1,0)	4	62	62	1.0
(5 ,17)	3	47	33	0.7
(0 ,11)	3	49	81	1.7
(2 ,-15)	4	61	48	0.8
(1 ,-1)	5	74	71	1.0
(0 ,18)	5	44	64	1.5
G29.96 3 mm				
(2 , 10)	8	632	118	0.2
(-2, 1)	5	251	64	0.3
(2 ,-15)	9	165	53	0.3
G35.20 1 mm				
(5, 0)	3	25	44	1.8
(13, 1)	4	26	111	4.3
(17, 4)	2	6	16	2.7
G35.20 3 mm				
(4 , -1)	6	180	135	0.7
(15, 2)	7	148	199	1.3
(55, -4)	9	111	–	–
(33, -4)	9	86	27	0.3
(25, 4)	7	74	68	0.9
(49, -13)	13	131	–	–
(-4, 3)	10	130	246	1.9
(43, -30)	10	59	–	–
(42, 1)	4	20	–	–
(-13,-12)	6	29	23	0.8
(-15, 12)	7	35	37	1.1
(-35, -5)	5	17	10	0.6

Notes: Columns are the Offset position relative to the map centre in arcsecs, size of the cores in arcsecs, gas mass estimated from 1 mm or 3 mm data, virial masses from NH_2D and the alpha parameter defined as in Eq.3.11.

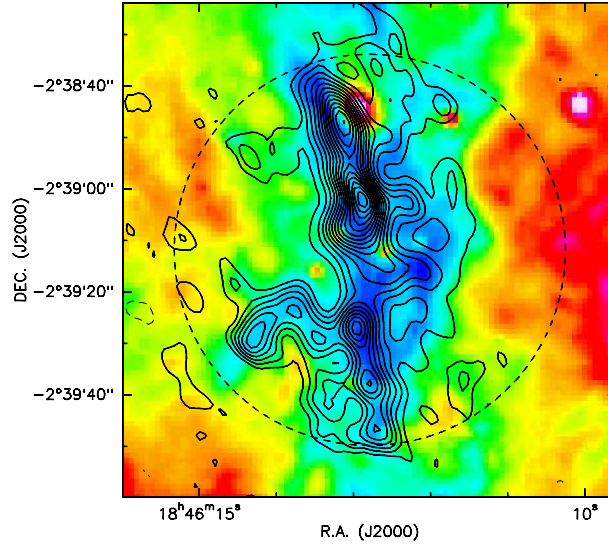


Figure 3.14: Overlay of Spitzer 8 micron in colorscale and NH_2D contours from the PdBI observations towards G29E. The primary beam of PdBI is shown as dashed circle. Note the correlation between MIR absorption and NH_2D emission.

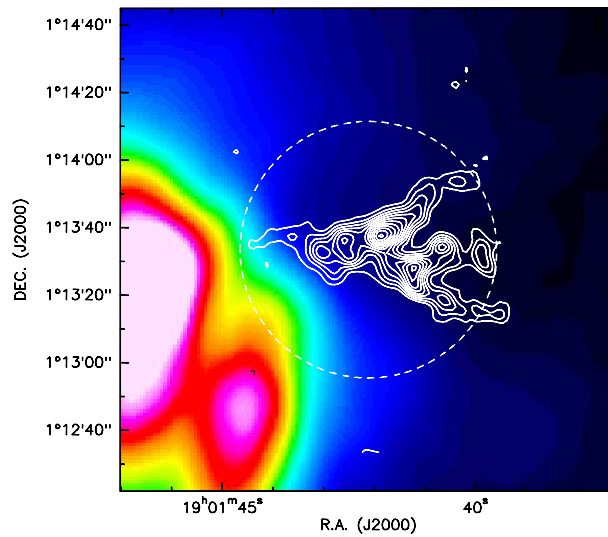


Figure 3.15: Overlay of MSX 8 micron in colorscale and NH_2D contours from the PdBI observations towards G35W. The primary beam of PdBI is shown as dashed circle. Note the correlation between MIR absorption and NH_2D emission.

deuterium bearing molecules. The deuterated gas is also quiescent compared to NH_3 . These observations also imply that we observe the colder, less condensed prestellar gas, the raw material for a massive cluster in formation. The velocity structure of NH_2D clearly indicates decay of turbulence away from the embedded protostar, in agreement with the turbulent core theory of high-mass stars. We have shown that ammonia fractionation together with the distribution of deuterated species in comparison with dust condensation can be used as indicators of the very earliest (pre-protostellar stages) of high-mass starless cores. Our observations provide strong evidence that these cores form a continuum from cores with all the expected characteristics for precluster cores which are gravitationally bound, cold, depleted and deuterated to very early stage clusters which are slightly warmer and drive outflows.

Chapter 4

Structure of High-Mass IR-Dark Clouds: Breakdown of Self-Similarity and Low-Density Envelopes

This chapter is based on a paper to be submitted to Astronomy & Astrophysics.

We present results of an analysis of mid-infrared observations of Infrared dark clouds (IRDCs). Archival data was obtained from the Spitzer GLIMPSE survey. This data has been used to produce extinction maps toward five IRDCs. Based on the extinction maps, we show that IRDCs are not just isolated dense condensations. IRDCs are enveloped in lower density material and the masses we derive confirm the previous findings that IR dark clouds have high mass. MIR absorption appears to be an excellent tracer of the dust content. Furthermore, comparison of extinction cuts through IRDCs indicate that high mass IRDCs might have high density contrast between the core and the envelope. This implies that initial stages of high mass dark clouds could be governed by highly compressive energetics, very likely shocks due to a SN explosion or stellar winds from nearby high mass stars. We use a simple method of analysing the fractal nature of the cloud indirectly by studying the extinction count distribution. This method has been previously applied to molecular clouds. We show that it is equally robust in the case of the dust clouds seen in extinction. Subsequently, from the extinction probability density function (PDF), we infer that self-similarity in IRDCs break down at scales of 0.2 – 0.5 pc. This scale regime is very much consistent with the turbulent Jeans length and therefore, IRDCs might be exhibiting a transition from turbulent fractals to thermal coherent cores at the sub-parsec scales.

4.1 Introduction

Advances in the field of star formation studies in the past decades have promoted a better understanding of the structure and the stability of molecular clouds. Observations supported by theoretical calculations suggest that the formation of a star is the result of a complex chain of processes. We now know that these processes are regulated by an intricate interaction between magnetic fields, turbulence, thermal pressure and gravity. Observations suggest that most molecular clouds are in virial equilibrium. In such clouds, the combined (but not equal) forces of magnetic field, turbulence and thermal pressure prevent any instability against its own gravity. We, however, do not understand well the collapse of molecular clouds and the subsequent evolution into stars.

Several techniques, from molecular spectroscopy, thermal dust continuum to stellar reddening methods have been used to study the structure of molecular clouds. (for a review see Williams 1999). All

the different analyses have one result in common, that there is a power law relationship between the measurable quantities. For example the relationship between the size and the line-width in a molecular cloud or the mass spectrum of the clumps identified in dust continuum methods can be expressed in terms of power laws. This has the immediate implication that the structures seen in molecular clouds are scale free i.e. the basic form of a cloud would be similar at all scales until one approaches the resolution limit. The structures are often referred to as “fractals”. Fractals usually possess “self similarity” across different scales. That is, as one zooms in or out the geometry/image has a similar appearance. Fractals are widely observed in nature, as Earth’s atmospheric clouds to rocks, ferns and coastlines.

Small-scale random fluctuations, more commonly known as *turbulence* between the sub-structures in a cloud can readily explain these observed fractal structures. This implies that on scales at which these fluctuations dissipate, one might see a breakdown in the self similarity of molecular clouds.

However there are several caveats to the commonly used methods (see Williams 1999); a) resolution limited data can mimic a fractal structure; b) in a cloud with a high-filling factor, projections effects due to the blending of structures in three dimensions can create confusion; c) the inherent noise in the data can imitate self-similar structures.

Blitz & Williams (1997) (hereafter BW97) have demonstrated a simple and indirect way to differentiate between fractal and clumpy clouds overcoming the above mentioned caveats. In this paper, we show that this method can be applied to IRDCs. We have also selected a low mass dark cloud L1709A belonging to the ρ Ophiuchi molecular complex to clarify whether moderate extinction in the IR can also project a dark cloud against a bright background and does not mandate a high mass.

Based on the Spitzer MIR observations of IRDCs, we have produced and analysed extinction maps toward five high mass IRDCs which probe densities on all scales. Kinematic distances derived for these dark clouds show that they are located at large distances (several kpc). The MIR observations from Spitzer with high dynamic range, large field of view and high spatial resolution are thus ideal for studying these clouds. In §4.2, we briefly describe the archival data obtained from the Spitzer Legacy Survey GLIMPSE. §4.4 discusses the modelling of the MIR extinction and the method used to verify whether the clouds are fractal. The validity of the underlying assumptions and the expected uncertainties are also summarised. In §4.5, based on our optical depth probability density function (PDFs) we show that IRDCs exhibit a departure from self-similarity. We also show that the high density regions are immersed in regions of diffuse material. Finally, potential implications of these findings on the formation mechanism of IRDCs are discussed in §4.5.

4.2 Archival Data from the Spitzer GLIMPSE Survey

The archival MIR data is part of the Galactic Legacy Infrared Mid-Plane Survey Extraordinaire (GLIMPSE) project of the Spitzer Space Telescope. The survey had imaged the galactic disk between longitudes, $|\ell|$, of 10 and 65 degrees and latitudes $|b| < 1$ degree in four of the infrared bands ($3.6 - 8\mu\text{m}$) of the Infrared Array Camera (IRAC) on the Spitzer Space Telescope. Not surprisingly, the IRDCs were clearly identified in stark contrast against the MIR emission. We analysed the data obtained in the $8\mu\text{m}$ band with an angular resolution of $1.9''$ toward six sources. The rms noise level in the images is typically 5 MJy/sr.

4.3 Source Selection

The sources selected have been well studied in molecular tracers and mm dust continuum. (Carey et al. 2000, Pillai et al. 2006b, Pillai et al. 2006a). There is an excellent correlation between MIR extinction, mm dust continuum emission and molecular emission. For these sources, a) the absorption features are due to cold condensations effectively absorbing the bright MIR background emission and are not random fluctuations in background or foreground material b) the kinematical distances from molecular studies

can be used to determine the angular scales probed and c) Pillai et al. (2006a) find that the cores are stable against gravitational collapse.

The field selection was done in a way so as to include both the darkest patches of the cloud and a significant fraction of material enveloping the IRDC. Since these are not targeted observations, we give the centre coordinates of our fields in Table 4.1.

4.4 Extinction: Map and PDF

The MIR extinction is a very sensitive tracer of column density of molecular material at both high and low extinctions.

Bacmann et al. (2000) have successfully used the MIR extinction to characterise the density structure of pre-stellar low mass cold cores. The observed absorption in MIR can be modelled as the combination of the foreground intensity and the dust extinguished background intensity (Bacmann et al. 2000). The line of sight absorption is

$$I_{\text{los}} = [\langle I_{\text{bg}} \rangle - \langle I_{\text{off}} \rangle] \cdot e^{-\tau_\lambda} + [\langle I_{\text{off}} \rangle]. \quad (4.1)$$

Here, $\langle I_{\text{bg}} \rangle$ is the mean observed background intensity, $\langle I_{\text{off}} \rangle$ is the mean foreground intensity shifted by the instrumental offset of the IRAC band used, τ_λ is the dust opacity at the observed wavelength λ . As an approximation, we do not consider the spatial fluctuations from the mean value of foreground and background intensities. $\langle I_{\text{bg}} \rangle$ and I_{off} estimated for each source is tabulated in Table 4.1.

The optical depth, τ_λ , is proportional to the dust opacity, σ_λ . Recently, Indebetouw et al. (2005) found that in the IRAC wavelength regime there is a source of extinction in excess of the power-law wavelength dependence exhibited by a grain model tuned to UV-optical extinction observed in the diffuse ISM. We adopt σ_λ values at $7.75\mu\text{m}$ from (Draine 2003). These are updated values¹ from Weingartner & Draine (2001) corresponding to an extinction curve with $R_V = 5.5$ (designated as ‘‘Case B’’) for the dense ISM.

Subsequently we construct a normalised histogram of the number of pixels, N_{A_V} , at each extinction (A_V). The probability density function (PDF) therefore is a normalised histogram with the A_V normalised to the maximum extinction A_V^{max} plotted against the fraction of pixels at that particular A_V .

Uncertainties

Foreground intensity must be less than the minimum intensity in the image (corresponding to maximum optical depth). This therefore puts strict upper limit on I_{off} while the background intensity is assumed to be uniform. We approximate the mean observed background intensity as the mean MIR intensity in the region. As given in Eq.4.1, $\langle I_{\text{bg}} \rangle$ is deduced by subtracting the contamination by both foreground emission and the instrumental offset.

In order to study the influence of incorrect determination of $\langle I_{\text{bg}} \rangle$ and I_{off} on the extinction and the extinction PDF, we varied $\langle I_{\text{bg}} \rangle$ and I_{off} . An illustration is shown in Fig.4.1.

Decreasing I_{off} can severely underestimate the extinction. This manifests as an increase in power of the extinction PDF. On the contrary an increase in $\langle I_{\text{bg}} \rangle$ can shift the offset of distribution to higher values and hence overestimate the highest extinction. However, its influence is not as drastic as an incorrect choice of I_{off} because of the weak statistics corresponding to the densest pixels. Thus, the overall slope of the PDF remains unchanged.

¹<http://www.astro.princeton.edu/~draine/dust/dustmix.html>.

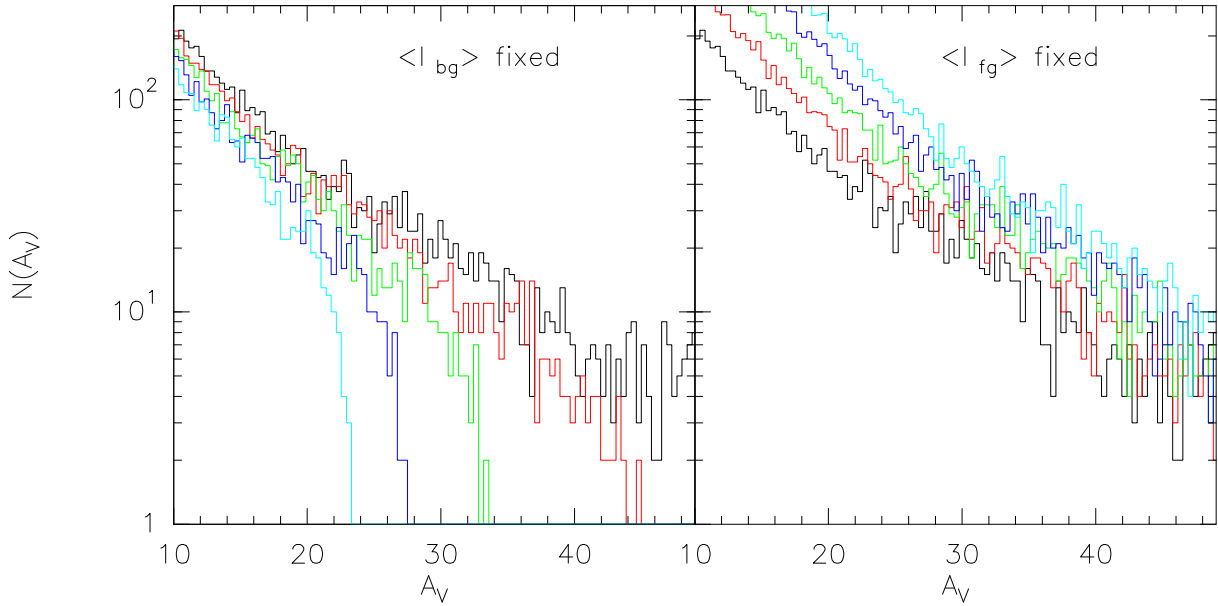


Figure 4.1: *Left panel:* A sample extinction PDF for different values of foreground intensity with fixed background intensity. *Right panel:* background intensity with fixed foreground intensity. The black line in both panels correspond to the same values of $\langle I_{bg} \rangle$ and I_{off} .

4.5 Results and Discussion

4.5.1 Extinction Maps

The extinction map toward the selected IRDCs (see Table 4.1) is shown in Figures 2 to 7. The morphology of IRDCs on these large scales are mostly filamentary. Visual extinctions upto ~ 180 mag are probed by these observations. We compared our extinction measurements toward the peaks with that of Carey et al. (2000) toward the corresponding submm peaks and for L1709A with Bacmann et al. (2000) toward the extinction peak (their Table 2 and Table 3 respectively). Given the large scatter in the dust opacities adopted by the different authors, our values are in good agreement within a factor 2 with the values reported toward the sources mentioned above (see Table 4.2). The values given in Table 4.2 for L1709A are for the same dust extinction cross section adopted by Bacmann et al. (2000) at $7.75\mu\text{m}$ while for other IRDCs, N_{H_2} has been compared to Carey et al. (2000) for a dust emissivity index $\beta = 1.75$.

The extinction maps reveal several compact clumps with high extinction (> 50 mag in the visual wavelength). These values are much higher than those obtained toward local low mass pre-stellar cores. In fact, the only low mass pre-stellar core in our present sample has the lowest extinction (< 50 mag A_V). The total mass derived for the entire cloud ranges from 500 for the low mass pre-stellar core to $\approx 1 \cdot 10^5 M_\odot$ (see Table 4.1). The dust mass is estimated from extinction and is given by,

$$M \propto (\theta d)^2 A_V. \quad (4.2)$$

Following Cambr esy (1999), we derive the dust mass using the expression given below.

$$\frac{M}{M_\odot} = \left(\frac{\theta}{''} \frac{d}{\text{pc}}\right)^2 \frac{X}{\text{cm}^{-2}\text{mag}^{-1}} \left(\frac{\mu}{g}\right) \sum_i \left(\frac{A_V(i)}{\text{mag}''^m}\right). \quad (4.3)$$

Here, θ is the size of the pixel, d is the distance to the source, X is the conversion factor from H

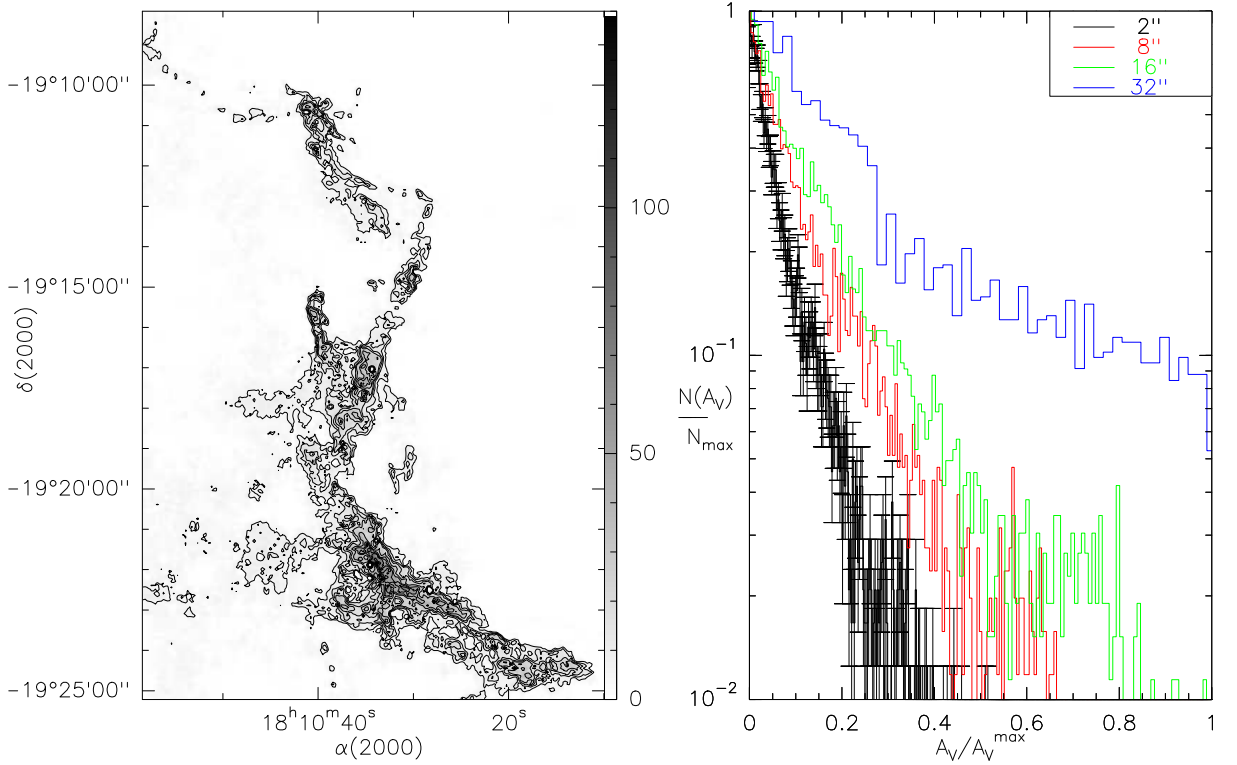


Figure 4.2: *Left panel:* Extinction map of G11.11-0.12. The contour levels are 5, 10,15, 20,30, 40, 50, 60 upto 150 A_V in steps of 20. *Right panel:* Normalised extinction histogram for different resolution indicated in the upper right corner. The Poisson error bars are also shown for the histogram with 1.9'' resolution.

column density to visual extinction and μ is the mean molecular weight. We have adopted X of $1.87 \cdot 10^{21} \text{ cm}^{-2} \text{ mag}^{-1}$ (Savage & Mathis 1979). The masses have been derived over regions with $A_V \geq 10$.

Low Density Envelopes in IRDCs

Based on observations of the formaldehyde molecule H_2CO , Carey et al. (1998) argue that IRDCs are dense ($n > 10^5 \text{ cm}^{-3}$), cold ($T < 20 \text{ K}$) cores, apparently without surrounding envelopes.

As shown in figures 4.2 to 4.7, IRDCs clearly have diffuse envelopes. The mean extinction of such a diffuse envelope is typically greater than 10 magnitudes. Therefore, the highly dense cloud appears to be shielded against the interstellar radiation field by a larger diffuse parent molecular cloud.

Core – Envelope Phase in IRDCs

In this section, we investigate the differences in the core to the envelope phase in IRDCs. In order to study the transition from diffuse clouds to dense cores, we analysed a radial strip through the cloud passing through the cores. In Fig.4.9 and Fig.4.10, we compare such an extinction cut for two high mass IRDCs and low mass IRDCs respectively. L1689B and L1709A are two low mass IRDCs belonging to the ρ Ophiuci cloud complex (Bacmann et al. 2000). The striking difference between Fig.4.9 and Fig.4.10 is the large extinction contrast seen in the high mass IRDCs G19.30+0.07 and G28.34+0.06 in contrast to the relatively smooth gradient from lowest to the highest extinction in the low mass IRDCs. The serrations in the extinction gradient in the high mass IRDCs are indications of the sudden density

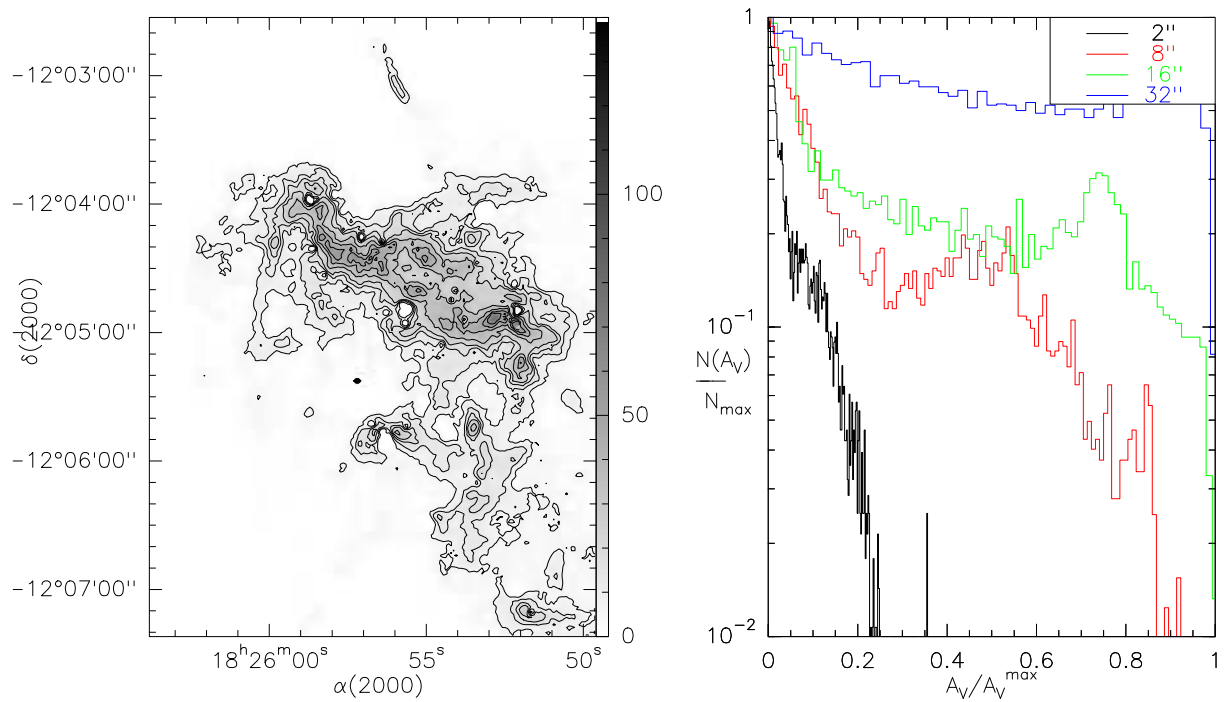


Figure 4.3: *Left panel:* Extinction map of G19.30+0.07. The contour levels are 5, 10,15, 20,30, 40, 50, 60 upto 150 A_V in steps of 20. *Right panel:* Normalised extinction histogram for different resolution indicated in the upper right corner.

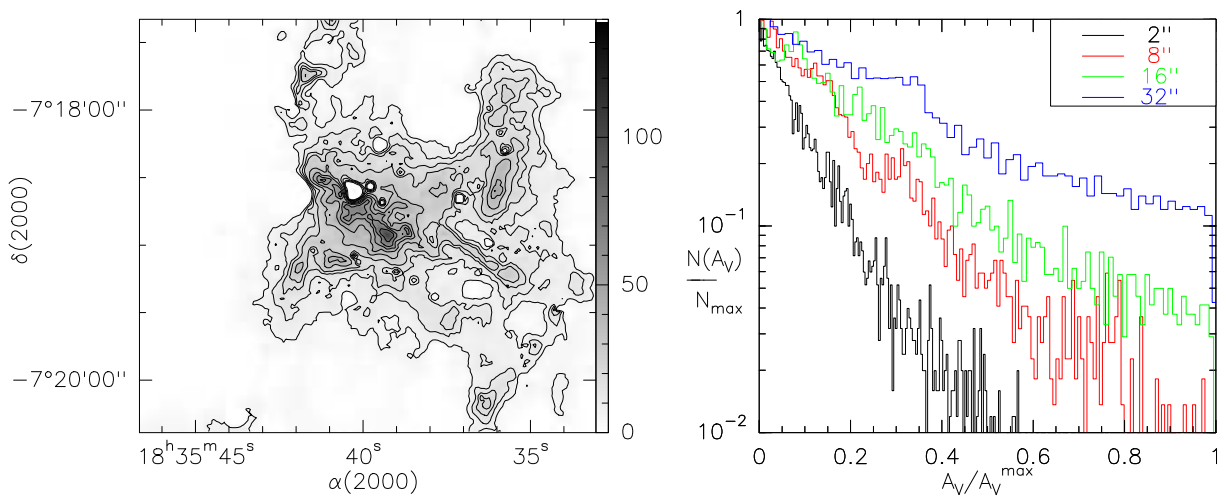


Figure 4.4: *Left panel:* Extinction map of G24.63+0.15. The contour levels are 5, 10,15, 20,30, 40, 50, 60 upto 150 A_V in steps of 20. *Right panel:* Normalised extinction histogram for different resolution indicated in the upper right corner.

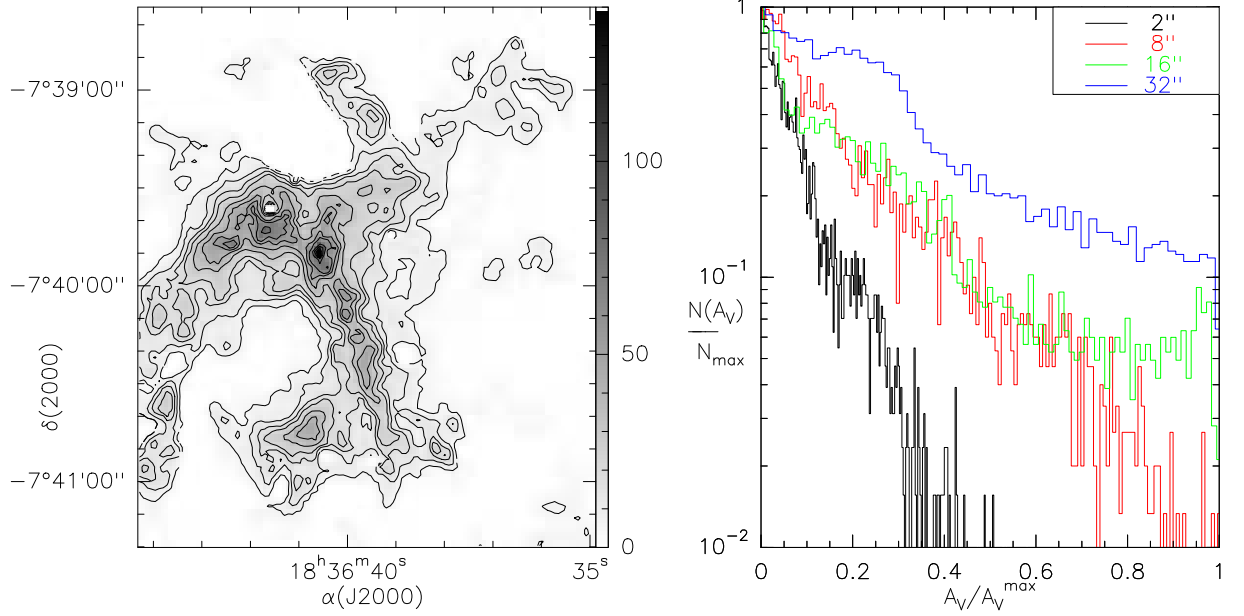


Figure 4.5: *Left panel:* Extinction map of G24.72-0.75. The contour levels are 5, 10,15, 20,30, 40, 50, 60 upto $150 A_V$ in steps of 20. *Right panel:* Normalised extinction histogram for different resolution indicated in the upper right corner.

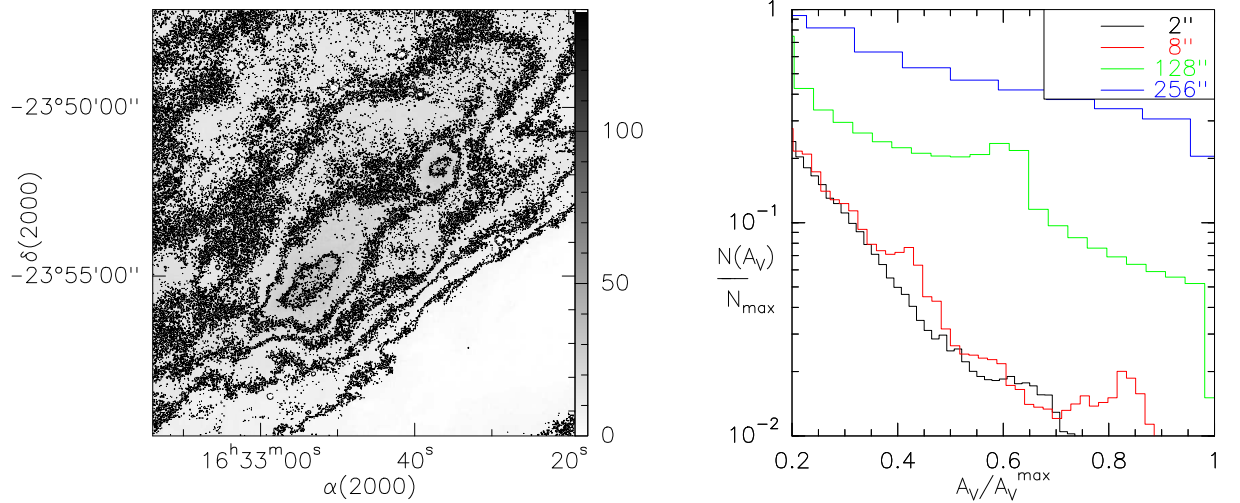


Figure 4.6: *Left panel:* Extinction map of the low mass pre-stellar core L1709A (see Bacmann et al. 2000). The contour levels are 5, 10,15, 20,30, 40, 50, 60 upto $150 A_V$ in steps of 20. *Right panel:* Normalised extinction histogram for different resolution indicated in the upper right corner.

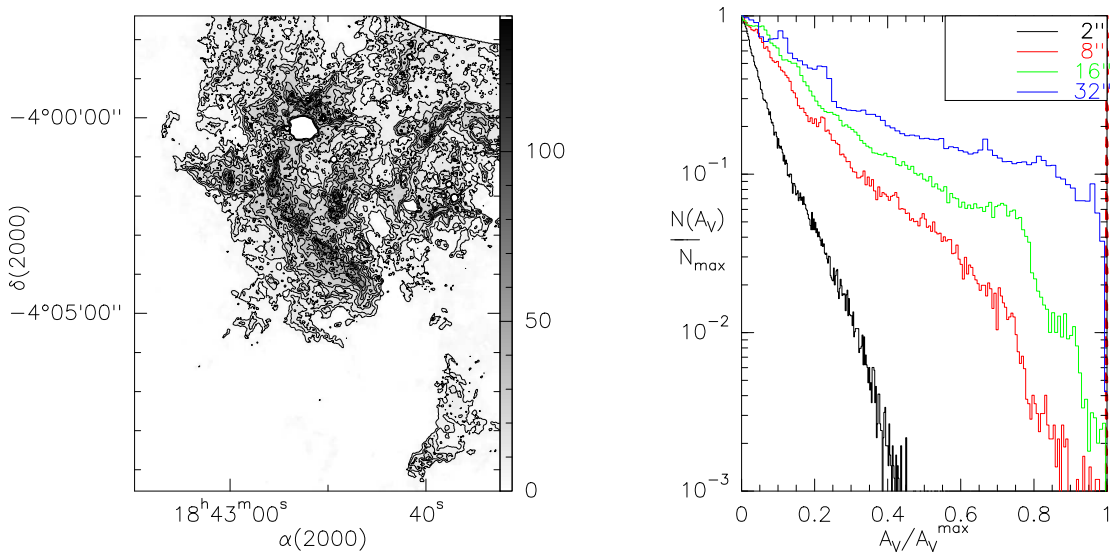


Figure 4.7: *Left panel:* Extinction map of G28.34+0.06. The contour levels are 5, 10,15, 20,30, 40, 50, 60 upto $150 A_V$ in steps of 20. *Right panel:* Normalised extinction histogram for different resolution indicated in the upper right corner.

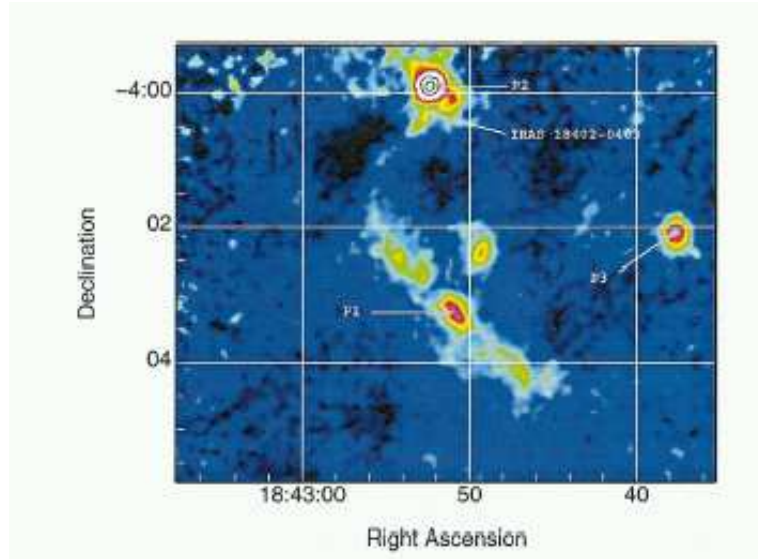


Figure 4.8: SCUBA 850 μ m scan map (Carey et al. 2000) of the same region G28.34+0.06 shown in Fig.4.7. Note that the brightest clump seen in extinction along the elongated ridge toward north in Fig.4.7 is hardly detected in the SCUBA map.

contrasts within them. This in turn implies that the turbulence within the high mass IRDCs is highly compressive. The injection of such highly compressive turbulence into the medium is very likely through sudden shock waves due to Supernovae explosions or stellar winds. For example, in G28.34+0.06, the density contrast is not very pronounced on one side of the cloud while there is a sharp drop toward the alternate edge. Such an asymmetry cannot be caused due to processes involving a balanced pressure drive. In contrast, a shock driving into the cloud from one direction can initiate such a sharp asymmetry. Reckon that the situation is markedly different for low mass IRDCs. A not far-fetched implication is that the energetics of the surrounding environment have a highly non-trivial role in accumulating the large masses into IRDCs and subsequently high-mass stars in IRDCs. However, we need to perform more rigorous and sophisticated analysis to draw firm conclusions on the nature of the initial conditions of formation of high-mass IRDCs.

4.5.2 Thermal Dust Continuum Emission and Absorption

In Fig.4.7 and Fig.4.8, we compare the extinction map and the SCUBA dust continuum emission map of Carey et al. (2000) toward IRDC G28.34+0.06. One can readily deduce two main points. First, the dust continuum traces only the dense cloud while the extinction is sensitive to material at low to the highest extinction. Second, there is a significant dearth of emission at 850 μ m along the ridge of the filament. However, the very same ridge harbours the brightest clump (referred to as IRAC P1) in the whole cloud in the extinction map. These discrepancies in the two data set can be inferred as an “instrumental limitation” of the SCUBA map.

Consider the thermal dust emission S_ν at a given frequency ν_1 ,

$$S_{\nu 1} \propto B_{\nu 1}(T) \cdot (1 - e^{-\tau_{\nu 1}}). \quad (4.4)$$

While, the MIR absorption $S_{\nu 2}$ is given by

$$S_{\nu 2} \propto S_{\text{bg}}(T) \cdot e^{-\tau_{\nu 2}} + S_{\text{fg}} \quad (4.5)$$

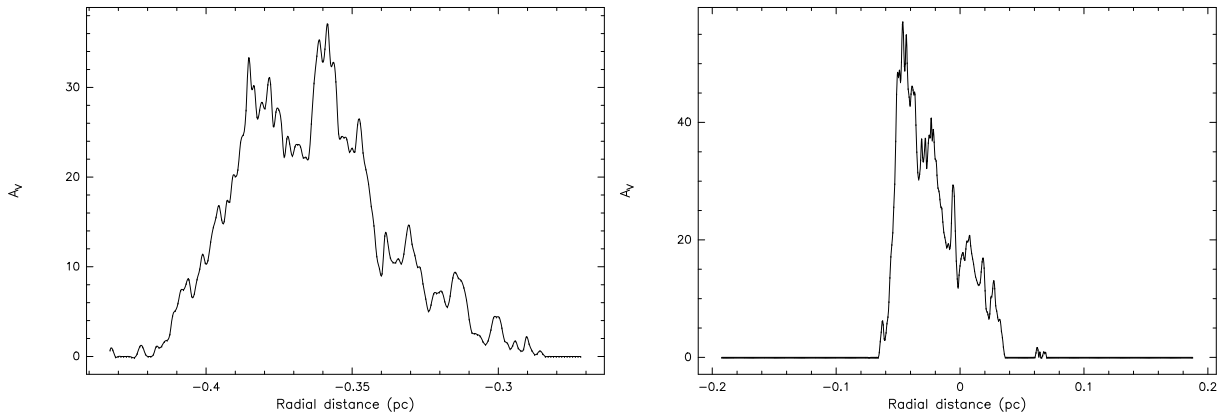


Figure 4.9: *Left panel:* North-East to South-West extinction cut through the cloud in G19.30+0.07. *Right panel:* East-West extinction cut through the cloud in G28.34+0.06. Note the striking contrast in profile along the cut, especially in G28.34+0.06.

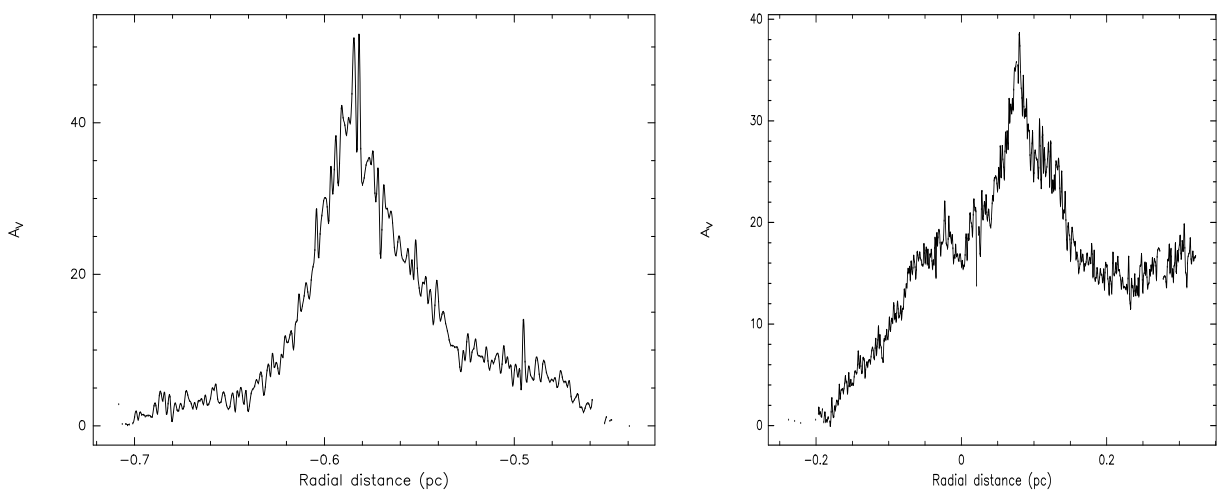


Figure 4.10: *Left panel:* East-West extinction cut through the cloud in L1689B. *Right panel:* East-West extinction cut through the cloud in L1709A. Note that contrary to the high mass clouds, the extinction profile for these two low mass star forming clouds are smooth.

Here, $B_{\nu_1}(T)$ is the Planck function and τ_{ν_1} is the submm opacity. Reckon that at submm wavelengths for moderate temperatures, the Rayleigh Jeans approximation is not valid anymore and therefore becomes sensitive to temperature.

From, Eq.4.4, we find that at very low optical depths, submm emission scales linearly with the optical depth. This means that the current bolometer arrays have insufficient sensitivity to detect the weak source signal with sufficient signal to noise. Moreover, the mapping modes of a bolometer array produces artefacts if the source structure is larger than the chop throw (Kauffman et al. in prep). These observations are therefore sensitive to the dense and not the diffuse cloud. This makes MIR absorption a superior tracer of both the cold dense regions in the clouds as well as the diffuse material surrounding it.

4.5.3 Do We See Non-self Similar Structures?

Finally, we would like to know whether IRDCs are self similar at all scales. If found to be self similar, then IRDCs must be fractals. As detailed in §4.4, we analyse the extinction PDFs of IRDCs to study their self similar nature. Why is the PDF of extinction a useful statistic? The amount of absorption in a molecular cloud along the line of sight is proportional to the column density. Hence the density structure is reflected in the radial extinction profile. Such density profiles would reveal structures on all scales upto the scales at which the coherent nature of the cores with a flat spectrum is revealed. It is not straightforward to calculate the average radial profiles for the complex morphology observed toward dark clouds. However, comparison of the extinction PDF at several resolutions is sufficient to disclose the fractal nature of the cloud. Consider the densest region of a cloud. As the resolution of the observation is degraded, the l.o.s extinction toward the most dense pixels within the dense core is diluted. However, this dilution affects all the pixels equally, nullifying the net effect of the smoothing. This implies that the PDF of the normalised (dimensionless) measurable (here A_V/A_V^{\max}) would stay invariant for fractal clouds.

In the right panels of Figures 4.2 to 4.7, we show the extinction PDF of six IRDCs including the low mass IRDC L1709A. The extinction histograms have been constructed for pixel values higher than 10 mag of A_V , in order to avoid the Gaussian noise distribution from influencing the shape of the histogram. We find that bumps in the PDF in some cases are due to the intervening inter-clump medium that affects PDFs at all resolutions in a similar fashion. All the extinction PDFs show significant loss in power as the resolution is degraded. Such a change in the shape of the normalised PDF with resolution for all clouds is an indication that IRDCs are not fractal.

Note that for L1709A, the PDF of the un-smoothed data is compared with data smoothed to resolutions $> 100''$. This IRDC is at a distance of 160 pc, and therefore, the cloud is fully resolved at resolutions less than $> 100''$. Hence, the data needs to be convolved with larger beams to see a deviation from self-similarity. Bacmann et al. (2000) find flattened radial density profiles within $100''$ of this core. In fact, this flattened profile is direct evidence of coherent self-gravitating structures within the cloud. The high mass IRDCs in our sample are not local and hence we readily see a deviation from similarity at resolutions lower than $50''$. This suggests that self similarity breaks down at scales between $0.2 - 0.5$ pc for IRDCs. This result is very similar to that obtained by Blitz & Williams (1997), where they show that Taurus molecular cloud exhibits a change in the character of structure on a scale of $0.25 - 0.5$ pc. BW97 argue that the preferred physical scale is the thermal Jeans length corresponding to a gas kinetic temperature of ≈ 10 K.

The turbulent Jeans length is given as (Blitz & Williams 1997),

$$\lambda_J = 2.39 \frac{\Delta V}{1 \text{ kms}^{-1}} \sqrt{\frac{10^3 \text{ cm}^{-3}}{n_{\text{H}_2}}} \text{ pc}, \quad (4.6)$$

and the thermal Jeans length by

$$\lambda_J = 0.37 \sqrt{\frac{T}{10 \text{ K}}} \sqrt{\frac{10^3 \text{ cm}^{-3}}{n_{\text{H}_2}}} \text{ pc}. \quad (4.7)$$

For a typical high mass IRDC, ΔV is observed to have values from $1 - 3 \text{ km s}^{-1}$, temperatures $< 20 \text{ K}$ (Pillai et al. 2006a) and gas densities of $\sim 10^5 \text{ cm}^{-3}$ (Carey et al. 1998). Therefore, the Jeans length for the turbulent gas is $\sim 0.34 \text{ pc}$ for an average line width of 2 km s^{-1} while thermal Jeans length is $< 0.05 \text{ pc}$ for gas temperatures less than $< 20 \text{ K}$. Therefore as speculated by (Blitz & Williams 1997), the turbulent Jeans length appears to be the characteristic scale at which high mass IRDCs exhibit non-fractality. The cloud appears to be supported by turbulence on large scales while at sub-parsec scale, it dissipates paving the way for thermal support against collapse.

4.6 Conclusion

From Spitzer MIR observations with high spatial $1.9''$ resolution and high sensitivity, we derive extinction maps of six Infrared Dark Clouds. Five of these are known to be high mass IRDCs while the sixth is a well studied low mass pre-stellar core. We find that high mass IRDCs have very high extinction upto 200 mag of A_V while the low mass IRDC has a peak extinction of $< 60 \text{ mag}$ along the line of sight. These IRDCs are very massive with total masses in the range $500 - 10^5 M_\odot$. Furthermore, we find that high mass IRDCs are not isolated but immersed in low density parent clouds. By comparison with thermal dust continuum observations, we find that the highest extinction clumps identified by the absorption analysis in an IRDC is not detected in the submm. This is attributed to limitations in submm Bolomtere observing techniques. Therefore, MIR absorption is a better tracer of density at the low as well as the highest extinction. We find that IRDCs might have high density contrast between the core and the envelope. This might imply that initial stages of high mass dark clouds might be governed by highly compressive energetics, very likely shocks due to a SN explosion or stellar winds from nearby high mass stars. Finally, analysing the extinction PDF of IRDCs, we find that there is a break down of self similarity. The characteristic scale of $0.2 - 0.5 \text{ pc}$ reflecting the transition from a self-similar to a coherent core might correspond to the turbulent Jeans length.

Table 4.1: List of IRDCs Studied.

Name	R.A.(J2000)	Dec.(J2000)	distance (pc)	I_{bg} [MJy/sr]	I_{off} [MJy/sr]	Mass [$10^4 M_{\odot}$]	$A_{\text{V}}^{\text{max}}$
G11.11-0.12	18:10:34.20	-19:16:41.5	3600	81.6	45.2	4.6	144
G19.30+0.07	18:25:51.22	-12:05:31.5	2200	72.4	36.3	0.4	78
G24.63+0.15	18:35:40.44	-07:18:42.3	1000	84.0	40.2	0.07	113
G24.72-0.75	18:36:39.60	-07:39:57.3	1000	102.6	49.1	0.05	154
G28.34+0.06	18:42:51.20	-04:01:51.0	4800	62.5	24.9	8.8	180
L1709a	16:32:46.60	-23:53:25.2	160	9.9	4.4	0.06	41

Notes: Columns are name, right ascension, declination, distance, chosen background intensity and foreground intensity, total mass within the selected field and the maximum extinction. Distances toward IRDCs are from Carey et al. (1998) and toward L1709A from Bacmann et al. (2000). The coordinates correspond to the reference positions of the maps.

Table 4.2: Comparison of Peak N_{H_2} We Derive with Values Quoted in Literature Based on submm Emission and MIR Absorption Analysis.

Name	$N_{\text{H}_2}^{\text{IRAC}}$ 10^{22}cm^{-2}	$N_{\text{H}_2}^{\text{SCUBA}}$ 10^{22}cm^{-2}
G19.30+0.07 P1	3.4	3.9
G19.30+0.07 P2	3.5	4.1
G28.34+0.06 P1	4.3	3.3
	$N_{\text{H}_2}^{\text{IRAC}}$	$N_{\text{H}_2}^{\text{ISO}}$
L1709a	7.3	5.1

Notes: Columns are name, H_2 column density derived from Spitzer observations, and H_2 column density derived from SCUBA dust continuum observations (Carey et al. 2000) or ISO MIR absorption (Bacmann et al. 2000). The P1/P2 designations corresponds to the (Carey et al. 2000) source positions.

Chapter 5

Tracing Active Star Formation in IR-Dark Clouds

We present results of a high resolution interferometric survey of 6.7 GHz CH_3OH maser and 22.2 GHz H_2O maser in a sample of infrared dark cloud cores with the goal to establish accurate positions. The survey has been carried out with the Very Large Array and the Australian Telescope Compact Array, as follow up of observations made at lower resolution with the Effelsberg 100 m telescope. The masers remain unresolved by the interferometer beam and show spread in the velocity structure. The maser detection is a clear evidence of active star formation already ongoing in Infrared dark clouds.

5.1 Introduction

We have discussed the physical and chemical properties of massive quiescent cores in IRDCs in the preceding Chapters. For a sample of sources, we have shown that the cores can collapse to form stars and that some of these source might be massive. For our understanding of the earliest phases of massive star formation, we started a new search for Class II CH_3OH masers (CIIMMs) at 6.7 GHz and 22 GHz H_2O methanol masers which is not biased towards hot sources, due to using IRAS and cm continuum sources as search beacons. We used as our search criterium strong mm/submm emission together with a lack of NIR/MIR emission, hence selecting presumably cold sources. The low temperature (10 – 20 K) of the sources are confirmed by ammonia rotational temperatures found by us with the 100m telescope (Chapter 2). Our subsequent study with the 30m telescope reveal a high deuteration of ammonia in these cores (Chapter 3).

The sample we searched for the masers consists of mainly two groups (discussed in the previous Chapters):

- Massive cores in infrared dark clouds (IRDCs) found in the MSX survey of the Galactic plane Carey et al. (1998).
- Massive secondary cores in the field of view of the (Thompson et al. 2005) study of Ultracompact HII regions using SCUBA at the JCMT.

Class II methanol (CH_3OH) masers (CIIMMs) are almost always found in high-mass star-forming regions (HMSFRs). It turned out that not all of the CIIMM are associated with UCHII R (Walsh et al. 1998). Based on high spatial-resolution radio continuum and 6.67 GHz methanol spectral-line data in 364 sources towards IRAS-selected regions, Walsh et al. (1998) show that the methanol maser is most

likely present before an observable UCHIR is formed around a massive star and is quickly destroyed as the UCHIR evolves. However, this is disputed by Phillips et al. (1998) who argue that the non detection of radio continuum emission associated with methanol masers is because of the association of the maser sites with low/intermediate mass stars which do not ionise their immediate surroundings. To date *no* CIIMM has ever been detected toward a low-mass SFR, with the possible exception of NGC 2024-FIR4 (Minier et al. 2003), which, by the way, is the *only* known CIIMM in the whole Orion Giant Molecular Cloud (GMC) complex. Walsh et al. (2001) in another study of 31 methanol maser sites and 19 UCHIR in Mid-infrared (10.5 and 20 μm) find that the observations are consistent with the maser emission being powered by the MIR source. Walsh et al. (2001) also find strong evidence of infall/outflow in different molecular tracer. Beuther et al. (2002c) find a mean separation of ~ 0.19 pc between the CH_3OH and cm emission for there sample of 29 massive star forming regions. Subsequently, in a continuum mapping reported by Walsh et al. (2003) toward 71 6.7 GHz maser fields, they find that most methanol masers are within $10''$ of a sub-mm peak. Furthermore, a recent 1.2 mm continuum survey in massive star forming regions with methanol maser sites and/or radio continuum emission, reported by Hill et al. (2005) shows that these tracers of massive star formation are associated with heavily embedded protostars. These arguments taken together with the non detection of radio continuum make a convincing case of CIIMMs signposting the earliest stages of high mass star formation.

The models of excitation conditions for H_2O and CH_3OH masers favour hot ($T \sim 90$ K for CH_3OH masers, higher T for H_2O masers) and dense ($n \sim 10^7 \text{ cm}^{-3}$) environments unusual for a dark cloud, unless star formation has already set going. Both maser types are believed to trace the earliest stages of star formation, while CIIMMs are almost always found in high-mass star-forming regions (HMSFRs)(Ellingsen 2005). The excitation schemes invoked, however are very different. Together with observational evidences, this leads to suggestions that both masers trace different evolutionary stages. H_2O masers are observed towards both low and high mass star forming regions. However, Class II methanol (CH_3OH) masers (CIIMMs) are almost always found in high-mass star-forming regions (HMSFRs) (Walsh et al. 1998, Walsh et al. 2001).

We obtained higher angular resolution (few arcsecs) observations of both masers after their detections in massive, cold cores with the Effelsberg 100m telescope. These detections are clear evidences for deeply embedded, very young sources, hence indicating that the core has left its quiescent state and started to form stars. Our aim was to spot the absolute positions of maser emissions towards the dense cores. This would constrain the location of the embedded source with respect to our submm continuum and molecular line observations of the cores with angular resolutions of 1.5 to 8 arcsec. While methanol masers appear to trace part of a circumstellar disk around the central source, the water masers appear to be associated to the outflow from the source (Edris et al. 2005). Comparison of the two maser types toward a larger sample of sources would improve our understanding of their different excitation conditions. A similar study by Beuther et al. (2002c) in a sample of 29 massive star-forming regions confirm earlier results, obtained for each maser species separately, that both maser types are signposts of high-mass star formation in very early evolutionary stages. Our sources are expected to be at a still earlier stage of evolution (see Chapter 2) and therefore, we expect to better understand the hierarchy in the evolution toward a high mass star based on these observations.

5.2 Observations

5.2.1 Single-dish H_2O and CH_3OH Maser Observations

We observed H_2O ($6_{16} \rightarrow 5_{23}$; 22 235.0798 MHz) and Class II CH_3OH Class ($5_1 - 6_0 \text{ A}^+$ transition 6.667 GHz) masers toward a sample of IRDCs targeted on the mm peaks, with the Effelsberg 100 m telescope ¹ in several runs from 2003 – 2004. The beam width at 6.7 GHz and 23 GHz is 122 and $40''$

¹Based on observations with the 100-m telescope of the MPIFR (Max-Planck-Institut fr Radioastronomie) at Effelsberg

respectively as determined from drift scans over compact continuum sources. We detected H₂O and cIIMM CH₃OH masers in 13 out of the 37 sources from the above mentioned groups. These detections are clear evidences for deeply embedded, very young sources, hence indicating that the core has left its quiescent state and started to form stars. 5 sources show both maser emission. Follow-up observations of the maser detections were conducted with high spatial resolution with the VLA and the ATCA.

5.2.2 H₂O Maser Observations with the VLA

Synthesis images of the 22.2 GHz H₂O maser line were obtained with the Very Large Array (VLA) in the C configuration with a spectral resolution of 0.16 km s⁻¹, a synthesized beam of $\approx 1.17''$, and a primary beam FWHM of $\approx 2'$. The snapshot mode was used with 5 minutes integrations spread over the transit of each source, interspersed with phase referencing. We reduced the data with the MIRIAD software package using standard procedures. The typical 1σ sensitivity is 1 Jy. Phase calibration was done using observations on J1733-130, J1743-038, J1751+096. The flux calibrator was 3C286.

For 10 out of 13 observed sources, we confirmed our previous detection with the single dish. In the other 3 sources, we detect strong radio continuum. The velocity of these 3 masers were out of the range of the band which was centered around the systemic velocity. Therefore, we quote the best fit position obtained from half beam sampled single dish data. The absolute positional accuracy of VLA data is $1''$. The accuracy of relative positions of different maser features is around $0.1''$.

5.2.3 CH₃OH Maser Observations with the ATCA

On 11 January 2004, we followed up the observations of the 6.7 GHz Class II CH₃OH maser with the Australian Telescope Compact Array (ATCA) in the FULL_4_1024-128 correlator configuration employing the snapshot mode with a series of 6 short integration cuts of 5 minutes for each source. Since ATCA can observe simultaneously two frequencies, we chose the 8.64 GHz continuum band covering a bandwidth of 128 MHz frequencies, the 1σ sensitivity achieved being ~ 0.2 mJy/beam. Phase calibration was done using B1817-254 and B1819-096. The primary beam of ATCA at this frequency is $\sim 8'$ and the effective HPBW of the synthesized beam is heavily dependant on the declination (for declination north of -24°). For our observations, the effective beam was in the range $1.28'' \times 5.28''$ to $1.8'' \times 51''$. The spectral resolution was 0.2 km s⁻¹, the 1σ sensitivity was 0.5 Jy. Maser emission is detected toward 12 of the 13 sources; three are new detections. The data reduction was performed with the MIRIAD software package using standard procedures. Absolute positions for ATCA observations are estimated to be accurate to $1''$ for sources with declination south of -24° whereas the relative positions should be accurate to $\sim 0.1''$. For other sources, the beam is highly elongated and we have a non-detection for one source. The observed positions and reference LSR velocities are given in Table 5.2.

5.3 Results

The absolute positions for both masers are given in Table 5.4.

We analysed the maser spots in the Position-Velocity Diagram. The kinematic structures we find in either maser species show no recognisable pattern except for G11.11-0.12 (Pillai et al. 2006b). H₂O masers are spread over a large range of velocities and in some sources have significant shifts from the systemic velocity of the source. However, CH₃OH masers are confined to smaller dispersions (< 20 km s⁻¹), around the source systemic velocity (see Fig.5.1 – Fig.5.4). This is an additional evidence that H₂O masers exists in shock environments, either outflows or disks. As given in Table 5.4, we report only three new detections for the 6.7 GHz methanol masers. Considering that the field of view ATCA is $\sim 7'$, the implication is that most massive clouds in our sample are devoid of active star formation in the densest cores.

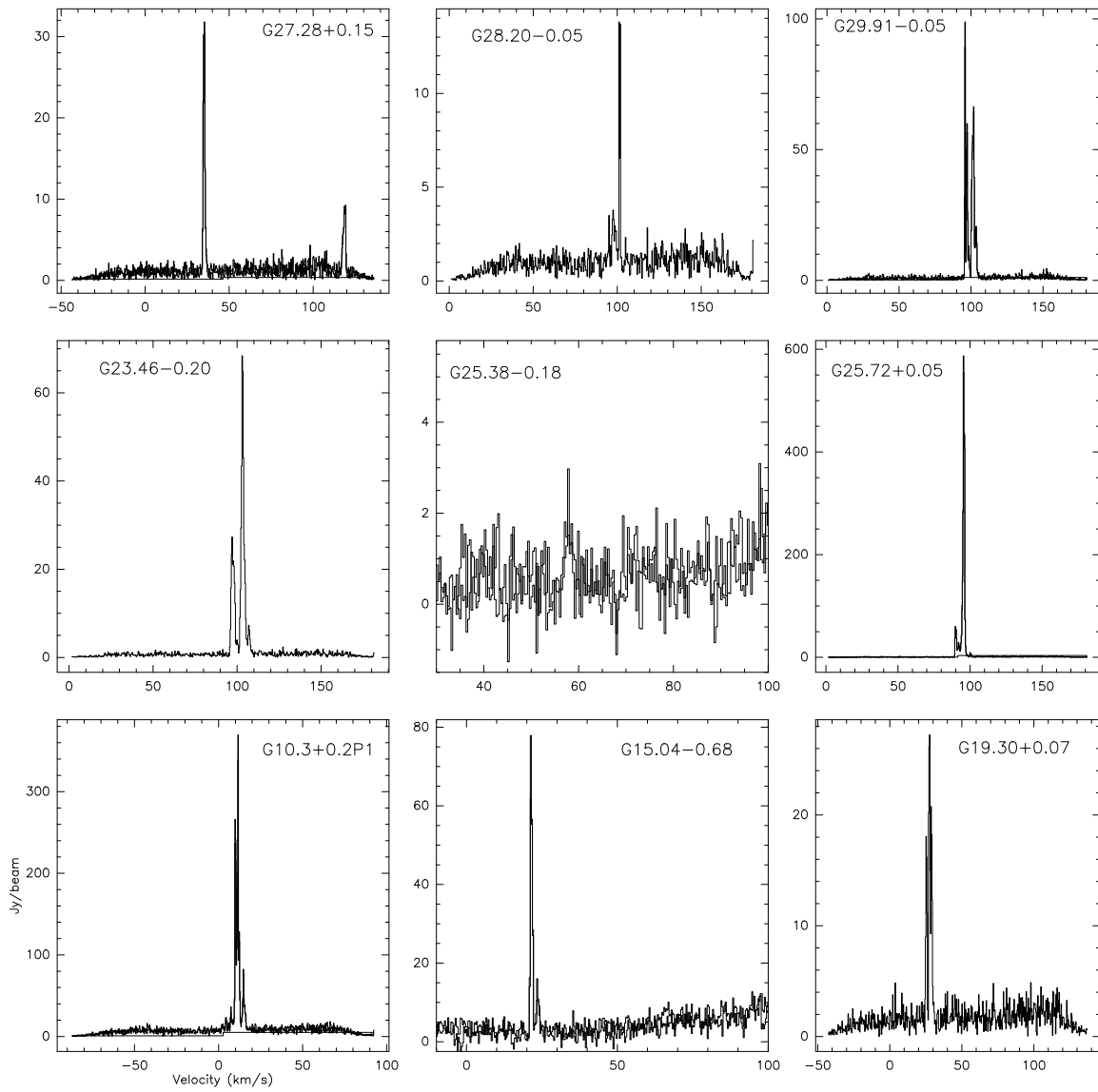


Figure 5.1: The CH_3OH maser spectra observed with VLA.

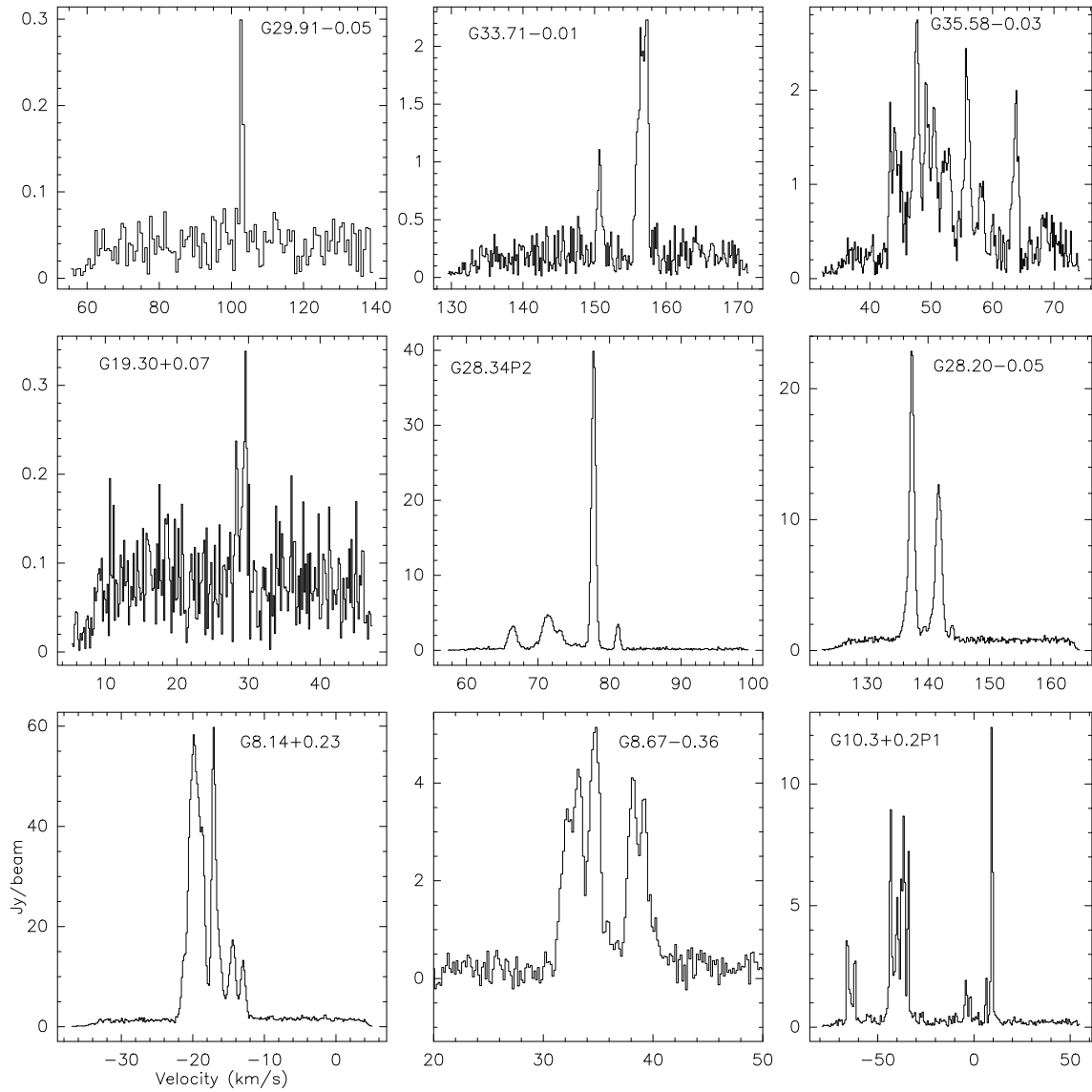


Figure 5.2: The H₂O maser spectra observed with VLA.

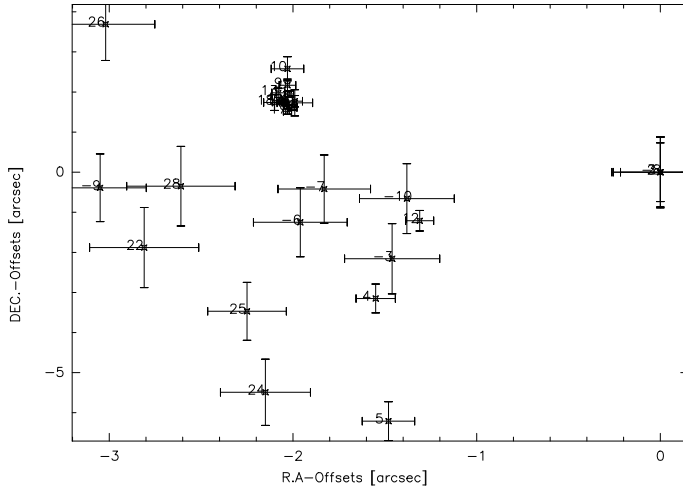


Figure 5.3: The velocity structure of the CH_3OH maser emission in G10.3+0.2 P1. Each data point gives the position of the model fits to the individual velocity channels. The corresponding V_{LSR} in km s^{-1} is also shown.

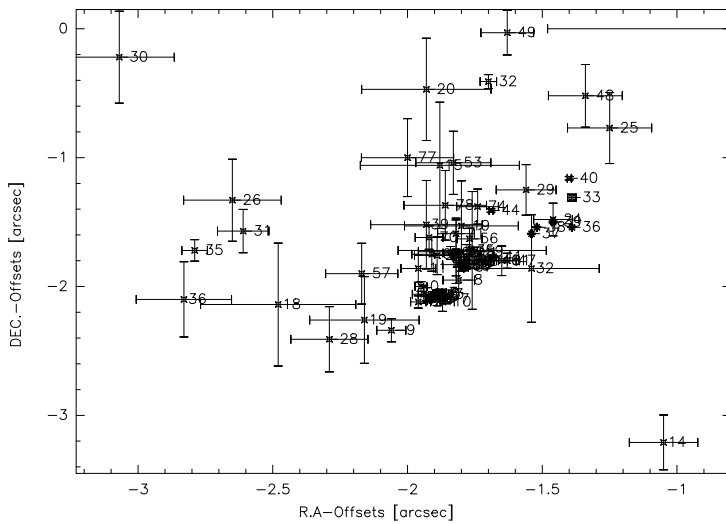


Figure 5.4: The velocity structure of the H_2O maser emission in G10.3+0.2 P1. Each data point gives the position of the model fits to the individual velocity channels. The corresponding V_{LSR} in km s^{-1} is also shown.

Table 5.1: Pointing Centers for the Observed Fields.

Name	R.A.(J2000)	Dec.(J2000)	V_{LSR} [km s ⁻¹]
H ₂ O			
G8.14+0.23	18:03:00.71	-21:48:08.43	19.4
G8.67-0.36	18:06:19.07	-21:37:31.96	33.5
G10.3+0.2P1	18:09:00.12	-20:03:37.44	13.1/65.1
G11.11P1	18:10:28.40	-19:22:29.00	29.20
G15.04-0.68	18:20:24.84	-16:11:35.11	59.9
G19.30+0.07	18:25:50.70	-12:05:15.83	26.3
G23.46-0.20	18:34:44.91	-08:31:06.51	104.2
G23.87-0.12	18:35:13.43	-08:06:52.43	74.5
G28.20-0.05	18:42:58.18	-04:13:59.86	97.4
G28.34P2	18:42:52.40	-03:59:54.00	78.4
G29.91-0.05	18:46:04.97	-02:42:35.09	97.4
G33.71-0.01	18:52:59.10	00:42:31.47	104.2
G35.58-0.03	18:56:23.46	02:20:37.77	53.2
CH ₃ OH			
G10.3+0.2P1	18:09:00.12	-20:03:37.43	13.1
G10.3+0.2P2	18:08:52.53	-20:06:06.01	13.1
G11.11P1	18:10:28.40	-19:22:29.00	29.20
G13.19+0.04	18:14:05.60	-17:28:38.76	51.60
G15.04-0.68	18:20:24.84	-16:11:35.11	59.9
G19.30+0.07	18:26:24.29	-12:03:46.0	26.3
G23.46-0.20	18:34:44.91	-08:31:06.49	104.2
G25.38-0.18	18:38:14.27	-06:47:53.34	95.90
G25.72+0.05	18:38:02.80	-06:23:47.15	109.5
G27.28+0.15	18:40:35.22	-04:57:44.14	26.00
G28.20-0.05	18:42:58.17	-04:13:59.86	97.4
G29.91-0.05	18:46:04.97	-02:42:35.09	97.4

Table 5.2: Columns are name, right ascension, declination and LSR velocity. Note that the source names in some cases are repeated for the tables corresponding to H₂O and CH₃OH maser observations. These are sources for which both masers have been detected and therefore, the field of view for both observations required different reference positions of the field centers.

5.4 Discussion

We detected water and methanol masers in 50% of the sources in our sample. Both water and methanol masers in our sample are associated with a mm cores. The mean separation of a mm core from the H₂O maser emission is 0.2 pc, while its separation from CH₃OH maser is 0.09 pc. However, these values are not accurate due to lower resolution of the mm data. For three sources with both H₂O and CH₃OH maser detections, we estimate the mean separation to be 1 mpc. The main result of our survey is the evidence of active star formation already ongoing in Infrared dark clouds. The high excitation conditions required to pump the masers is confined to very compact regions which imply that beam dilution severely influences the observations (see next Chapter). The discovery of both maser types in different cores makes them ideal test grounds for studying a range of objects at very different evolutionary stages.

Table 5.3: Absolute Positions of Observed Masers.

source	R.A.(J2000)	Dec.(J2000)	Comments
H ₂ O			
G8.14+0.23	18:03:00.86	-21:48:12.41	Braz & Epchtein (1983), absolute position uncertain
G8.67-0.36 ^h	18:06:19.08	-21:37:33.95	OH maser (Forster & Caswell 1989) within 10''
G10.3+0.2P1	18:08:59.99	-20:03:39.44	CH ₃ OH maser (Walsh et al. 1998) within 10''
	18:08:59.99	-20:03:37.44	
G11.11P1	18:10:28.29	-19:22:30.50	
G15.04-0.68 ^{sd}	18:20:25.94	-16:12:40.50	radio continuum
G19.30+0.07	18:25:52.07	-12:05:13.83	
G23.46-0.20 ^{sd}	18:34:44.92	-08:31:06.51	radio continuum
G23.87-0.12 ^{sd}	18:35:13.11	-08:07:17.72	radio continuum
G28.34P2	18:42:51.87	-03:59:54.00	
G28.20-0.05	18:42:58.05	-04:13:57.86	OH (Argon et al. 2000), CH ₃ OH masers (Walsh et al. 1998) within 10''
G29.91-0.05	18:46:04.17	-02:42:25.10	
G33.71-0.01	18:52:59.11	00:42:27.44	
G35.58-0.03	18:56:22.54	02:20:27.78	OH maser (Argon et al. 2000) within 10''
CH ₃ OH			
G10.3+0.2P1 ^c	18:09:1.48	-20:05:8.88	
	18:08:59.99	-20:03:35.6	
G10.3+0.2P2 ^c	"	"	
G11.11P1	18:10:28.25	-19:22:30.45	
G13.19+0.04	-	-	
G15.04-0.68 ^c	18:20:24.81	-16:11:35.61	H ₂ O maser within 10''(Forster & Caswell 1989)
G19.30+0.07 ^w	18:26:25.79	-12:03:52.49	
G23.46-0.20 ^c	18:34:39.18	-08:31:29.86	
G25.38-0.18	18:38:08.29	-06:46:00.42	
G25.72+0.05	18:38:03.14	-06:24:20.63	Błaszkiwicz & Kus (2004), absolute position ucertain
G27.28+0.15 ^g	18:40:33.9	-04:57:18	
G28.20-0.05 ^c	18:42:58.17	-04:13:59.86	OH maser (Argon et al. 2000) within 10''
G29.91-0.05 ^c	18:46:02.5	-02:40:08	

Table 5.4: Positions of the CH₃OH & H₂O maser. The following symbols refer to the citation for allready known sources : ^c Caswell (1996), ^g Goedhart et al. (2000), ^w Walsh et al. (1998), ^h Hofner & Churchwell (1996). ^{sd} denotes those sources for which we have single-dish data from Effelsberg and VLA continuum observations.

Chapter 6

High mass star formation in the IR-Dark Cloud G11.11–0.12

This chapter is based on a paper accepted for publication in Astronomy & Astrophysics.

Here we report detection of moderate to high-mass star formation in an infrared dark cloud (G11.11–0.12) where we discovered class II methanol and water maser emissions at 6.7 GHz and 22.2 GHz, respectively. We also observed the object in ammonia inversion transitions. Strong emission from the (3,3) line indicates a hot (60 K) compact component associated with the maser emission. The line width of the hot component (4 km s^{-1}), as well as the methanol maser detection, are indicative of high mass star formation. To further constrain the physical parameters of the source, we derived the spectral energy distribution (SED) of the dust continuum by analysing data from the 2MASS survey, HIRAS, MSX, the Spitzer Space Telescope, and interferometric 3mm observations. The SED was modelled in a radiative transfer program: *a)* the stellar luminosity equals $\sim 1200 L_{\odot}$ corresponding to a ZAMS star of $8 M_{\odot}$; *b)* the bulk of the envelope has a temperature of 19 K; *c)* the mass of the remnant protostellar cloud in an area $8 \times 10^{17} \text{ cm}^2$ or $15''$ across amounts to $500 M_{\odot}$, if assuming standard dust of the diffuse medium, and to about $60 M_{\odot}$, should the grains be fluffy and have ice mantles; *d)* the corresponding visual extinction towards the star, A_V , is a few hundred magnitudes. The near IR data can be explained by scattering from tenuous material above a hypothetical disk. The class II methanol maser lines are spread out in velocity over 11 km/s. To explain the kinematics of the masing spots, we propose that they are located in a Kepler disk at a distance of about 250 AU. The dust temperatures there are around 150 K, high enough to evaporate methanol-containing ice mantles.

6.1 Introduction

Identifying the earliest stages in the formation of massive stars is currently a crucial step in our understanding of massive star formation, so we started a project to search for methanol and water masers toward cold massive cores (see Previous Chapter on the survey).

Here we report the discovery of Class II CH_3OH maser (CIIMM) and water maser emission toward the IRDC G11.11–0.12 and discuss the properties of the protostar heavily embedded in the IRDC detected with SPITZER in the MIR. In §6.2, we describe our observation in various molecular tracers with the Effelsberg 100-m telescope, Australian Telescope Compact Array, Very Large Array and the Berkeley-Illinois-Maryland-Association interferometer. In §6.3 we present the evidences for active star formation in the IRDC and model the ammonia emission. The discussion on the Spectral Energy Distribution (SED) of the embedded source and modelling in spherical symmetry follows through in §6.4. The observed

properties of the CIIMM are entirely comparable with the properties of numerous other such sources detected in high-mass star forming regions. Therefore, its presence makes G11.11–0.12, an IRDC in which active high-mass star formation has been unequivocally established.

6.2 Observations

6.2.1 CH₃OH Maser

We observed the class II methanol maser at 6.7 GHz (5_1-6_0 A⁺ transition) toward the submm peak IRDC G11.11 P1 ($\alpha_{J2000} = 18 : 10 : 28.402$, $\delta_{J2000} = -19 : 22 : 29.00$) with the Effelsberg 100-m telescope¹ on 15 June 2003. The frontend was the facility 5 cm receiver tuned to 6668.518 MHz. We used the 8192 channel auto-correlator with 2 subunits of 10 MHz bandwidth to be able to reach a spectral resolution of ≈ 0.25 km s⁻¹. The beam width of 122'' was determined from drift scans over compact continuum sources, which also served to check the pointing. The observations were repeated with the 100-m telescope on 5 August 2004.

On 11 January 2004, we followed up the observations of the 6.7 GHz Class II CH₃OH maser with the Australian Telescope Compact Array (ATCA) in the FULL_4_1024-128 correlator configuration, employing the snapshot mode with a series of 6 short integration cuts of 5 minutes. Since ATCA can observe two frequencies simultaneously, we chose the 8.64 GHz continuum band covering a bandwidth of 128 MHz frequencies. The 1 σ sensitivity achieved is ~ 0.2 mJy/beam. Phase calibration was done using B1817-254. The primary beam of ATCA at this frequency is $\sim 8'$, and the effective HPBW of the synthesized beam equals $2.03'' \times 6.24''$. The spectral resolution was 0.2 km/s, and the 1 σ sensitivity 0.5 Jy. The ATCA spectrum is essentially identical to the 2003 Effelsberg spectrum.

6.2.2 Ammonia Observation

The maser detection prompted us to search for the NH₃ (3,3) and (4,4) transitions with the Effelsberg 100-m telescope in April 2004. With the AK 8192 backend, we were able to observe the (1,1), (2,2), (3,3), and (4,4) transitions in both polarisations simultaneously using the K-band receiver. With 8 subunits of 10 MHz bandwidth, the resulting spectral resolution was ≈ 0.2 km s⁻¹ after smoothing the data to improve the signal-to-noise ratio. The beam at the NH₃ frequencies was 40''. The observations were performed in the frequency switching mode. Pointing was checked at hourly intervals by continuum scans on G10.62. We estimate, the pointing to be accurate within 6'', with the pointing scans used for the absolute calibration.

6.2.3 VLA H₂O Maser Observation

The 22.2 GHz H₂O maser observations were done with the Very Large Array (VLA) on 24 August 2004 in its D configuration and in 2 polarisations with a spectral resolution of 0.33 km/s, a synthesized HPBW of $\sim 0.4''$, and a primary beam of $\sim 120''$. The standard interferometer mode was used with a total integration time of 20 minutes on source, split into sessions. Phase calibration was done using J1733-130, and the flux calibrator was 3C286.

6.2.4 BIMA Observation

The 3mm observations were carried out from September 1999 to July 2000 with the Berkeley-Illinois-Maryland-Association interferometer (BIMA) in its B, C, and D configuration sampling spatial structures from 3'' to 60''. Continuum images were obtained with a combination of 86 and 93 GHz tracks centred

¹Based on observations with the 100-m telescope of the MPIfR (Max-Planck-Institut für Radioastronomie) at Effelsberg

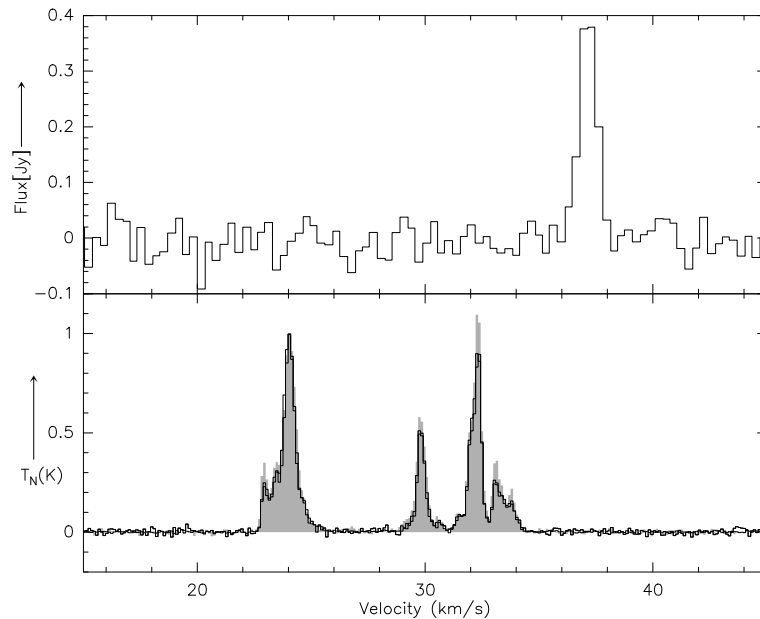


Figure 6.1: Lower panel: Effelsberg 100-m Spectra of the CH_3OH emission at 6.7 GHz. The filled spectrum corresponds to June 2003 and the solid lines to August 2004 observations. The blue shifted component is normalised to unity in both cases. Upper panel: 22.2 GHz water maser spectra obtained with the VLA.

with a beam size of $8.3'' \times 3.9''$ reaching an rms of 1.6 mJy. The total bandwidth of both sidebands was ~ 900 MHz.

6.3 Results

6.3.1 CH_3OH Maser

The solid line in Fig.6.1 displays the 6.7 GHz methanol maser spectrum toward G11.11P1 detected in August 2004 with the Effelsberg 100-m telescope, while the filled region shows the June 2003 data. As the Effelsberg 100-m absolute calibration has an uncertainty of $\sim 20\%$, the observations taken with two different instruments and at different times have been normalised with respect to one of the features, so that absolute calibration is no longer an issue. The maser features cover a velocity range of about 11 km/s, with the peaks at 32 km/s in June 2003 and at 24 km/s in August 2004. Thus there is clear evidence of a variation in the relative line intensities of about 10 %. From mapping the source, we find that the masing spots originate at the position P1 from an area that is point-like with respect to the Effelsberg beam. There is no evidence of another maser source. The follow-up observations obtained six months later with ATCA reveal no obvious changes in the spectrum and also indicate that the maser originates from a single core. The peak flux of the brightest maser feature from the ATCA observations is 22 Jy.

The position of the integrated maser emission is plotted in Fig.6.2. There, the left panel shows the MSX map of the filamentary dark cloud overlaid on the SCUBA submm map from Carey et al. (2000), and the right panel is a blow-up of the SCUBA image around P1, together with contours of 2MASS K_s ²

²The atlas image obtained is part of the Two Micron All Sky Survey (2MASS), a joint project of the University of Massachusetts and the Infrared Processing and Analysis Center/California Institute of Technology, funded by the NASA and the NSF

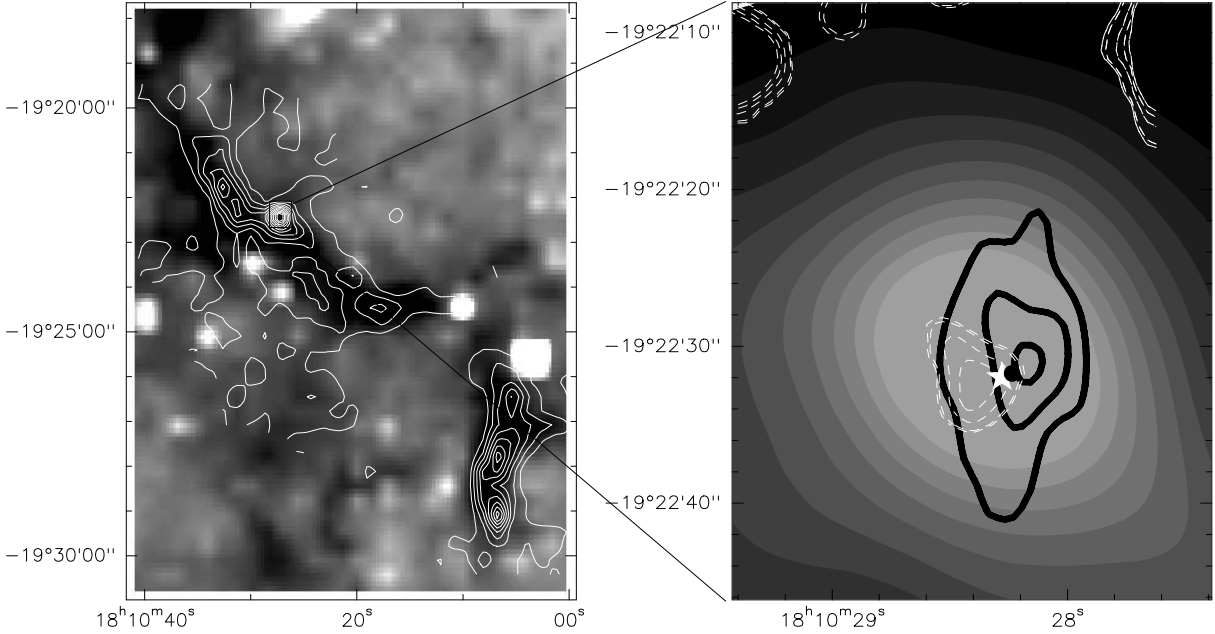


Figure 6.2: *Left:* The $8\ \mu\text{m}$ image of G11.11 with SCUBA $850\ \mu\text{m}$ (Carey et al. 2000) overlay *Right:* BIMA 3mm continuum image towards P1 in contours, with contour level $\sim 1.6\ \text{mJy}$ (-3,3,5,7) and 2MASS K_s band in dashed contours on the $850\ \mu\text{m}$ image. The star denotes the H_2O maser and the filled circle the CH_3OH maser position.

band and the 3mm continuum emission. To estimate the positional accuracy of the maser observations, we split the phase calibrator observations into two sets and cross-calibrate the second set with a self-calibrated first set, which results in a position accuracy of $(0.05'', -0.15'')$. This is a lower limit, but since our source is less than 10° away from the calibrator, baseline errors are not likely to add to the error. To cross-check this, we reduced other observations towards an already known maser source and found a positional accuracy of $(0.105'', -0.75'')$. ATCA is an east west array, so the beam width in declination is greater by a factor $\text{cosec}(\text{DEC})$; and for those sources with declination north of $-24\ \text{deg}$, complete u - v coverage is unobtainable.

When the sub-spots are analysed in position–velocity plots, they fall nicely along an arc, as predicted for a disk (Minier et al. 1998, Norris et al. 1998). There is also a linear velocity trend. This is shown in Fig.6.3 where a point source model was fitted to individual velocity channels. The one sigma position uncertainty is proportional to the SNR (Reid et al. 1988); hence, with a SNR 15-30 for the different velocity features, we reach a sub-arcsecond accuracy. The relatively weak peak at $34\ \text{km/s}$ was not included due to its large positional uncertainty.

6.3.2 3mm Continuum Emission

The BIMA image shows a compact, slightly resolved 3mm continuum source that coincides with the SCUBA sub-mm peak shown in Fig.6.2. A 2-D Gaussian fit to the emission yields a source size of $0.25 \times 0.12\ \text{pc}$ with a PA 3° . The peak flux of $\sim 12\ \text{mJy}$ corresponds to a brightness temperature of $\sim 28\ \text{mK}$. Our cm continuum observations with ATCA at $8.4\ \text{GHz}$, along with searches in Galaxy-wide cm continuum surveys, reveal no detectable free-free emission. In order to check whether one expects to find free-free emission at 3mm , we extrapolated the ATCA upper limit to that at 3mm , assuming optically thick emission. We estimated a mm flux of $25.3\ \text{mJy}$ relative to the ATCA upper limit of

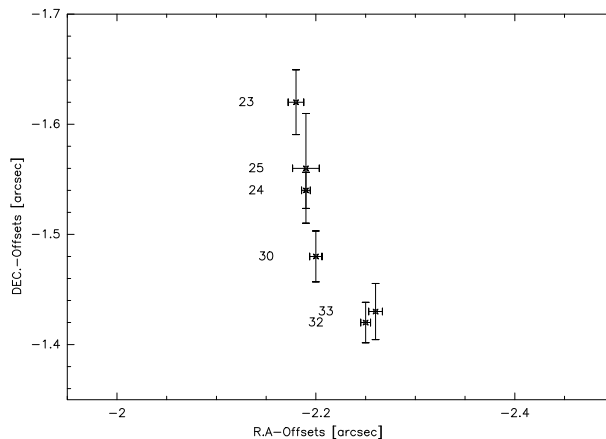


Figure 6.3: Velocity structure of the CH₃OH maser emission. Each data point gives the position of the model fits to the individual velocity channels. The corresponding V_{LSR} in km s⁻¹ is also shown.

~ 0.2 mJy. Thus the contribution from free-free emission cannot be ruled out. For a typical value of 10000 K for the ionisation temperature from an optically thick ionised gas cloud, we get an emission measure $EM > 4 \times 10^{10}$ pc cm⁻³ at 90 GHz, a very high value that is more suitably assigned to Hypercompact HII regions (Kurtz 2002). Such a region with typical sizes < 0.05 pc would have been point-like with respect to the BIMA beam, while we found that the source is partially resolved. Thus, the 3mm emission is most likely due to dust.

6.3.3 H₂O Maser

The position of the H₂O maser appears offset from the CH₃OH maser position, as well as from the BIMA 3mm continuum peak, within the respective positional errors. This might indicate that, although both CH₃OH and H₂O masers occur in warm and dense environments, they may not spatially coincide due to different excitation mechanisms (Beuther et al. 2002c).

Water masers can be explained by collisional pumping with H₂ molecules in shocks associated with outflows (Elitzur et al. 1989). Alternatively, the pumping can occur by accretion shocks in disks (Garay & Lizano 1999). The maser is weak (~ 0.3 Jy) with a feature offset of ~ 7 km s⁻¹ from the systemic velocity as shown in the upper panel of Fig.6.1. This agrees well with the picture of water masers being variable and having large velocity spread.

The maser spot is not spatially resolved over its velocity structure. We performed a model fit to the individual velocity channels over the single feature. Unlike the CH₃OH masers, the H₂O maser spots do not show any systematic gradient. Since the velocity structure is also found to be spread on a much higher angular scale than the CH₃OH maser, it may be tracing the outflow. Higher angular resolution is needed to reveal structures that could be either a shock front of the high-velocity outflow very close to the central object or part of the accretion disk itself. We also serendipitously discovered another water maser that was offset by more than 1'. The feature is brighter and situated at the systemic velocity of the source. The absolute position of the maser peak is at $\alpha_{J2000}=18:10:33.58$, $\delta_{J2000}=-19:22:50.3$.

6.3.4 Ammonia towards G11.11P1

Figure 6.4 shows the ammonia lines observed with the 100-m telescope toward G11.11P1, and the line parameters are given in Table 6.1. For the (4,4) line that was not detected, the 1σ r.m.s noise in the spectrum is given instead.

Table 6.1: Effelsberg 100m Line Parameters.

Transition	v_{LSR} (km s^{-1})	T_{MB} (K)	FWHM (km s^{-1})
NH ₃ 1–1	29.78(0.01)	4.1 (0.4)	1.29(0.02)
NH ₃ 2–2	29.78(0.02)	1.58(0.07)	1.81 (0.06)
NH ₃ 3–3	29.77(0.07)	0.64(0.05)	3.22 (0.21)
NH ₃ 4–4		(0.065)	

The line widths from Gaussian fits when taking the hyperfine satellites for the (1,1) and (2,2) spectra into account increases with the excitation of the lines. The (3,3) transition even shows, a broad wing besides the line core. From a Boltzmann plot of the ammonia emission, we conclude that the ammonia emission cannot be explained with a single temperature. From just the NH₃ (1,1) and (2,2) data, we got a rotational temperature of ~ 14 K. The rotational temperature derived from the (2,2) and (3,3) lines was estimated to be ~ 30 K.

This evidence of two temperature components prompted us to fit the spectrum with two components simultaneously using XCLASS (Schilke, P., private communication). The program then yields the rotation temperature, column density and source size for a given telescope size assuming a Gaussian structure, and produces a synthetic spectrum in agreement with observations. Table 2 lists the fit results. Thus the broader component appears to be much hotter (60 K) and is very compact (3.3"). Actually, the fit is not unique since there is degeneracy between column density and the source size. But a large source size would mean a still higher luminosity, which would put the source in the spectral type O9. It is highly unlikely that an HII region around such a star goes undetected. On the other hand, a much smaller source size with very high column density would mean extremely dense gas with critical density high enough to excite the (4,4) level, which we do not detect.

Additionally, we fit the ammonia spectra with a spherical symmetric model (Wyrowski et al. 2003) using both a core component with a temperature power law, consistent with internal heating from a $1200 L_{\odot}$ embedded source, and a more extended, cooler (10 K) lower density clump. For the core component, the luminosity, and the outer and inner radii were taken from the dust continuum modelling, which will be presented in §6.4.3. Assuming an ammonia abundance of 10^{-8} , the density in the core is $7 \times 10^5 \text{ cm}^{-3}$, which is consistent with the modelling in §6.4.3, and is a factor 10 lower in the cooler clump with a size of 40". For the core component, a line width gradient was modelled with 4 km/s in the inner 2 arcsec and then decreasing to the clump component with 1.2 km/s. The increasing line widths/turbulence towards the centre of the core is another indication of an embedded, massive young stellar object that is stirring up its environment, as well as the remaining line wings of the (3,3) line, which indicates an additional outflow component.

Table 6.2: Model Fit Results.

Component	T_{rot} (K)	size (")	N_{NH_3} (10^{15} cm^{-2})	FWHM (km s^{-1})
NH ₃ cold	15.4	23	1.8	1.34
NH ₃ hot	60	3.3	13.7	4

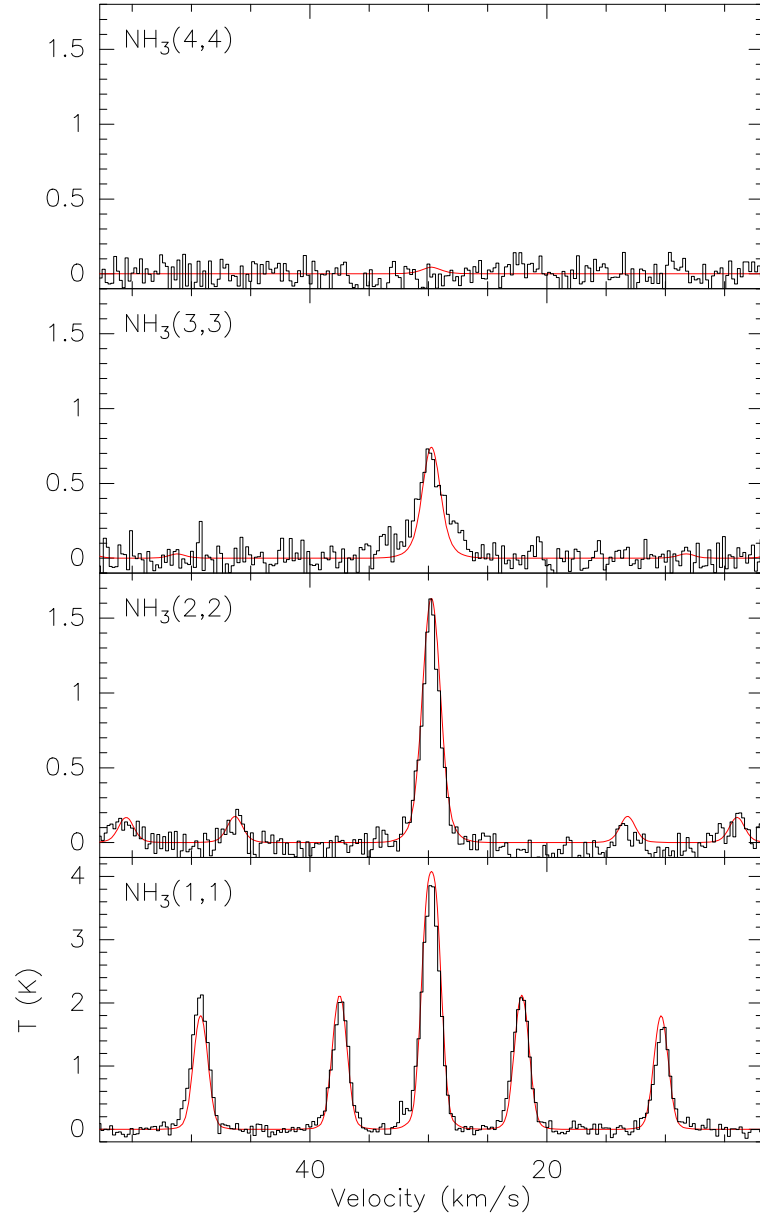


Figure 6.4: *top to bottom:* Spectra of the NH_3 $(J, K) = (1, 1), (2, 2), (3, 3),$ and $(4, 4)$ transitions. All spectra were taken towards the submm peak position given in the text. The fit discussed in §6.3.4 is overlaid in red.

6.3.5 Archival Data

We collected the data from 4 galactic sky survey archives, namely 2MASS, Spitzer, MSX, and IRAS. The 2MASS point source catalog contains the JHK fluxes for 3 point sources all within the $14''$ of the SCUBA beam. The Spitzer MIR data collected from the Spitzer data archive is part of the GLIMPSE Legacy survey in 4 of the Infrared Array Camera (IRAC) bands from $3.6 - 8\mu\text{m}$. We found 3 point sources in the $3.6\mu\text{m}$ band, while in the higher wavelength bands we found a single source that were coincident with the MSX $8\mu\text{m}$ point source. The FIR emission obtained from the high resolution IRAS data is not point like

and might suffer from background emission. But IRAS point sources generally do not appear circular, primarily because the detector aperture were rectangular. We adopted an flux uncertainty of 20% in all cases as given by the respective Space centres.

6.4 Discussion

6.4.1 CH₃OH Maser Disk Scenario

Figure 6.1 contains 3 major peaks that is very reminiscent of a classical maser triplet, which is usually ascribed to a maser amplification from a disk in Keplerian rotation viewed edge on (Elmegreen & Morris 1979).

According to Cesaroni (1990) and Ponomarev et al. (1994), the intensity ratio of the central to the red and blue peaks is determined by the width of the ring in which the conditions for line amplification are favourable, and the central peak vanishes when the ring becomes very small. The red and blue components of our spectrum are not equidistant to the central component that marks the systemic velocity (see also Table 6.2 of NH₃ velocities). Such a distortion may be due to a tilt of the disk, in which case the physical parameters (density, temperature, and velocity) along the line of sight depend not only on the radial distance, but also on the height above the disk.

In principle, equidistant triplets can also arise from an expanding shell. We favour the disk scenario for several reasons. *a)* Variations in the line ratios, as argued by Cesaroni (1990), are readily explained for disks by radiative interaction between masing spots, whereas such an interaction would not be possible for an expanding shell because of opposite velocities of the masing. *b)* All 3 major peaks contain sub-peaks, which we interpret as arising from irregularities associated with the tilt or warp of the disk. *c)* The near-infrared emission and the Spitzer data discussed in §4.1.2 also seem to require a disk structure.

6.4.2 Mass & Luminosity Estimates

The kinematic distance to G11.11 derived as 3.6 kpc using the rotation curve of Clemens (1985) and the IAU standard values of $R_0 = 8.5$ kpc and $V_0 = 220$ km s⁻¹ by Carey et al. (1998) is 3.6 kpc. Carey et al. (2000) quote a gas mass of 67 M_⊙ from their dust continuum observations at 850 micron. The virial masses estimated from ammonia observations range from 150 – 240 M_⊙ for the hot and the cold components within the beam (40'') of Effelsberg. Similarly, by assuming the fractional abundance of NH₃ (relative to H₂) to be on the order of 10⁻⁸, the NH₃ column density translates to masses of 200 – 1600 M_⊙.

The CIIMM need elevated temperatures for two reasons: first, high methanol abundances are required to produce an adequate maser gain, and second, high temperatures are needed to produce pump photons. To effectively evaporate methanol off icy grain mantles, temperatures in excess of 100 K are needed (Sandford & Allamandola 1993). Recent models of CIIMM pumping require gas temperatures ~ 100 K, somewhat higher dust temperatures, and densities of about 10⁷ cm⁻³. Therefore, the compact CH₃OH maser emission we observe must arise from a hot, dense source. We may adopt the spread of the maser components, 0.25'' or 900 AU, as the size of that source, which is comparable to the sizes of numerous other CIIMM regions. The Stefan-Boltzmann law delivers with a luminosity of 830 L_⊙ for a source of the corresponding area and $T = 100$ K. To fit all observed ammonia lines simultaneously, we presented a model in §6.3.4 that assumes an optically thin spherical dust cloud illuminated by a central point source, which then results in a radial temperature distribution of $T \propto r^{-0.4}$ (Wilner et al. 1995). With a luminosity of 1200 L_⊙, we could explain the observed warm ammonia core embedded within a larger cold clump. In the model, the temperature reaches a temperature of 240 K at the inner radius, hence large enough to excite the methanol maser observed.

6.4.3 SED

MIR and Longer Wavelengths

The SED of G11.11 P1 shown in Fig.6.5 contains fluxes due to dust emission at (i) 3mm (BIMA, $8'' \times 4''$ beam), (ii) at 450 and $850\mu\text{m}$ (JCMT), (iii) IRAS data, (iv) MSX upper limits at 12 and $21\mu\text{m}$, (v) an MSX detection at $8.2\mu\text{m}$, (vi) four detections with the Spitzer Space Telescope (at 3.6, 4.5, 5.8 and $8.0\mu\text{m}$), and (vii) three NIR data points from 2MASS.

Although for massive young stars, a time sequence from class 0 to class 3 has not been established, a high-mass-star equivalent to a class 0 object should also emit more than half a percent of its energy at submm wavelengths (André et al. 1993). For G11.11, the luminosity at $\lambda > 300\mu\text{m}$ amounts to almost 3% of the total, so in this respect it could be considered an object equivalent to a Class 0 source. Similar arguments of a Class 0 equivalent object in high-mass-star-forming region have also been proposed by Motte et al. (2003) in the submm protoclusters in W43. They derive a submillimeter to bolometric luminosity ratio of 1.5-3% in W43-MM1 and MM2.

To estimate how the dust temperature and density vary within the envelope, we tried to reproduce the continuum emission in a self-consistent way by calculating the radiative transfer in spherical symmetry. However, when including the NIR fluxes, as well as the recently published data from the Spitzer archive, the assumption of strict radial symmetry had to be abandoned. We sketch below a possible, or even likely, structure of the source; but to confirm its correctness we need information with higher spatial resolution, a difficult requirement for such a distant source. The model therefore remains rather qualitative.

Nevertheless, the observations yield a number of important constraints. *a)* The total luminosity is determined by the IRAS fluxes. While the $100\mu\text{m}$ flux may contain a fair contribution by diffuse emission (from cloud heating by the interstellar radiation field or scattered stellar sources), the $60\mu\text{m}$ flux indicating warm dust comes from a compact source with a luminosity of $\sim 10^3 L_\odot$. *b)* As the source is only marginally resolved at 3mm, its outer cloud radius r_{out} has to be smaller than 4×10^{17} cm. *c)* The submm/mm fluxes lead to a total mass of several hundred M_\odot when adopting standard interstellar dust with an absorption coefficient at 1mm of $\sim 4 \times 10^{-3}$ cm² per gram of interstellar matter (Krügel 2003). However, as this emission is optically thin, a substantial part may not be directly linked to the star, but may come from the background within the IRDC. *d)* The visual extinction to the star depends on how the dust is distributed. It is about 400 mag if all the mass is in a sphere with constant density around the star, and even higher for a centrally condensed envelope, and less than 400 mag in case of an additional background cloud. For comparison, we derive a column density $A_V > 60$ mag from the peak of the ammonia emission in a $40''$ beam. This column density is probably two or three times larger, depending on the compactness of the source. We then assumed conversion factors $[\text{NH}_3]/[\text{H}_2] = 10^{-8}$ and $N_{\text{H}} = 2 \times 10^{21} A_V \text{ cm}^{-2}$ (Motte et al. 1998).

The solid line in Fig.6.5, which is compatible with the observations between $10\mu\text{m}$ and 3mm, comes from a spherical radiative transfer model (see Appendix A) with a central star of $L = 1200 L_\odot$ and 15000 K surface temperature that is surrounded by a envelope whose inner and outer radii are 10^{15} and 3.5×10^{17} cm, respectively. The exact number for T_{eff} is irrelevant, because the stellar radiation gets immediately absorbed. The dust density in the envelope is constant ($\rho_{\text{dust}} = 3 \times 10^{-20}$ g cm⁻³) implying an optical extinction $A_V \simeq 400$ mag. It may, at most, be two times less, otherwise the model spectrum would not comply with the $21\mu\text{m}$ upper limit. If it is less than 400 mag, one has to invoke the above mentioned background cloud to explain the sub-mm fluxes. These model results are also consistent with our fits to the ammonia lines described in §6.3.4

It is important to note that the model spectrum for the FIR does not rise again at shorter wavelengths and cannot account for the $8.2\mu\text{m}$ MSX and the Spitzer fluxes. Here an independent source is required. We propose that besides the star, there is a second blackbody emitter close to it. Its temperature is approximately $T = 550$ K, its total luminosity $150 L_\odot$, and it suffers 150 mag of visual extinction. This is below the minimum estimate for A_V of the envelope, but the latter may, of course, be patchy. It is natural

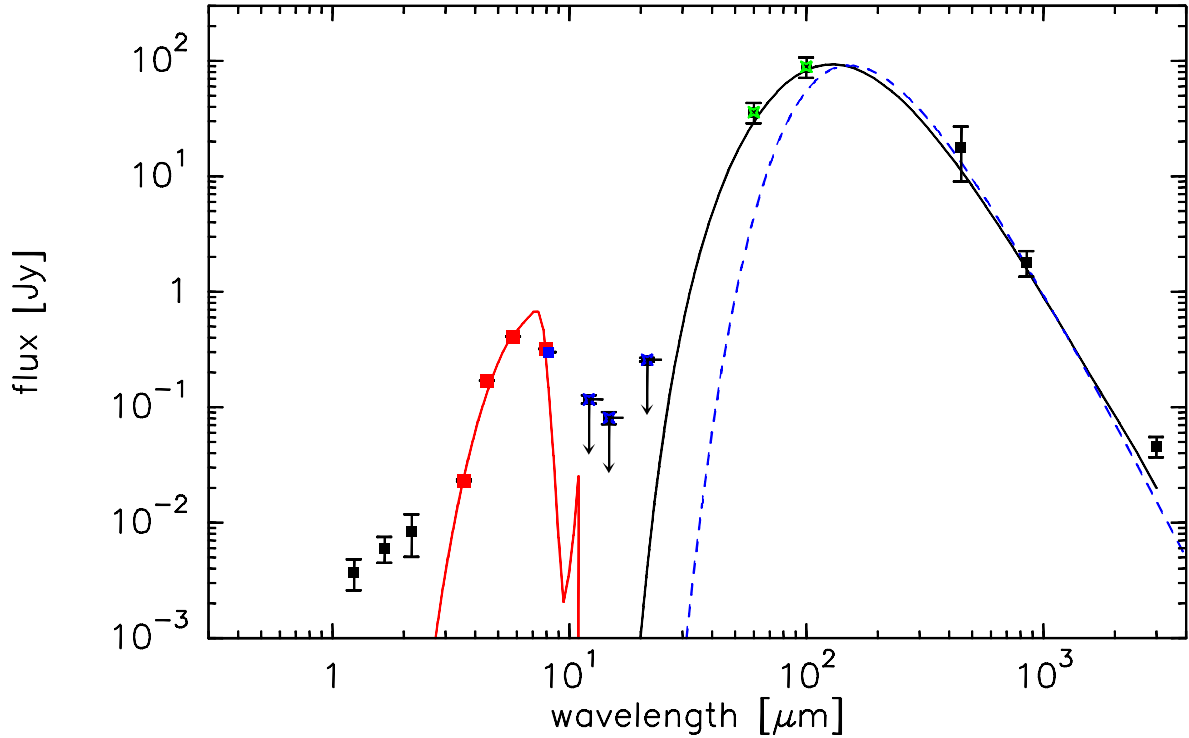


Figure 6.5: The Spectral Energy Distribution of G11.11-0.12 P1. Squares with errorbars indicate observations, where two almost coincide at 8 and $8.2\mu\text{m}$. The upper limits from MSX corresponding to bands C ($12.13\mu\text{m}$), D ($14.65\mu\text{m}$), and E ($21.3\mu\text{m}$) are shown. The solid curve represents the semi-spherical model described in the text. The solid line at FIR wavelengths corresponds to the SED of a central star of $L = 1200 L_{\odot}$ and to the 15000 K surface temperature that is surrounded by an envelope. Possible second blackbody emitter is shown as solid curve at shorter wavelengths. The dashed curve represents a grey body fit of 19 K . The NIR fluxes is explained by scattering (see §6.4.3).

to associate the second blackbody with an accretion disk of about 12 AU radius (outer). Considering the paucity of the data, more refined calculations seem, at present, unwarranted.

The dashed line that fits the long wavelength data in Fig.6.5 is a modified Planck curve of the form $\nu^2 B_{\nu}(T)$ with $T = 19\text{ K}$, possibly the emission of the background cloud with a total mass of $350 M_{\odot}$.

2MASS Sources

As shown in Fig.6.2, the CH_3OH peak is offset from the 2MASS source by $\sim 2''$. It is highly unlikely that the ATCA observations have errors on the order of $2''$ (cf §3.1). Though the rms uncertainty in the

case of 2MASS data is on the order of $0.4''$, we cannot completely rule out that the embedded object triggering maser emission is not associated with the 2MASS source. Because of the high column density towards the centre of the core, it could be that we are seeing light from the embedded object scattered out from the edges of the NIR core. We now discuss such a situation in detail.

The 2MASS J and H bands reveal 3 faint point sources detached from the sub-mm peak, while at K, where the resolution is inferior, there is only one single source. These 2MASS points lie far above any possible fits to a spherical cloud model. We first investigated whether they can come from an unrelated foreground star of lower bolometric luminosity but suffering less obscuration. Analysing the observed JHK fluxes in a colour-colour diagram, we found that they cannot be explained by reddening, so we discarded the possibility of a foreground star.

Instead, we propose that we are dealing with three knots of scattered light that escapes from the star into an optically thin cone above a hypothetical disk. We estimate the flux scattered by the cone at frequency ν from the formula

$$S_\nu = \frac{f_\nu L_\nu}{4\pi D^2}, \quad (6.1)$$

where D is the source distance and L_ν the stellar spectral luminosity, so $L = \int L_\nu d\nu$. If Ω_{cone} denotes the solid angle of the cone and τ_ν^{sca} its (small) scattering optical depth, then $f_\nu = \tau_\nu^{\text{sca}} \Omega_{\text{cone}} / 4\pi$. Because of the basically unknown geometry, our estimates are very rough. But assuming the star to be a blackbody, only about one percent of the light has to be scattered (the exact number depends on the stellar temperature).

As regards the wavelength dependence, scattering of pure stellar light would suggest decreasing fluxes at longer (K) wavelengths. However, foreground extinction and, more importantly, hot dust from an accretion disk ($T \sim 1000$ K) could easily explain the observed spectral shape at near IR wavelengths. In view of the geometrical requirements posed by the near IR fluxes, we propose a more realistic configuration. In such a model, the protostar is part of a massive (several $100 M_\odot$) clumpy cloud complex. Such a patchy dust distribution is shown in Fig.6.6. As seen in Fig.6.2, the emission at NIR is concentrated at only one edge of the BIMA 3mm emission. In the configuration envisaged in Fig.6.6, the stellar radiation is scattered by the dust clump above the disk at NIR wavelengths toward the observer. However, the stellar photons scattered from regions below the disk suffer severe extinction from the disk and fail to reach the observer at NIR wavelengths, resulting in a uni-polar nebula in NIR.

We therefore regard the JHK knots as further indirect evidence of a stellar disk.

6.5 Conclusion

Our main result is the detection of what is most likely a high-mass young stellar object within the IRDC G11.11. If the luminosity we derived is an overestimation that corresponds to an intermediate star, this would be the first reported case of CIIMM detection towards an IM mass-star-forming region. This evidence comes from the following observations and arguments:

- CH_3OH and H_2O masers appear during the earliest phases of massive star formation, so their detection in G11.11 is evidence of an embedded object.
- The systematic velocity gradient and the linear feature in the P-V diagram of the CH_3OH lines is a signature of a disk encompassing a protostar.
- The higher excited NH_3 (3,3) thermal line points towards a compact and hot central component. The thermal CH_3OH emission (Leurini et al. in preparation) suggests an outflow, in agreement with the claim by Johnstone et al. (2003), based on H_2CO observations. However, Johnstone et al. (2003) do not find any evidence of high-mass star formation.

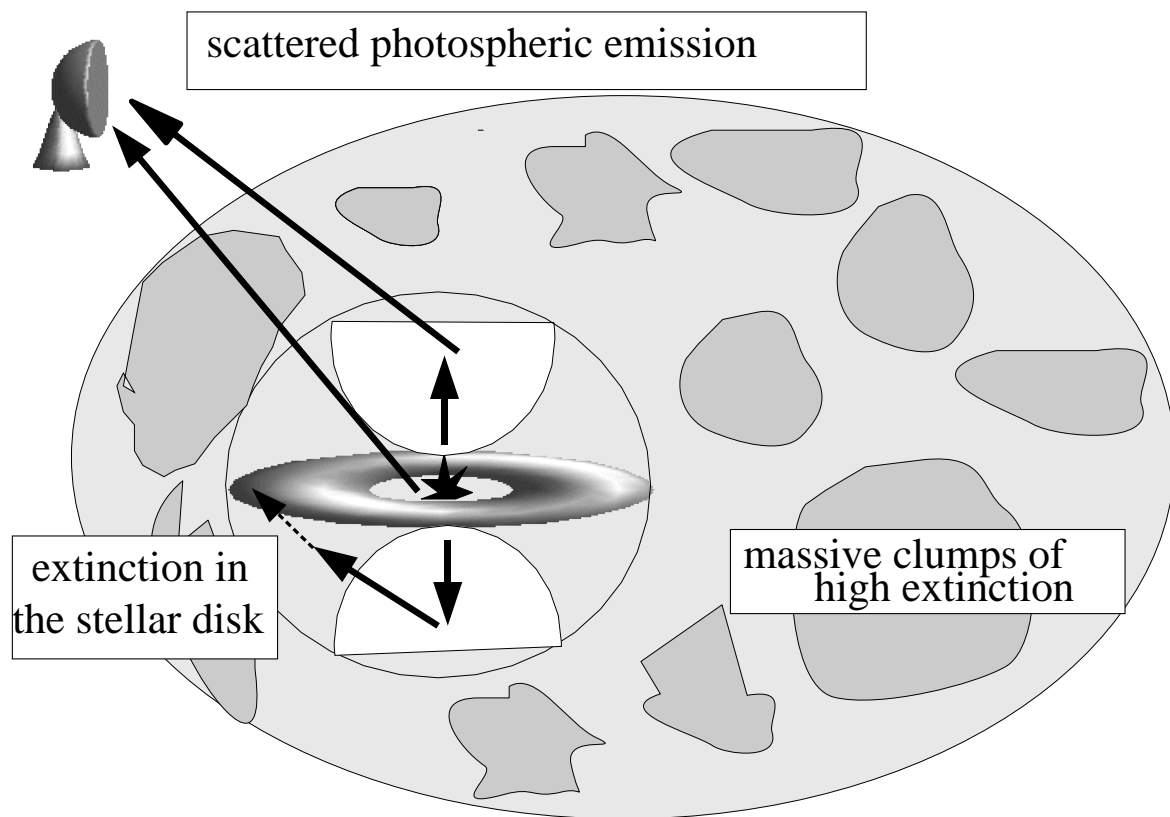


Figure 6.6: Illustration of an intuitive model of the source geometry needed to explain the NIR emission. The protostar is part of a massive (several $100 M_{\odot}$) clumpy cloud complex. The optically thin outflow cone scatters the stellar light at NIR wavelengths toward the observer. The stellar photons scattered from the cone below the disk is extinguished by the optically thick disk; consequently, we observe a uni-polar nebula at NIR.

- The strong FIR fluxes ($\geq 60 \text{ Jy}$) derived from analysing the high resolution IRAS data imply a powerful central source ($> 1000 L_{\odot}$).
- The radiative transfer additionally requires blackbody emission of about 550 K from a separate, less embedded source, probably from a disk, in order to reproduce the Spitzer data between 3.6 and $8.0 \mu\text{m}$. A non-spherical geometry is also indicated by the 2MASS NIR fluxes, which can only be explained by scattering and not through reddening.
- The high-extinction estimates also suggest an extremely young object, probably the Class 0 equivalent of a high-mass protostar.

Chapter 7

Properties of Dense Cores in IR-Dark Clouds at High Angular Resolution

We report on the first high angular resolution observations towards Infrared dark clouds (IRDCs). The VLA mosaics of four Infrared dark clouds observed in NH_3 (1,1) and (2,2) is presented. The mosaics were created using the CLEAN algorithm. To obtain information on large scales, we combined the interferometer image with single dish data. The combined image were created using Maximum Entropy Method. We also present NH_3 (3,3) observations with the VLA. The cloud morphology in NH_3 bears remarkable similarity to that observed in extinction seen with Spitzer and N_2H^+ emission observed with the Berkeley-Illinois-Maryland-Association interferometer (BIMA). At high angular resolution, the filaments appear to fragment into dense cores. The clumps have significant velocity gradients. The mass estimates from our BIMA 3 mm continuum observations as well as from virial equilibrium calculations reveal that the cores are massive and stable entities. The observed line widths are much higher than the thermal line width. The warm material traced by NH_3 (3,3) is confined to only the densest core while the secondary cores are pre-dominantly cold. On the basis of this data, we can confirm that there is a clear bifurcation in the initial conditions of a high and low mass pre-stellar core.

7.1 Introduction

All of the studies on IRDCs have been done at low resolution (Carey et al. 1998, Carey et al. 2000, Ormel et al. 2005, Pillai et al. 2006b etc), Pillai et al. 2006a). Since the kinematic distance estimates to IRDCs studied upto now reveal that typical distances to IRDCs are several kpc, high resolution is a necessary to constrain their properties without ambiguities.

The present study is a follow up of our single dish observations in NH_3 (1,1) and (2,2) transitions for four IRDCs with the Very Large Array. Additionally, N_2H^+ and 3 mm dust continuum images of the sources have been obtained with the BIMA interferometer. We also present high resolution NH_3 (3,3) and maser (H_2O and CH_3OH) data obtained with the VLA and ATCA. NH_3 is the best temperature probe to search for cold cores in IRDCs (Walmsley & Ungerechts 1983). N_2H^+ is also known to trace well cold and dense molecular gas (Tafalla et al. 2002). The masers and the higher excited NH_3 (3,3) line are ideal as probes of warmer, more evolved cores in IRDCs. Therefore, our aim is to identify candidate sources that are currently forming stars, are still starless and constrain the evolutionary properties at these earlier stages.

7.2 Observations

7.2.1 VLA Observations

The NH_3 (1,1), (2,2) and (3,3) observations were carried out with the Very Large Array (VLA) of the National Radio Astronomy Observatory on two different periods October 22, 23, 27, 28 and November 4, 1999 and August 2004. For the 1999 period, the ammonia (J, K) = (1, 1) and (2, 2) inversion transitions were observed simultaneously towards G11.11, G19.30, G28.34 and G33.71 with rest frequencies of 23.694495 GHz and 23.722633 GHz, respectively. In 2004, the ammonia (J, K) = (2, 2) and (3, 3) inversion transitions were observed simultaneously, with rest frequencies of 23.722633 GHz and 23.870129 GHz respectively, in the same sources except G19.30. The pointing centers for the four sources, observed with the VLA in its compact D configuration are listed in Table 7.1. The primary beam width of an antenna is approximately $2'$ (FWHM). The total on-source integration time was approximately 30 minutes per field. In combination, the total field coverage was approximately 4 in right ascension and 8 in declination for most of the region. NH_3 (1,1) and (2,2) lines were observed by using the dual-IF correlator mode 2AD, with a bandwidth of 3.125 MHz. Therefore, the main quadrupole hyperfine component and the inner pair of satellite hyperfine components for each transition were included. The resulting spectral resolution was 0.3 km s^{-1} for 127 channels.

The data was retrieved in the uncompressed format, therefore resulting in no loss of information on the weights attributed to each antenna. The data was loaded in AIPS with the task FILLM, which applies by default the opacity and gain curve corrections. The options DOWEIGHT = 1 to calculate UV-weights using the nominal sensitivity on each baseline, IF, and polarisation and DOCAL = 2 to apply the weights was used. The parameter CPARM was set to CPARM(8) = 0.05 to create a calibration table (CL table) that can be interpolated over very short intervals. The absolute flux calibrator was 3C 286, with a calculated flux density of 2.44 Jy at 1.3 cm. Source pointings were interspersed with 5 minute integrations on the nearest phase calibrators. A phase closure solution was applied based on observations of the phase calibrators 1733-130, 1751+096, 1743-038 which were observed for every source at intervals of less than 30 minutes. The bandpass calibrator used for the 1999 observations was 3C 279.

7.2.2 Short spacing : Effelsberg 100m observations

To study the large scale structure of the filaments, we merge the VLA data with the data obtained from Effelsberg 100m telescope ¹. We mapped the IRDCs with the Effelsberg 100m telescope of the Max-Planck-Institut für Radioastronomie in October 1999. The frontend was the facility 1.3 cm maser receiver tuned to a frequency of 23.7 GHz centered between the NH_3 (1,1) and (2,2) transitions. Our spectrometer was a 8192 channel auto-correlator which we used with 2 subunits of 20 MHz bandwidth each. The resulting spectral resolution was $\approx 0.2 \text{ km s}^{-1}$ after smoothing the data to increase the signal-to-noise ratio. The beam width at the frequencies of the NH_3 lines is $40''$ (FWHM). The observations were made in the frequency switching mode with a frequency throw of 7.5 MHz. The maps toward all sources covered the extinction seen in the MSX images and were made with full-beam width spacing ($40''$). Alternate scans were interspaced at half the full-beam width resulting in $\approx 20 \times \sqrt{2}$ spacing. Pointing was checked at roughly hourly intervals by means of continuum drift scans on nearby pointing sources. The details of the observation are given in Chapter 2.

7.2.3 BIMA Observations

The observations were conducted with the Berkeley-Illinois-Maryland-Association interferometer (BIMA) in its B, C and D array configurations at 3 mm, sampling spatial structures from 3 to 60 seconds of arc. Five sources with distances from 1 to 7 kpc were observed. In this paper, we report observations toward

¹Based on observations with the 100-m telescope of the MPIfR (Max-Planck-Institut für Radioastronomie) at Effelsberg

four sources for which we obtained complementary VLA data. We obtained simultaneously continuum and spectral line images of N_2H^+ (1–0) at 93 GHz. C^{34}S was observed in the other sideband and detected toward all sources. Mosaics with 2 – 7 pointing centers were used to cover most of the infrared dark clouds.

7.3 Data Reduction

The data were calibrated, Fourier transformed and deconvolved using the MIRIAD package. The synthesized beam used to restore the final image and the rms noise in the map is given in Table 7.2. We used the non-linear deconvolution algorithms CLEAN and MEM (maximum entropy method) for image restoration.

While MEM works well on high S/N data with reasonable constraints of the large scale flux, CLEAN is more appropriate to recover, even with low S/N, the small scale information of data without the short spacing information. Hence we used for our integrated intensity images the MEM algorithm and for the data cube restoration, the CLEAN method. The VLA integrated images were deconvolved together with the corresponding Effelsberg observations using the miriad task MOSMEM. No short spacing information were available for the BIMA data but given the high S/N of the data and the fact that the BIMA antennas in the D array have minimal baselines down to 6.5m, we are confident that all flux up to spatial scales of 1 arcmin is recovered, again using MOSMEM. An illustration of the joint deconvolution of VLA and 100m data is shown in Fig.7.1: Note that while the large scale details are filtered out by the Interferometer (negative bowls in the image), the combined image restores the large scale information in addition to resolving structures at the smaller scales. The joint deconvolution image reproduces the single dish emission when smoothed to the resolution of the single dish beam. This gives us confidence in the appropriateness of the method we use. However, recollect that our single dish observations were not Nyquist sampled but with $\approx 20 \times \sqrt{2}$ spacing and this is reflected in the small differences between the two images.

See Wiseman & Ho (1998) for a detailed discussion on the challenges of mapping large-scale elongated emission structures and the description of the two widely used methods of mosaicking.

The single dish spectra obtained from Effelsberg 100m telescope were reduced using the CLASS package (Forveille, Guilloteau, & Lucas 1989). For a given source, the spectra were averaged and a polynomial baseline of order 3 – 5 subtracted.

7.4 Results, Interpretation and Discussion

7.4.1 From Parsec to Sub-parsec Scale

In Fig. 7.2 and 7.3, we show the results of the interferometer mosaics towards the four sources in N_2H^+ and NH_3 with the MEM method. The striking feature in all the maps is the remarkable correlation of the dust extinction and line emission. Our high resolution maps confirm the predictions of the chemical models (Bergin & Langer 1997) that, unlike most other molecules, NH_3 and N_2H^+ do not deplete from the gas phase for the densities observed in IRDCs (10^6 cm^{-3}).

The VLA mosaics reveal that the molecular emission is distributed into small cores, which remained unresolved with a full width half maximum beam of $40''$ (Pillai et al. 2006a). IRDC G11 and G28 have a streamer-like morphology even at the high resolution while IRDC G19 and G33 have a clumpy structure.

Does the correlation between dust and gas continue into the densest part of the core? In order to analyse this, we modelled the mid-infrared(MIR) extinction (see also Chapter 4). The observed absorption in MIR can be modelled as the combination of the foreground intensity and the dust extinguished background

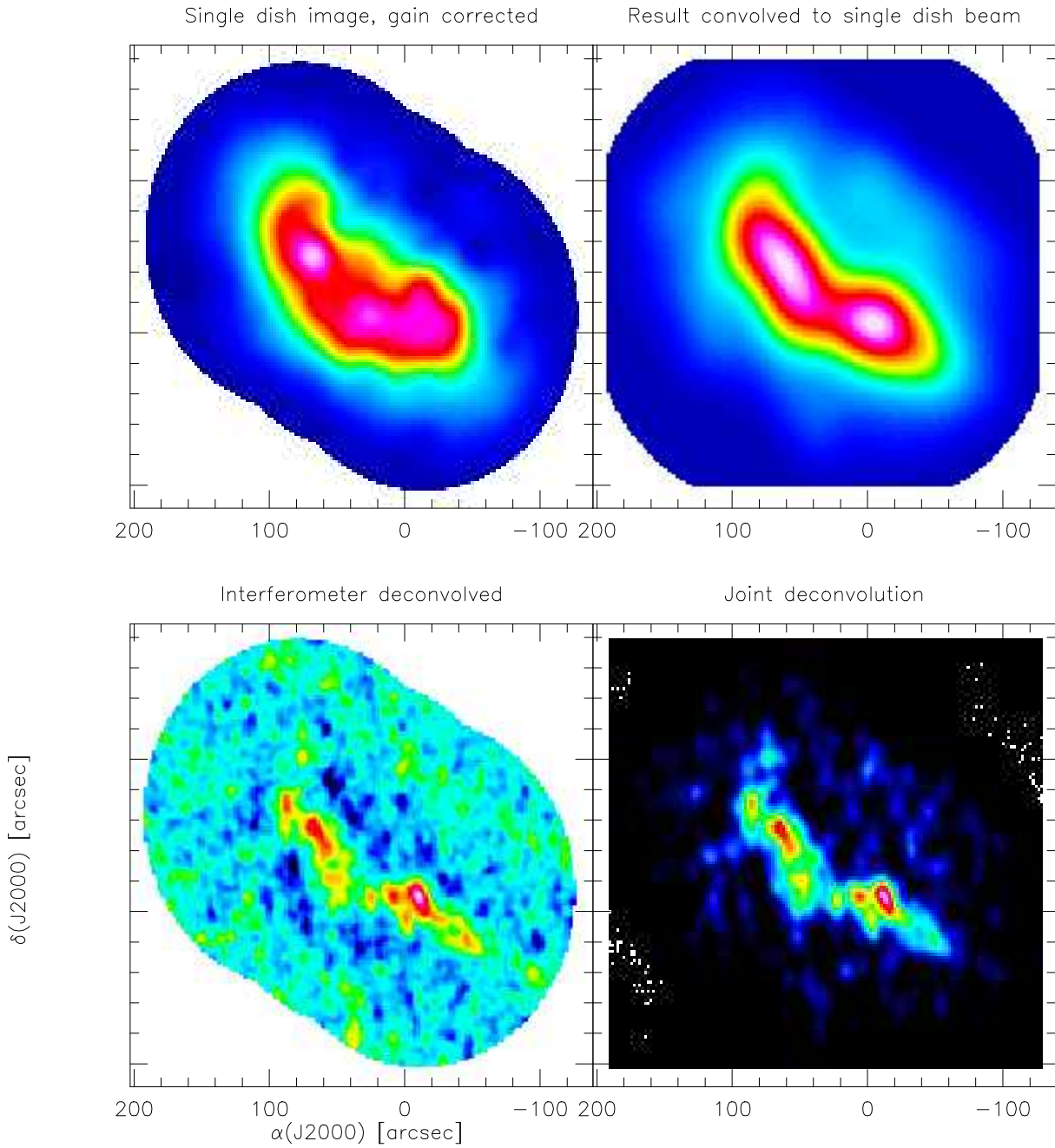


Figure 7.1: *Top left panel:* The Effelsberg 100m NH_3 (1,1) integrated intensity image corrected for the antenna response of a VLA dish. *Bottom left panel:* The VLA NH_3 (1,1) integrated intensity image for the same cloud deconvolved using CLEAN algorithm. *Bottom right panel:* The result of the joint deconvolution of the Interferometer and single dish data *Top right panel:* The combined image smoothed to the resolution of the single dish beam.

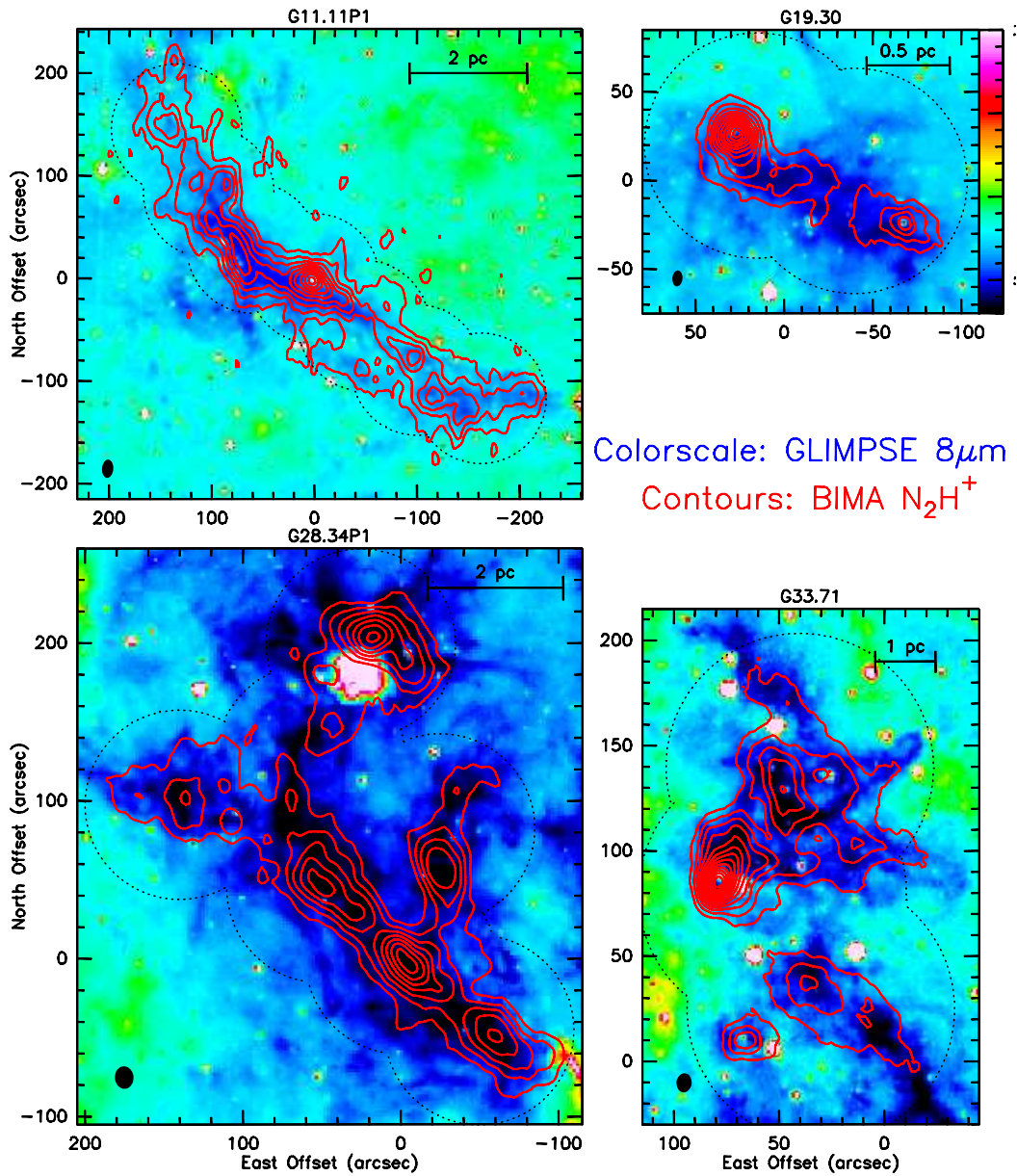


Figure 7.2: GLIMPSE image of IRDC G11.11-0.12 at 8 μ m (colorscale) with N₂H⁺ (1,1) integrated intensity as contours. The colorscale corresponds to intensity range shown by the wedge in the upper right corner. The contour levels are (-1σ , 1σ ...) in steps of 1σ . The rms noise level is given in Table 7.2. The approximate map coverage is shown as dashed arcs.

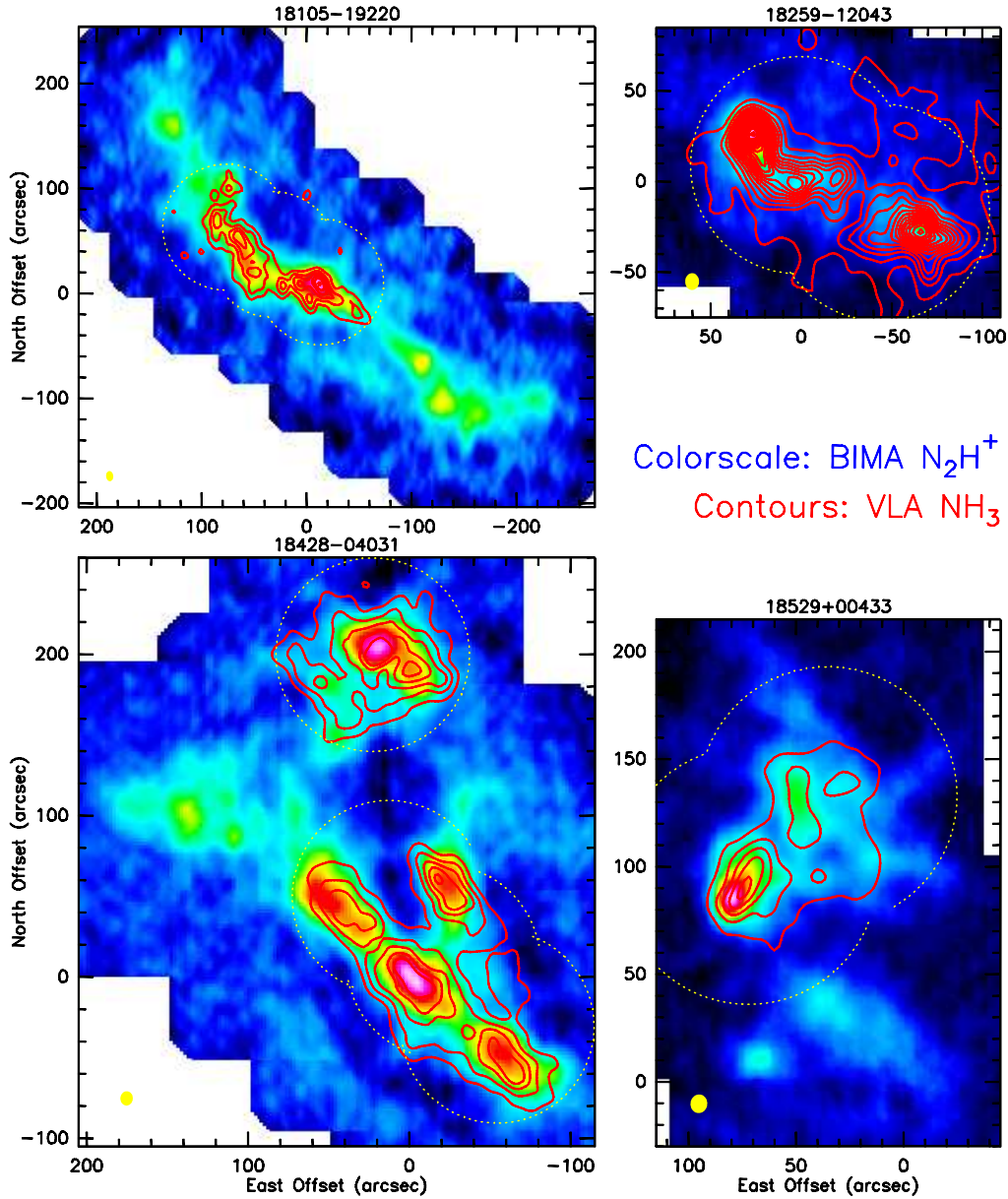


Figure 7.3: N_2H^+ image (color scale) with NH_3 (1,1) intensity over $\pm 3 \text{ km s}^{-1}$ of the LSR velocity as contours. The contour levels are $(-5\sigma, 5\sigma\dots)$ in steps of 5σ for all sources except G33.71-0.01. The contour levels for G33.71-0.01 are $(-5\sigma, 10\sigma\dots)$ in steps of 5σ . The rms noise level is given in Table 7.2. The approximate map coverage is shown as dashed arcs.

intensity (Bacmann et al. 2000) ,i.e., the line of sight absorption is

$$I_{\text{los}} = [\langle I_{\text{bg}} \rangle - \langle I_{\text{off}} \rangle] \cdot e^{-\tau_\lambda} + [\langle I_{\text{off}} \rangle]. \quad (7.1)$$

Here, I_{bg} is the observed background intensity, I_{off} is the foreground intensity, τ_λ is the dust opacity at the observed wavelength λ .

The result of such a modelling is shown in Fig.7.4. One can immediately conclude three points from the figure: *i*) There is marked anti-correlation between the MIR intensity and the NH_3 (1,1) integrated intensity; *ii*) The anti-correlation continues to the lowest MIR intensity and hence the highest optical depth; *iii*) The model fit reproduces well the observed anti-correlation upto the highest optical depth in IRDC G11.11-0.12 and G33.71-0.01. However there is a divergence from the anti-correlation toward the other two sources where the densest NH_3 core is not starless and is therefore associated with a MIR source.

However, the remarkable anti-correlation is difficult to interpret, since one would naively expect that the MIR absorption is proportional to the NH_3 optical depth, for the high optical depths (> 2) observed in IRDCs and not to the integrated intensity.

In the large scale CO $J = 1 \rightarrow 0$ surveys in our and external galaxies, CO integrated intensity is observed to measure the mass, although being optically thick (Rohlfs & Wilson 2004). The argument put forward for the support of such a measurement is that the total emission measured within the beam is due to a large number of clouds in virial equilibrium. These clouds in turn consists of clumps that have the same temperature, however are excited sub-thermally. Under such conditions, a large velocity gradient (LVG) analysis of CO excitation shows that CO intensity as well as the line width increases proportional to the H_2 density as $\sqrt{n(\text{H}_2)}$. The widely used "X" factor then defines the relation between the H_2 column density and CO integrated intensity. If this is applicable in the case of NH_3 then one may derive the "X" factor between the H_2 column density (traced by the MIR absorption) and NH_3 column density from Eq.7.1.

7.4.2 Core Properties

In order to identify the cores in NH_3 we created a clump finding algorithm that starts with a single Gaussian component fit to the brightest source position (see also Chapter 3). The image is then cleaned by subtracting the identified clump and searches for the next clump and so on, very similar to GAUSS-CLUMPS (Stutzki & Guesten 1990). 2 – 8 cores were identified from the NH_3 (1,1) integrated intensity maps for the different IRDCs, as listed in Table 7.4. We derive the properties of the core measured with NH_3 namely the core size, the (1,1) line width, gas temperatures, NH_3 column density, the virial mass and the gas mass. The (1,1) line width is measured from hyperfine fit to the line and the gas temperatures are derived following the standard formulation for temperature determination from NH_3 (1,1) and (2,2) line parameters (optical depth and line ratios). The method has been discussed in Chapter 2. The virial mass from the NH_3 (1,1) is estimated from the virial equilibrium calculations given in Chapter 2. The gas mass has been derived from the BIMA 3 mm continuum observations using the equations given in Chapter 3.

The primary cores are cold and massive, except for the brightest cores in each source where the temperatures are higher than average (> 20 K), however not necessarily the most massive core in the field. Thus the fragmentation of the cloud appears to create a hierarchy of structures, including the evolved core and the massive pre-protostellar clump which might undergo further fragmentation.

The 3 mm dust continuum observations with BIMA reveal several compact emission coincident with the extinction peak (see Fig.7.5). For IRDC G11.11-0.12, the core associated with NH_3 P1 position is the only region identified at 3 mm. Most of the extended emission is likely filtered out by the interferometer beam. In Fig.7.6, we compare the virial mass (M_{vir}) derived from NH_3 (1,1) line properties and the gas mass (M_{gas}) estimated from the 3 mm data. The mean ratio $M_{\text{vir}}/M_{\text{gas}}$ for the sample is 2.2, very

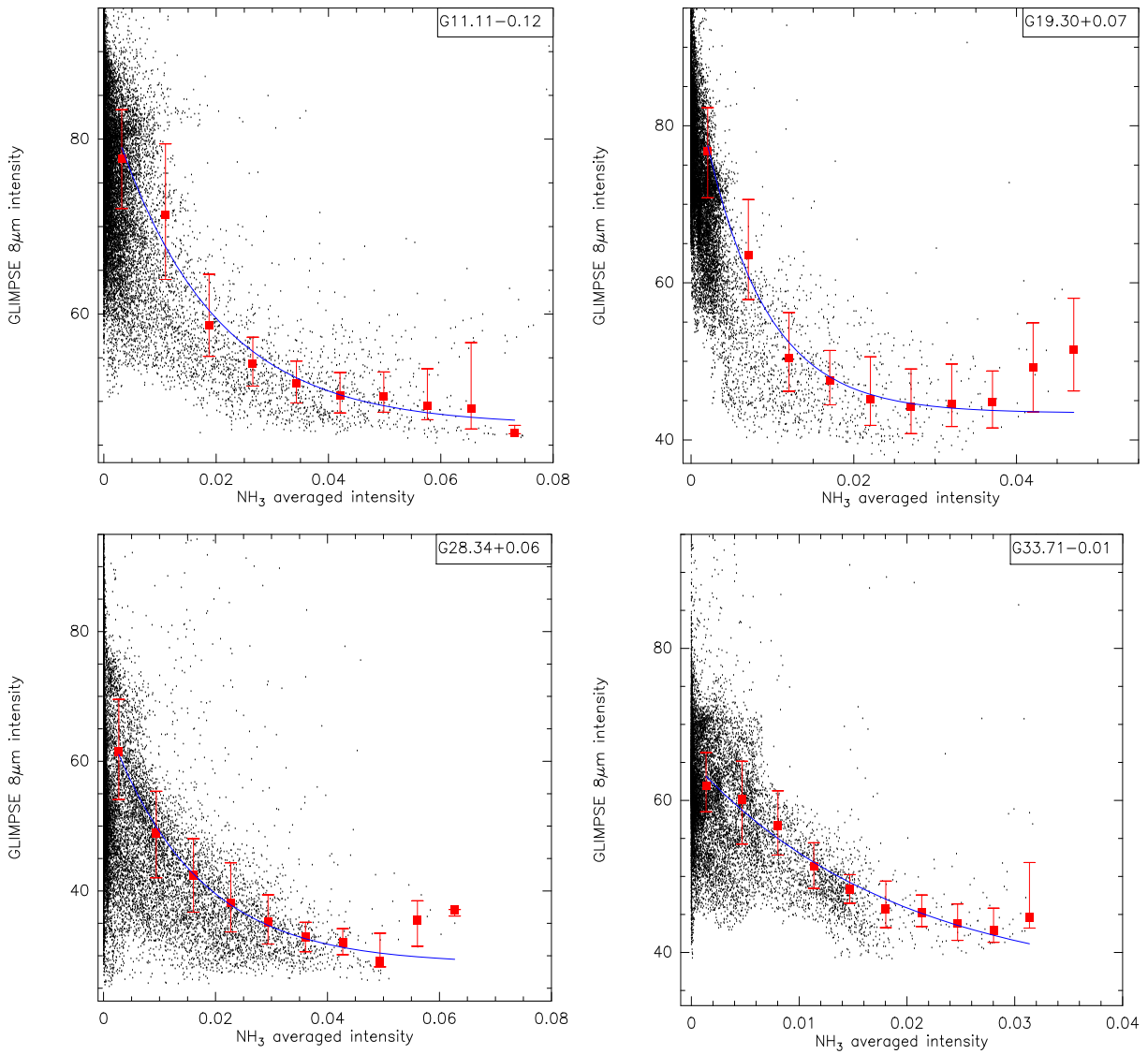


Figure 7.4: Correlation plot of MIR (GLIMPSE) absorption vs NH₃ (1,1) integrated intensity. The squares mark the median value for each bin with the bars corresponding to the range of 50% of the data points. The MIR intensity is modelled as given in Eq.7.1 as a function of the NH₃ (1,1) integrated intensity for each source.

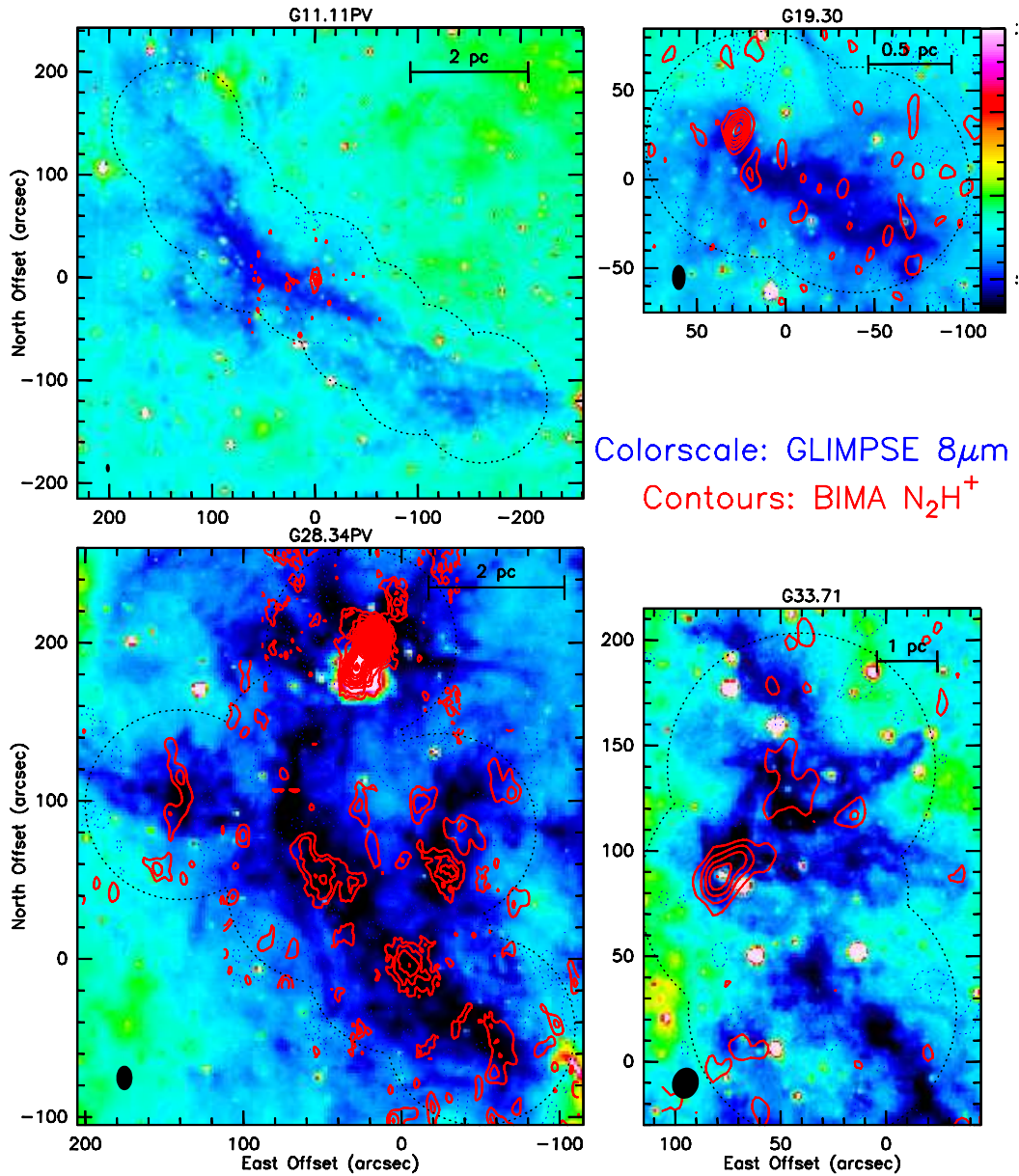


Figure 7.5: GLIMPSE image of IRDCs at $8\mu\text{m}$ (colorscale) with the BIMA 3 mm continuum emission as contours. The colorscale corresponds to intensity range shown by the wedge in the upper right corner. The contour levels are $(-5\sigma, 5\sigma\dots)$ in steps of 5σ . The approximate map coverage is shown as dashed arcs.

similar to the value we derived on the basis of the single dish observations (see Chapter 2). Given that the uncertainty in the dust opacity alone is a factor of 2, $\alpha \sim 1$, these cores appear to be stable.

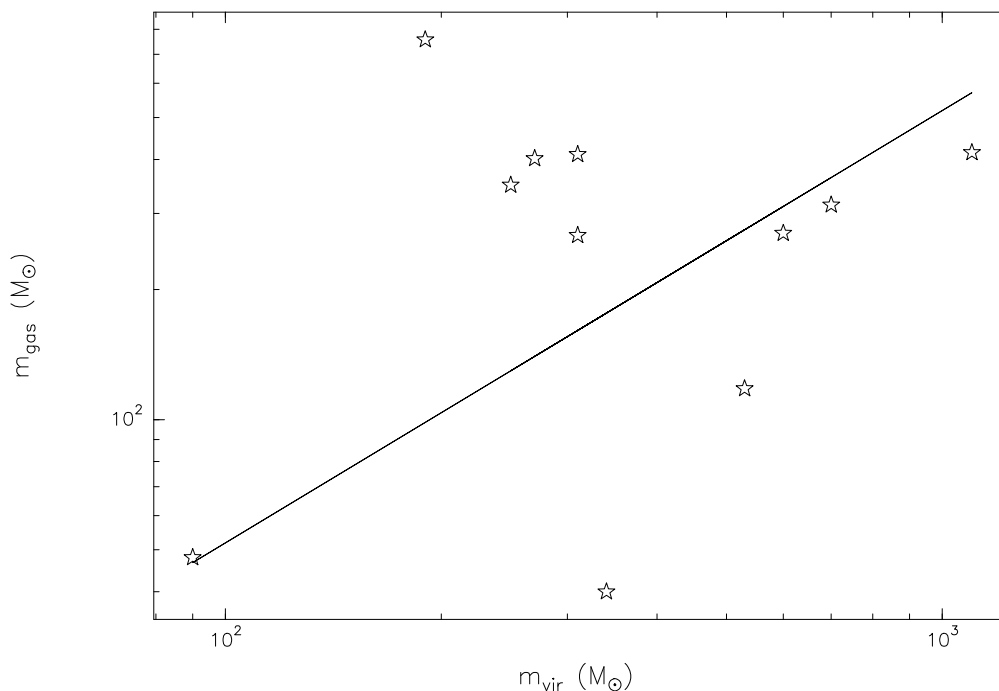


Figure 7.6: Comparison of the virial mass to the gas mass for all cores identified in NH_3 (1,1) with associated 3 mm emission

Line Widths

Within a beam of $40''$, Pillai et al. (2006a) find that the NH_3 line widths are much higher than the expected thermal linewidth ($\approx 0.2 \text{ km s}^{-1}$) for a typical dark cloud temperature of 20 K. While clumping might have played an important role in the apparent broadening of the lines, high line widths is a strong indication of intrinsically high line widths indicative of significant turbulence. With the high resolution of the presented VLA maps, the most clumps are resolved within the beam. However, our analysis is incomplete without an analysis of the cloud structure in the third dimension (velocity). The anti-correlation between the extinction and the integrated intensity continues to the densest core (see §7.4.1) is a hint for further substructure. This is also supported by the derived excitation temperatures much lower than the kinetic temperature. In no case do we find a decay of turbulence and evidence of coherent structures. The cores identified with the VLA are still turbulence dominated, although some cores show now with the higher angular resolution much smaller line width closer to the thermal line width (Fig.7.7). This figure also demonstrate the large spread in velocity between the individual cores within a IRDC.

7.4.3 Gas Kinematics

The velocity fields for all sources are shown in Fig.7.8. They have been obtained as the first moment intensity weighted velocity integral in the N_2H^+ emission. We chose to use the N_2H^+ map with a higher S/N ratio to compute the first moments. The dense cores within the dark clouds have distinct velocities and almost all of the cores show velocity gradients, some of which might be due to sub-cores, as seen in the higher angular resolution ammonia maps, with different velocities.

The northern part of G11.11-0.12 appears to exhibit a velocity gradient along the filament, in agreement with the single dish velocity field analysis in NH_3 (1,1) (Pillai et al. 2006a). There is a velocity

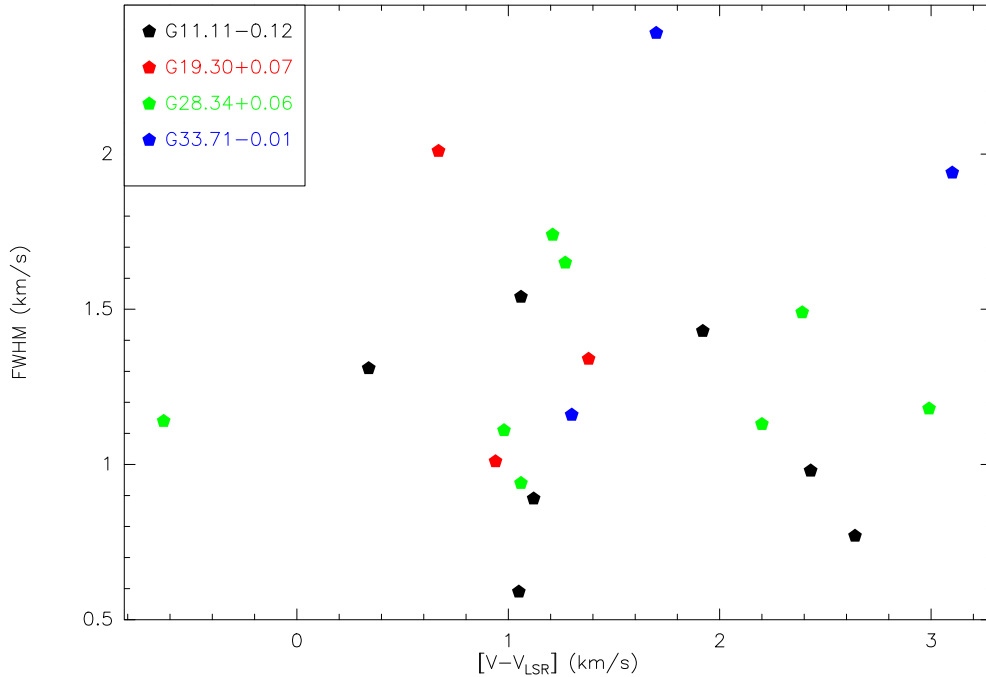


Figure 7.7: Correlation plot of linewidth vs velocity for the primary cores identified toward each IRDC (Table 7.4). The velocity refers to the shift from the LSR velocity.

separation in G28.34 of $\approx 2\text{ km s}^{-1}$ between the north core and the cores in the southern filament, as already inferred from 100m NH_3 (1,1) maps by Pillai et al. (2006a). Also, G33.71 shows very large velocity differences within the N_2H^+ emission. IRDC G19.30 is an exception where the two primary cores are separated by the inter-clump medium, with the same LSR velocity.

7.4.4 NH_3 (3,3) and Maser Emission

From our single dish search for evidence of active star formation in IRDCs, we observed NH_3 (3,3), (4,4) (simultaneous to NH_3 (1,1) and (2,2)) as well as the H_2O and CH_3OH maser transitions. We followed up these observations in several sources with the VLA and ATCA. The observational details of the maser survey have been discussed in the previous Chapter. We detected NH_3 (3,3) with the VLA toward the brightest NH_3 (1,1) cores in G11.11 and G28.34. In both cases, the hot NH_3 (3,3) emission also correlates with either or both maser types. The P1 source in G11.11-0.12 has been studied in detail by Pillai et al. (2006b) (see Chapter 3). For the other three sources, the masers as well as the warm core detected in NH_3 have no association with any MIR source identified with GLIMPSE and appear to peak toward region of high extinction. This implies that we are observing dust cocoons around protostars at a very early stage of evolution. There is no evidence of an outflow traced by NH_3 (3,3) emission in G11.11P1 and G28.34P2.

7.4.5 Dense Cores in IRDCs and Orion

Orion being the prototypical and nearest high mass star forming region, we compare the gas properties derived from NH_3 toward dense cores in the Orion streamer (Cesaroni & Wilson 1994) with our results. The comparison is shown in Fig.7.10. Cesaroni & Wilson (1994) report the observations of the integral

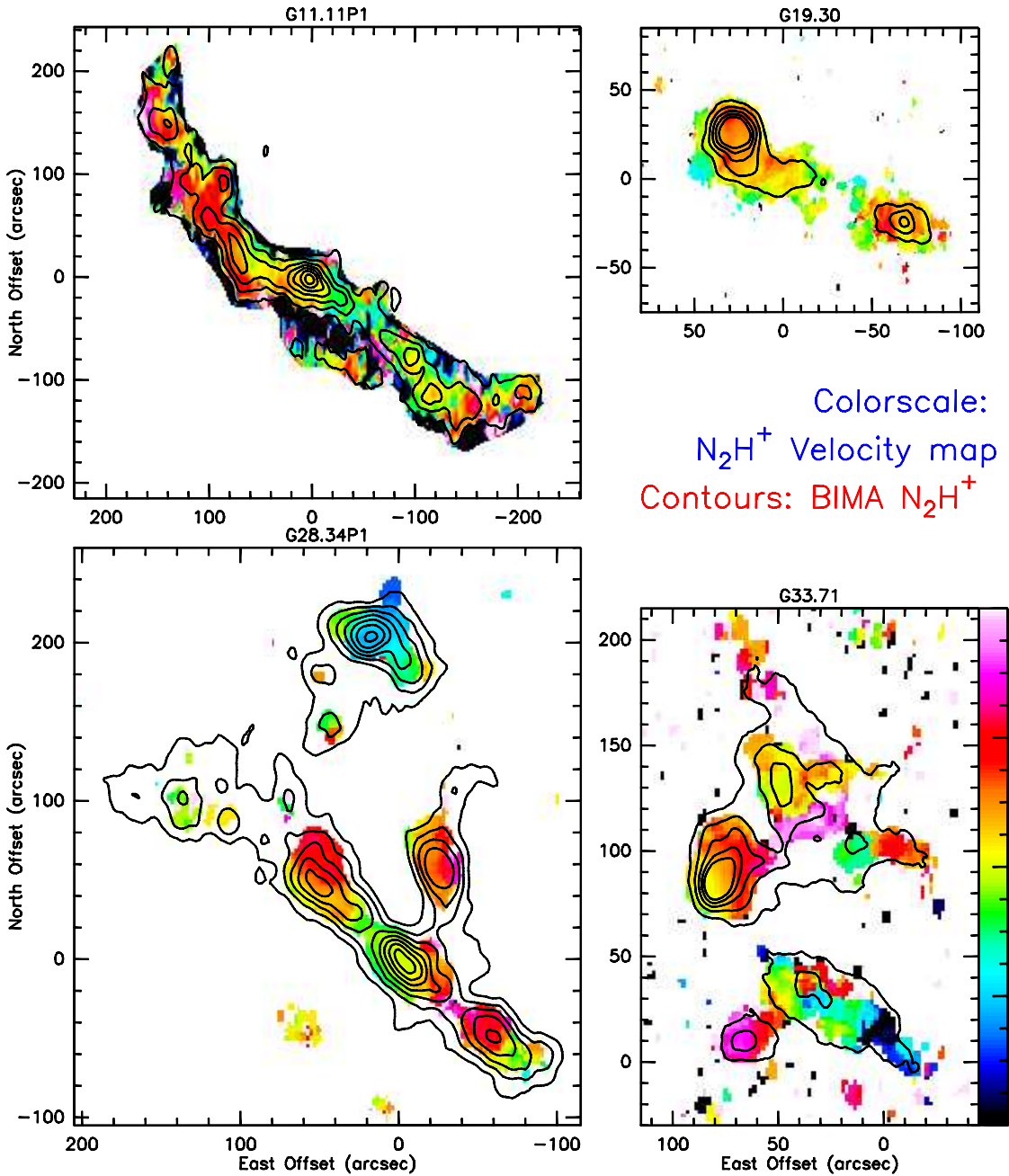


Figure 7.8: The N_2H^+ velocity fields (colorscale) with the integrated intensity as contours. The colorscale corresponds to intensity range shown by the wedge in the upper right corner, with the range of $\pm 4 \text{ km s}^{-1}$ of the LSR velocity (listed in Table 7.1) in all cases.

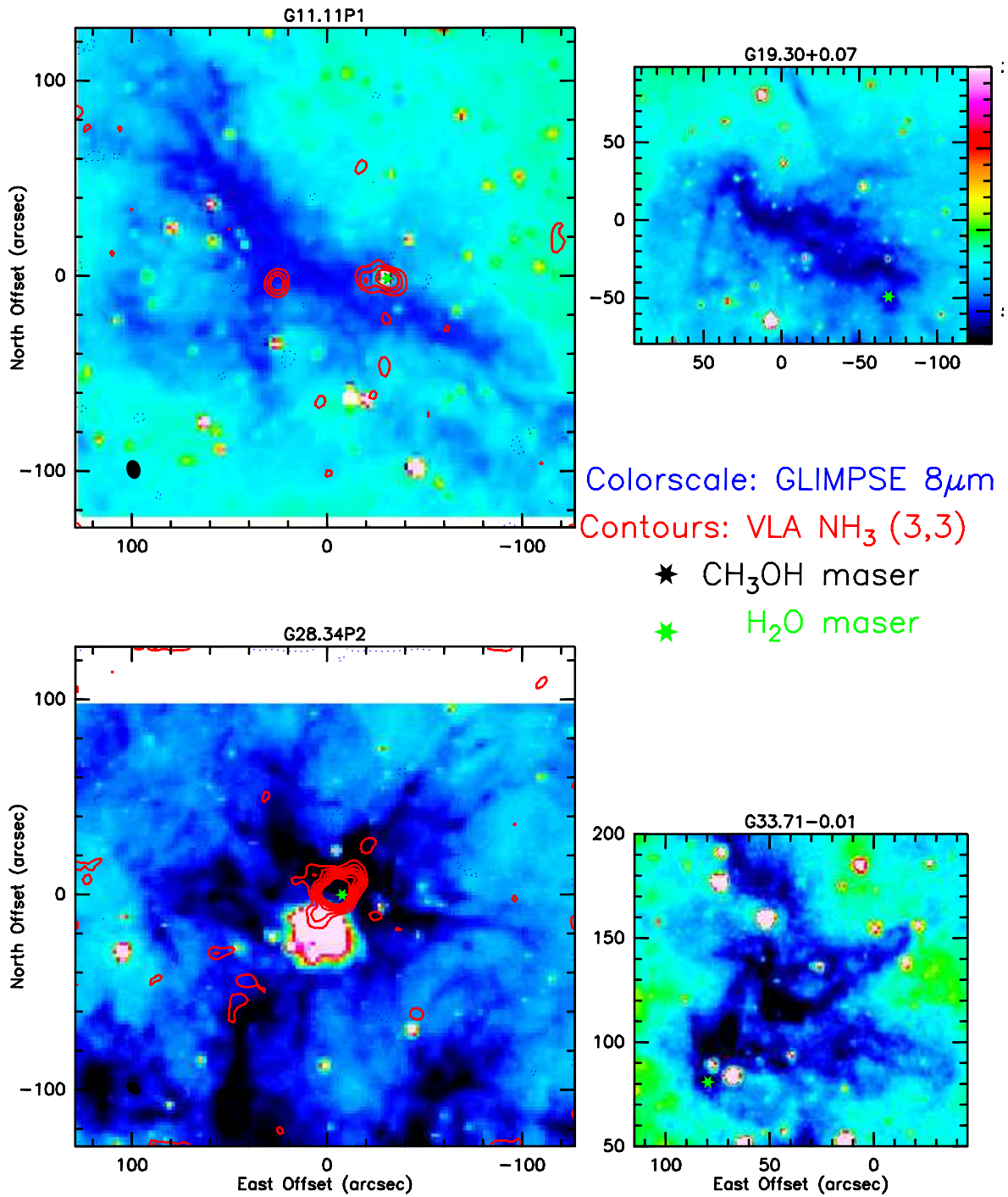


Figure 7.9: GLIMPSE image of IRDC G11.11-0.12 at 8 μ m (color scale) with NH₃ (3,3) integrated intensity as contours. The positions of methanol (black stars) and water masers (green stars) in the region discovered with the ATCA and VLA are also marked.

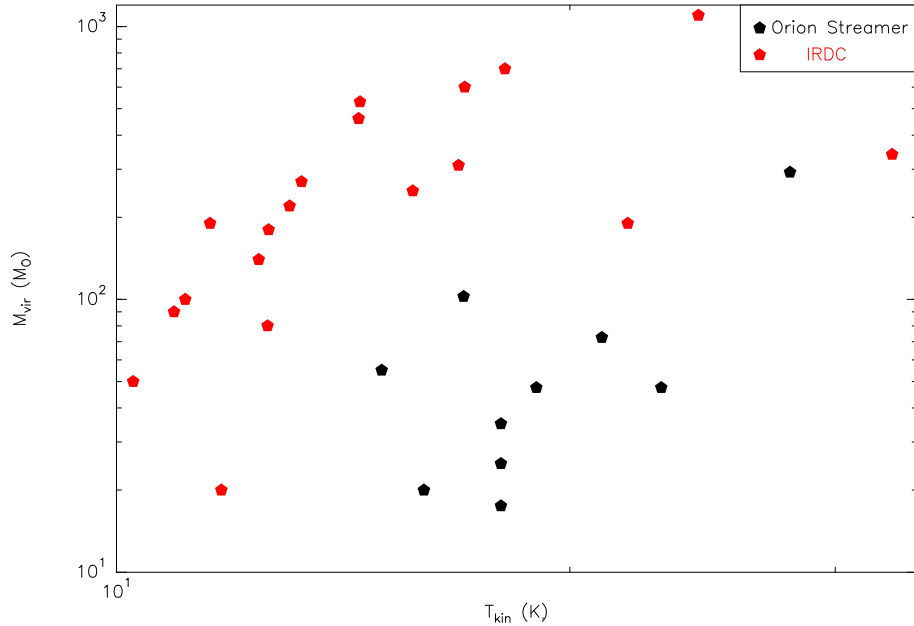


Figure 7.10: A comparison of the virial masses and gas temperatures derived from NH_3 for cores in the Orion Streamer (Cesaroni & Wilson 1994) and dense cores in IRDCs.

shaped gas streamer in Orion with the Effelsberg 100m telescope. Adopting a distance of ~ 450 pc to Orion and a typical distance of 3 kpc to an IRDC, the 100m beam resolves structures in Orion on a similar spatial scale to the VLA beam in a typical IRDC. Most of the dense cores in the Orion streamer are less massive and warmer compared to IRDCs. OMC2/3 are sites of ongoing intermediate mass star formation and OMC1 harbours the Orion-KL region, hence luminous sources for the heating of the cores are already widespread, which is not (yet) the case for the IRDCs. Their on average higher masses are another support for the claim that IRDCs will form high mass stars.

What might one expect at still higher angular resolution. Wiseman & Ho (1998) have discussed in detail the properties of cores identified in OMC-1 with VLA. Unlike the sources in our sample, there is a clear evidence of heating, particularly around the central Orion-KL core. The average line widths of these cores (1.2 km s^{-1}) is still smaller than the observed line widths in our cores. Consequently, the virial mass derived are smaller for cores in OMC-1 ($< 15 M_\odot$).

7.5 Conclusions

The main results of the observations presented here is given in terms of the core properties inferred from NH_3 (1,1) and (2,2) observations together with 3 mm continuum (see Table 7.4).

The remarkable correlation of the molecular emission with the dust absorption on size scales of $\sim 10^{17}$ cm. This is in agreement with the predictions of chemical models that unlike most molecules NH_3 and N_2H^+ do not freeze out easily onto the grains at high densities. NH_3 is a very good probe of the temperature of cold clouds and we find that most of the cores in the dark cloud are cold (< 20 K). In addition, our high resolution data allows us to conclude that these cores are inherently turbulent as evident by the observed line widths much higher than the thermal line width even with the higher angular resolution obtained with the VLA. The masses of the cores are very high, $> 100 M_\odot$ in most cases. In addition, we find that the active star formation has started in some of the brightest cores. However, lack

Table 7.1: Pointing Centers for the Observed Fields.

Source	R.A.(J2000)	Dec.(J2000)	V_{LSR} [km s ⁻¹]	D [kpc]
G11.11-0.12	18:10:31.49	-19:22:02.87	29.2	3.6
	18:10:34.69	-19:21:36.75		
	18:10:28.30	-19:22:29.00		
G19.30+0.07	18:25:56.84	-12:04:15.77	26.3	2.2
	18:25:53.76	-12:04:41.90		
G28.34+0.06	18:42:49.48	-04:03:04.33	78.4	4.8
	18:42:47.24	-04:03:44.36		
	18:42:51.73	-04:02:24.30		
	18:42:52.40	-03:59:54.00		
G33.71-0.01	18:52:56.14	+00:43:19.54	104.2	7.2
	18:52:58.61	+00:42:42.59		
NH ₃ (3,3)				
G11.11-0.12	18:10:30.47	-19:22:29.39	29.2	3.6
G28.34+0.06	18:42:52.40	-03:59:54.00	78.4	4.8

Notes: Δ (T_{rot}) is the difference in the mean temperature of the core and the envelope. $p(\text{null})$ is the probability that the null hypothesis of the difference between the 2 groups being Δ (T_{rot}) or greater is a chance event. $r(T_{\text{int}})$ is the Pearson's correlation coefficient that indicates the level of correlation between the 2 quantities and 'p' stands for the null hypothesis probability for the same.

of MIR emission indicated that the embedded protostars are very young. With our high resolution data, for the first time we can infer that low temperatures, high masses and significant turbulence signposts the early stages of high mass star formation.

Table 7.2: The Effective Beam Parameters for the Interferometer Observations.

Source	Instrument	Frequency(Type)	$\theta_{\text{maj}} \times \theta_{\text{min}}$	pa	rms
	GHz	arcsec	degrees	mJy/beam	
G11.11-0.12	BIMA	93 [N ₂ H ⁺ (1 -0)]	17.9×10.9	-4.4	–
	VLA	23.6 [NH ₃ (1,1)]	9.6 × 6.8	4.4	3
		23.8 [NH ₃ (3,3)]	9.8×7.2	13	2.7
G19.30+0.07	VLA		9.3 × 7.7	-0.4	0.5
G28.34+0.06	VLA	23.6 [NH ₃ (1,1)]	8.9 × 7.7	-3.7	4
		23.8 [NH ₃ (3,3)]	8.0×5.7	53.5	3.0
G33.71-0.01	VLA		8.7 × 7.8	-7.9	0.5

Notes: Columns are the source name, Interferometer array used, the wavelength with the molecule in brackets for line observations, the major and minor axis of the effective beam, its position angle and the the rms noise in the final image. We discuss G35.20w, followed by G29.96e in each subsection below.

Table 7.3: NH₃ (1,1) and (2,2) Map Results: Peak Position.

Source	Transition	T_{MB} [km s ⁻¹]	V_{LSR} [K]	FWHM [km s ⁻¹]	τ_{main}
G11.11-0.12 NH ₃ P1	1-1	3.11 (0.61)	30.26 (0.05)	1.54 (0.14)	3.14 (0.6)
	2-2	1.77 (0.34)		1.34 (0.19)	
G19.30+0.07 NH ₃ P1	1-1	3.68 (0.75)	26.97 (0.07)	2.01 (0.19)	2.68 (0.68)
	2-2	3.68 (0.39)		1.6 (0.133)	
G28.34+0.06 NH ₃ P1	1-1	3.82 (1.13)	77.77 (0.02)	1.14 (0.07)	1.42 (0.33)
	2-2	2.67 (0.56)		1.96 (0.31)	
G33.71-0.01 NH ₃ P1	1-1	2.37 (0.37)	105.9 (0.07)	2.39 (0.16)	2.15 (0.49)
	2-2	2.01 (0.19)		3.17 (0.24)	

Notes: Columns are name, NH₃ (J,K) transition, LSR velocity, (1,1) main beam brightness temperature, full linewidth at half maximum, main group optical depth. The error estimates are given in brackets.

Table 7.4: Physical Properties of Observed IRDCs.

Source	Offsets [arcsecs]	Size [arcsecs]	FWHM [km s ⁻¹]	T_{EX} [K]	T_{ROT} [K]	$N(\text{NH}_3)$ [10 ¹⁴ cm ⁻²]	M_{vir} [M_{\odot}]
G11.11-0.12 NH ₃ P1	(-12 , 8)	0.42	1.54 (0.14)	5.77 (0.72)	15.68 (2.64)	20.2 (4.4)	310
G11.11-0.12 NH ₃ P2	(66 , 52)	0.75	1.43 (0.09)	5.40 (0.63)	12.61 (1.94)	28.4 (7.0)	480
G11.11-0.12 NH ₃ P3	(6 , 6)	0.38	0.89 (0.08)	5.52 (0.99)	11.11 (1.69)	29.2 (10.0)	100
G11.11-0.12 NH ₃ P4	(-50 , -20)	0.33	1.31 (-)	4.21 (1.04)	12.62 (5.16)	14.0 (9.6)	180
G11.11-0.12 NH ₃ P5	(52 , 6)	0.24	0.77 (-)	4.94 (1.02)	10.26 (3.11)	19.4 (11.7)	50
G11.11-0.12 NH ₃ P6	(90 , 58)	0.26	0.98 (-)	5.74 (2.68)	12.60 (4.54)	5.9 (4.1)	80
G11.11-0.12 NH ₃ P7	(24 , 8)	0.17	0.59 (0.08)	5.41 (1.10)	11.74 (3.20)	18.5 (8.8)	20
G19.30+0.07 NH ₃ P1	(24,18)	0.27	2.01 (0.19)	6.39 (1.14)	32.73 (29.75)	22.8 (8.7)	340
G19.30+0.07 NH ₃ P2	(-64,-36)	0.38	1.34 (0.05)	6.18 (0.4)	13.03 (1.26)	24.1 (3.2)	220
G19.30+0.07 NH ₃ P3	(18,-4)	0.29	1.01 (0.06)	6.70 (0.78)	10.92 (1.10)	38.4 (8.1)	90
G28.34+0.06 NH ₃ P1	(20 ,202)	0.47	1.14 (0.07)	6.18 (0.9)	21.85 (6.28)	6.3 (1.1)	190
G28.34+0.06 NH ₃ P2	(-2 ,190)	0.54	1.65 (0.07)	4.68 (0.37)	14.48 (1.96)	28.1 (5.1)	460
G28.34+0.06 NH ₃ P3	(-28 , 54)	0.86	1.49 (0.10)	5.26 (0.55)	17.03 (4.91)	23.7 (5.4)	600
G28.34+0.06 NH ₃ P4	(-6 , -6)	0.65	1.11 (0.08)	5.18 (0.61)	15.73 (2.77)	15.2 (3.4)	250
G28.34+0.06 NH ₃ P5	(-68 , -58)	0.56	1.74 (0.22)	4.09 (0.49)	14.51 (4.37)	15.7 (6.1)	530
G28.34+0.06 NH ₃ P6	(24 ,34)	0.51	0.94 (0.09)	4.32 (0.56)	12.43 (2.07)	18.3 (6.1)	140
G28.34+0.06 NH ₃ P7	(46 ,54)	0.67	1.13 (0.11)	4.63 (0.68)	13.27 (2.33)	16.4 (.3)	270
G28.34+0.06 NH ₃ P8	(-52 , -40)	0.44	1.18 (0.05)	5.20 (0.42)	11.54 (1.44)	30.9 (6.5)	190
G33.71-0.01 NH ₃ P1	(78 , 86)	0.63	2.39 (0.16)	5.42 (0.71)	24.34 (5.79)	17.4 (3.3)	1100
G33.71-0.01 NH ₃ P2	(48 , 136)	0.73	1.16 (0.14)	5.20 (1.16)	16.87 (3.38)	8.4 (3.0)	310
G33.71-0.01 NH ₃ P4	(72 , 100)	0.59	1.94 (0.10)	5.68 (0.5)	18.11 (3.17)	18.5 (2.7)	700

Notes: Columns are name, Offset Position from map center, size of the cores, excitation temperature, NH₃ rotational temperature, NH₃ column density and virial masses from NH₃ for the primary cores. The formal errors are given in brackets.

Chapter 8

Summary

As part of my PhD thesis, I conducted a comprehensive observational study of infrared dark clouds (IRDCs) under the supervision of Dr.F.Wyrowski and Prof.Dr.K.M.Menten. The main objective was to identify the physical and chemical properties of the massive cores embedded in IRDCs, the progenitors of high-mass stars. I used mm/cm single dish and interferometer observations and mid-infrared data from Space Telescopes (MSX/SPITZER) for the study. The project delivered several new and important results that significantly enhanced our understanding of the initial conditions of high mass star formation.

8.1 Introduction

IRDCs are cold, dense molecular clouds seen in silhouette against the bright diffuse mid-infrared (MIR) emission of the Galactic plane. They were discovered during mid-infrared imaging surveys with the Infrared Space Observatory (ISO) and the Mid-course Space Experiment (MSX). Recently, we have reviewed the observational studies on IRDCs. While low mass clouds have been relatively well studied, our picture of high-mass star formation remains unclear. IRDCs appear to be the long sought population of cold and dense aggregations with the potential of harbouring the earliest stages of massive star formation. Up to now there has been no systematic study on the temperature distribution, velocity fields, chemical and physical state toward this new cloud population. Therefore, we started a multiwavelength study of IRDCs in various molecular tracers and dust continuum.

8.2 Ammonia in Infrared Dark Clouds

The first phase of the project dealt with characterising the temperature structure of IRDCs with NH_3 (1,1) and (2,2) observations from the Effelsberg 100m telescope. Toward all of the sources in our sample previously submillimeter dust continuum emission and millimeter rotational lines of H_2CO had been studied. Our observations allow the most reliable determination of gas temperatures in IRDCs to date. We analyse temperature structures and velocity fields and gain information on chemical evolution. The gas emission is remarkably coextensive with the extinction seen at infrared wavelengths and with the submillimeter dust emission. Our results show that IRDCs are on average cold ($T < 20$ K) and have variations among the different cores. IRDC cores are in virial equilibrium, are massive ($M > 100 M_\odot$), highly turbulent ($1 - 3 \text{ km s}^{-1}$) and exhibit significant velocity structure (variations around $1 - 2 \text{ km s}^{-1}$ over the cloud). We find a trend in temperature from colder IRDCs with high ammonia column density to high mass protostellar objects and hot core/Ultracompact HII regions, believed to trace different stages of early high-mass star formation. The line widths of IRDCs are smaller than those observed in high mass protostellar objects and hot core/Ultracompact HII regions. On basis of this sample, and by comparison

of the ammonia gas properties (line widths, mass, and temperature) within a cloud and between different clouds, we infer that while active star formation is not yet pervasive in most IRDCs, local condensations might collapse in the future or have already begun forming stars including high-mass ones.

8.3 Deuteration and Depletion in High Mass Cold Cores

In order to identify the chemical signature of high mass pre-stellar/cluster cores, we studied the ammonia deuteration and CO depletion toward a new sample of massive pre/protocluster cores. In a program we call SCAMPS (the SCUBA Massive Pre/Protocluster core Survey), we searched for massive pre/protocluster cores by taking a complete wide-field (10×10 arcmin) census of cloud cores in ≈ 30 massive star-forming regions, harbouring UCHII regions and with evidence of secondary cores. Using the IRAM 30m telescope, we find that 65% of the observed sources have strong NH_2D emission and a high degree of deuteration ($\geq 1\%$). We show that high deuteration is a definitive signature of pre/protocluster (thus cold) cores and that there is a trend of significant decrease in deuteration with temperature. The enhancement in deuteration coincides with strong CO depletion onto dust grains. Based on simultaneously observed HCN and H^{13}CN lines, the galactocentric gradient of the $^{12}\text{C}/^{13}\text{C}$ ratio is revisited with no evidence for a trend between 1 and 6 pc from the Sun. In addition, we present interferometer observations of NH_3 and NH_2D using the Very Large Array (VLA), Berkeley-Illinois-Maryland Association Array (BIMA), and Plateau de Bure Interferometer (PdBI) array for two sources from the SCAMPS project. The spatial distribution of NH_2D is clearly different from NH_3 as well as thermal dust continuum. The appearance of a protostar, as evidenced by outflow activity, destroys the deuterium-bearing molecules. Deuteration thus appears to signposts the cold, earliest stages of evolution in high mass molecular clouds. The cores identified within the clouds are massive and virial equilibrium calculations show that these cores are self-gravitating. The non-thermal motions in these cold clouds are clearly supersonic. Furthermore, turbulence appears to be the byproduct of an outflow activity, it steadily decays down with distance from the embedded protostar. These findings prove that these high mass cold cores are the raw materials out of which high mass stars and star clusters form in the vicinity of Ultracompact HII regions.

8.4 Structure of High-Mass Cold IR-Dark Clouds

We then analysed the structure of infrared dark clouds as seen in the mid-infrared as extinction. The archival data was obtained from the Spitzer GLIMPSE survey. This data has been used to produce extinction maps toward five IRDCs. Based on the extinction maps, we show that IRDCs are not just isolated dense condensations. IRDCs are enveloped in lower density material and the masses we derive confirm the previous findings that IR dark clouds have high mass. A comparison with the available submm dust continuum observations for one high mass IRDC reveal that the clump/cluster of clumps with the highest extinction in this source is hardly detected with the bolometer array camera. MIR absorption appears to be an excellent tracer of the dust content. Furthermore, comparison of extinction cuts through IRDCs indicate that high mass IRDCs might have high density contrast between the core and the envelope. This might imply that initial stages of high mass dark clouds might be governed by highly compressive energetics, very likely shocks due to a Supernovae explosion or stellar winds from nearby high mass stars. We use a simple method of analysing the fractal nature of the cloud indirectly by studying the extinction count distribution. This method has been previously applied to molecular clouds. We show that it is equally robust in the case of the dust clouds seen in extinction. Subsequently, from the extinction probability density functions, we infer that self-similarity in IRDCs break down at scales of $0.2 - 0.5$ pc. This scale regime is very much consistent with the turbulent Jeans length and therefore, IRDCs might be exhibiting a transition from turbulent fractals to thermal coherent cores at the sub-parsec scales.

8.5 Tracing Active Star Formation in Infrared Dark Clouds

We performed a high resolution imaging survey of 6.7 GHz CH₃OH maser and 22.2 GHz H₂O maser in a sample of infrared dark cloud cores. The survey has been carried out with the Very Large Array and the Australian Telescope Compact Array, as follow up of observations made at lower resolution with the Effelsberg 100 m telescope. We detected masers of both type associated with the mm cores in IRDCs. The masers remain unresolved by the interferometer beam and show spread in the velocity structure. The maser detection is a clear evidence of active star formation already ongoing in Infrared dark clouds.

8.6 High mass star formation in an Infrared Dark Cloud.

We studied the nature of active star formation toward the brightest core of the IRDC G11.11-0.12. We detected moderate to high-mass star formation in an infrared dark cloud (G11.11-0.12) where we discovered class II methanol and water maser emissions at 6.7 GHz and 22.2 GHz, respectively. We also observed the object in ammonia inversion transitions. Strong emission from the (3,3) line indicates a hot (60 K) compact component associated with the maser emission. The line width of the hot component (4 km s⁻¹), as well as the methanol maser detection, are indicative of high mass star formation. To further constrain the physical parameters of the source, we derived the spectral energy distribution (SED) of the dust continuum by analysing data from the 2MASS survey, HIRAS, MSX, the Spitzer Space Telescope, and interferometric 3mm observations. The SED was modelled in a radiative transfer program: *a*) the stellar luminosity equals $\sim 1200 L_{\odot}$ corresponding to a ZAMS star of 8 M_⊙; *b*) the bulk of the envelope has a temperature of 19 K; *c*) the mass of the remnant protostellar cloud in an area 8×10^{17} cm or 15'' across amounts to 500 M_⊙, if assuming standard dust of the diffuse medium, and to about 60 M_⊙, should the grains be fluffy and have ice mantles; *d*) the corresponding visual extinction towards the star, A_V , is a few hundred magnitudes. The near IR data can be explained by scattering from tenuous material above a hypothetical disk. The class II methanol maser lines are spread out in velocity over 11 km/s. To explain the kinematics of the masing spots, we propose that they are located in a Kepler disk at a distance of about 250 AU. The dust temperatures there are around 150 K, high enough to evaporate methanol-containing ice mantles.

8.7 High Angular Resolution Observation Toward Infrared Dark Clouds

Finally, we followed up our single dish NH₃ observations with high angular resolution. There exists remarkable correlation of the molecular emission with the dust absorption on size scales of $\sim 10^{17}$ cm. This is in agreement with the predictions of chemical models that unlike most molecules NH₃ and N₂H⁺ do not freeze out easily onto the grains at high densities. NH₃ is a very good probe of the temperature of cold clouds and we find that most of the cores in the dark cloud are cold (< 20 K). In addition, our high resolution data allows us to conclude that these cores are inherently turbulent as evidenced by the observed line widths much higher than the thermal line width even with the higher angular resolution obtained with the VLA. The masses of the cores are very high, > 100 M_⊙ in most cases. In addition, we find that the active star formation has started in some of the brightest cores. However, lack of MIR emission indicated that the embedded protostars are very young. With our high resolution data, for the first time we can infer that low temperatures, high masses and significant turbulence signposts the early stages of high mass star formation.

To summarise, we can now infer that IRDCs comprise of a continuum from cores with all the expected characteristics for precluster cores which are gravitationally bound, cold, depleted and deuterated and turbulent to cores harboring clusters at very early stage which are slightly warmer and drive outflows.

Thus, this work has provided evidence that within IRDCs, the long sought progenitors of high mass stars can be found.

8.8 Outlook

8.8.1 Evolutionary sequence for Massive YSOs

As part of my thesis, I have shown that there is clear evidence of active high mass star formation (Pillai et al. 2006b) in IRDCs. Further, I have shown that the high mass dense starless cores in IRDCs are larger in size, more turbulent, and much more massive than a typical low mass star forming (LMSF) core. These observations suggests that IRDCs due to their youth are the best hunting grounds for the still relatively undisturbed earliest phases of massive star formation. Moreover, their large extend (typically several pc) and distribution through out the galactic plane (several 1000 sources) would mean that we can identify a huge number of embedded sources at different stages of evolution.

The earliest stages in the formation of a high mass star are expected to be highly extincted. At present and in the immediate future, Spitzer by virtue of its high resolution and sensitivity in the MIR-FIR is the only telescope that can reveal the true nature of the sources embedded in IRDCs. High resolution is essential to resolve the sources at several kpc distances while the sensitivity is crucial in detecting the youngest and hence most extincted sources.

The GLIMPSE legacy program surveyed the inner part of our galaxy and revealed several 1000 IRDCs at $3.6 - 8\mu\text{m}$. The data has already been made available to the public via the Spitzer archive. MIPS GAL is a 220 deg^2 survey of the inner Galactic plane, at 24 and $70\mu\text{m}$ with MIPS with a significant overlap in the sky coverage of GLIMPSE. The enhanced data from this survey is being released to the public starting from October 2005. Together these surveys allow an unprecedented view onto the properties of MYSOs and their parental gas and dust cocoons.

The pioneering work by André et al. (1993) in the LMSF regime has shown that there is a clear hierarchy in the evolution of a low mass YSO, (LYSOs) from Class 0 to Class III, mostly determined by the SEDs of the objects. André et al. (1993) also find that the envelope mass is proportional to the mechanical outflow luminosity and has a distinct turnover as the source evolves from Class 0 to Class I. Their results are consistent with the accretion model of star formation.

The crucial question is not so much how a massive star evolves but how they basically form. If we are able to converge to a classification scheme that is similar to that of LYSOs, then the answer is clear: high mass stars form similar to their low mass counterparts via accretion. Such a scheme must self-consistently explain the evolution of several components of a MYSO: the infrared source, the dust cocoon and the outflows. We would begin with obtaining the SED of MYSOs embedded in IRDCs from GLIMPSE and MIPS GAL. The luminosity of the embedded source would be undoubtedly constrained by the data from GLIMPSE and MIPS GAL.

Complementary to analysing the SEDs of MYSOs with Spitzer, we would propose ground based studies with the Interferometer arrays like SMA, PdBI and CARMA (in the coming year) of the objects. Furthermore, interferometer SiO and CO observations of the outflows of the sources would determine the outflow luminosity while searches for infall with observations of N_2H^+ , CS and HCO^+ will give us additional information about their accretion rates. Observing the submm lines of these molecules allows us to probe the higher density regime needed to analyse the dense inner envelopes of the MYSOs.

8.8.2 Very Compact Radio Emission from the Massive Protostar with VLA

One of the least understood property of a massive protostar is its association with clustered star formation (see Testi 1999). Addressing this question requires very high angular resolution (sub-arcsecond), not yet possible with Spitzer and SMA. However, the cm observations with the Very Large Array are readily

capable of reaching these resolutions. Very recently, van der Tak & Menten (2005) have shown that VLA observations provide an important diagnostic tools for high mass star formation; of continuum emission from dense ionised gas. van der Tak & Menten detect weak compact radio emission from three high mass protostars heavily embedded in molecular envelopes. They infer that in two sources, the emission is due to thermal bremsstrahlung from gravitationally bound HII regions. Their observations support a picture of high mass star formation by accretion onto the protostar for regions with luminosities less than $10^5 L_{\odot}$. van der Tak & Menten's interpretation is along the following lines: at small radii, the stellar Lyman continuum ionizes the accretion flow without halting it. The ionized region expands quasi-statically with accretion until its radius reaches a critical value (Keto 2002). Beyond the limit, the HII region rapidly expands, halting accretion.

In contrast, sources with luminosity $> 10^5 L_{\odot}$ appear to produce clusters of HII regions and un-collimated outflows. This is argued to be the result of mergers of protostars or pre-stellar cores (van der Tak & Menten 2005). However, the statistics are too weak to confirm this bifurcation. We want to build up a two dimensional evolutionary sequence (ie in time and luminosity), that validates these findings.

Appendix A

Radiative Transfer Calculations

A.1 Radiative Transfer Equations used for Column Density Determination

We used the following expressions to determine the column density of the different molecules. The column density is given by,

$$N_{\text{tot}} = \frac{3h\varepsilon_0}{2\pi^2 s\mu^2 g} J(T_{\text{ex}}) Q(T_{\text{ex}}) \tau \Delta v, \quad (\text{A.1})$$

where, Δv is the linewidth, ε_0 is the dielectric permittivity, $s\mu^2 g$ is the dipole moment, τ is the optical depth, h is the Planck constant, T_{ex} is the excitation temperature and $Q(T_{\text{ex}})$ is the partition function.

Here, $J(T_{\text{ex}})$ is defined as

$$J(T_{\text{ex}}) = \frac{\exp(E_{\text{u}}/kT_{\text{ex}})}{\exp(h\nu/kT_{\text{ex}}) - 1}, \quad (\text{A.2})$$

where E_{u} is the upper energy level, k is the Boltzmann constant and ν is the frequency of observed transition. We assume that the excitation temperature is the same for all rotational levels. Equation(A.1) is valid for the optically thick case.

In the optically thin case,

$$N_{\text{tot}} = \frac{3h\varepsilon_0}{2\pi^2 s\mu^2 g} \frac{J(T_{\text{ex}}) Q(T_{\text{ex}}) W}{J1(\nu, T_{\text{ex}}) - J1(\nu, 2.7)}, \quad (\text{A.3})$$

where W is the integrated intensity and $J1(\nu, T)$ is defined as $J1(\nu, T) = \frac{h\nu/k}{\exp(h\nu/kT) - 1}$.

The partition function $Q(T_{\text{ex}})$ at temperature T_{ex} is estimated as $Q(T_{\text{ex}}) = \alpha T^{\beta}$, where α and β are the best fit parameters from a fit to the partition function obtained from JPL catalogue at different excitation temperatures from 10 – 300 K. In Table A.1, we give the dipole moments we used for different molecules and the partition function, $Q(T_{\text{ex}})$ at temperature $T_{\text{ex}} = 9.375$. The kinetic temperature and NH_3 column density, have been derived using the standard formulation for NH_3 spectra (Ho & Townes 1983). For the estimation of column density of C^{18}O we used the same formalism as Caselli et al. (2002).

A.2 Radiative Transfer Model

We iteratively solved the energy equation

$$\int \kappa_{\nu} J_{\nu} d\nu = \int \kappa_{\nu} B_{\nu}(T_{\text{d}}) d\nu$$

Table A.1: Molecular Parameters Used to Estimate N_{tot}

Transition	$s\mu^2g$	$Q(9.375)$
	D	
NH ₂ D 1 ₁₁ -1 ₀₁	11.9	26.2956
NHD ₂ 1 ₁₀ -1 ₀₁	0.722	25.62
H ¹³ CN J=1-0, F=2-1	8.912	4.87
HC ¹⁵ N 1-0	8.909	4.88

, together with two integral radiative transfer equations

$$I^+(\tau) = e^{-\tau} \left(I^+(0) + \int_0^\tau S(x) e^x dx \right)$$

$$I^-(t) = e^{-t} \int_0^t S(x) e^x dx$$

Here κ_ν denotes the dust extinction coefficient, J_ν the mean intensity, and $B_\nu(T_d)$ the Planck function at dust temperature T_d . In the formulae for the radiative transfer, $I^+(\tau)$ is the intensity directed towards the observer at optical depth τ , frequency ν , and impact parameter p , while I^- refers to beams away from the observer. The source function $S(\tau)$ includes a scattering term. The optical thickness τ and geometrical length z are related through $d\tau = \rho\kappa dz$, where ρ is the density. Index ν has been dropped for convenience of writing.

There are two boundary conditions. One states that the standard interstellar radiation field (ISRF) impinges at the cloud surface ($I_\nu^- = I_\nu^{\text{ISRF}}$), the other reads $I^+ - I^- = 0$ at $\tau = 0$ (where also $z = 0$) at impact parameters p greater than the stellar radius R_* , and that $I^+ - I^- = F_*\nu/\pi$ at the stellar surface ($F_{*\nu}$ is the stellar flux at frequency ν).

Appendix B

List of Publications

Refereed Articles

Pillai, T., Wyrowski, F., Menten, K.M., Krügel, E. 2006, ArXiv Astrophysics e-prints, arXiv:astro-ph/0510622 , Accepted for Publication in A&A, *High mass star formation in the infrared dark cloud G11.11-0.12*

Szymczak, M., Pillai, T., & Menten, K.M. 2005, A&A, 434, 613: *Masers as signposts of high-mass protostars: A water maser survey of methanol maser sources*

Pillai, T., Wyrowski, F., Carey, S.J., Menten, K.M. 2006, Accepted for Publication in A&A: *Ammonia in Infrared dark clouds*

Pillai, T., Wyrowski, F., Hatchell, J., Gibb, A.G., & Thompson, M.A. 2005, to be submitted to A&A: *Deuteration and Depletion in Massive Cold Cores: Probing the initial conditions of High Mass Star formation*

Pillai, Thushara, Kauffmann, Jens, Friedrich Wyrowski. 2005, to be submitted to A&A: *The Structure of High-Mass Cold IR-Dark Clouds: Breakdown of Self-Similarity and Low-Density Envelopes*

Conference Proceedings

Menten, K. M., Pillai, T., & Wyrowski, F. 2005, IAU Symposium, 227, 23 : *Initial conditions for massive star birth-Infrared dark clouds*

Wyrowski, F., Pillai, T., Hatchell, J., Gibb, A.G., & Thompson, M.A. 2005, The Dusty and Molecular Universe: A Prelude to Herschel and ALMA, 443 : *High deuteration towards a new sample of massive cold cores*

Thompson, M. A., Gibb, A. G., Hatchell, J., Wyrowski, F., & Pillai, T. 2005, The Dusty and Molecular Universe: A Prelude to Herschel and ALMA, 425 : *SCAMPS: the SCUBA Massive Precluster Survey*

Acknowledgements

To start with, I would like to thank Dr. Friedrich Wyrowski (my advisor) for offering me this project and giving me all timely support and advice even amidst his APEX responsibilities.

I am grateful to Prof. Karl Menten, who has been the most understanding supervisor one could imagine. I had lots of fun spending long nights and days of observing runs with him in Effelsberg.

I am thankful to Dr. Endrik Krügel for being the most friendly person in the group. A piece of wisdom that I happened to gather from him: There are three kinds of people who survive in Astronomy: *i*) ones who are naturally brilliant; *ii*) ones who are technically useful; *iii*) ones who are protected. “Thushara, you may now know every thing about these infrared dark clouds, but that isn’t worth much.”

A big thanks goes to Prof. Frank Bertoldi for having consented to be the referee for my thesis.

I am grateful to Prof. Brock (Physics Department) and Prof. Baier (Informatics Department), for having agreed to read a thesis in Astronomy.

I thank Dr. Malcolm Walmsley for volunteering to read my thesis on short notice and giving me valuable advice on several occasions.

A lot of thanks goes to my colleagues in the Kinderzimmer: Hauke, Jan, Lars and Jens. Without the occasional chats with Hauke at the oddest time in the nights and the competition among us as to who would survive until the break of the dawn breaking our backs in front of our PCs, I think I would have been half as enthusiastic. I thank Anu, Silvia, Edward and Caroline for cheering me up during the little breaks.

I am grateful to Frau Lahr-Nilles, Frau Lewinsky, Frau Breuer and Frau Fingas for seeing me through all administration hurdles. I thank Dr. Alex Kraus and the Operators of Effelsberg Telescope for their kind cooperation. I thank Dr. Zensus and Dr. Eduardo Ros for giving me the opportunity to attend conferences and summer schools.

As a colleague, I am grateful to Jens for persistently trying to show me the right way of doing Science.

Finally, I feel too formal to thank my dear parents and my sister, who are waiting for me to come back home. I know that their blessings are with me.

Curriculum Vitae

Name: Thushara Pillai
Date of Birth: 20.06.1980
Nationality: Indian
Sex: Female
Present Address: Max-Planck-Institut fuer Radioastronomie
Auf dem Huegel 69, 53121, Bonn

Education:

06/1985 – 04/1995: Primary and Secondary School,
Kendriya Vidyalaya, Pattom, Thiruvananthapuram
06/1995 – 04/1997: Senior Secondary School,
Kendriya Vidyalaya, Pattom, Thiruvananthapuram
06/1997 – 04/2000: BSc (Physics),
University of Kerala, Thiruvananthapuram
05/2000 – 05/2002: MSc (Physics),
Indian Institute of Technology (IIT), Madras
12/2002 – 12/2005: Graduate student,
Max-Planck-Institut fuer Radioastronomie (MPIFR)

Research Experience:

Summer Project, 2001: Theoretical and Experimental Studies towards RFI shielding of PCs
at a Radio astronomy station,
National Center for Radio Astrophysics, Pune
Master Thesis, 2002: Study of Trapped Atoms,
Physics department, IIT Madras
PhD Thesis, 2002 – 2005 : Initial Conditions of High Mass Star Formation,
Millimeter and Submillimeter Astronomy Group , MPIFR, Bonn

Bibliography

- André, P., Ward-Thompson, D., & Barsony, M. 1993, *ApJ*, 406, 122
- Argon, A. L., Reid, M. J., & Menten, K. M. 2000, *ApJS*, 129, 159
- Bachiller, R., Guilloteau, S., & Kahane, C. 1987, *A&A*, 173, 324
- Bacmann, A., André, P., Puget, J.-L., et al. 2000, *A&A*, 361, 555
- Bacmann, A., Lefloch, B., Ceccarelli, C., et al. 2002, *A&A*, 389, L6
- . 2003, *ApJ*, 585, L55
- Bergin, E. A. 2003, in *SFCHEM 2002: Chemistry as a Diagnostic of Star Formation*, proceedings of a conference held August 21-23, 2002 at University of Waterloo, Waterloo, Ontario, Canada N2L 3G1. Edited by Charles L. Curry and Michel Fich. NRC Press, Ottawa, Canada, 2003, p. 63., 63–+
- Bergin, E. A. & Langer, W. D. 1997, *ApJ*, 486, 316
- Bertoldi, F. & McKee, C. F. 1992, *ApJ*, 395, 140
- Beuther, H., Schilke, P., Menten, K. M., et al. 2002a, *ApJ*, 566, 945
- Beuther, H., Schilke, P., Sridharan, T. K., et al. 2002b, *A&A*, 383, 892
- Beuther, H. & Shepherd, D. 2005, *ArXiv Astrophysics e-prints*
- Beuther, H., Sridharan, T. K., & Saito, M. 2005, *ArXiv Astrophysics e-prints*
- Beuther, H., Walsh, A., Schilke, P., et al. 2002c, *A&A*, 390, 289
- Błaszkiwicz, L. & Kus, A. J. 2004, *A&A*, 413, 233
- Blitz, L. & Williams, J. P. 1997, *ApJ*, 488, L145+
- Blitz, L. & Williams, J. P. 1999, in *NATO ASIC Proc. 540: The Origin of Stars and Planetary Systems*, 3–+
- Bohlin, R. C., Savage, B. D., & Drake, J. F. 1978, *ApJ*, 224, 132
- Bonnell, I. A., Bate, M. R., & Zinnecker, H. 1998, *MNRAS*, 298, 93
- Boss, A. P. 1995, *ApJ*, 439, 224
- Braz, M. A. & Epchtein, N. 1983, *A&AS*, 54, 167
- Brogan, C. L., Devine, K. E., Lazio, T. J., et al. 2004, *AJ*, 127, 355

- Brown, P. D. & Millar, T. J. 1989a, MNRAS, 240, 25P
- . 1989b, MNRAS, 237, 661
- Cambrésy, L. 1999, A&A, 345, 965
- Carey, S. J., Clark, F. O., Egan, M. P., et al. 1998, ApJ, 508, 721
- Carey, S. J., Feldman, P. A., Redman, R. O., et al. 2000, ApJ, 543, L157
- Caselli, P., Benson, P. J., Myers, P. C., & Tafalla, M. 2002, ApJ, 572, 238
- Caselli, P., van der Tak, F. F. S., Ceccarelli, C., & Bacmann, A. 2003, A&A, 403, L37
- Caselli, P., Walmsley, C. M., Tafalla, M., Dore, L., & Myers, P. C. 1999, ApJ, 523, L165
- Caswell, J. L. 1996, MNRAS, 279, 79
- Cesaroni, R. 1990, A&A, 233, 513
- Cesaroni, R., Churchwell, E., Hofner, P., Walmsley, C. M., & Kurtz, S. 1994, A&A, 288, 903
- Cesaroni, R., Hofner, P., Walmsley, C. M., & Churchwell, E. 1998, A&A, 331, 709
- Cesaroni, R. & Wilson, T. L. 1994, A&A, 281, 209
- Codella, C., Lorenzani, A., Gallego, A. T., Cesaroni, R., & Moscadelli, L. 2004, A&A, 417, 615
- Crapsi, A., Caselli, P., Walmsley, C. M., et al. 2005, ApJ, 619, 379
- Dahmen, G., Wilson, T. L., & Matteucci, F. 1995, A&A, 295, 194
- Dobashi, K., Uehara, H., Kandori, R., et al. 2005, PASJ, 57, 1
- Draine, B. T. 2003, ARA&A, 41, 241
- Draine, B. T. & Lee, H. M. 1984, ApJ, 285, 89
- Edris, K. A., Fuller, G. A., Cohen, R. J., & Etoke, S. 2005, A&A, 434, 213
- Egan, M. P., Shipman, R. F., Price, S. D., et al. 1998, ApJ, 494, L199+
- Elitzur, M., Hollenbach, D. J., & McKee, C. F. 1989, ApJ, 346, 983
- Ellingsen, S. P. 2005, ArXiv Astrophysics e-prints
- Elmegreen, B. G. & Morris, M. 1979, ApJ, 229, 593
- Forster, J. R. & Caswell, J. L. 1989, A&A, 213, 339
- Forveille, T., Guilloteau, S., & Lucas, R. 1989, Grenoble: IRAM
- Ferking, M. A., Langer, W. D., & Wilson, R. W. 1982, ApJ, 262, 590
- Garay, G., Faúndez, S., Mardones, D., et al. 2004, ApJ, 610, 313
- Garay, G. & Lizano, S. 1999, PASP, 111, 1049
- Goedhart, S., van der Walt, D. J., & Schutte, A. J. 2000, MNRAS, 315, 316

- Green, D. A. 1989, *MNRAS*, 238, 737
- . 2002, *VizieR Online Data Catalog*, 7227, 0
- Green, D. A. & Dewdney, P. E. 1992, *MNRAS*, 254, 686
- Hatchell, J. 2003, *A&A*, 403, L25
- Hennebelle, P., Pérault, M., Teyssier, D., & Ganesh, S. 2001, *A&A*, 365, 598
- Hill, T., Burton, M. G., Minier, V., et al. 2005, *MNRAS*, 796
- Hirota, T., Yamamoto, S., Mikami, H., & Ohishi, M. 1998, *ApJ*, 503, 717
- Ho, P. T. P. & Townes, C. H. 1983, *ARA&A*, 21, 239
- Hofner, P. & Churchwell, E. 1996, *A&AS*, 120, 283
- Ikeda, M., Hirota, T., & Yamamoto, S. 2002, *ApJ*, 575, 250
- Indebetouw, R., Mathis, J. S., Babler, B. L., et al. 2005, *ApJ*, 619, 931
- Jijina, J., Myers, P. C., & Adams, F. C. 1999, *ApJS*, 125, 161
- Johnstone, D., Fich, M., Mitchell, G. F., & Moriarty-Schieven, G. 2001, *ApJ*, 559, 307
- Johnstone, D., Fiege, J. D., Redman, R. O., Feldman, P. A., & Carey, S. J. 2003, *ApJ*, 588, L37
- Keto, E. 2002, *ApJ*, 580, 980
- Kramer, C., Alves, J., Lada, C. J., et al. 1999, *A&A*, 342, 257
- Krügel, E. 2003, *Astronomy and Geophysics*, 44, 35
- Krügel, E. & Siebenmorgen, R. 1994, *A&A*, 288, 929
- Kuiper, T. B. H., Peters, W. L., Forster, J. R., Gardner, F. F., & Whiteoak, J. B. 1995, *ApJ*, 446, 692
- Kurtz, S. 2002, in *ASP Conf. Ser. 267: Hot Star Workshop III: The Earliest Phases of Massive Star Birth*, 81–+
- Lada, C. J. 1987, in *IAU Symp. 115: Star Forming Regions*, 1–15
- Ladd, E. F., Myers, P. C., & Goodman, A. A. 1994, *ApJ*, 433, 117
- Lai, S.-P., Velusamy, T., Langer, W. D., & Kuiper, T. B. H. 2003, *AJ*, 126, 311
- Langer, W. D. & Penzias, A. A. 1993, *ApJ*, 408, 539
- Launhardt, R. 1996, Ph.D. Thesis
- Launhardt, R. & Henning, T. 1997, *A&A*, 326, 329
- Leurini, S., Schilke, P., Menten, K. M., et al. 2004, *A&A*, 422, 573
- Lis, D. C. & Carlstrom, J. E. 1994, *ApJ*, 424, 189
- Lis, D. C. & Menten, K. M. 1998, *ApJ*, 507, 794
- Lis, D. C., Menten, K. M., Serabyn, E., & Zylka, R. 1994, *ApJ*, 423, L39

- Lucas, R. & Liszt, H. 1998, *A&A*, 337, 246
- Lutz, D., Feuchtgruber, H., Genzel, R., et al. 1996, *A&A*, 315, L269
- Mangum, J. G. & Wootten, A. 1993, *ApJS*, 89, 123
- McKee, C. F. & Tan, J. C. 2003, *ApJ*, 585, 850
- Menten, K. M., Pillai, T., & Wyrowski, F. 2005, in *IAU Symposium*, 23–34
- Millar, T. J. 2002, *Planet. Space Sci.*, 50, 1189
- . 2003, *Space Science Reviews*, 106, 73
- Minier, V., Booth, R. S., & Conway, J. E. 1998, *A&A*, 336, L5
- Minier, V., Ellingsen, S. P., Norris, R. P., & Booth, R. S. 2003, *A&A*, 403, 1095
- Molinari, S., Testi, L., Rodríguez, L. F., & Zhang, Q. 2002, *ApJ*, 570, 758
- Motte, F., Andre, P., & Neri, R. 1998, *A&A*, 336, 150
- Motte, F., Schilke, P., & Lis, D. C. 2003, *ApJ*, 582, 277
- Norris, R. P., Byleveld, S. E., Diamond, P. J., et al. 1998, *ApJ*, 508, 275
- Ormel, C. W., Shipman, R. F., Ossenkopf, V., & Helmich, F. P. 2005, *A&A*, 439, 613
- Ossenkopf, V. & Henning, T. 1994, *A&A*, 291, 943
- Ott, M., Witzel, A., Quirrenbach, A., et al. 1994, *A&A*, 284, 331
- Padoan, P. & Nordlund, Å. 2002, *ApJ*, 576, 870
- Perault, M., Omont, A., Simon, G., et al. 1996, *A&A*, 315, L165
- Phillips, C. J., Norris, R. P., Ellingsen, S. P., & McCulloch, P. M. 1998, *MNRAS*, 300, 1131
- Pillai, T., Wyrowski, F., Menten, K. M., & Carey, S. 2006a, accepted *A&A*
- Pillai, T., Wyrowski, F., Menten, K. M., & Krügel, E. 2006b, *A&A*, 447, 929
- Ponomarev, V. O., Smith, H. A., & Strelitski, V. S. 1994, *ApJ*, 424, 976
- Price, S. D. 1995, *Space Science Reviews*, 74, 81
- Price, S. D., Egan, M. P., Carey, S. J., Mizuno, D. R., & Kuchar, T. A. 2001, *AJ*, 121, 2819
- Pudritz, R. E. 2002, *Science*, 295, 68
- Rathborne, J. M., Jackson, J. M., Chambers, E. T., et al. 2005, *ArXiv Astrophysics e-prints*
- Redman, R. O., Feldman, P. A., Wyrowski, F., et al. 2003, *ApJ*, 586, 1127
- Reid, M. J., Schneps, M. H., Moran, J. M., et al. 1988, *ApJ*, 330, 809
- Roberts, H. & Millar, T. J. 2000a, *A&A*, 364, 780
- . 2000b, *A&A*, 361, 388

- Rodgers, S. D. & Charnley, S. B. 2001, *ApJ*, 553, 613
- Rohlfs, K. & Wilson, T. L. 2004, *Tools of radio astronomy* (Tools of radio astronomy, 4th rev. and enl. ed., by K. Rohlfs and T.L. Wilson. Berlin: Springer, 2004)
- Roueff, E., Lis, D. C., van der Tak, F. F. S., Gerin, M., & Goldsmith, P. F. 2005, *A&A*, 438, 585
- Saito, S., Ozeki, H., Ohishi, M., & Yamamoto, S. 2000, *ApJ*, 535, 227
- Savage, B. D. & Mathis, J. S. 1979, *ARA&A*, 17, 73
- Schilke, P., Walmsley, C. M., Pineau Des Forets, G., et al. 1992, *A&A*, 256, 595
- Shah, R. Y. & Wootten, A. 2001, *ApJ*, 554, 933
- Simon, R., Jackson, J. M., Rathborne, J. M., & Chambers, E. T. 2005, *ArXiv Astrophysics e-prints*
- Simon, R., Shah, R. Y., Rathborne, J., et al. 2004, in *ASP Conf. Ser. 317: Milky Way Surveys: The Structure and Evolution of our Galaxy*, 159–+
- Stutzki, J. & Guesten, R. 1990, *ApJ*, 356, 513
- Tafalla, M., Myers, P. C., Caselli, P., & Walmsley, C. M. 2004, *A&A*, 416, 191
- Tafalla, M., Myers, P. C., Caselli, P., Walmsley, C. M., & Comito, C. 2002, *ApJ*, 569, 815
- Tafalla, M. & Santiago, J. 2004, *A&A*, 414, L53
- Tan, J. C. 2005, *ArXiv Astrophysics e-prints*
- Testi, L. & Sargent, A. I. 1998, *ApJ*, 508, L91
- Teyssier, D., Hennebelle, P., & Pérault, M. 2002, *A&A*, 382, 624
- Thompson, M. A., Gibb, A. G., Hatchell, J. H., Wyrowski, F., & Pillai, T. 2005, in *The Dusty and Molecular Universe: A Prelude to Herschel and ALMA*, 425–426
- van der Tak, F. F. S. & Menten, K. M. 2005, *A&A*, 437, 947
- Walmsley, C. M. & Ungerechts, H. 1983, *A&A*, 122, 164
- Walsh, A. J., Bertoldi, F., Burton, M. G., & Nikola, T. 2001, *MNRAS*, 326, 36
- Walsh, A. J., Burton, M. G., Hyland, A. R., & Robinson, G. 1998, *MNRAS*, 301, 640
- Walsh, A. J., Macdonald, G. H., Alvey, N. D. S., Burton, M. G., & Lee, J.-K. 2003, *A&A*, 410, 597
- Ward-Thompson, D. 2002, *Science*, 295, 76
- Weingartner, J. C. & Draine, B. T. 2001, *ApJS*, 134, 263
- Wielen, R. & Wilson, T. L. 1997, *A&A*, 326, 139
- Williams, J. 1999, in *Interstellar Turbulence*, 190–+
- Wilson, T. L. & Rood, R. 1994, *ARA&A*, 32, 191
- Wiseman, J. J. & Ho, P. T. P. 1998, *ApJ*, 502, 676
- Wolfire, M. G. & Cassinelli, J. P. 1987, *ApJ*, 319, 850

- Wood, D. O. S. & Churchwell, E. 1989, *ApJS*, 69, 831
- Wyrowski, F., Schilke, P., Thorwirth, S., Menten, K. M., & Winnewisser, G. 2003, *ApJ*, 586, 344
- Zinnecker, H. & Bate, M. R. 2002, in *ASP Conf. Ser. 267: Hot Star Workshop III: The Earliest Phases of Massive Star Birth*, 209–+